Investigation of Hybrid Battery Thermal Management Systems Utilising Metal Foam, Phase Change Material, and Liquid Cooling

A thesis submitted to the Department of Engineering, School of Architecture, Built Environment, Computing and Engineering, in partial fulfilment for the degree of
Doctor of Philosophy

By
Alireza Keyhani Asl

Supervised by

Dr. Noel Perera

Dr. Jens Lahr

Professor Reaz Hasan

September 2025

DECLARATION OF AUTHORSHIP

I, Alireza Keyhani Asl, assert my right to be identified as the author of this work in accordance with the Copyright, Designs and Patents Act 1988.

The work contained in this thesis has not been previously submitted to meet requirements for an award at this or any other higher education institution. To the best of my knowledge and belief, the thesis contains no material previously published or written by another person except where due reference is made.

Signature:

Alireza Keyhani
Asl

ABSTRACT

Effective thermal management is critical for ensuring the safety, efficiency, and longevity of lithium-ion batteries (LIBs), particularly under high C-rate operation. This thesis presents the development and investigation of a novel Hybrid Battery Thermal Management System (HBTMS) that integrates phase change material (PCM), copper metal foam (in the form of porous fins and layers), and liquid cooling to overcome the limitations of conventional thermal management approaches. The system aims to enhance thermal regulation, energy density, and long-term performance stability under dynamic cycling conditions.

A validated numerical framework was developed using ANSYS Fluent to simulate transient heat generation in cylindrical LIBs, incorporating a lumped-capacitance thermal model. The enthalpy–porosity method was used to model the phase change behaviour of the PCM, while fluid flow through the copper foam was simulated using the Darcy–Brinkman–Forchheimer (DBF) model. Local Thermal Equilibrium (LTE) and Local Thermal Non-Equilibrium (LTNE) models were applied to represent heat transfer within the copper foam fins and copper foam layers, respectively. Multi-objective optimisation was conducted using the Taguchi Design of Experiments (DOE) and ANOVA to identify dominant design and operational parameters.

The results demonstrate that the proposed HBTMS effectively reduced maximum surface temperature ($T_{Max,Sur}$) by up to 9.2 K compared to pure PCM, while maintaining ΔT_{Max} below 5 K. The system showed up to 97% reduction in PCM liquid fraction and enabled full latent heat recovery across repeated discharge–rest–charge cycles. Energy density improved by up to 25% due to lightweight copper foam structures. Parametric studies identified ambient and coolant temperatures, flow rate, and number of cooling plates as the most influential factors. The optimised configuration provided high thermal performance with enhanced energy density and improved repeatability across cyclic conditions. Overall, this research contributes a robust and scalable hybrid cooling solution for high-performance battery systems, offering enhanced safety, durability, and energy efficiency suitable for electric vehicle and energy storage applications.

Keywords:

Hybrid Battery Thermal Management System; Energy Density; Lithium-ion Battery; Phase Change Material; Copper foam; Cooling Plates

ACKNOWLEDGEMENTS

This thesis was made possible through the funding provided by Birmingham City University and the invaluable support of many individuals, to whom I am sincerely grateful.

Above all, I would like to express my heartfelt appreciation to my supervisory team: Dr. Noel Perera, my Director of Studies, and my supervisors, Dr. Jens Lahr and Professor Reaz Hasan. Their expert guidance, constructive feedback, and unwavering support have been instrumental throughout my PhD journey. Their depth of knowledge and thoughtful mentorship have significantly shaped both my research and the writing of this thesis.

I am especially thankful to Dr. Roger Tait for his expert advice on High-Performance Computing resources. I also extend my thanks to the staff of the Doctoral Research College (DRC), the Department of Engineering, the technical team, and the IT help desk at Birmingham City University for their assistance and the facilities that contributed to the success of this research.

I owe immense gratitude to my family for their unconditional love, patience, and encouragement. Their unwavering belief in me has been the foundation of my resilience and accomplishments. No words can truly convey how thankful I am to have them in my life.

I would also like to thank my colleagues and fellow PhD students for making my time at the university both enjoyable and intellectually stimulating. Finally, I extend my deepest thanks to my closest friends, whose emotional support and understanding carried me through the most challenging moments of this journey.

TABLE OF CONTENTS

DECLARATION OF AUTHORSHIP ii

ABSTRACT iii

ACKNOWLEDGEMENTS iv

Table of Contents v

List of Figures vii

List of Tables xiii

NOMENCLATURE xv

Chapter 1: Introduction 1

1.1 Research Question 4

1.2 Research Aim 4

1.3 Research Objectives 4

1.4 Thesis Outline 5

1.5 Publications 6

Chapter 2: Literature Review 9

2.1 Influence of Temperature on Battery Performance 10

2.2 Modelling and Analysis of Heat Generation in Lithium-Ion Batteries 11

2.3 Role of Porous Media and Metal Foams in Battery Thermal Management Systems ... 16
  2.3.1 Heat Transfer Mechanisms and Enhancements Through Porous Structures 17
  2.3.2 Effect of Porous Media Characteristics on the Efficiency of BTMS 19
  2.3.3 Numerical Simulation of Porous Media 22

2.4 Applications, Challenges, and Limitations of Porous Media in Different BTMSs 27
  2.4.1 Air-Cooled BTMS Enhanced by Porous Media 27
  2.4.2 PCM-Based BTMS Enhanced by Porous Media 32
  2.4.3 Impact of Adding Porous Media on PCM Properties and Performance of PCM-based BTMS 44
  2.4.4 Liquid Cooling-Based BTMS Enhanced by Porous Media 46
  2.4.5 Hybrid Cooling-Based BTMS Enhanced by Porous Media 51

2.5 Conclusion 60

Chapter 3: Research Methodology 63

3.1 Problem Statement and Description of the Proposed HBTMS 63

3.2 Numerical Modelling 66
  3.2.1 Modelling of Transient Heat Generation in Batteries 66
  3.2.2 Governing Equations, Boundary Conditions, and Assumptions 68

3.3 Taguchi's Design of Experiments (DOE) 74

3.4 ANOVA Technique 75

3.5 Mesh Independence, Time-step Independence Studies, and Validation 76

Chapter 4: Comparative Assessment and Parametric Study of the Proposed Copper Foam-Enhanced HBTMS 83

4.1 Comparison of the Proposed HBTMS with PCM Based BTMSs 83

4.2 Copper Foam Fins Porosity and Pore Density 99

4.3 Copper Foam Layer Porosity and Pore Density Within the Copper Tube 104

4.4 Quantity of Copper Foam Fins and Thickness 113

4.5 Number of the Cooling Plates 121

4.6 Copper Foam Layers Thickness 127

4.7 Liquid Cooling Inlet Mass Flow Rate and Temperature 133

4.8 Ambient Temperature 140

Chapter 5: Multi-Objective Optimisation and Performance Evaluation of the Proposed HBTMS 145

5.1 Taguchi Design of Experiments for Multi-Parameter Analysis of HBTMS 145

5.2 Multi-Response Statistical Analysis for HBTMS Optimisation via Taguchi and ANOVA 152
- 5.2.1 Impact Assessment of Design and Operational Parameters on $T_{Max,Sur}$ 153
- 5.2.2 Impact Assessment of Design and Operational Parameters on ΔT_{Max} 157
- 5.2.3 Impact Assessment of Design and Operational Parameters on PEC 161
- 5.2.4 Impact Assessment of Design and Operational Parameters on E_d 166

5.3 Multi-Objective Optimisation and Evaluation of HBTMS Design Parameters 170

Chapter 6: Cyclic Performance of the Proposed HBTMS 175

6.1 Cyclic Charge and Discharge Performance of the HBTMS 175
- 6.1.1 Type I Cycles 176
- 6.1.2 Type II Cycles 179
- 6.1.3 Type III Cycles 183

Chapter 7: Conclusions and Future Work 189

7.1 Conclusions 189

7.2 Future Work 191

References 193

Appendices 214

LIST OF FIGURES

Figure 1-1. Ragone plot of various types of batteries in terms of specific power and energy [9]..2

Figure 1-2. Different type of lithium-ion batteries (a) cylindrical, (b) prismatic, and (c) pouch cells [10]...2

Figure 1-3. Impact of the various temperature on LIB [27] 3

Figure 2-1. Temperature-dependent discharge performance of 18650 LIB [59]........11

Figure 2-2. Schematic of different heat generation forms in LIB [62]. 12

Figure 2-3. Heat generation in LIBs [75]..15

Figure 2-4. Heat generation of a single battery during charge–discharge cycles at 25℃ [89]...16

Figure 2-5. (a) Copper metal foam [103] and (b) tortuosity in porous media [104]...17

Figure 2-6. Heat transfer enhancement offered by porous media.............................18

Figure 2-7. Application trends of various foams for thermal performance improvement in the literature [136]. 21

Figure 2-8. Thermal behaviour of a PCM-based system [49]. 33

Figure 2-9. Impact of PCM cooling on 18650 LIBs charging and discharging performance [79]. 34

Figure 2-10. Distribution of different porous materials and foams for PCM thermal conductivity enhancement [233]...44

Figure 3-1. Proposed HBTMS (a) system components, (b) dimensional specifications for different number of cooling plates, and (c) dimensional specifications for copper tube with copper foam layer (DETAIL B) shown in mm............................65

Figure 3-2. Generated mesh for the HBTMS..77

Figure 3-3. Validation of the transient battery heat generation model: (a) experimental set up for battery thermal model validation [273] (b) comparison of present numerical and experimental battery surface temperatures [273, 278, 279], (c) absolute error (K) and relative error (%), and (d) corresponding transient volumetric heat generation at various discharge rates.................................78

Figure 3-4. Validation of PCM filled metal foam model based on the experimental and numerical study of Hu et al.[310]: (a) experimental setup with aluminium foam–paraffin composite, (b) corresponding numerical model and boundary conditions, (c) comparison of the present numerical results with experimental data, and (d) absolute error (K) and relative error (%)...............................80

Figure 3-5. Validation of the liquid cooling model against the experimental and numerical study of Xin et al. [278]: (a) liquid-cooled BTMS configuration, (b) comparison between the present numerical results and the reported maximum battery surface temperatures, and (c) absolute error (K) and relative error (%). 81

Figure 3-6. Validation of the copper foam filled tube model based on the experimental study of Amani et al. [311]: (a) experimental configuration of the copper foam filled tube; (b) comparison of average Nusselt number; (c) comparison of pressure drop; and (d, e) corresponding absolute error and relative error (%).82

Figure 4-1. Maximum battery surface temperature for different BTMS under various battery discharge rates: (a) 5C, (b) 3C, and (c) 1C. 85

Figure 4-2. PCM liquid fraction for different BTMS under various battery discharge rates: (a) 5C, (b) 3C, (c) 1C, and (d) cross sectional velocity field of the molten PCM within the copper foam fins under natural convection. 88

Figure 4-3. PCM liquid fraction contour plots for different BTMS at the end of the 5C discharge rate: (a) pure PCM, (b) PCM with solid fins, (c) PCM with copper foam fins, (d) PCM with copper foam fins and liquid cooling, and (e) PCM with copper foam fins, liquid cooling with copper foam layers. 89

Figure 4-4. Average Nusselt number on batteries surface for different BTMS under various battery discharge rates: (a) 5C, (b) 3C, and (c) 1C. 91

Figure 4-5. Comparison of dimensionless (a) velocity and (b) temperature at the middle of the copper tube along the vertical axis with and without copper foam layer at the end of 5C discharge rate. 92

Figure 4-6. Maximum temperature difference within the battery module for different BTMS under various battery discharge rates: (a) 5C, (b) 3C, and (c) 1C. ...95

Figure 4-7. Static temperature contour plots for different BTMSs and HBTMS at the end of the 5C discharge rate: (a) pure PCM, (b) PCM with solid fins, (c) PCM with copper foam fins, (d) PCM with copper foam fins and liquid cooling, and (e) PCM with copper foam fins, liquid cooling with copper foam layers..........96

Figure 4-8. $T_{Max,Sur}$, $\Delta T_{Max,b}$ at the end of discharge for the HBTMS under investigation for different discharge rates: (a) 5C, (b) 3C, and (c) 1C..............................97

Figure 4-9. Comparison of HBTMS performance in terms of (a) the PCM volume in different fin configurations (b) energy density with different fin configurations and (c) PEC value at various discharge rates..99

Figure 4-10. Effect of copper foam fin properties on maximum battery surface temperature in terms of (a) porosity and (b) pore density. 101

Figure 4-11. Effect of copper foam fin properties on PCM liquid fraction in terms of (a) porosity and (b) pore density. 101

Figure 4-12. Effect of copper foam fin properties on the average Nusselt number on the battery surface in terms of (a) porosity and (b) pore density. 102

Figure 4-13. $T_{Max,Sur}$, $\Delta T_{Max,b}$ at the end of 5C discharge for the HBTMS with different copper foam fins' (a) porosity and (b) pore density. 103

Figure 4-14. Comparison of (a) PCM volume and (b) energy density for HBTMS with different copper foam fins' porosity. 104

Figure 4-15. Effect of copper foam layer properties on maximum battery surface temperature in terms of (a) porosity and (b) pore density. 106

Figure 4-16. Effect of copper foam layer porosity on (a) dimensionless velocity, (b) dimensionless temperature, and (c) local Nusselt number at the middle of the copper tube along the vertical axis at the end of 5C discharge rate. 107

Figure 4-17. Effect of copper foam layer pore density on (a) dimensionless velocity, (b) dimensionless temperature, and (c) local Nusselt number at the middle of the copper tube along the vertical axis at the end of 5C discharge rate. 108

Figure 4-18. Effect of copper foam layer properties on PCM liquid fraction in terms of (a) porosity and (b) pore density...108

Figure 4-19. Effect of copper foam layer properties on the average Nusselt number on the battery surface in terms of (a) porosity and (b) pore density. 109

Figure 4-20. $T_{Max,Sur}$, $\Delta T_{Max,b}$ for the HBTMS with different copper foam layers' (a) porosity and (b) pore density at the end of 5C discharge rate. 111

Figure 4-21. Effect of copper foam layer properties on PEC in terms of (a) porosity and (b) pore density at the end of 5C discharge rate. 112

Figure 4-22. Comparison of energy density for HBTMS with different copper foam layers' porosity. 112

Figure 4-23. Impact of the different (a) quantity and (b) thickness of copper foam fins on batteries maximum surface temperature. 114

Figure 4-24. Impact of the different (a) quantity and (b) thickness of copper foam fins on PCM liquid fraction. 115

Figure 4-25. PCM liquid fraction contour plots for the HBTMS at the end of the 5C discharge, showing the effect of copper foam fin quantity with (a) 4 fins, (b) 6 fins, and (c) 8 fins, and fin thickness with (d) 2 mm, (e) 4 mm, and (f) 6 mm. 116

Figure 4-26. Battery surface average Nusselt number for HBTMS with different (a) quantity and (b) thickness of copper foam fins. 117

Figure 4-27. Maximum temperature difference within the battery module for HBTMS with different (a) quantity and (b) thickness of copper foam fins. 118

Figure 4-28. $T_{Max,Sur}$, $\Delta T_{Max,b}$ for the HBTMS at the end of the 5C discharge rate, showing the effect of copper foam fin quantity with (a) 4 fins, (b) 6 fins, and (c) 8 fins, and fin thickness with (d) 2 mm, (e) 4 mm, and (f) 6 mm.........................120

Figure 4-29. Energy density of the HBTMS with different (a) quantity and (b) thickness of copper foam fins. 120

Figure 4-30. Impact of the different number of cooling plates on (a) batteries maximum surface temperature and (b) PCM liquid fraction. 123

Figure 4-31. PCM liquid fraction contour plots for pure PCM and HBTMS with different number of cooling plates at the end of 5C discharge: (a) pure PCM, (b) one cooling plate with copper foam layers, (c) one cooling plate without copper foam layers, (d) two cooling plates with copper foam layers, (e) two cooling plates without copper foam layers, (f) three cooling plates with copper foam layers, and (g) three cooling plates without copper foam layers. 124

Figure 4-32. Battery surface average Nusselt number for pure PCM and HBTMS with different number of cooling plates at the end of 5C discharge..................125

Figure 4-33. Comparison of the $T_{Max,Sur}$ and $\Delta T_{Max,b}$ of the (a) pure PCM and (b) HBTMS with three cooling plates with copper foam layers at the end of 5C discharge. 126

Figure 4-34. Comparison of the static temperature contour plots of (a) pure PCM and (b) HBTMS with three cooling plates with copper foam layers at the end of 5C discharge. 126

Figure 4-35. Energy density of the HBTMS with different number of cooling plates with or without copper foam layers. 127

Figure 4-36. Impact of the copper foam layer thickness on (a) batteries maximum surface temperature and (b) PCM liquid fraction....128

Figure 4-37. Comparison of the $T_{Max,Sur}$ and $\Delta T_{Max,b}$ of the HBTMS at the end of the 5C discharge rate, showing the effect of copper foam layer thickness with (a) 0 mm, (b) 1 mm, (c) 2 mm, (d) 2.5 mm, (e) 3 mm, and (f) 4.2 mm. 130

Figure 4-38. Batteries surface average Nusselt number for HBTMS with different copper foam layer thickness at the end of 5C discharge. 132

Figure 4-39. (a) Dimensionless velocity and (b) temperature within the copper tube with different copper foam layer thickness at the end of 5C discharge....132

Figure 4-40. Impact of copper foam layer thickness on PEC. 133

Figure 4-41. Impact of the liquid cooling inlet (a) mass flow rate and (b) temperature on batteries maximum surface temperature. 134

Figure 4-42. Impact of the liquid cooling inlet (a) mass flow rate and (b) temperature on PCM liquid fraction. 135

Figure 4-43. PCM liquid fraction contour plots for the HBTMS at the end of the 5C discharge rate, showing the effect of liquid cooling inlet mass flow rate with (a) 0.0002 kg/s, (b) 0.001 kg/s, and (c) 0.002 kg/s, and inlet temperature with (d) 298.15 K, (e) 303.15 K, and (f) 308.15 K. 136

Figure 4-44. Impact of the liquid cooling inlet (a) mass flow rate and (b) temperature on battery surface average Nusselt number. 137

Figure 4-45. $T_{Max,Sur}$ and $\Delta T_{Max,b}$ for the HBTMS at the end of the 5C discharge rate, showing the effect of liquid cooling inlet mass flow rate with (a) 0.0002 kg/s, (b) 0.001 kg/s, and (c) 0.002 kg/s, and inlet temperature with (d) 298.15 K, (e) 303.15 K, and (f) 308.15 K. 139

Figure 4-46. Impact of the liquid cooling inlet (a) mass flow rate and (b) temperature on PEC. 140

Figure 4-47. Impact of the ambient temperature on (a) batteries maximum surface temperature and (b) PCM liquid fraction....142

Figure 4-48. PCM liquid fraction contour plots at different ambient temperatures at the end of the 5C discharge: (a) T_{Amb} = 303.15 K, (b) T_{Amb} = 308.15 K, (c) T_{Amb} = 313.15 K, and (d) T_{Amb} = 318.15 K. 142

Figure 4-49. Batteries surface average Nusselt number for HBTMS at different ambient temperatures at end of the 5C discharge. 143

Figure 4-50. $T_{Max,Sur}$ and $\Delta T_{Max,b}$ for the HBTMS at the end of the 5C discharge rate for different ambient temperatures: (a) T_{Amb} = 303.15 K, (b) T_{Amb} = 308.15 K, (c) T_{Amb} = 313.15 K, and (d) T_{Amb} = 318.15 K. 144

Figure 5-1. Static temperature and PCM liquid fraction contour plots at the end of the 5C discharge for different cases. 151

Figure 5-2. Mean of maximum battery surface temperature ($T_{Max,Sur}$) for various factors and levels at the end of the 5C discharge rate. 155

Figure 5-3. Mean of maximum temperature difference within the battery module (ΔT_{Max}) for various factors and levels at the end of the 5C discharge rate. 159

Figure 5-4. Mean of performance evaluation criteria (PEC) for various factors and levels at the end of the 5C discharge rate...163

Figure 5-5. Mean of energy density (E_d) for various factors and levels at the end of the 5C discharge rate. 167

Figure 5-6. Mean of means for various factors and levels at the end of the 5C discharge rate. 172

Figure 6-1. Performance of the HBTMS under Type I cycles in terms of (a) maximum battery surface temperature, (b) PCM liquid fraction, and (c) maximum temperature difference within the battery module....................................178

Figure 6-2. Static temperature and PCM liquid fraction contour plots of the HBTMS and pure PCM under Type I cycles at the end of the first and fifth cycle.........179

Figure 6-3. Performance of the HBTMS under Type II cycles in terms of (a) maximum battery surface temperature, (b) PCM liquid fraction, and (c) maximum temperature difference within the battery module....................................182

Figure 6-4. Static temperature and PCM liquid fraction contour plots of the HBTMS and pure PCM under Type II cycles at the end of the first and fifth cycle. 183

Figure 6-5. Performance of the HBTMS under Type III cycles in terms of (a) maximum battery surface temperature, (b) PCM liquid fraction, and (c) maximum temperature difference within the battery module....................................186

Figure 6-6. Static temperature and PCM liquid fraction contour plots of the HBTMS and pure PCM under Type III cycles at the end of the first and fifth cycle. 187

Figure 7-1. Dimensional details of designed HBTMS for single cell......................218

Figure 7-2. Dimensional details of designed HBTMS for battery pack. 218

Figure 7-3. Samsung 25R 18650 battery dimensions. 219

Figure 7-4. Chroma battery tester device...220

Figure 7-5. Handheld spot welding device. 220

Figure 7-6. Sketch of the experimental set up of HBTMS for (a) single cell and (b) battery pack...221

Figure 7-7. (a) Spot welding device gears and (b) connection of the battery cycler wires. 222

Figure 7-8. Developed test plan for single battery charge and discharge................223

Figure 7-9. Printed battery holder..224

LIST OF TABLES

Table 2-1. Summary and evaluation of thermal models applied to LIBs. 12

Table 2-2. Thermophysical properties of different porous materials 21

Table 2-3. Applicability criteria for LTE and LTNE thermal models. 24

Table 2-4. Assessment of numerical methods for simulating porous media in BTMS.26

Table 2-5. Summary of the work carried out on porous media-based air cooling BTMS. 29

Table 2-6. Summary of the work carried out on CPCM cooling BTMS. 35

Table 2-7. Thermophysical properties of various common coolants for liquid cooling in BTMSs [86, 244] 47

Table 2-8. Summary of the work carried out on liquid cooling BTMS. 48

Table 2-9. Summary of the work carried out on HBTMS. 52

Table 3-1. Specification and thermophysical properties of the battery [273].............65

Table 3-2. Thermophysical properties of the materials [123, 274]............................66

Table 3-3. Total internal resistance at various temperatures [279]............................67

Table 3-4. 18650 lithium-ion battery heat generation during charge [281]................68

Table 3-5. Specifications of the HPC system used for numerical simulations. 74

Table 3-6. GCI analysis for different studied grids. 77

Table 3-7. Different time steps for time step independency study 77

Table 4-1. Performance Evaluation Criterion (PEC) values for different discharge rates. 99

Table 5-1. Factors and levels used in Taguchi method analysis. 146

Table 5-2. L27 orthogonal array based on the Taguchi method. 146

Table 5-3. Results of simulations for different cases based on L27 orthogonal array.149

Table 5-4. Response table for signal to noise ratios (S/N) for each level of factors for maximum battery surface temperature ($T_{Max,Sur}$). 156

Table 5-5. ANOVA analysis results for maximum battery surface temperature ($T_{Max,Sur}$). 156

Table 5-6. Response table for signal to noise ratios (S/N) for each level of factors for maximum temperature difference within the battery module (ΔT_{Max}). 160

Table 5-7. ANOVA analysis results for maximum temperature difference within the battery module (ΔT_{Max})...161

Table 5-8. Response table for signal to noise ratios (S/N) for each level of factors for performance evaluation criteria (PEC). 164

Table 5-9. ANOVA analysis results for performance evaluation criteria (PEC). 165

Table 5-10. Response table for signal to noise ratios (S/N) for each level of factors for energy density (E_d). 168

Table 5-11. ANOVA analysis results for energy density (E_d). 169

Table 5-12. Response table for signal to noise ratios (S/N) for each level of factors for mean of means. 173

Table 6-1. Specifications of the investigated cycles 176

Table 7-1. AlSi10Mg thermophysical properties..217

Table 7-2. Specification of a Samsung 25R 18650 battery. 219

NOMENCLATURE

A_m	Mushy zone constant ($kg\cdot m^{-3}\cdot s^{-1}$)
C	Inertial factor
C_0	Nominal capacity
C_F	Geometric function
C_p	Specific heat capacity ($J\cdot kg^{-1}\cdot K^{-1}$)
D	Copper tube diameter (m)
E	Open circuit voltage (V)
E_d	Energy density ($Wh\cdot kg^{-1}$)
F	Faraday's constant ($C\cdot mol^{-1}$)
$\vec{F}$	Source term
F_s	Safety factor
f_r	Friction factor
I	Electric current (A)
K	Permeability of the porous medium (m^2)
L_b	Battery height (m)
L_f	Liquid fraction
N	Total number of grids
$\overline{Nu}$	Average Nusselt number
P	Pressure (Pa)
p	Rate of convergence
Q	Heat generation rate (W)
Re	Reynolds number
R_t	Total internal resistance (Ω)

$\vec{S}$	Source term
S_L	Source term
T	Temperature (K)
$T_{Max,Sur}$	Maximum battery surface temperature (K)
U	Nominal voltage
V	Voltage (V)
$\vec{V}$	Velocity vector ($m \cdot s^{-1}$)
V_b	Battery volume (m^3)
V_i	Volume of each grid cell (m^3)
a_{sf}	Specific surface area (m^{-1})
d_f	Ligament diameter (m)
d_p	Pore size (m)
f	Solution value
g	Gravitational acceleration ($m \cdot s^{-2}$)
h	Sensible enthalpy ($J \cdot kg^{-1}$)
h_f	Latent heat of fusion ($J \cdot kg^{-1}$)
h_{sf}	Solid-fluid heat transfer coefficient ($W \cdot m^{-2} \cdot K^{-1}$)
k	Thermal conductivity ($W \cdot m^{-1} \cdot K^{-1}$)
k_{td}	Thermal dispersion coefficient ($W \cdot m^{-1} \cdot K^{-1}$)
n	Number of electrons
q_b	Heat generation per unit volume ($W \cdot m^{-3}$)
$q_{b,s}$	Heat flux on battery surface ($W \cdot m^{-2}$)
q_{int}	Heat flux at the interface ($W \cdot m^{-2}$)
r	Grid refinement ratio
t	Time (s)
ΔP	Pressure drop (Pa)

ΔS	Change in entropy ($J\cdot K^{-1}$)
ΔT	Temperature difference (K)
ΔT_{Max}	Maximum temperature difference within the battery module (K)
$\Delta T_{Max,b}$	Battery maximum surface temperature difference (K)
$\frac{dE}{dT}$	Entropy coefficient ($V\cdot K^{-1}$)

Greek Letters

ω	Pore density (PPI)
β	Thermal expansion coefficient (K^{-1})
ε	Porosity
ε_r	Relative error
μ	Dynamic viscosity ($Pa\cdot s$)
ρ	Density ($kg\cdot m^{-3}$)
θ	Dimensionless temperature

Subscripts

Max	Maximum
m	mean value
amb	Ambient
b	Battery
eff	Effective
f	Fluid phase
gen	Generated
irr	Irreversible
m	Melting
ref	Reference

rev	Reversible
s	Solid phase
Sur	Surface
t	Total

Acronyms

ARC	Accelerated-rate calorimetry
BTMS	Battery Thermal Management System
DBF	Darcy–Brinkman–Forchheimer
DOE	Design of experiments
EV	Electric Vehicle
FVM	Finite Volume Method
GCI	Grid Convergence Index
HBTMS	Hybrid Battery Thermal Management System
HEV	Hybrid Electric Vehicle
HPC	High-Performance Computing
HPPC	Hybrid Pulse Power Characterization
IHC	Isothermal heat conduction calorimetry
LIB	Lithium-ion Battery
LTE	Local Thermal Equilibrium
LTNE	Local Thermal Non-Equilibrium
NMC	Lithium Nickel Manganese Cobalt Oxide
PCM	Phase Change Material
PCT	Phase change temperature
PEC	Performance evaluation criteria
PPI	Pores per inch

RC	Radiation calorimetry
r.e.v	Representative elementary volume
SOC	State of charge
Sur	Surface
TPMS	Triply periodic minimal surfaces
UDF	User Defined Function

Chapter 1: Introduction

The escalating rate of carbon emissions, predominantly resulting from fossil fuel consumption, has raised serious environmental and public health concerns. This issue is further aggravated by the incomplete combustion of diesel and petrol in internal combustion engines, which contributes significantly to air pollution and associated health risks [1]. The transportation sector has been identified as a major contributor to international carbon footprints, accounting for approximately 28% and 29% of total emissions in the UK (2017) and the US (2019), respectively [2, 3]. In response, various governmental bodies, including the UK Department for Transport and the European Union's Horizon programme, have implemented legislative measures aimed at mitigating these impacts [2, 4]. The UK government, for instance, has set ambitious targets to transition towards near-zero-emission transportation, aiming for 50–70% of cars and 40% of vans sold by 2030 to meet this standard [2]. As a result, electric vehicles (EVs) and hybrid electric vehicles (HEVs) have garnered substantial interest within both academic research and industrial development as viable alternatives to conventional vehicles. Owing to their reliance on battery systems for power, EVs offer a promising strategy for reducing emissions and minimising the environmental footprint of the transport sector [5].

Among various battery technologies used in electric vehicles (EVs) and hybrid electric vehicles (HEVs), lithium-ion batteries (LIBs) are particularly distinguished due to their high specific energy and power density, as depicted in Figure 1-1. LIBs offer several advantageous features, including a negligible memory effect and low self-discharge rates, which enhance their suitability and reliability for automotive applications [6]. However, reliance on battery systems introduces several challenges, such as limited driving range, prolonged charging times, and reduced power-to-weight efficiency [7]. As shown in Figure 1-2, lithium-ion batteries are commonly available in three primary forms including cylindrical, prismatic, and pouch cells. Among these, cylindrical cells are particularly valued for their structural integrity under internal pressure during standard operation, extended service life, cost-effective manufacturing, and robust cycling performance [8]. Given these advantages and their growing utilisation in electric vehicles, this PhD research focused on the analysis of a commercially available cylindrical lithium-ion battery.

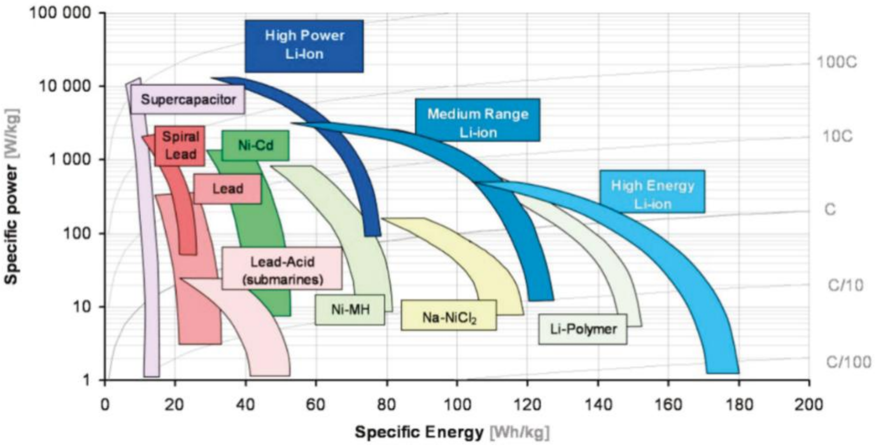

Figure 1-1. Ragone plot of various types of batteries in terms of specific power and energy [9]

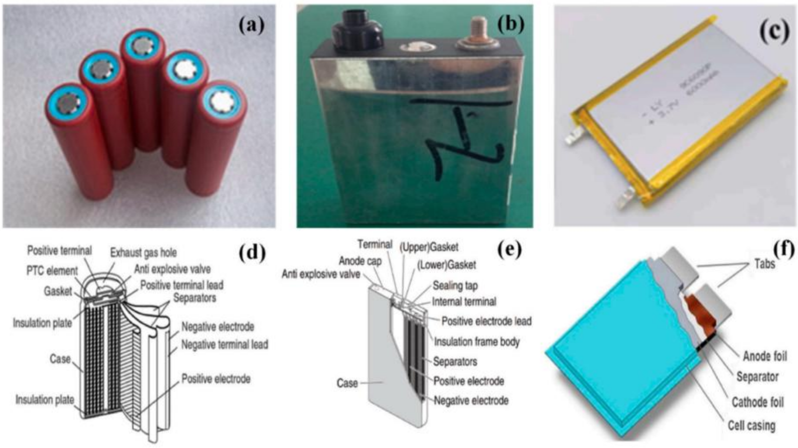

Figure 1-2. Different type of lithium-ion batteries (a) cylindrical, (b) prismatic, and (c) pouch cells [10]

LIBs exhibit strong sensitivity to the operating temperature, as illustrated in Figure 1-3 Deviations from the optimal temperature range can significantly affect their performance, safety, and longevity. At low temperatures, LIBs suffer from diminished charge acceptance, reduced energy and power capacity, decreased round-trip efficiency, and accelerated ageing, with severe performance losses reported at temperatures as low as –40 °C [11-14]. In contrast, elevated temperatures can lead to accelerated capacity degradation, internal short circuits, gas release, thermal runaway, and, in extreme cases, combustion or explosion [15-17]. Studies show that continuous operation at high temperatures, such as 45 °C or above, substantially shortens battery life, with capacity losses exceeding 70% after 490 cycles at 55 °C [16]. Moreover, non-uniform temperature distribution within battery modules, often arising from variations in geometry and material properties, exacerbates performance degradation. A temperature difference as small as 5 °C across cells can lead to a 1.5–2% reduction in capacity and a 10% decline in power capability [18-20]. The safe and optimal operating temperature range for LIBs is generally identified as 15 °C to 35 °C [21], 20 °C to 40 °C [22-24], or up to

50 °C under certain conditions [25, 26]. Additionally, to maintain uniform performance across modules, the maximum temperature variation should not exceed 5 °C [6, 52, 53].

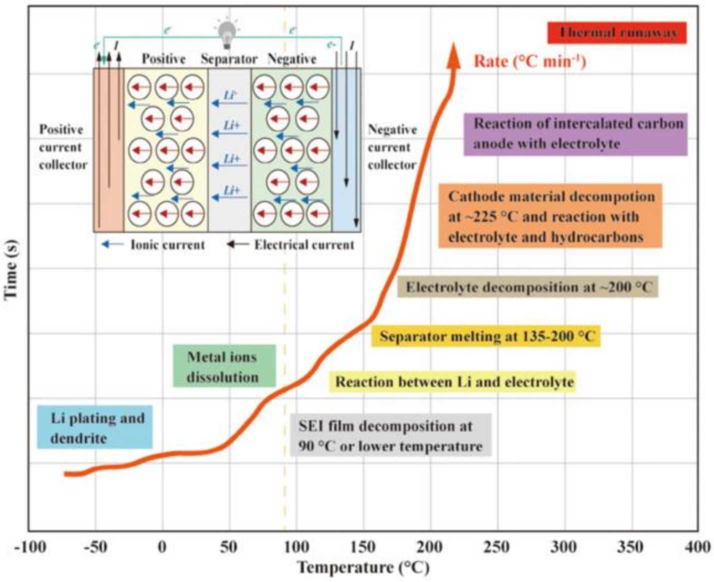

Figure 1-3. Impact of the various temperature on LIB [27]

Given these constraints, effective thermal management is imperative for ensuring safe, reliable, and high-performance operation of LIBs. The design of a robust battery thermal management system (BTMS) is therefore a critical component in electric and hybrid vehicle applications. Hybrid battery thermal management systems (HBTMS), which integrate both passive and active cooling methods, have attracted considerable interest as an effective solution to the thermal challenges posed by LIBs [28, 29]. Passive cooling via phase change materials (PCMs) enables efficient heat absorption through latent heat at nearly constant temperatures. However, the inherently low thermal conductivity of PCMs limits their standalone performance [26, 30]. Embedding high-conductivity porous media such as metal foams improves thermal conductivity and facilitates multidirectional heat transfer [31-33]. Experimental and numerical studies have shown that the integration of copper or aluminium foam into PCM matrices enhances temperature uniformity, reduces maximum battery temperatures, and extends battery lifespan under high-rate discharges [34-36]. On the active side, liquid cooling systems offer high heat dissipation capacity, and their performance is further improved by the inclusion of porous structures, which disrupt boundary layer formation, increase coolant mixing, and enhance convective heat transfer [31, 37-39]. Studies have demonstrated that metal foam-enhanced liquid cooling can reduce maximum battery temperatures while maintaining low flow rates and energy consumption [31, 38, 40-42]. The synergy of PCM and liquid cooling in HBTMS, especially when augmented by metal foams or triply periodic minimal surfaces

(TPMS) structures, results in reduced thermal resistance, improved heat distribution, and enhanced safety [40, 43, 44]. These findings underscore the vital role of advanced materials and optimised configurations in developing effective and lightweight thermal management solutions, which not only enhance heat dissipation but also improve energy density and overall system efficiency in high-performance battery applications.

1.1 Research Question

What are the impacts of hybrid cooling on the heat transfer performance of the battery thermal management system and temperature distribution within the battery module?

1.2 Research Aim

The present investigation aims to study a battery thermal management system based on hybrid cooling incorporating liquid cooling, phase change materials and porous metal foam to enhance heat transfer and uniform temperature distribution within the battery module.

1.3 Research Objectives

1. Compare different cooling methods combined with porous media and metal foam by investigating them as individual and hybrid cooling systems and evaluating their contribution to keeping the battery within the required operating temperature range.
2. Validate the numerical models developed in this research with experimental and numerical results available in the literature, ensuring the accuracy and reliability of the simulation outcomes for the proposed HBTMS configurations.
3. Conduct various sets of numerical simulations to investigate the impact of parameters such as porosity and pore density of the copper metal foam, thickness and quantity of copper foam fins, copper foam layer thickness, number of cooling plates, inlet mass flow rate and temperature, and ambient temperature on the HBTMS's performance in terms of energy density, heat transfer rate, maximum temperature, and maximum temperature difference within the battery module.
4. Study the performance of the optimised HBTMS during both charge and discharge cycles to assess its thermal behaviour under realistic operating conditions.

1.4 Thesis Outline

This thesis is structured into seven chapters, each building on the previous to present a comprehensive investigation into the design, modelling, optimisation, and evaluation of a novel hybrid battery thermal management system (HBTMS) enhanced with copper metal foam. The content and contribution of each chapter are summarised as follows:

Chapter 1: Introduction

This chapter introduces the research problem, contextualises the importance of thermal management in LIBs, and presents the research question, aim, and objectives. It also outlines the structure of the thesis and lists the author's related publications.

Chapter 2: Literature Review

A critical review of the current state of research in BTMS is presented, with particular focus on the role of porous media and metal foams in improving thermal performance. The chapter also explores various cooling strategies including air-based, PCM-based, liquid-based, and hybrid BTMS, highlighting their limitations and potential enhancements through porous media.

Chapter 3: Research Methodology

This chapter details the development of the proposed HBTMS, describing the numerical models, governing equations, and simulation setup used in ANSYS Fluent. It also outlines the optimisation approaches employed, including Taguchi Design of Experiments (DOE) and Analysis of Variance (ANOVA), as well as validation.

Chapter 4: Comparative Assessment and Parametric Study of the Proposed Metal Foam-Enhanced HBTMS

A comprehensive evaluation of the proposed HBTMS is conducted by comparing it with conventional PCM-based BTMS. The chapter presents a parametric study of key design variables, including porosity, pore density, fin and layer geometry, coolant conditions, and ambient temperature, to understand their influence on system performance.

Chapter 5: Multi-Objective Optimisation and Performance Evaluation of the Proposed HBTMS

This chapter employs statistical analysis techniques to assess the influence of various parameters on critical thermal and system-level metrics, including maximum battery surface temperature ($T_{Max,Sur}$), maximum temperature difference within the battery module (ΔT_{Max}), performance evaluation criteria (PEC), and energy density (E_d). Multi-objective optimisation is performed to identify an optimal HBTMS configuration.

Chapter 6: Cyclic Performance of the Proposed HBTMS

The thermal resilience of the HBTMS is examined under repeated discharge–rest–charge cycles, simulating realistic operational conditions. Three cycle types are analysed to assess system durability, PCM recovery behaviour, and performance consistency compared to pure PCM.

Chapter 7: Conclusions and Future Work

The final chapter summarises the key findings of the research, highlighting the major contributions to battery thermal management. It also outlines potential avenues for future work, including model enhancements, experimental validation, and sustainability considerations.

Appendix A provides the details of the User-Defined Functions (UDFs) developed and implemented in this study for battery heat generation modelling for single discharge and cyclic charge–discharge.

Appendix B presents the initial experimental design and setup for the proposed HBTMS. It outlines the fabrication process using 3D metal printing, the integration of copper foam components, and instrumentation for thermal measurement and control. Key equipment, including the Chroma battery tester and data acquisition systems, are described alongside safety protocols and risk assessments. The appendix also highlights challenges encountered in constructing the experimental rig.

1.5 Publications

The following publications have emerged from this PhD research, contributing to the advancement of the field and disseminated through reputable peer-reviewed journals.

Keyhani-Asl, A., Perera, N., Lahr, J. and Hasan, R., 2025. Numerical analysis of copper foam-enhanced hybrid battery thermal management systems for lithium-ion batteries: advancing energy density and thermal control. Applied Thermal Engineering, p.127183.

(https://doi.org/10.1016/j.applthermaleng.2025.127183)

Keyhani-Asl, A., Perera, N., Lahr, J. and Hasan, R., 2025. Innovative hybrid battery thermal management system incorporating copper foam porous fins and layers with phase change material and liquid cooling. Applied Thermal Engineering, p.125848. (https://doi.org/10.1016/j.applthermaleng.2025.125848)

Keyhani-Asl, A., Perera, N., Lahr, J. and Hasan, R., 2024. Porous media and foam application in battery thermal management systems: A comprehensive review focused on its impact, numerical modeling, and experimental preparation. Journal of Energy Storage, 93, p.112306. (https://doi.org/10.1016/j.est.2024.112306)

Keyhani-Asl, A., Perera, N., Lahr, J. and Hasan, R., 2025. Numerical Investigation of Copper Foam-Integrated Hybrid Battery Thermal Management System for Enhanced Thermal Control and Cyclic Performance. Advances in Computational Heat and Mass Transfer II - Proceedings of ICCHMT 2025, Antalya, Turkey, May 19-22, 2025.

Keyhani-Asl, A., Perera, N., Lahr, J. Hasan, R. and Zare, P, 2025. Multi-Objective Optimisation and Cyclic Performance Evaluation of a Metal Foam-Enhanced Hybrid Battery Thermal Management System (Under review - International Communications in Heat and Mass Transfer)

Keyhani-Asl, A., Perera, N., Lahr, J. and Hasan, R., 2025. A comprehensive review of the application of porous media and foam and its impact on enhancing common battery thermal management systems. (Under preparation - to be submitted to the Journal of Energy Storage)

Chapter 2: Literature Review

In response to growing concerns over climate change and the environmental impact of fossil fuels, significant research efforts have been directed toward the development of alternative sources aimed at reducing greenhouse gas emissions [45]. Among these, LIBs have emerged as a leading energy storage solution due to their high energy efficiency, minimal self-discharge, and resistance to the memory effect, making them highly reliable for electrical applications [6]. Nevertheless, the performance of LIBs is strongly influenced by temperature conditions. At low temperatures, their operational efficiency declines, resulting in diminished charge acceptance, reduced energy and power output, and accelerated degradation [14, 46]. On the other hand, elevated temperatures can lead to capacity loss, shortened service life, and critical safety issues such as thermal runaway [15, 16]. The recommended operating temperature for LIBs typically lies between 25 °C and 50 °C [47, 48], with a maximum allowable temperature difference of 5 °C to maintain thermal uniformity [23, 49, 50]. Therefore, the implementation of an effective BTMS is crucial to preserving performance, enhancing safety, and extending battery lifespan.

The hybrid cooling approach, which combines active and passive cooling strategies, offers an efficient and reliable solution for regulating battery temperature [28, 29]. The incorporation of metal foam plays a pivotal role in enhancing thermal performance across both cooling modes, primarily due to its interconnected porous structure that supports various heat transfer mechanisms [31]. Furthermore, the lightweight nature of metal foams contributes to a substantial reduction in the overall system mass, thereby improving energy density and overall system efficiency [51].

This chapter provides a comprehensive review of the literature on the thermal behaviour of LIBs under varying operating conditions, modelling approaches for heat generation, and the use of porous media and metal foams to improve the performance of the BTMS. It begins by investigating the influence of temperature on battery performance and continues with an overview of heat generation models. The role of porous structures in enhancing heat transfer is then explored in detail, including a discussion on their thermophysical characteristics, numerical modelling strategies, and their application across air, PCM, liquid, and hybrid cooling systems. The chapter concludes by evaluating the challenges, limitations, and design considerations associated with integrating porous media into different BTMS configurations.

2.1 Influence of Temperature on Battery Performance

Battery performance deteriorates significantly under low-temperature conditions, restricting their functionality in cold climates and at high altitudes. Low temperatures adversely impact charge acceptance, energy and power output, round-trip efficiency, and overall battery lifespan [11, 12]. Specifically, LIBs show a sharp decline in performance, with studies indicating that at –40 °C, LIBs can deliver only 1.25% of their power and 5% of their energy density compared to optimum operation at 20 °C [11]. Additionally, LIBs experience accelerated ageing below 0 °C; for instance, a 11.5 Ah Li-ion cell may lose up to 25% of its capacity after just 40 cycles at –10 °C [13]. The primary cause is the increased viscosity of the electrolyte at low temperatures, which significantly hinders lithium-ion diffusion and raises internal resistance. This results in fewer lithium ions participating in electrochemical reactions, ultimately reducing both power output and energy storage capacity [14]. Furthermore, low-temperature charging can lead to the formation of lithium dendrites, which may pierce the separator film, causing internal short circuits and compromising battery safety [45]. Finally, low temperatures can create large thermal gradients within the battery module, leading to uneven temperature distribution and localised degradation [12].

High-temperature conditions can adversely affect the operational stability and performance of LIBs. Due to the high chemical reactivity and flammability of lithium, overheating a single cell in a battery module, whether connected in series or parallel, can have cascading effects, potentially leading to combustion, explosions, or the emission of hazardous gases such as CO, C_2H_4, H_2S, and HF [52]. Moreover, the intricate design of LIB power circuits increases the likelihood of internal short circuits when exposed to high thermal conditions [15, 53]. Elevated temperatures also accelerate the loss of battery capacity and reduce overall service life [54, 55]. For example, a study on Sony 18650 cells reported a 36% reduction in capacity after 800 cycles at 45 °C, and more than 70% capacity loss after 490 cycles at 55 °C [16]. One of the most critical risks associated with high temperatures is thermal runaway, a dangerous phenomenon characterised by three stages: the onset of thermal instability, cell venting and propagation, and finally, an explosive decomposition reaction [17, 56].

Beyond the effects of extreme temperatures, maintaining a uniform temperature distribution within the battery is crucial for its efficient and reliable operation. Variations in cell geometry and the thermophysical properties of internal materials often lead to temperature gradients as heat is generated and transferred throughout different components [57]. Studies have shown that the highest temperatures typically occur near the electrode region [18]. This thermal non-uniformity can cause uneven electrochemical reaction rates across the electrodes [19], ultimately impairing battery performance and reducing cycle life [58]. Studies indicate that a temperature variation as small as 5 °C can lead to a capacity reduction of 1.5–2% and a power output loss of up to 10% [20]. The influence of operating temperature on discharge capacity for LIB is illustrated in Figure 2-1, emphasising the significant influence of temperature.

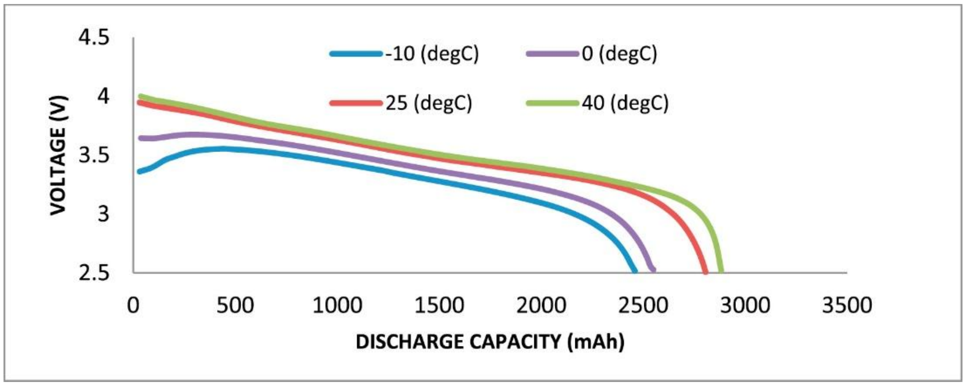

Figure 2-1. Temperature-dependent discharge performance of 18650 LIB [59].

2.2 Modelling and Analysis of Heat Generation in Lithium-Ion Batteries

Designing an effective BTMS requires a thorough understanding of the different forms and quantities of heat generated within LIBs, as illustrated in Figure 2-2. Although heat generation is generally higher during discharge, thermal failures are more likely to occur during charging due to the rapid temperature rise and uneven heat distribution [60]. Battery modelling approaches are typically categorised into electrochemical models and electrical equivalent circuit models [61]. Electrochemical models provide in-depth representation of the internal electrochemical processes using a set of partial differential equations. These models range in complexity from the single particle (SP) model to the porous electrode model with polynomial approximation (PP model), and the pseudo-two-dimensional (P2D) model. While electrochemical models offer high accuracy, their complexity and computational demands make them less suitable for applications involving power and dynamic system simulations [61].

Alternatively, electrical equivalent circuit models simplify the system by representing battery behaviour using basic electrical components such as resistors and capacitors [49]. More advanced versions, including Thevenin-based, impedance-based, runtime-based, combined circuit-based, and generic models, can enhance model accuracy and fidelity by incorporating additional components [61]. Extensive reviews on thermal modelling approaches for batteries have been published in recent literature, and an overview of the commonly used thermal models is presented in Table 2-1.

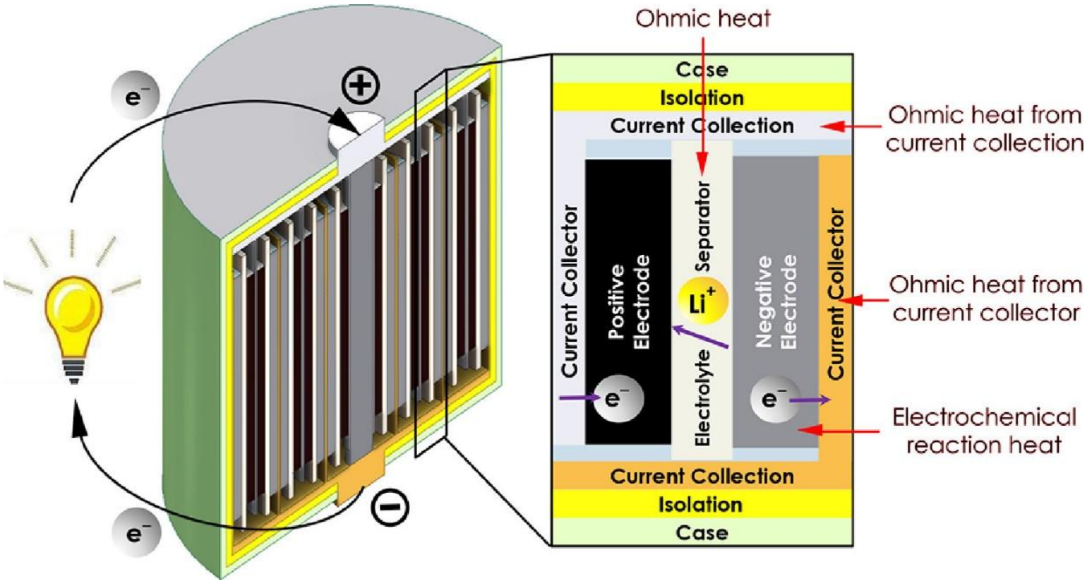

Figure 2-2. Schematic of different heat generation forms in LIB [62].

Table 2-1. Summary and evaluation of thermal models applied to LIBs.

Model	Key Parameters	Model Insights and Contributions
Single Particle Model (SP Model) [63]	Open-circuit voltage, reaction rate constants, diffusion coefficients	- Estimates internal temperature profiles and thermal gradients - Informs heat dissipation strategies - Assists in thermal runaway prediction - Supports evaluation of cooling system integration
Porous Electrode Model [64]	Electrode microstructure (porosity, tortuosity), thermal properties, reaction kinetics, heat sources	- Investigates the influence of porous structures on thermal behaviour - Deepens understanding of electrochemical-thermal interactions

Model	Key Parameters	Model Insights and Contributions
		- Helps optimise electrode architecture for better thermal regulation
Pseudo-Two-Dimensional Model (P2D Model) [65]	Reaction-diffusion processes, current flow, spatial gradients	- Incorporates spatial dimensions in simulations. - Offers a comprehensive battery behaviour framework. - Useful for detailed battery performance analysis and optimization.
3D Pseudo-Electrochemical-Thermal Model [66]	Mass and charge transfer, electrochemical parameters	- Evaluates heat effects from current collector tabs - Maps non-uniform temperature distributions - Assists in holistic battery system design improvements
Electrical Equivalent Circuit Model [67]	Resistance, capacitance, state of charge (SOC), depth of discharge (DOD)	- Simplifies battery behaviour using electrical analogues - Facilitates system-level simulations - Enhances SOC and DOD estimation accuracy
Mesoscale Electro-Thermal Model [68]	Voltage, current, entropy coefficients, open-circuit voltage	- Analyses electro-thermal coupling - Identifies local heat generation regions - Supports BTMS design and validation
1D Thermal Mathematical Model [69]	Heat generation rates, discharge conditions, geometry, material properties	- Simplifies internal temperature prediction - Focuses on quantifying heat generation - Aids in basic BTMS development
Finite Element Thermal Model [70]	Physical geometry, internal reactions	- Utilises geometry for accurate thermal distribution mapping - Links structural and electrochemical effects - Useful for design improvement through detailed simulations
Kalman Filter Based Electrochemical Model [71]	Electrolyte concentration, current density, Butler-Volmer kinetics	- Enables precise SOC estimation - Offers insights into internal dynamic reactions - Valuable for predictive modelling and real-time system control
Thermal-Electrochemical Coupled Model [72]	Temperature, current density	- Captures the interdependence between thermal and electrochemical responses - Promotes comprehensive analysis of battery dynamics - Contributes to advanced thermal management design

Model	Key Parameters	Model Insights and Contributions
3D Thermal Model [73]	Spatially resolved convection and radiation effects	- Explores how external conditions influence temperature gradients - Identifies asymmetric heat distribution - Informs design for more uniform thermal performance
Bernardi Model [74]	Electrical energy input, reaction enthalpy, mixing heat, phase change effects	- Serves as a foundational heat generation model - Simplifies complex interactions - Highlights the role of phase change in thermal behaviour

Numerous investigations adopt a modelling approach based on the energy balance, as expressed in Equation (2-1), which accounts for the heat stored within the cell (left-hand side) as well as the heat generated and dissipated. As illustrated in Figure 2-3, total heat generation comprises both reversible and irreversible components [75]. The foundational model for battery heat generation was introduced by Bernardi et al. [75], incorporating contributions from electrical power, reaction enthalpy, mixing processes, and material phase transitions. A widely used simplified version, commonly found in the literature, neglects mixing and phase change effects. This form, expressed in Equation (2-2), uses U and V to denote the open-circuit and operating voltages, respectively. The terms $I(U-V)$ and $IT(\frac{\partial U}{\partial T})$ correspond to the heat generated through Joule (irreversible) heating and reversible entropy change.

$$\mathrm{m}C_p\frac{dT}{dt} = Q_{gen} - \ Q_{dis} \tag{2-1}$$

$$Q_{gen} = I(U-V) - IT(\frac{\partial U}{\partial T}) \tag{2-2}$$

Jindal et al. [76] conducted an experimental investigation to evaluate the accuracy of the Bernardi model in estimating heat generation during both continuous and pulse discharge of lithium-ion batteries. The results demonstrated that the model provided reasonably accurate predictions under continuous discharge conditions. However, during pulse discharge, the model tended to overestimate the heat generation when compared with direct experimental observations.

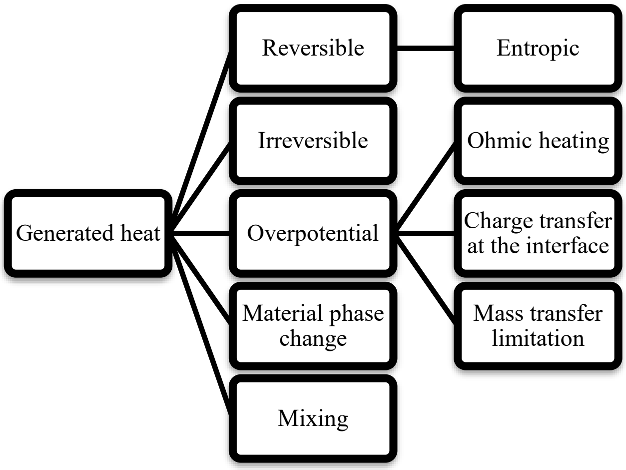

Figure 2-3. Heat generation in LIBs [75]

Lumped-parameter thermal model assumes a spatially uniform temperature throughout the battery during heat transfer. The validity of this simplification is governed by the Biot number (Bi), which represents the ratio between internal thermal resistance and surface heat transfer resistance. For the lumped-parameter approach to be considered valid, Bi must be less than 0.1 [49, 77]. This modelling assumption is frequently employed in numerical studies, often accompanied by the simplification of constant heat generation, effectively neglecting the entropy-related term in Equation (2-2). However, such assumptions must be applied cautiously to ensure accurate thermal predictions. Numerous experimental studies [36, 78-83] have shown that heat generation and temperature distribution in LIBs are inherently non-uniform. Rizk et al. [78] demonstrated that the relative contributions of Joule and entropy heat vary with the C-rate. Their findings revealed that at a discharge rate of 2/3C, entropic heat accounts for approximately 50% of total heat generation, whereas at 1C, its contribution drops to around 39%, indicating a reduced influence. Therefore, as the discharge rate increases, the proportion of reversible (entropy) heat becomes less significant.

While some studies [84, 85] simplify thermal modelling by neglecting the reversible heat term in Equation (2-2) (the second term of the Bernardi model) or by assuming constant heat generation, several studies have focused on developing more realistic models that account for temperature, state of charge (SOC), and depth of discharge (DOD) to better represent the thermal behaviour of LIBs [26, 86-89]. Furthermore, other studies [85, 90, 91] have emphasised the anisotropic thermal conductivity of cylindrical LIBs, noting that axial and radial conductivities differ due to variations in material composition and structural orientation (as shown in Figure 1-2), which affects the accuracy of models that assume constant heat generation.

As illustrated in Figure 2-4, and in line with the discussed models, the rate of heat generation varies significantly during the discharge (left side of Figure 2-4) and charge (right side of Figure 2-4) processes. The charging phase typically consists of two stages: constant current (CC) and constant voltage (CV). Numerous experimental studies have been conducted to quantify heat generation rates using techniques such as accelerated-rate calorimetry (ARC) [92-95], radiation calorimetry (RC) [96], intermittent current combined with voltage–current (V–I) analysis [97], and isothermal heat conduction calorimetry (IHC) [98, 99].

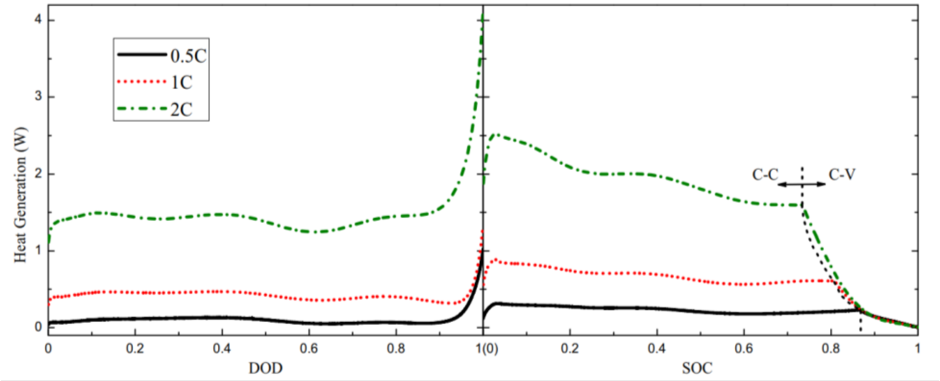

Figure 2-4. Heat generation of a single battery during charge–discharge cycles at 25°C [89].

2.3 Role of Porous Media and Metal Foams in Battery Thermal Management Systems

A porous medium, as shown in Figure 2-5 (a), consists of a solid framework containing a network of irregularly distributed and interconnected cavities or pores, typically arranged without a discernible pattern. The behaviour and performance of porous materials are primarily influenced by key properties such as porosity, pore density, permeability, effective thermal conductivity, and tortuosity [100, 101]. Porosity refers to the proportion of the total volume occupied by voids relative to the overall volume of the porous medium, including both the pores and the solid matrix. While some of these voids may be isolated, others form interconnected networks. As isolated pores have limited impact on transport processes, the concept of effective porosity is introduced, representing the fraction of interconnected pores within the total volume. Pore density refers to the number of pores or cells per unit length (typically expressed in pores per inch, PPI) within a porous material, such as metal foam [37].

Permeability, another crucial characteristic, is determined by the size, shape, and connectivity of internal pathways that facilitate fluid flow through the medium. Higher permeability allows fluids to penetrate more deeply into the porous structure. Structural features such as porosity, pore geometry and size, and void connectivity all influence permeability. In terms of heat transfer, the effective thermal conductivity of a porous medium depends on its porosity as well as the thermal conductivities of the solid matrix and the fluid occupying the pores. As illustrated in Figure 2-5 (b), tortuosity quantifies the complexity of the flow path by comparing the actual path length of fluid molecules through the porous network to that in a straight path within a non-porous medium [102].

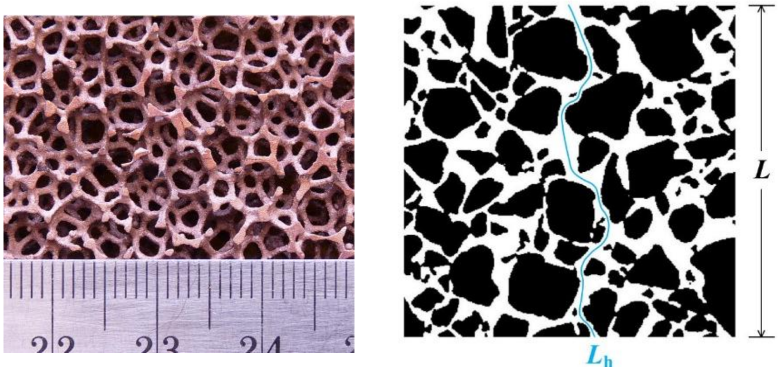

(a)

(b)

Figure 2-5. (a) Copper metal foam [103] and (b) tortuosity in porous media [104].

2.3.1 Heat Transfer Mechanisms and Enhancements Through Porous Structures

As illustrated in Figure 2-6, heat transfer enhancement in porous media arises from a complex interplay between the medium’s structural characteristics and its dynamic thermal behaviour. A fundamental contributor to this enhancement is the significantly increased surface area for heat exchange provided by the porous structure. The presence of solid ligaments within the porous matrix creates additional heat transfer surfaces within the same volume, thereby facilitating more effective thermal interaction as the fluid flows through the medium [37]. This interaction promotes greater heat exchange between the solid and fluid phases. Additionally, the concept of thermal dispersion conductivity [105, 106] is critical, as it introduces an extra conduction mechanism that supplements the inherent thermal conductivity of the porous material. This dispersion effect contributes to an overall improvement in the effective thermal conductivity of the system. Furthermore, the tortuous nature of the pore pathways leads to randomised fluid distribution, which further enhances the efficiency of heat transfer within the medium [100].

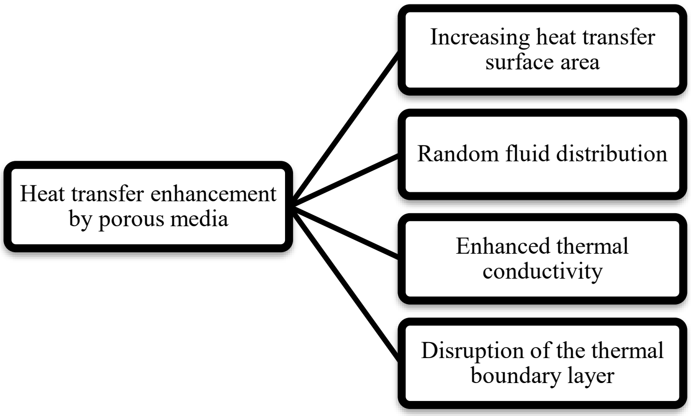

Figure 2-6. Heat transfer enhancement offered by porous media.

The integration of porous media can significantly influence heat transfer processes in both BTMS and HBTMS, thereby improving the overall efficiency of thermal regulation in batteries. The interconnected voids or channels within the porous structure enable multiple modes of heat transfer to occur simultaneously within the system.

In PCM-based BTMS integrated with porous media, various heat transfer mechanisms are observed. Before the onset of melting in the PCM, conduction serves as the primary mode of heat transfer. However, once melting begins, heat transfer is predominantly governed by a combination of conduction and natural convection [107]. A key limitation of pure PCMs is their inherently low thermal conductivity, which limits heat dissipation during high charge or discharge rates, often resulting in non-uniform temperature distribution and heat accumulation issues [108]. A widely adopted method to overcome this limitation involves incorporating porous media or metal foams into PCMs, forming composite phase change materials (CPCMs) [109]. This structural enhancement significantly improves the thermal conductivity of the PCM. Moreover, the porous framework of metal foam can retain the melted PCM through capillary action, thereby helping to preserve the material’s form and stability during phase transitions [110]. Additionally, within the melted region of the PCM, the inclusion of porous media enhances thermal conductivity, thereby intensifying buoyant forces and promoting stronger natural convection currents. Foams with lower pore density, having larger pore sizes, further encourage this convective movement, particularly at the mushy–liquid interface, which accelerates fluid motion in the mushy zone and improves overall heat transfer [107]. As a result, CPCMs are expected to exhibit enhanced natural convection relative to conventional PCMs. Furthermore, pore-scale convection can occur within CPCMs [111], enhancing localised heat transfer near the battery surface. Nonetheless, some studies [112-114] have reported that the presence of porous media may, in certain cases, restrict natural convection by impeding the flow of liquid PCM.

The limitations of convective heat transfer in air-cooled BTMS, namely low thermal conductivity, specific heat capacity, and heat transfer coefficient, can be partially overcome through the integration of porous foams. Incorporating porous materials, either fully or partially, into the heat sinks or airflow passages of the BTMS can significantly enhance the thermal performance of the battery module [115]. Moreover, the addition of a porous medium can promote more uniform air distribution [116]. These structures offer a larger effective heat transfer area and higher thermal conductivity than air alone, while also inducing turbulence and increasing fluid mixing near the battery cells. By disrupting the thermal boundary layer, the porous medium contributes to a higher overall heat transfer rate [117].

Similarly, in liquid-cooled BTMS, the introduction of porous layers or flow obstacles influences the redevelopment of the thermal boundary layer. The presence of porous media within the cooling channels induces crossflow mixing, which interferes with boundary layer formation and reduces undesired temperature increases along the coolant path. This enhancement results in improved heat transfer and greater cooling effectiveness [37, 38]. Additionally, the target operating temperature can be achieved with lower coolant flow rates when porous structures are used. However, the trade-off lies in the increased pressure drop caused by the presence of porous media, which must be carefully considered in the system design [38, 39].

2.3.2 Effect of Porous Media Characteristics on the Efficiency of BTMS

There are conflicting perspectives in the literature regarding the influence of porous media and foam properties, particularly porosity, on heat transfer performance [118, 119]. When narrowing the focus to studies related specifically to BTMS, a general consensus suggests that increasing porosity tends to reduce heat transfer efficiency. This results in elevated maximum temperatures and larger maximum temperature differences within the battery module [120-122]. This observation can be attributed to the reduction in the solid matrix content, which typically possesses higher thermal conductivity, as porosity increases, thereby lowering the effective thermal conductivity and limiting overall heat dissipation [100]. Numerous researchers [123-125], have also emphasised the necessity of identifying an optimal porosity level to balance thermal performance. Higher permeability in porous media is generally associated with improved heat transfer, owing to enhanced fluid penetration and increased interaction between the fluid and cooling surfaces. Studies have confirmed that greater permeability can effectively reduce maximum temperature; however, some have also reported that it may result in higher maximum temperature difference under certain conditions [121, 122, 126]. Additionally, thermal performance is often found to improve with increased tortuosity, as more convoluted pathways extend the residence time of the fluid within the medium, thereby promoting greater heat exchange between the solid structure and the working fluid [100, 127].

Porous media used in BTMS primarily consist of metal- and carbon-based foams. A summary of commonly employed porous materials in BTMS is provided in Table 2-2 , while Figure 2-7 illustrates the distribution of foam types investigated in the literature for thermal enhancement purposes. As indicated, approximately one-third of the studies have utilised copper foam. Copper foam plays a vital role in advancing BTMS due to its unique porous architecture and superior thermal conductivity. A research by Tian and Zhao [128, 129] has demonstrated that integrating copper foam into PCMs can significantly increase heat transfer performance, up to 20 times greater than that of pure PCM. Additional studies further highlight the influence of copper foam parameters, particularly porosity and pore density, on thermal effectiveness [130-132].

Aluminium foam is also widely recognised for its lightweight nature and excellent thermal performance. Its highly porous structure provides an extensive surface area, ensuring efficient heat transfer during both charging and discharging processes. Experimental investigations by Zhang et al. [67] and Hong and Herling [71] confirm aluminium foam's positive effect on reducing PCM melting time and enhancing overall BTMS thermal efficiency [133, 134]. Although aluminium foam has limitations in high-temperature environments, it remains a reliable and efficient choice for thermal control in advanced battery applications [135].

Nickel foam, despite its lower thermal conductivity (89 W/m·K), is advantageous in high-temperature scenarios due to its high melting point (1455 °C), making it suitable for use in thermally demanding BTMS environments [136]. Graphite foam, with a melting point exceeding 400 °C [137], is also well-suited for BTMS applications, particularly those involving PCM. Its high natural permeability increases surface area, thereby improving heat transfer. However, in PCM-based BTMS, this enhancement may be accompanied by compromises such as reduced latent heat capacity and slower melting and solidification rates [138, 139]. Among carbon-based foams, expanded graphite (EG) has received notable attention in PCM-integrated BTMS due to its ability to significantly improve thermal conductivity without increasing the system's density. This advantage arises from its exceptionally high porosity [136, 140].

In addition, a specialised category of metal foam coated with carbon-based materials has been explored for use in BTMS. Hussain et al. [141] conducted an experimental study on graphene-coated nickel foam, evaluating its thermophysical properties and performance within a paraffin-saturated BTMS. The results demonstrated a significant improvement in both thermal conductivity and overall cooling efficiency of the system.

Table 2-2. Thermophysical properties of different porous materials

Material	ρ (kg/m^3)	C_p (J/kg.K)	K (W/m.K)	Ref.
Aluminum foam	2719	871	202.4	[142]
Copper foam	8978	386	398	[143]
Aluminum oxide foam	3891	765	35	[144]
Nickel foam	8907	442	82	[145]
Graphite foam	2130	700	1700	[146]
Silicon Carbide	3210	700	430	[147]
CF-20 (Carbon foam)	250	750	3.1	[148]
KL1-250 (Carbon foam)	240	884	40	[148]

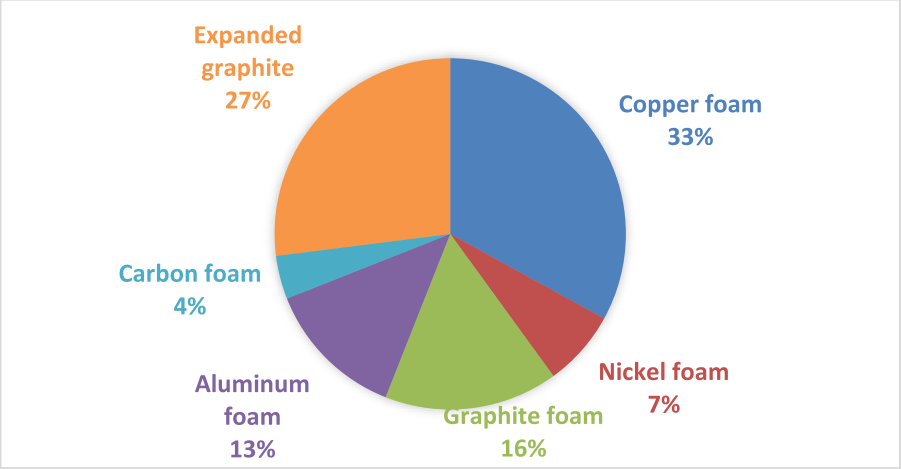

Figure 2-7. Application trends of various foams for thermal performance improvement in the literature [136].

2.3.3 Numerical Simulation of Porous Media

Porous media can be analysed from two distinct perspectives: microscopic and macroscopic. From a microscopic standpoint, only a limited number of channels within the porous structure are visible, allowing for the application of conventional fluid mechanics equations [37]. In contrast, the complexity of the porous medium at the macroscopic scale renders the direct use of these equations impractical. To address this, a volume-averaging approach has been introduced to model fluid flow through porous media. This method involves selecting a control volume that represents the structural characteristics of the medium, with parameter values defined as the average over that volume. These averaged properties are then used to characterise the porous medium in the analysis. The chosen control volume is known as the "representative elementary volume (r.e.v)" [37].

One of the earliest models for describing fluid flow through porous media was introduced by Darcy [149], which applies to creeping flow regimes with Reynolds numbers below 1. In such low-velocity conditions, the Darcy law assumes a linear relationship between pressure drop and velocity. However, as the Reynolds number increases, boundary layer effects begin to develop near the solid surfaces, rendering the Darcy model less accurate [150]. To account for these effects, Forchheimer [151] extended the Darcy model by incorporating a quadratic velocity term, allowing for the consideration of nonlinear drag forces within the porous medium [100].

In cases involving highly porous media (porosity > 0.95) [152] or elevated flow velocities [153], the influence of solid boundaries on flow becomes significant, an aspect not addressed by either the Darcy or Forchheimer models. To address this, the Brinkman model [154] introduces an additional term into the Darcy framework, incorporating the no-slip condition at solid walls within the porous domain [155]. For improved accuracy in simulating flow behaviour in porous structures, many researchers recommend the use of the Darcy–Brinkman–Forchheimer (DBF) model [100, 150, 156, 157] which has been shown to better align with experimental observations. The DBF model combines terms representing viscous (Darcy), boundary (Brinkman), and inertial (Forchheimer) effects, offering a more comprehensive approach to modelling flow in porous media [100]. This model is particularly suitable for numerical simulations in BTMS applications involving phase change materials (PCM), liquid cooling, and hybrid cooling strategies [36, 85, 126, 148, 158, 159].

To analysis heat transfer in porous media, two primary modelling approaches are employed: (1) the local thermal equilibrium (LTE) model and (2) the local thermal non-equilibrium (LTNE) model. The LTE approach assumes that the fluid and solid phases within the porous structure share an identical local temperature, whereas the LTNE model allows for distinct temperatures in each phase [150, 156]. In other words, the LTE condition suggests that the temperature difference between the solid and fluid phases is negligible at any given location in the medium. Consequently, a single effective thermal conductivity is applied, and temperature distribution is determined using a unified energy equation, without separately modelling the thermal behaviour of each phase. This simplification inherently neglects convective and radiative heat transfer interactions between the phases.

In contrast, the LTNE approach accounts for the thermal disparity between the solid and fluid phases by solving separate energy equations for each, allowing for more accurate modelling of heat exchange mechanisms within the porous structure [150, 160]. Although the LTNE method is computationally more demanding [157, 160-162], several studies [37, 150, 161, 163-166] have demonstrated its superior accuracy in capturing the thermal behaviour of porous media when compared to the LTE model.

Extensive research efforts [37, 150, 160, 167-171] have been devoted to evaluating the applicability of the LTE and LTNE models under varying thermal and physical conditions. Depending on the thermophysical properties of the fluid and solid phases, as well as the nature of the transient thermal process, the assumption of equal phase temperatures may not hold. In many thermal applications, the temperature difference between the fluid and solid phases can be substantial. Since heat transfer is inherently unsteady, system performance often depends on the extent of thermal non-equilibrium between the phases. The LTE assumption is particularly prone to failure when thermal energy accumulates within the porous structure [37, 167].

Vadasz [168] suggests that the LTE model is generally applicable under conditions involving constant temperature or thermally insulated boundaries. However, most heating processes in thermal engineering are transient in nature, thereby making the use of the LTNE model more appropriate [167]. Lin et al. [169] noted that the LTE model can still be applied reliably in high-flow-velocity scenarios. Similarly, Li et al. [172] recommend LTE when the local thermal resistances of the solid matrix and fluid phase are comparable. Isfahani et al. [173] advised using the LTE model when the thermal conductivity of the fluid is below 10 W/m·K. In contrast, Torabi et al. [170] identified specific conditions under which the LTNE model should be used: (1) significant disparity in thermal conductivity between the solid and fluid phases; (2) conduction-dominated systems or those with a low internal Biot number; and (3) systems with internal heat generation. The detailed criteria for selecting between these models are summarised in Table 2-3.

Table 2-3. Applicability criteria for LTE and LTNE thermal models.

Criteria for Model Suitability	LTE	LTNE
Reynolds (Re) and Darcy numbers (Da)	Suitable for conditions with low Re and Da, where convective effects are minimal, and flow remains largely laminar [174].	Recommended when Re and Da are high, indicating dominant convective transport and potential turbulence, particularly when notable temperature gradients exist between solid and fluid phases [170].
Boundary conditions	Valid near isothermal walls with uniform temperature; however, its accuracy decreases farther from the wall and into the flow core[175].	Necessary in unsteady heating scenarios or where significant heat accumulation occurs, as LTE assumptions break down under such conditions [37, 167].
Heat transfer coefficient	Applicable when convective heat transfer is efficient, such as in systems with high heat transfer coefficients, ensuring effective thermal exchange between phases [176].	Preferred in systems with low heat transfer coefficients, where substantial temperature differences between fluid and solid phases can arise [175].
Fluid thermal conductivity	High fluid thermal conductivity supports rapid heat diffusion, making LTE a valid assumption [156].	Required when a large disparity exists in thermal conductivity between solid and liquid phases, which leads to notable temperature differences [170].
Flow velocity	High flow velocity without internal heat generation supports the LTE assumption, as fast flow inhibits phase temperature divergence [177].	More accurate under low flow velocity conditions, especially in metal foam systems where the solid matrix influences heat distribution [169]
Pore size	Smaller pores favour thermal equilibrium due to closer phase interaction, justifying LTE [178].	-
Heat transfer coefficient relative to Re	When the heat transfer coefficient increases with Reynolds number raised to a power greater than one, LTE is considered appropriate due to enhanced convective transfer [179].	-
Porous media heterogeneity	When porosity variation is minimal, uniform flow and thermal fields are established, making LTE a valid model [180].	-
Internal heat generation	-	LTNE is more reliable in systems with internal heat sources, which inherently create non-equilibrium conditions [177].
High-porosity porous medium	-	Higher porosity increases the likelihood of temperature differences between phases, making LTNE the preferred approach [175].

Criteria for Model Suitability	LTE	LTNE
Applications in reactors, biological systems, and high-speed flows	-	LTNE offers improved accuracy in systems with rapid thermal dynamics, such as chemical/nuclear reactors, biological environments, and high-speed flows [177].
Biot number	-	LTNE is necessary when the Biot number is low, indicating that the conduction resistance of the solid phase dominates over interfacial convection, preventing LTE validity [181].
Two-phase flow with rapid phase change	-	LTNE is essential for capturing distinct energy exchanges in systems with rapid phase transitions [178].
High thermal conductivity porous media	-	In porous media with high conductivity, LTE assumptions fail to capture inter-phase temperature differences, necessitating LTNE [182].
Nanofluid flow in porous structures	-	LTNE is appropriate for nanofluid systems due to the complex interaction between nanoparticles, base fluid, and porous matrix [183].
Chemically reactive porous media	-	Required when chemical reactions induce substantial local heat generation, disrupting thermal equilibrium [180].
No significant thermal resistance difference between phases	LTE is suitable when the thermal resistance of the solid and fluid phases is nearly equal, minimising temperature disparity [172].	-

In the context of numerical simulations of BTMS incorporating porous foams, it is noteworthy that the majority of existing studies adopt the LTE approach, primarily due to its lower computational cost. Nonetheless, a limited number of investigations [38, 123] have employed the LTNE model, particularly in systems combining PCM with porous media. Despite the prevalence of LTE-based studies, comparative evaluations between LTE and LTNE models are crucial for accurately capturing thermal behaviour in BTMS applications involving porous structures and foams [38, 123].

The LTNE model's ability to capture temperature differences between the solid and fluid phases within porous media underscores its versatility and relevance, particularly in the context of heat transfer modelling and cooling strategies in BTMS. This model provides essential insight into the thermal interactions between the generated heat and the porous structure, especially when accounting for the transient and spatially non-uniform heat generation that occurs during battery charge and discharge cycles. In parallel, the DBF model demonstrates its effectiveness by offering a robust framework for simulating fluid flow through porous media. Considering that flow in most liquid-cooled BTMS configurations is laminar and that battery heat generation is characterised by complex and dynamic behaviour, the DBF model proves to be well-suited for analysing fluid dynamics within porous structures. Collectively, these models are particularly valuable for accurately representing the coupled interactions between the liquid and solid phases in porous media under the dynamic operating conditions of battery systems [31]. A comparative overview of the models discussed is presented in Table 2-4.

Table 2-4. Assessment of numerical methods for simulating porous media in BTMS.

Model	Typical Use Case	Strengths	Limitations	Application in BTMS	Important Considerations	Modelling Accuracy
Darcy	Applicable to low-velocity regimes ($Re < 1$)	Straightforward and broadly applicable at low flow rates	Not reliable at higher velocities	Not commonly applied	Most suitable for preliminary analysiss or simplified flow conditions	High for $Re < 1$; significantly less accurate at higher flow rates
Forchheimer	Suitable for moderate velocities where nonlinear drag is relevant	Provides improved accuracy over Darcy in moderate flow scenarios	Ignores boundary layer development	Not commonly applied	Useful when flow behaviour is more complex than Darcy's applicability	More accurate than Darcy at moderate velocities; accuracy drops at higher flow rates
Brinkman	Ideal for high-porosity media or flow near solid boundaries	Incorporates effects of solid boundary conditions	Complexity increases with geometric detail	Not commonly applied	Effective for simulations involving detailed structures	Good near solid walls; accuracy diminishes in geometrically complex domains
DBF (Darcy-Brinkman-Forchheimer)	Applicable to a wide range of BTMS, especially with complex flows	Captures viscous, inertial, and boundary effects comprehensively	Computationally intensive	Suitable for complex BTMS involving PCM, liquid, or hybrid cooling	Best suited for high-fidelity simulations requiring accuracy in both flow and thermal fields	High accuracy across a wide range; computational cost may limit feasibility in large systems
LTE (Local Thermal Equilibrium)	Used where temperature differences between phases are negligible	Computationally efficient and simple to apply	Inadequate for modelling distinct thermal behaviour between phases	Appropriate for simplified BTMS with minimal thermal gradients	Recommended when inter-phase temperature differences are minor	Sufficient for minor gradients; accuracy declines as gradient increases
LTNE (Local Thermal Non-Equilibrium)	Designed for systems with noticeable temperature disparity between phases	Enables detailed and phase-specific thermal characterisation	Greater computational demand	Essential for BTMS studies with non-uniform or transient heat generation	Critical for accurate predictions in thermally complex systems	Highly accurate for significant phase temperature differences; accuracy depends on

Model	Typical Use Case	Strengths	Limitations	Application in BTMS	Important Considerations	Modelling Accuracy
						computational resolution

2.4 Applications, Challenges, and Limitations of Porous Media in Different BTMSs

Porous media, including metal and carbon-based foams, have been increasingly applied in various BTMSs due to their capacity to enhance heat transfer. Their integration spans passive, active, and hybrid cooling strategies, offering improvements in thermal conductivity and uniformity across the battery module [115, 117, 184]. Copper and aluminium foams are commonly used in PCM-based systems to overcome the low thermal conductivity of pure PCMs and stabilise structural integrity during melting and solidification processes [50, 110, 185]. In liquid-cooled configurations, embedding porous structures within flow channels can significantly disrupt the thermal boundary layer, induce turbulence, and promote crossflow mixing, thereby improving the convective heat transfer rate [37, 38].

However, the use of porous media is not without limitations. One key challenge is the increased pressure drop caused by the presence of solid structures in the fluid path, which may lead to higher pumping power requirements in liquid-based BTMSs [37, 38, 156]. In PCM-based systems, while foams improve thermal conductivity, they also reduce the available volume for latent heat storage, thus decreasing the total thermal capacity of the composite [50, 185]. Additionally, porous structures may hinder natural convection if not optimally designed, particularly at lower pore densities. The effects of foam porosity, pore density, and permeability remain critical design considerations, as they influence the trade-off between heat transfer enhancement and system efficiency [31, 117].

The following sections will provide a detailed exploration of the integration of porous media in air-cooled, PCM-cooled, liquid-cooled, and hybrid BTMSs, with particular emphasis on their thermal performance, operational benefits, and inherent limitations.

2.4.1 Air-Cooled BTMS Enhanced by Porous Media

Air-based cooling is among the most widely adopted thermal management systems with various applications in vehicles, computers, and residential sections. Natural and forced convection, which are categorised as passive and active cooling methods, are the two fundamental types of air cooling used in BTMS. Air-cooled BTMSs are often favoured for their simplicity, low maintenance and replacement costs, high reliability, design flexibility, and elimination of leakage risks associated with liquid-based systems [186, 187]. Furthermore, air provides an adequate heat transfer coefficient for certain applications, particularly under low charge and discharge rates [186]. Forced convection is predominantly employed in air-based BTMSs [46], using mechanically driven systems such as fans to circulate air around battery modules. Active air cooling is generally unnecessary when the discharge rate is below 3C and ambient temperatures remain under 20 °C. Conversely, its effectiveness diminishes at ambient temperatures above 35 °C, where significantly higher fan power is required to maintain thermal stability [188]. Moreover, depending on the ambient temperature, active systems may also include air conditioning/heating pre-conditioning of the air used in the battery module [189]. Despite these advantages, air cooling presents several limitations. These include relatively low thermal efficiency due to air's poor heat transfer properties, the need for higher airflow rates compared to liquid coolants, dependency on ambient conditions, increased power consumption by fans, higher acoustic noise levels, potential exposure to airborne contaminants, and the tendency for uneven temperature distribution, particularly under high charging or discharging conditions [186].

The identified limitations of air cooling in BTMS, such as low thermal conductivity, specific heat capacity, and heat transfer coefficient, can be partially mitigated through the incorporation of porous metal foams. These porous structures can be strategically integrated, either partially or entirely, within airflow channels or heat sinks to enhance the thermal performance of battery modules [115]. Additionally, the inclusion of porous media improves airflow distribution [116], while providing an expanded effective heat transfer surface due to their higher thermal conductivity compared to air. Moreover, the porous matrix promotes turbulent flow and enhances mixing around the battery cells, disrupting the thermal boundary layer and thereby increasing the overall heat transfer rate [117]. However, these benefits come with the drawback of increased pressure drop. The presence of porous structures obstructs the flow path and reduces the available flow area, which collectively contribute to a significant rise in pressure drop across the system [37, 156]. Thus, achieving an optimal balance between improved heat transfer and acceptable pressure loss is essential to avoid the necessity for high-power fans. Consequently, the geometry, porosity, and permeability of the porous inserts must be carefully optimised [190]. Furthermore, the addition of porous foams can potentially reduce temperature uniformity within the system [121, 190]. As air enters the BTMS at a relatively low temperature, it absorbs heat along the flow path, diminishing its convective heat transfer capacity downstream. When porous foam is positioned near the inlet, it effectively lowers battery temperatures in that region. However, the heated air continuing through the system may cause uneven cooling, especially in the latter segments. Therefore, the design of the porous inserts should be optimised not only to minimise pressure drop but also to ensure uniform temperature distribution. Table 2-5 summarises key findings from the literature concerning the use of porous media in air-cooled LIB systems.

Table 2-5. Summary of the work carried out on porous media-based air cooling BTMS.

Author (year)	Battery type	Porous media type	Type of study	Findings	Configuration
Yang et al. [191] (2024)	Prismatic cell	Sintered porous metal foam	Num.	a novel air-based BTMS design using intermittent porous metal foam zones, optimised to achieve near-equivalent thermal performance to fully porous channels while significantly reducing material usage and system cost. With only 10% porous volume, the system achieved a maximum cell temperature of 317.79 K, just 2.5 K higher than the fully porous case, but with 90% less metal foam, a 15% weight reduction, and an 88.5% drop in pressure loss and fan power requirement.	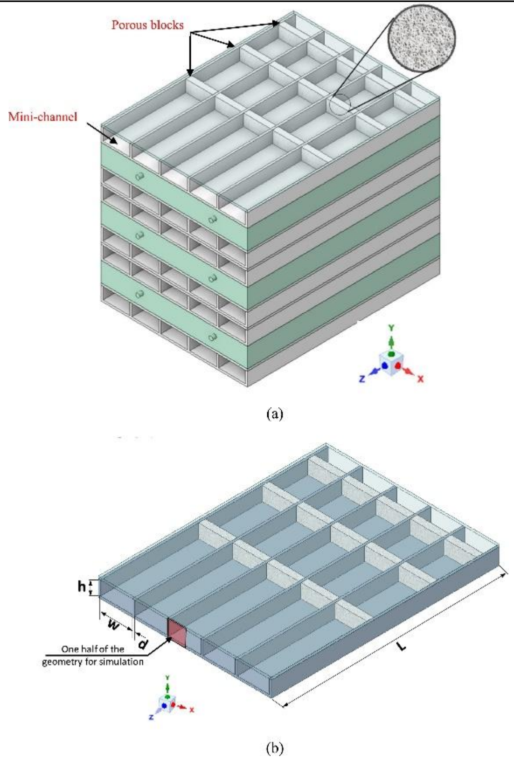
Bashiri et al. [85] (2022)	18650 Li-ion battery	Aluminum Foam Copper Foam Silicon Carbide Aluminum Oxide Graphite	Num.	The presence of a porous medium significantly lowers the module's maximum temperature while raising the pressure drop inside the battery module. Graphite tends to have the best performance in terms of heat transfer enhancement and	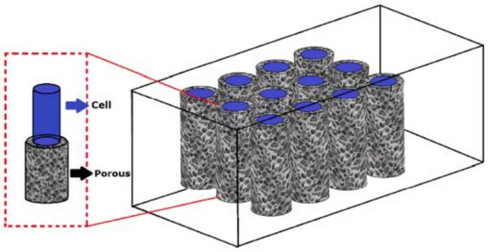

Author (year)	Battery type	Porous media type	Type of study	Findings	Configuration
				provides 4 °C reduction in T_{max}.	
Wang et al. [192] (2022)	Prismatic cell	Aluminum Foam	Num.	The average temperature of the battery drops when the porosity of the aluminum foam is decreased, but the temperature gradient increases. The increase in pore density (PPI) results in a rise in pressure drop but has a negligible impact on battery temperature.	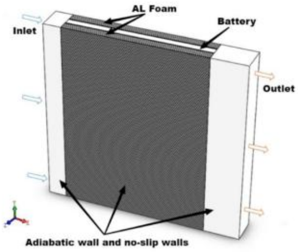
Wang et al. [190] (2021)	$LiFePO_4$ pouch cell	Aluminum Foam	Num.	By decreasing the porosity of Al foam, the mean surface temperature of the battery is reduced, but the temperature difference is increased. Changing the flow direction of cooling air from length to width increases the average temperature of all batteries while decreasing the temperature difference.	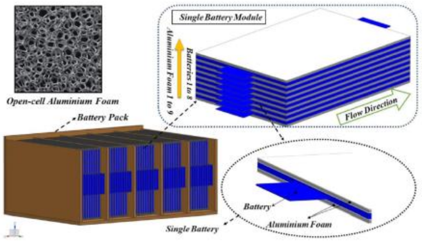
Saw et al. [117] (2017)	$LiFePO_4$ pouch cell	Aluminum Foam	Num.	Reducing the porosity of the aluminum foam will reduce the battery module's surface temperature and increase the friction factor. Aluminum foam is a viable replacement for conventional folded fin or liquid cold plate in battery module cooling.	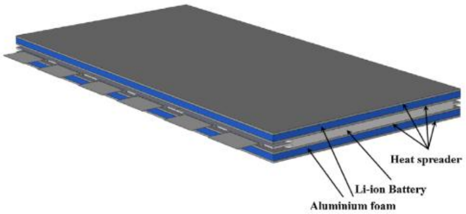

Author (year)	Battery type	Porous media type	Type of study	Findings	Configuration
Mohammadian and Zhang [193] (2017)	$LiFePO_4$ pouch cell	Aluminum Foam	Num.	Increasing the air flow inlet velocity increases the temperature field's standard deviation within the battery. The incorporation of porous aluminum foam within the airflow channel optimizes the battery's temperature decrease. Nonetheless, it cannot enhance temperature uniformity.	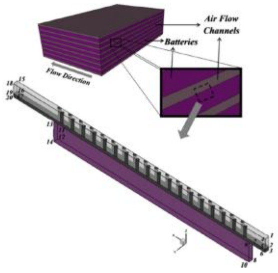
Mohammadian and Zhang [194] (2016)	Prismatic cell	Aluminum Foam Ceramic Foam	Num.	The usage of ceramic foam increases temperature uniformity by around 25.8 percent, from 4.5 °C to 3.34 °C. By partially inserting a porous conductor substance (aluminum foam) from the outside into the airflow channel, temperature uniformity and temperature decrease within the battery module are improved.	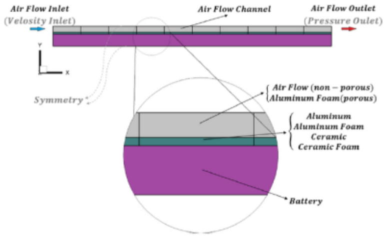

Author (year)	Battery type	Porous media type	Type of study	Findings	Configuration
Mohammadian et al. [121] (2015)	Prismatic cell	Aluminum Foam	Num.	The maximum temperature and the standard deviation of the temperature field inside the battery are both reduced as the porosity of the porous material is decreased. The maximum temperature inside the battery is reduced when the permeability of the metal foam is increased, and the temperature distribution throughout the battery is improved when the permeability is decreased.	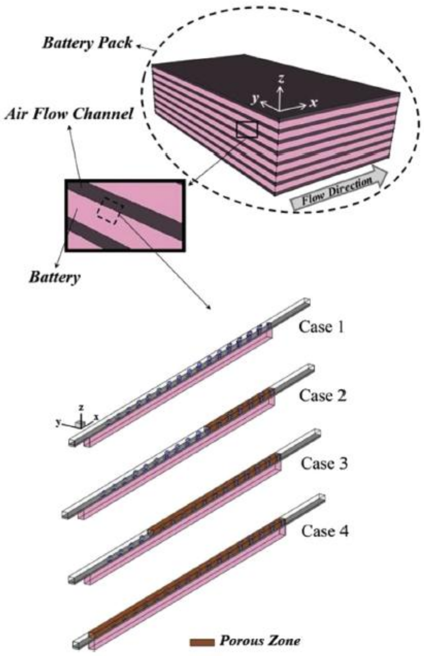
Giuliano et al. [116] (2012)	Lithium-titanate battery	Aluminum Foam	Exp.	Even for 200 A charge-discharge cycles, an airflow of 1100 ml/s per cell limits the coolant air temperature rise to less than 10 °C above ambient. Compared to a conventional liquid-cooled thermal management system, less energy is required to propel air through the porous heat exchanger.	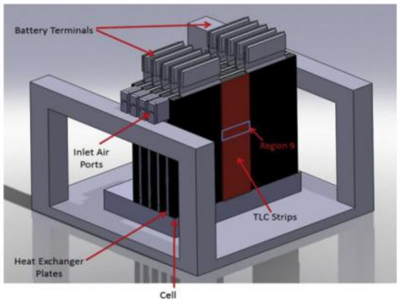

2.4.2 PCM-Based BTMS Enhanced by Porous Media

PCM is capable of absorbing generated heat via latent heat. Since the phase change process occurs at a nearly constant temperature, as depicted in Figure 2-8, PCM offers a stable and reliable approach for thermal regulation. As a passive thermal management strategy, PCM-based BTMSs provide several advantages. These systems are structurally simple, resulting in reduced weight and spatial requirements compared to air- and liquid-based cooling systems. Moreover, PCM-based systems operate without external power input, making them more environmentally sustainable and energy-efficient [195, 196]. The inherent characteristics of PCMs facilitate benefits such as prolonged thermal energy retention [197], enhanced battery lifespan, and a reduced risk of thermal runaway events [198].

Phase change can occur in various forms, including solid–gas, solid–liquid, and liquid–gas transitions. For BTMS applications, however, the selected PCM must exhibit certain critical properties, such as high latent heat, an appropriate phase transition temperature, minimal volumetric expansion, high thermal conductivity, low toxicity, and robust chemical stability [50, 199]. Given these requirements, solid–liquid PCMs are commonly recommended by researchers for battery cooling [50, 200-204] and are typically classified as organic, inorganic, or eutectic materials [205].

Among the key selection criteria, the PCM's melting point plays a vital role, as it directly influences the system's ability to regulate the high operating temperatures encountered during charge–discharge cycles [197, 206, 207]. The operating temperature is recommended to be lower than maximum permissible battery temperature [50, 207, 208]. A melting point around 30°C [209, 210] is recommended to maintain battery temperature within safe limits, thereby reducing the rate of degradation commonly observed at elevated temperatures [211, 212].

It is also important to consider the trade-off between phase change temperature (PCT) and PCM performance. While a higher PCT is typically associated with greater latent heat capacity, a lower PCT ensures a safer operational range for lithium-ion batteries. However, reducing the PCT may also compromise the PCM's heat discharge efficiency. This balance must therefore be carefully evaluated when selecting a PCM for a specific battery application [79].

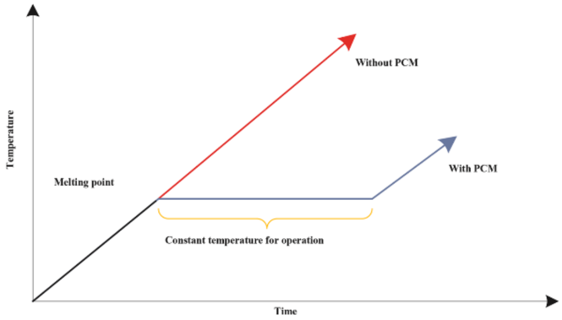

Figure 2-8. Thermal behaviour of a PCM-based system [49].

As shown in Figure 2-9, the incorporation of PCM combined with porous foam into BTMS can also influence battery charging times, particularly during the constant current (CC) and constant voltage (CV) phases. As enhanced cooling lowers the battery temperature, the migration rate of Li$^+$ ions through the graphite anode decreases. This reduction leads to the accumulation of lithium ions on the graphite surface, causing ion concentration polarisation. As a result, the cut-off voltage is reached more rapidly during the charging process, thereby extending the overall charging duration. In PCM-integrated systems, this effect becomes more pronounced, leading to longer charge times. Regarding the discharging behaviour, it has been reported that the initial discharge voltage of a LIB equipped with PCM is typically lower than that of a system without PCM. This is attributed to the significantly reduced operating temperature in the presence of PCM, which may impair the electrochemical activity of the electrodes, consequently resulting in a lower output voltage during discharge [79].

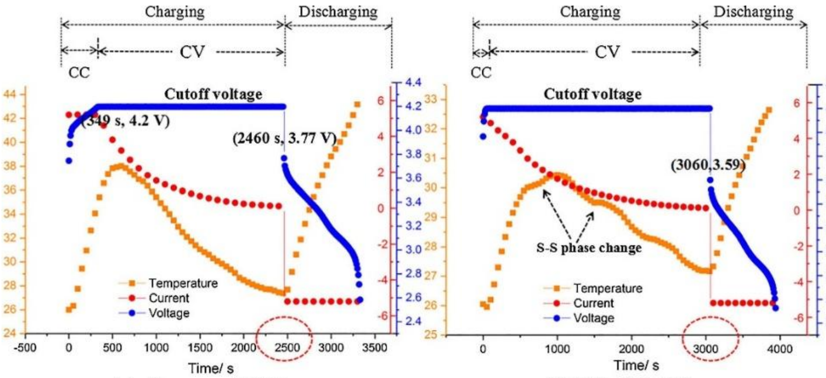

(a) Absence of PCM (b) With PCM 35

Figure 2-9. Impact of PCM cooling on 18650 LIBs charging and discharging performance [79].

One of the primary challenges associated with the use of PCMs in BTMS is their inherently low thermal conductivity [26]. This limitation can be addressed by embedding high-conductivity porous structures such as metal foams (copper, nickel, and aluminium), aluminium meshes, polyurethane foams, or expanded graphite (EG) matrices. While these materials significantly enhance thermal conductivity, their inclusion also reduces the volume fraction of pure PCM within a given volume. As a consequence, the latent heat and overall thermal storage capacity of the composite are diminished. Therefore, to achieve an effective balance between improved thermal conductivity and sufficient latent heat storage, it is essential to optimise the quantity and type of additive material used [50, 110, 213].

Table 2-6 provides a summary of the research studies focused on the application of CPCM in BTMS. As observed in the table, paraffin emerges as the most frequently employed PCM in CPCM-based BTMS. This widespread utilisation is attributed to paraffin's advantageous thermophysical and chemical properties, which align well with the requirements of lithium-ion battery cooling systems. These desirable characteristics include: (1) a suitable phase change temperature range, (2) high latent heat, (3) relatively good thermal conductivity, (4) minimal volumetric expansion during phase transition, (5) resistance to phase segregation, (6) low degree of supercooling, (7) high chemical stability, (8) compatibility with various supporting matrices, (9) non-toxicity, non-corrosiveness, and overall environmental safety, and (10) economic feasibility due to its low cost. Collectively, these properties make paraffin an ideal candidate for enhancing thermal regulation in lithium-ion battery systems [214, 215].

Table 2-6. Summary of the work carried out on CPCM cooling BTMS.

Author (year)	Battery type	Material	Type of study	Findings	Configuration
Saxena et al. [216] (2024)	Prismatic Li-ion battery	Paraffin wax, Copper foam	Num.	The optimal PCM thickness for effective heat absorption was identified as 8 mm for a 20 Ah prismatic cell at 5C discharge, reducing the average temperature significantly (from 334 K without PCM to approximately 315 K). The PCM-MF composite with a porosity of 0.95 offered superior performance, achieving up to a 56% reduction in temperature rise compared to natural convection	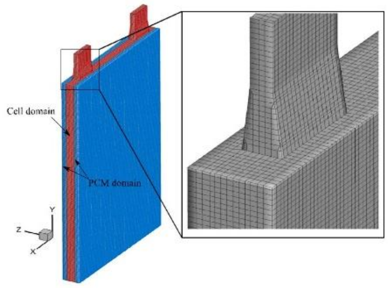
Kurşun et al. [217] (2024)	18650 Li-ion battery	Paraffin, Copper foam	Num.	Integrating a bio-inspired hybrid PCM-foam structure significantly enhances the thermal performance of a cylindrical battery module. Compared to pure PCM, the hybrid system reduced the maximum temperature by 8.7 °C and improved	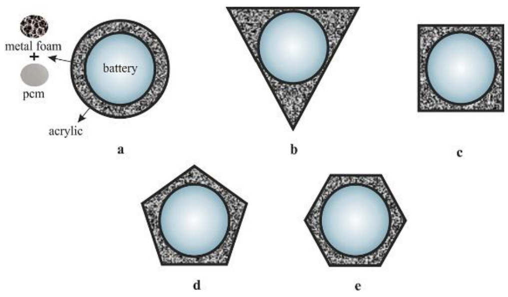

Author (year)	Battery type	Material	Type of study	Findings	Configuration
				temperature uniformity by 57.5%.	
Li et al. [33] (2024)	Cylindrical Li-ion battery	Different PCM, aluminium and copper foam	Num.	An optimal thickness of 0.273R offered the best overall performance by balancing conduction and convection, while more scattered porous distributions improved latent heat utilisation. The results were consistent across different PCM types (Pr = 2.0 and 7.0) and porous media (aluminium and copper), demonstrating the universality of the proposed design.	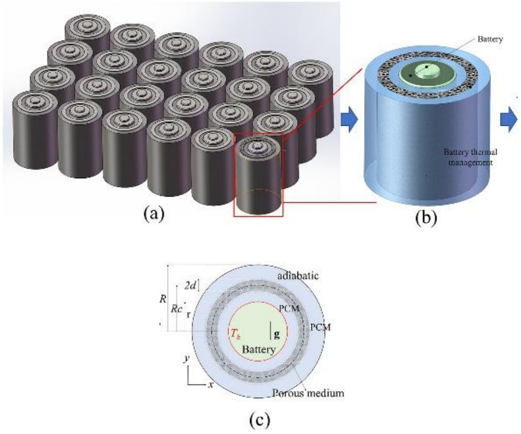
Sun et al. [32] (2023)	LG 21,700 NMC811 Battery	Paraffin, Copper foam	Exp.	By selecting a PCM with a higher latent heat, it is possible to improve the cell-to-pack ratio of the battery pack. At a discharge rate of 3C, the greatest temperature difference in the battery module containing copper foam-PCM is limited to less than 5 °C.	
Zhou et al. [218] (2023)	18650 Li-ion battery	Paraffin wax, MIL-101(Cr) NH2/RGO	Exp.	By adding MIL-101(Cr)–NH2 (35 wt%) and RGO (5 wt%) to PW (60 wt%), a CPCM with excellent anti-leakage properties is created. The battery pack's susceptibility to thermal runaway is exacerbated by the high discharge rate and high ambient temperature, which can be mitigated by the	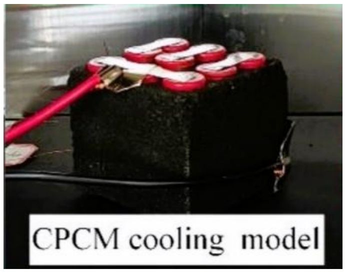

Author (year)	Battery type	Material	Type of study	Findings	Configuration
				superior thermal management capabilities of CPCM.	
Li et al. [219] (2023)	Square terpolymer lithium battery	Paraffin wax (PW), Myristic acid (MA), Palmitic acid (PA), Expanded graphite (EG), Carbon black (CB), and short carbon fiber (SCF)	Exp.	The maximum discharge temperature for a large capacity square ternary polymer lithium battery is restricted to 47.03 °C. When the ratio of MA, PA, and PW is 3:1:4, two-phase transitions are detected at temperatures of 35.88 °C and 46.26 °C, respectively.	
Zhou et al. [220] (2023)	$LiFePO_4$ battery	Paraffin, melamine, Expanded graphite	Exp. /Num.	At 3C discharge rate, the temperature of the batteries in the module with two-sided CPCM and two-sided and bottom CPCM is obviously higher than 48 °C. In comparison, the battery module with all sided CPCM can manage temperatures below 48 °C. The maximum temperature of the battery module with all-sided CPCM can be managed to be less than 47.5 °C, and the	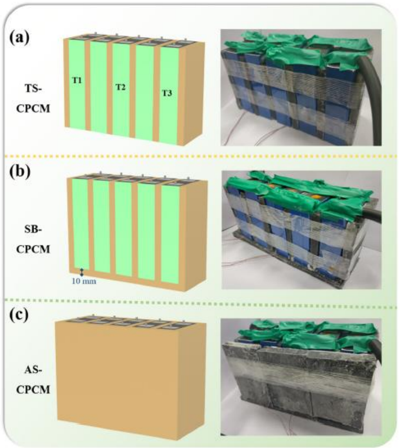

Author (year)	Battery type	Material	Type of study	Findings	Configuration
				temperature difference can be kept to less than 1.1 °C.	
Zhang et al. [221] (2023)	$LiFePO_4$ battery	Lauric acid-paraffin, Expanded graphite	Exp.	With CPCM, the highest temperature difference is 1.96 °C, and the maximum temperature could be maintained below 43 °C. After five cycles of charging and discharging, the CPCM system's temperature management remains effective.	
Mei et al. [222] (2022)	18650 Li-ion battery	Paraffin, Expanded graphite	Exp. /Num.	The maximal temperature of the proposed BTMS is reduced by approximately 35% when both EG and fins are utilized. The ambient temperature has a noticeable impact on the PCM's thermal management capability, and as the temperature rise, thermal management efficacy decreases.	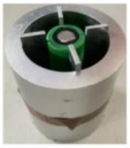 Battery with Fins  Battery with PCMP  Battery with EGPCMP
Buonomo et al. [35] (2022)	Li-ion battery	Paraffin RT42, Copper foam	Num.	There are not any considerable differences in temperature between 20 PPI and 40 PPI. The case containing only PCM demonstrates significant temperature differences between the top of the battery and the top of the domain.	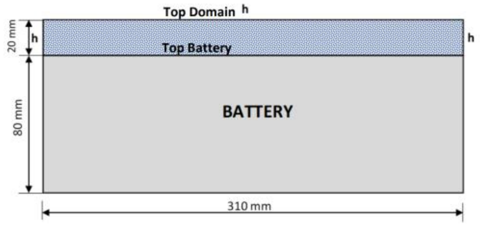

Author (year)	Battery type	Material	Type of study	Findings	Configuration
Rajan et al. [34] (2022)	LiFePO4 battery	1-Tetradecanol, Copper foam	Exp. /Num.	When BTMS is utilized, the maximum temperature of the cell is reduced by a maximum of 7 C. By incorporating the copper foam, the latent heat is absorbed more uniformly, a reasonable thermal conductivity is achieved, and a uniform temperature profile is achieved across the cross-section.	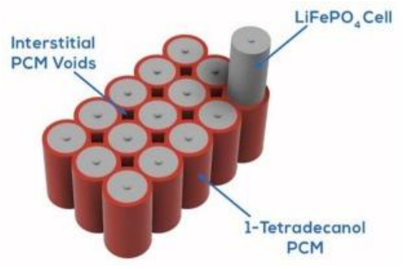
El Idi et al. [91] (2021)	18650 Li-ion battery	Paraffin RT27, Aluminum foam	Exp. /Num.	The axial thermal conductivity is more important than the radial one, using the Hot-Disk analysis of the thermal conductivity of the cell. The proposed system decreased the cell's temperature by approximately 11°C while maintaining an operating temperature of approximately 25°C.	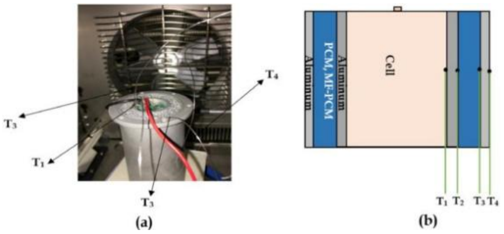
El Idi et al. [36] (2022)	18650 Li-ion battery	Paraffin RT27, Aluminum foam	Exp. /Num.	An increase in PCM volume has little effect on the temperature of the cell surface. Cell surface temperature is influenced by current rate, charge/discharge cycle duration, and ambient temperature.	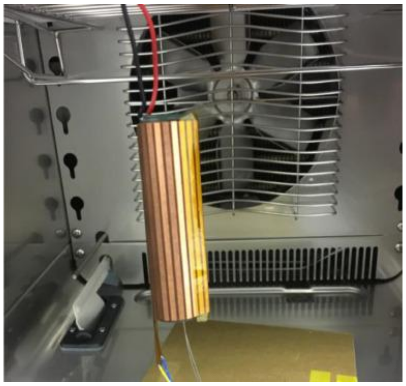

Author (year)	Battery type	Material	Type of study	Findings	Configuration
Ranjbaran et al. [126] (2020)	18650 Li-ion battery	Paraffin wax, Copper foam	Num.	The addition of metal foam has a significant effect on the evolution of the PCM liquid fraction over time. The addition of 1% to 6% of copper foam to pure paraffin wax mildly increases the liquid fraction, allowing PCM to absorb sufficient heat from the battery cell.	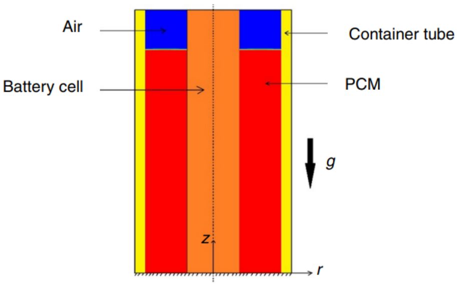
Huang et al. [223] (2020)	18650 Li-ion battery	Aluminum nitride Paraffin, Expanded graphite, Epoxy resin	Exp.	In comparison to air cooling, there is a 19.4% reduction in maximum temperature and a temperature difference of less than 1 °C at a high discharge rate of 3C. After four 2C discharge cycles, the maximum temperature of the PCM-cooled module decreases by 12%.	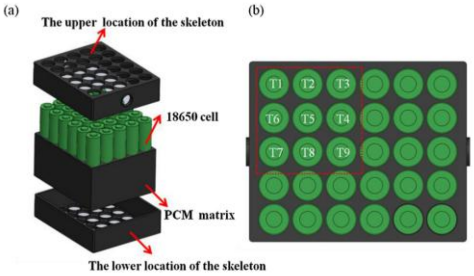
Heyhat et al. [123] (2020)	18650 Li-ion battery	n-eicosane. Copper foam	Num.	Battery mean temperature is lowered by 4 and 6 K with metal foam at 4.6 and 9.2 W generation rates, respectively. The reduction in porosity from 95% to 85% had no appreciable effect on the thermal management system's efficiency.	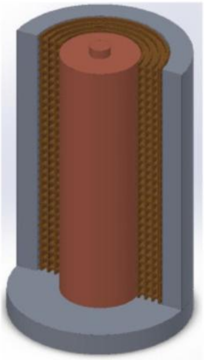
Cao et al. [224] (2020)	Rectangular ternary lithium battery	Paraffin wax, Expanded graphite, Carbon fiber,3D printed	Exp.	At a discharge rate of 2.5 C, the battery reached a maximum surface temperature of 45.5°C, which remained below the maximum safe temperature of 50°C. The CPCM's thermal conduction and heat	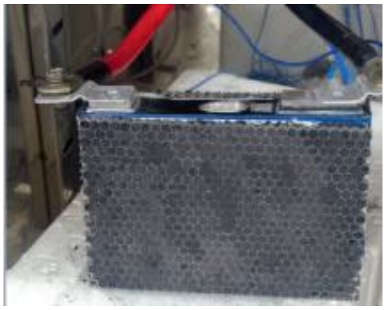

Author (year)	Battery type	Material	Type of study	Findings	Configuration
		aluminum honeycomb with a prickly structure		dissipation capabilities are enhanced by the metal framework provided by the 3D aluminum honeycomb.	
Barnes and Li [225] (2020)	LiFePO4 pouch cell battery	Paraffin, Aluminum foam	Exp. /Num.	For 3C discharge rate at room temperature, the PCM-Al foam (5 PPI) system maintained battery temperatures below 28.1 and maximum temperature differences below 5.2 °C. It is preferable to use metal foams with a larger pore size (or higher permeability) to increase the overall thermal conductivity of the composite material without substantially inhibiting natural convection.	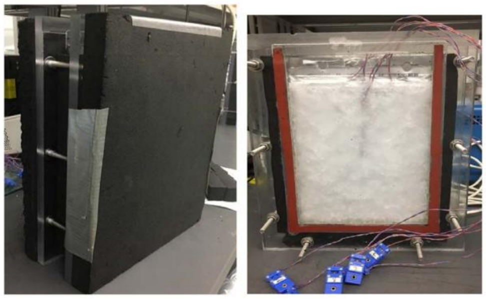
Veismoradi et al. [226] (2020)	-	Paraffin wax, Copper foam	Num.	During the steady-state condition, the thermal distribution becomes more uniform, particularly at the bottom of the heatsink. A stabilized convection-dominant regime (high Rayleigh Darcy number) decreases wall temperature during a severe heat discharge. However, increasing the Rayleigh-Darcy number has little influence on wall temperature when convection flow is high.	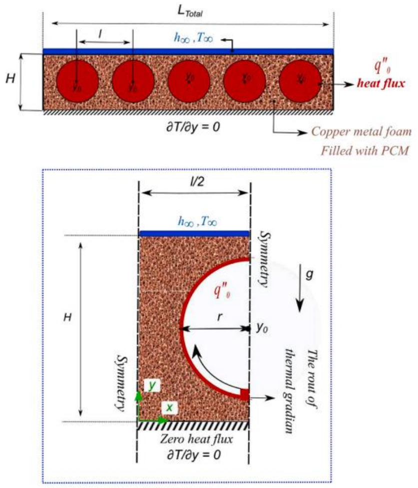

Author (year)	Battery type	Material	Type of study	Findings	Configuration
Mehrabi-Kermani et al. [227] (2019)	Pouch lithium-ion battery	Paraffin, Copper foam	Exp. /Num.	Copper foam with high thermal conductivity played a pivotal role in heat transfer enhancement and achieving temperature uniformity. At Re = 1050, which corresponds to an EV's velocity of 3.2 km/h, it is possible to maintain the LIB modules' surface temperature in a steady condition below the 60 °C limit at high constant current discharge (5 W).	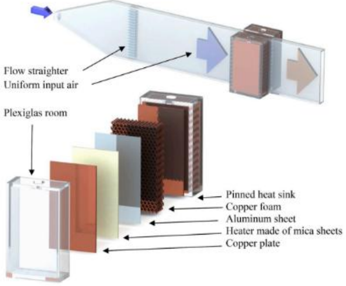
He et al. [228] (2019)	Pouch LiCoO2 battery	Paraffin, Expanded graphite, Copper foam	Exp.	Expanded porous graphite absorbs paraffin and acts as a micro-thermally conductive framework, transferring heat to the adjacent copper foam skeleton. During the cycling charge-discharge experiments under forced air flow, the battery pack demonstrates a stable maximum temperature and temperature difference of 48.0 and 3.9 °C, respectively.	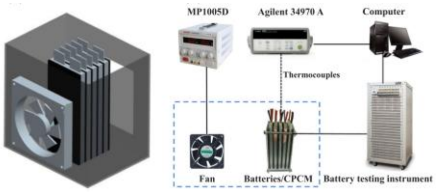
Zou et al. [229] (2019)	38120-type LiFeO4 battery	Paraffin, Graphene, Carbon tube, Expanded graphite	Exp.	Upon enhancing 4 batteries with CPCM, the maximum temperature in a 36-battery module during a 3C discharge is limited at 44.6 °C, while the maximum temperature difference is limited at 0.8 °C. The more uniform battery module temperature is achieved by decreasing the size of the enhanced zone.	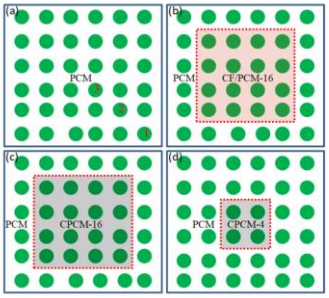

Author (year)	Battery type	Material	Type of study	Findings	Configuration
Buonomo et al. [230] (2019)	-	Paraffin RT42, Aluminum foam	Num.	The PCM has the capacity to postpone the battery's critical temperature achieving its melting point. The foam serves as a heat vector, which is required for the uniform distribution of thermal energy within the PCM and to prevent the PCM from acting as a thermal insulator due to its low thermal conductivity.	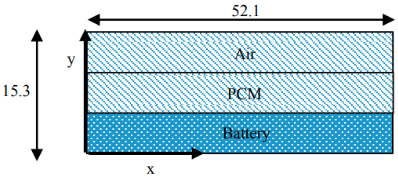
Hussain et al. [141] (2018)	18650 Li-ion battery	Paraffin wax, Graphene coated nickel foam	Exp.	After infiltrating graphene-coated nickel foam, the thermal conductivity of pure paraffin wax increased 23 times. Using graphene-coated nickel foam saturated with paraffin wax under a discharge current of 1.7 A reduces the rise in battery surface temperature by 17% compared to using nickel foam alone.	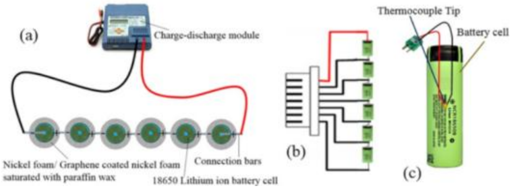
Pan and Zhong [231] (2018)	18650 Li-ion battery	Paraffin, Copper fiber sintered skeleton (CCFSS)	Exp. /Num.	The CCFSS/paraffin composite PCM improves heat transfer performance and maintains temperature differences within 5°C. Longer phase changes and lower heating rates are achieved by increasing the distance between the cells in a battery pack.	

Author (year)	Battery type	Material	Type of study	Findings	Configuration
Wang et al. [232] (2018)	Li-ion battery	Paraffin, Copper foam	Exp. /Num.	The maximum temperature of the battery module could be maintained below 28 °C, 35 °C, and 42 °C with the passive thermal management system at 3C and 4C charge/discharge rates, respectively. The passive thermal management system could accomplish up to three 4C charge and discharge cycles at 35 °C while maintaining the battery module's maximum temperature below 52 °C.	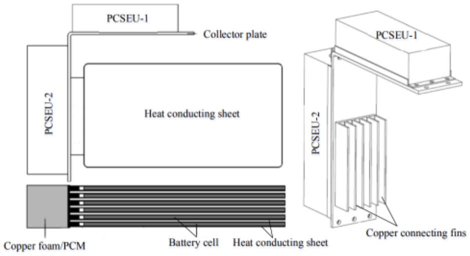

2.4.3 Impact of Adding Porous Media on PCM Properties and Performance of PCM-based BTMS

An effective strategy to enhance the thermal conductivity of various types of PCMs is the incorporation of porous media or foams, resulting in the formation of CPCMs [109]. Among the materials investigated, copper foam demonstrates the most pronounced enhancement, followed by aluminium and nickel foams. Expanded graphite (EG) also contributes to thermal conductivity improvement, with performance situated between that of nickel and aluminium foams [201]. The distribution of various porous materials and foams employed in the literature for improving PCM thermal conductivity is illustrated in Figure 2-10.

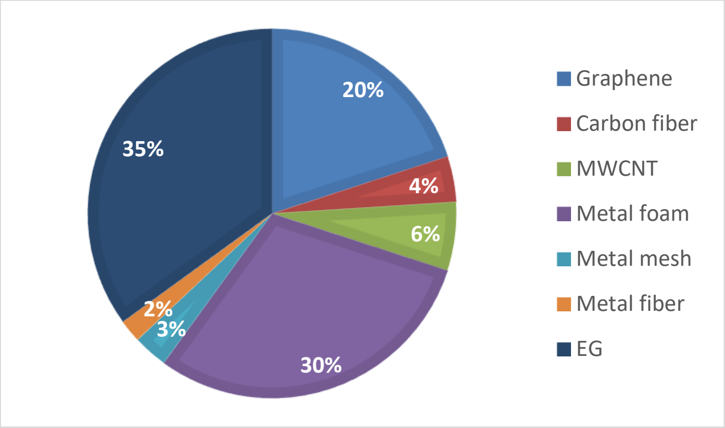

Figure 2-10. Distribution of different porous materials and foams for PCM thermal conductivity enhancement [233].

The thermal performance of CPCMs is strongly influenced by the physical characteristics of the porous scaffold, such as pore size, porosity, and ligament geometry, which directly affect their applicability in BTMS. CPCMs exhibiting higher thermal diffusivity and lower Stefan numbers, which is defined as the ratio of sensible heat to latent heat, demonstrate superior temperature uniformity and control compared to those with lower diffusivity and higher Stefan numbers. Additionally, BTMS performance is improved by the use of metal foams with reduced porosity. Studies have shown that decreasing porosity leads to a reduction in battery temperature, attributable to improved heat conduction via increased solid material within the foam structure [117, 120, 128, 234].

Similarly, reducing pore size enhances thermal management by increasing the contact surface area between the PCM and the metal ligaments, thereby facilitating greater heat transfer [128]. However, the porosity of metal foams must be optimised, as higher porosity allows for greater PCM loading but typically reduces overall thermal conductivity due to the lower proportion of conductive solid matrix [185]. Furthermore, pore size critically affects the structural stability of CPCMs. If the pores are too small, PCM infiltration is incomplete, compromising latent heat capacity. Conversely, excessively large pores improve permeability but may lack sufficient capillary force to retain the PCM within the porous structure, thereby limiting thermal performance [235].

The solidification and recovery rates of the PCM used in BTMS are critical factors, particularly as the PCM is subjected to repeated charge and discharge cycles at varying C-rates. The integration of porous media can have a substantial influence on these aspects. During the PCM recovery phase, natural convection plays a key role in enhancing heat transfer. The inclusion of porous structures improves this process by increasing the effective thermal conductivity and influencing local vortex formation [123], thereby accelerating both solidification and recovery rates [236, 237]. Lower porosity levels have been shown to yield even better performance in this regard [238]. Moreover, the addition of porous matrices not only significantly reduces the total time required for complete melting and solidification but also minimises the time difference between these two phases, enabling a more balanced and time-aligned heating and cooling cycle within the BTMS [237].

In PCM-based BTMS, the solid-state PCM absorbs heat from the batteries and melts accordingly. During this phase transition, the PCM experiences a volume change, which may lead to leakage and a corresponding reduction in its heat absorption capacity. To address this challenge, several strategies have been developed to mitigate PCM leakage during the melting process. One widely adopted approach involves embedding porous materials within the PCM to physically restrict the spread of the molten phase [110, 239]. As the PCM melts, the associated volume expansion induces PCM flow. The introduction of hierarchical pore structures in porous materials can effectively limit this mobility and help confine the PCM within the matrix [240]. Furthermore, the incorporation of expanded graphite (EG) has been shown to preserve the structural integrity of CPCMs after multiple solid–liquid transitions, significantly reducing leakage compared to pure PCM [110].

In addition to leakage control, the integration of porous media such as metal foams or mesh materials enhances the mechanical strength of the PCM. The high porosity and specific surface area of these materials contribute to improved structural stability, supporting the form-retention of CPCMs under repeated thermal cycling [240, 241].

2.4.4 Liquid Cooling-Based BTMS Enhanced by Porous Media

Liquid cooling offers superior heat transfer rates and enhances thermal performance compared to air and PCM cooling, making it one of the most widely adopted methods in practical BTMS applications. As a result, it has been implemented in several commercial electric vehicles, including the Chevrolet Volt, Tesla Model S and Model 3, as well as the BMW i3 and i8 [49]. This approach not only improves thermal regulation but also plays a crucial role in preventing thermal runaway in LIBs. The higher thermal conductivity of liquid coolants relative to natural or forced convection air cooling makes liquid-based BTMSs particularly desirable for EV applications [242].

Liquid cooling systems are typically categorised into direct and indirect configurations based on the manner in which the coolant interfaces with the battery surface [243]. In direct liquid cooling, battery modules are submerged in a circulating dielectric or non-conductive liquid, such as mineral oil, deionised (DI) water, or silicone oils. Conversely, indirect cooling systems rely on circulating fluid through jackets, pipes, or cooling plates positioned adjacent to the battery modules. In such systems, common coolants include water, liquid metals, nanofluids, or water–

ethylene glycol mixtures [49]. The thermophysical properties of commonly used liquids in BTMSs are presented in Table 2-7.

Table 2-7. Thermophysical properties of various common coolants for liquid cooling in BTMSs [86, 244]

Property	Mineral oil	Silicone oil	Water/Glycol
Density (kg/m^3)	924.1	920	1069
Kinematic viscosity (m^2/s)	5.60×10^{-5}	-	2.58×10^{-6}
Specific heat capacity (J/(kg·K))	1900	1370	3323
Thermal conductivity (W/(m·K))	0.13	0.15	0.3892

Despite its excellent thermal performance, direct liquid cooling poses risks such as potential short-circuiting and leakage, necessitating careful design considerations [245]. Moreover, high-viscosity dielectric fluids used in direct systems require elevated pumping power. On the other hand, indirect systems, though safer, tend to suffer from reduced thermal effectiveness due to resistance introduced by the cooling plate or tubing materials [242].

To further enhance thermal performance, nanofluids, suspensions of nanoscale metal or metal oxide particles like ZnO, Al_2O_3, TiO_2, or CuO, are often introduced into base fluids to increase their thermal conductivity [246]. Although nanofluids may introduce challenges such as high costs, increased system complexity, and maintenance difficulties [247], their heat transfer enhancements, particularly under high charging or discharging rates, often justify these trade-offs. Despite an associated pressure drop, this is still generally lower than what would be required to achieve equivalent cooling by simply increasing fluid velocity [242].

Nonetheless, liquid cooling systems are not without limitations. Drawbacks include increased design complexity and cost, the need for additional components, added system weight compared to air-cooled BTMSs, and a potentially shorter operational lifespan [248, 249].

The configuration of liquid flow channels in cooling plates or jackets plays a pivotal role in the overall effectiveness of a liquid-based BTMS. In systems utilising conventional straight channels, a thermal boundary layer tends to form along the coolant flow path, leading to a gradual rise in coolant temperature downstream [37, 150]. To address this limitation, the introduction of porous layers or obstacles within the flow channels has been explored. The presence of porous media can promote the redevelopment of the thermal boundary layer and induce additional crossflow mixing effects, thereby disrupting the formation of a stable boundary layer. This disruption mitigates the undesired temperature rise of the coolant along the channel length and enhances both heat transfer and cooling efficiency [37, 38].

Furthermore, the inclusion of porous materials within cooling channels allows the desired temperature control to be achieved at lower coolant flow rates. This reduction in flow requirement can lead to energy savings in pumping power. However, a significant trade-off arises in the form of increased pressure drop due to the obstruction and reduced flow area introduced by the porous structure. Therefore, the design must carefully balance heat transfer enhancement against the associated hydraulic resistance [38, 39].

Table 2-8 provides a summary of the studies conducted on the integration of porous media with liquid cooling in BTMSs. Due to the significant increase in pressure drop resulting from fluid interaction with metal foams and porous structures, the application of this approach in BTMSs remains relatively limited. The elevated pressure drop demands greater pumping power, which increases system complexity and energy consumption. Consequently, the use of liquid cooling in conjunction with complementary techniques, such as hybrid cooling systems, has gained more traction in the literature, offering a more balanced and efficient solution to enhance thermal regulation while mitigating associated drawbacks.

Table 2-8. Summary of the work carried out on liquid cooling BTMS.

Author (year)	Battery type	Material	Type of study	Findings	Configuration
Choi et al. [250] (2025)	Prismatic lithium-ion battery	Novec 7500, Water, glycol, Copper foam	Exp. /Num.	Under fast-charging conditions, the MCMF design significantly improved cooling, reducing the maximum battery temperature from 50.9 °C (traditional system) to 39.8 °C. the optimized MCMF structure provided superior thermal management by reducing temperature differences by 56.7% and coolant operating time by 22.7%	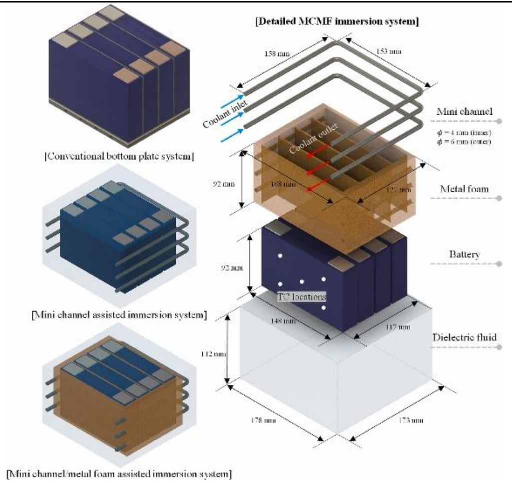

Author (year)	Battery type	Material	Type of study	Findings	Configuration
					
Jongpl-uempiti et al. [251] (2025)	18650 Li-ion battery	Water-based ferrofluid, Copper foam	Exp. /Num.	Integrating copper foam significantly enhanced heat transfer, reducing the maximum temperature difference to 0.35 °C (compared to 0.75 °C without foam), thereby improving temperature uniformity. Continuous monitoring and management of the cooling system are crucial, particularly given the varying heat generation associated with different battery charging and discharging rates.	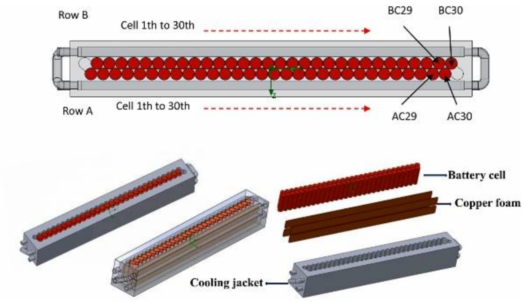
Du et al. [252] (2024)	18650 Li-ion battery	Water, TPMS (Triply Periodic Minimal Surface)	Num.	Compared to conventional straight tube cooling, the Primitive porous structure reduced battery maximum temperature rise by 12.43%, improved temperature uniformity by 8.41%, and showed optimal comprehensive performance at a 20% volume fraction. Adjusting mass flow rate and contact angles further improved thermal management, confirming the system's effectiveness under extreme conditions and demonstrating feasibility for lightweight, energy-efficient BTMS designs.	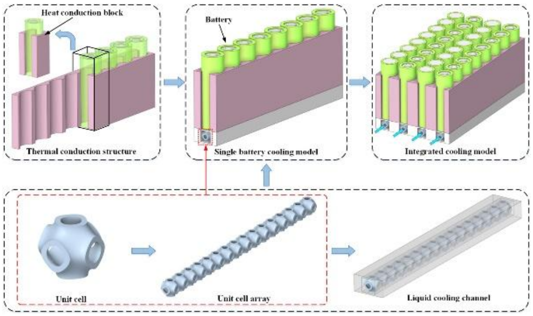

Author (year)	Battery type	Material	Type of study	Findings	Configuration
Rabiei et al. [41] (2023)	Prismatic LiFePO4 battery	Water, Aluminum foam	Num.	The implementation of the wavy microchannel resulted in a significant reduction in pumping power, ranging from 50% to 73%. Similarly, the utilization of a thin layer of metal foam led to a 50% decrease in pumping power. When the cooling channel is entirely filled with metal foam, a greater temperature difference exists, but the maximum temperature is reduced.	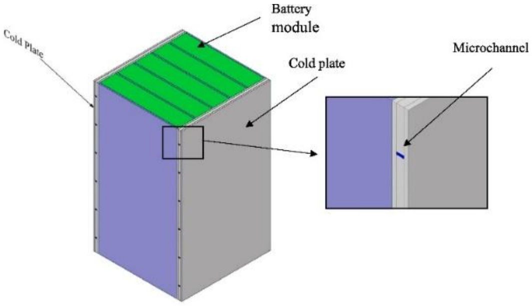
Ki et al. [38] (2022)	Pouch-type lithium-ion battery	Water, Aluminum foam	Exp. /Num.	Due to effective coolant distribution and enhanced thermal spreading effects, the proposed BTMS is able to provide a maximum cell temperature of 43.3 °C and a temperature difference of less than 2 °C while consuming only 3 L/min. In addition to increasing the heat exchange area, the porous metal layer decreases the thermal dispersion resistance. The vortex generation within the liquid flow path can be minimized and thermohydraulic performance can be maximized by modifying the geometrical parameters of the channel and the physical properties of the porous aluminum layer.	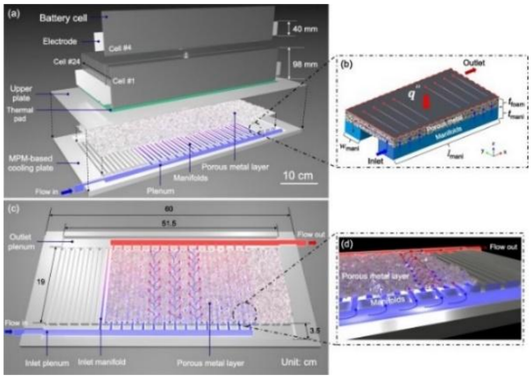

Author (year)	Battery type	Material	Type of study	Findings	Configuration
Xu et al. [253] (2021)	Square lithium iron phosphate battery	Water, Expanded graphite	Exp.	The liquid cooling module with a water flow rate of 0.8 m/s can maintain T_{max} below 42.7 °C and temperature difference within 2.7 °C at a discharge rate of 4C. Due to their high thermal conductivity, expanded graphite (EG) and copper foam added to silica gel (SG) can efficiently transfer the heat generated by batteries to copper tubes.	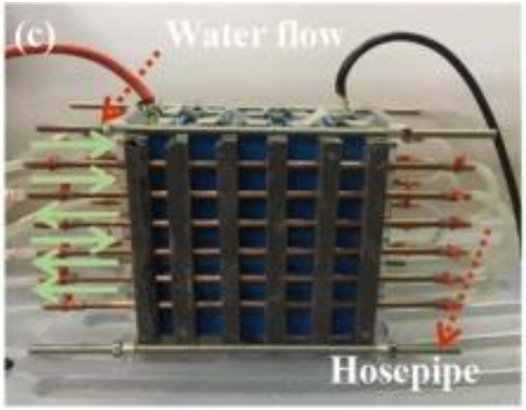

2.4.5 Hybrid Cooling-Based BTMS Enhanced by Porous Media

To address the limitations associated with individual cooling strategies, HBTMSs integrate both passive and active cooling techniques. This approach enhances the heat transfer performance of passive methods while allowing for dynamic control through active mechanisms. Hybrid configurations generally combine passive-active or active-active components. For instance, an active-active HBTMS may merge air and liquid cooling systems. However, using two active methods can result in excessive power consumption, making such configurations less practical for efficient BTMS operation. More commonly, hybrid systems pair active cooling (air or liquid) with passive elements such as heat sinks, heat pipes, or PCMs. This integration reduces energy consumption or coolant demand while improving thermal regulation. Combining two passive methods can also enhance thermal performance but often at the cost of increased system size and mass [249]. In many designs, PCM is incorporated to ensure a more uniform temperature distribution and prevent localised overheating when used alongside active cooling techniques [189]. Despite these advantages, HBTMSs face ongoing challenges related to volume, weight, power demand, and system complexity [254].

Incorporating porous media and metal foams into HBTMSs can significantly enhance heat transfer and temperature regulation by strengthening both passive and active cooling mechanisms. The dominant modes of heat transfer in such systems, conduction and convection, are notably improved through the introduction of porous structures. As discussed in previous sections, the use of porous media substantially increases the effective thermal conductivity of the system due to the high-conductivity solid matrix. Additionally, key convection parameters, such as the heat transfer surface area and mixing efficiency of the cooling fluid near heated surfaces, are favourably influenced. These enhancements contribute to more uniform temperature distribution and improved overall thermal performance of the HBTMS [31]. A summary of the research efforts focused on integrating porous media and metal foams into HBTMS is presented in Table 2-9.

Table 2-9. Summary of the work carried out on HBTMS.

Author (year)	Battery type	Coolant	Type of Study	Findings	Configuration
Khaboshan et al. [255] (2025)	18650 Li-ion battery	Water, n-eicosane, Copper foam	Num.	The fourth design, which combined PCM, metal foam, and counterflow minichannels, showed the best thermal performance, reducing the maximum battery temperature by up to 11.5 K compared to the passive PCM-only system and maintaining temperature differences below 5 K. The design ensured safe battery operation, extended PCM lifespan, and showed strong thermal uniformity under the UDDS drive cycle, making it a promising candidate for high-performance BTMS in electric vehicles	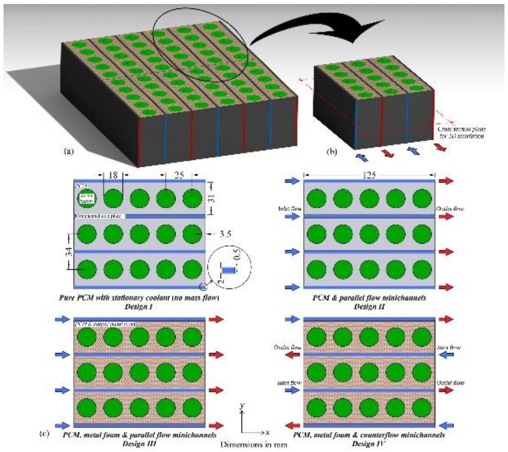
Yang et al. [44] (2025)	Prismatic lithium-ion battery	Water, PCM, TPMS metal skeleton	Num.	Under high discharge conditions (3C), this system reduced peak battery temperature by up to 16 K, and using a delayed cooling strategy improved PCM utilization to 97% while reducing energy consumption by 73%. The IWP-type TPMS structure provided the best overall thermal performance, achieving an	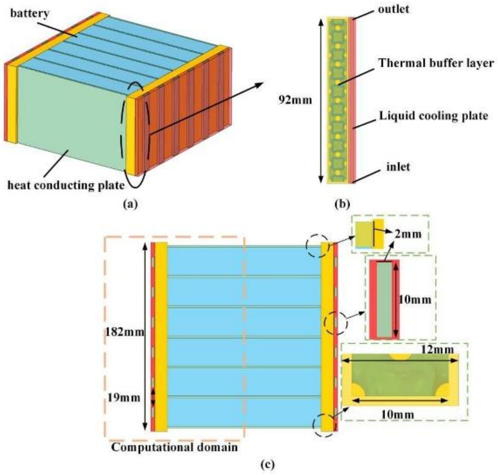

Author (year)	Battery type	Coolant	Type of Study	Findings	Configuration
				effective thermal conductivity 101 times greater than pure PCM and markedly improving melting efficiency.	
Lee et al. [256] (2024)	(LiNiMnCo) pouch-type lithium-ion polymer battery	Water–ethylene glycol, n-eicosane, Copper foam	Exp. /Num.	Under severe charging (3C) at room temperature, the system maintained a maximum cell temperature of 39.3 °C with a uniformity within 3 °C, and during preheating from −10 °C, achieved a stable temperature of 29.2 °C with 2.5 °C uniformity. A dual PCM pouch, evenly divided into pure PCM and copper-foam-enhanced PCM (CPCM), combined with a 1 mm thickness of PCM and graphite fins, proved optimal for effective heat management and rapid thermal distribution across the battery module.	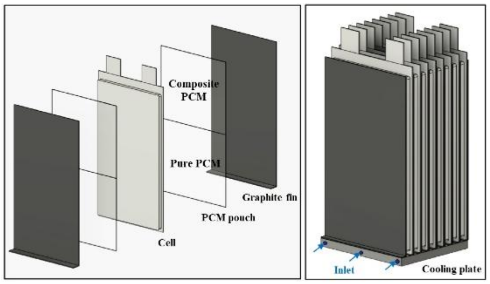
Yu et al. [257] (2024)	Squares lithium iron phosphate batteries	Air, paraffin, Copper foam	Exp.	integrating copper foam with paraffin PCM reduced the battery surface temperature by 4.1 °C compared to pure paraffin, enhancing structural stability and thermal consistency. Coupling PCM cooling with air-cooling at a wind speed of 30 km/h effectively maintained the battery temperature at 43.0 °C, rapidly lowering it to 35 °C within 80 minutes post-discharge without forced cooling.	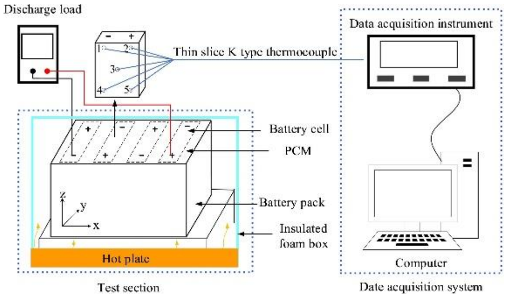

Author (year)	Battery type	Coolant	Type of Study	Findings	Configuration
Moaveni et al. [258] (2024)	18650 Li-ion battery	Water, RT44HC, Copper foam	Num.	Incorporating copper foam and a hybrid nanocomposite PCM (RT44HC enhanced with 5% CuO and 5% graphene nanoparticles) significantly improves the thermal regulation of lithium-ion batteries. Compared to pure PCM, the hybrid system reduced the maximum cell temperature by 10.6 °C and improved temperature uniformity, with a notable 76.5% decrease in temperature difference across cells.	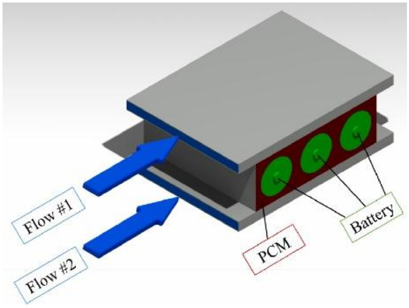
Jiang et al. [42] (2024)	Prismatic Li-ion battery	Water, n-eicosane, Aluminum and copper foam	Num.	The use of a PCM heat sink alone reduced the maximum battery temperature by 4.2 to 5 K across different inlet velocities. The combination of a PCM heat sink and porous-filled mini-channels reduced the maximum temperature by approximately 13 K at a 3C discharge rate. This improvement in thermal performance required only a 14% increase in pumping power	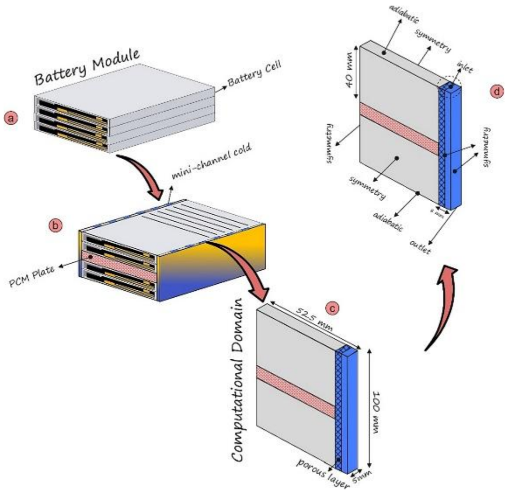
Yang et al. [259] (2023)	Prismatic lithium-ion battery	Water, RT35 paraffin wax, Aluminum foam	Num.	By intermittently circulating the coolant at a higher flow rate, the delayed cooling strategy permits a high utilization rate of the latent heat of the PCM, thereby drastically reducing power consumption while maintaining a safe battery temperature. Due to PCM's significantly lower density than aluminum's, the hybrid cold plate design can	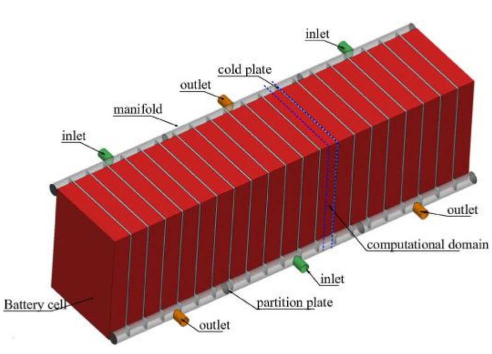

Author (year)	Battery type	Coolant	Type of Study	Findings	Configuration
				achieve a 53% reduction in overall weight compared to the standard cold plate design. Such a weight reduction, coupled with the 90% reduction in circulating power, has the potential to save each EV owner more than 200 kWh of electricity per year.	
Khaboshan et al. [260] (2023)	18650 Li-ion battery	Copper fin, N-eicosane, Copper foam	Num.	The optimal BTMS, comprised of PCM, metal foam, and four fins, can decrease the battery surface temperature by 3 K. The affixed fins act as a network of heat sources to distribute heat throughout the system's core.	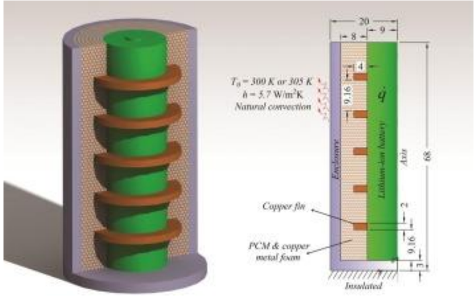
Zhao et al. [159] (2023)	18650 Li-ion battery	Water, Paraffin, Copper foam	Exp. /Num.	Increased Reynold numbers (Re) will result in temperature non-uniformity within the battery pack, whereas temperature differences decrease as Re increases. As the Re increased to 112, the T_{max} is reduced by 6 K, while the pump power consumption increased by 59 W.	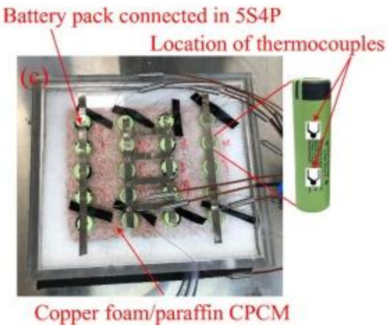
Liu et al. [43] (2021)	18650 Li-ion battery	Water, PCM28HC PCM 35HC PCM44HC, Copper foam	Num.	The hybrid system decreased the temperature by more than 30 K compared to natural convection. Maximum temperatures for the 10 mm and 40 mm helical pitch systems are 332.28 K and 332.88 K, respectively, versus 334.17 K for the straight-channel system.	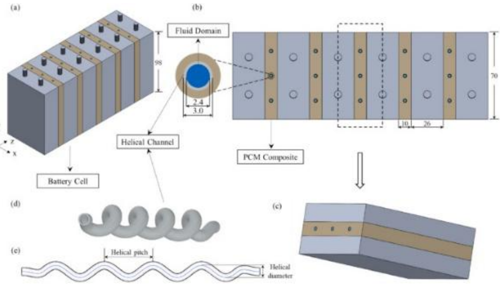

Author (year)	Battery type	Coolant	Type of Study	Findings	Configuration
				The increase in flow velocity could considerably reduce the temperature of the battery, but beyond 0.05 m/s, the temperature stabilized.	
Kiani et al. [261] (2021)	-	Al_2O_3-H_2O and Cuo-H_2O Nanofluid, Magnetic field Paraffin wax, Copper foam	Exp.	At Re = 1250, a battery thermal management system using Al_2O_3-H_2O nanofluid as a coolant can maintain its maximum temperature within the safe operating range of 318.7 K. HBTMS with a magnetic field reduces the maximum temperature and temperature difference by 22.5% and 79.3%, respectively, compared to BTMS with pure paraffin.	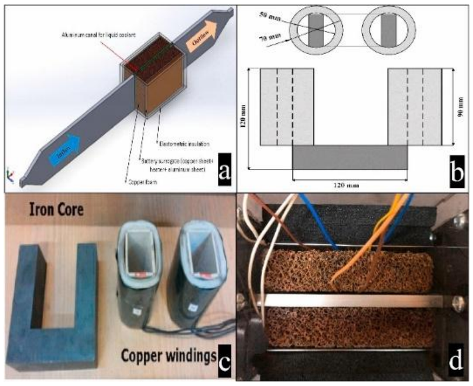
Kiani et al. [158] (2020)	-	Al_2O_3-H_2O Nanofluid, Paraffin, Copper foam	Exp. /Num.	The combination of the high latent heat of paraffin and the increased thermal conductivity of the copper foam reduces the rate of temperature rise. Increasing the volume fraction of the nanofluid from 1% to 2% accelerated the complete melting of the PCM by 24% at a Reynolds number of 420.	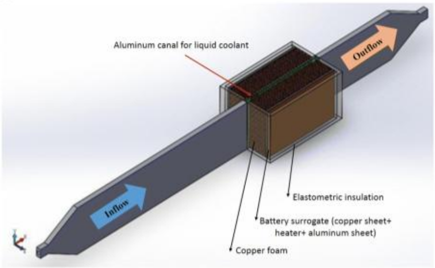
Zhao et al. [262] (2020)	18650 Li-ion battery	Water, Paraffin, Copper foam, Expanded graphite	Exp. /Num.	With an inlet velocity of 0.001 m/s for liquid cooling and EG-based composite cooling, the maximum temperature of a battery can be maintained below 325 K during three 2C-2C charge/discharge cycles.	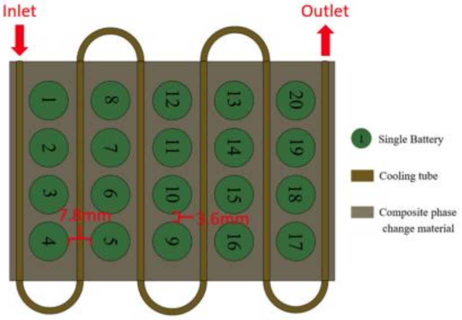

Author (year)	Battery type	Coolant	Type of Study	Findings	Configuration
				Copper foam-based CPCM is less effective at cooling than EG-based CPCM.	
Mashayekhi et al. [263] (2020)	18650 Li-ion battery	Al_2O_3-H_2O Nanofluid, Paraffin, Copper foam	Exp.	Increasing the Reynolds number in HBTMS has a negligible effect on temperature homogeneity, particularly at low heat generation power levels. The melting procedure can be divided into three phases: At the beginning of the melting process, conduction is the predominant mode of heat transfer. In reality, heat transfer from the battery to the PCM is conduction. In the midst of the melt, convective heat transfer predominates, whereas conduction predominates at the end.	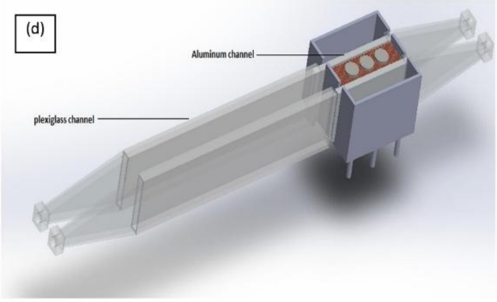
Bamdezh et al. [264] (2020)	18650 Li-ion battery	Water, RT27 paraffin wax, Aluminum foam	Num.	As cool water flows from the top to the bottom of the tube, it absorbs latent heat from the composite's top, resulting in a change of phase from liquid to solid and axial temperature reduction. The water temperature increases as a result of heat absorption from the composite, which delays the recovery of the lower section until 100 seconds have passed. Increasing axial thermal conductivity positively affects regulating the maximum temperature difference within a cell.	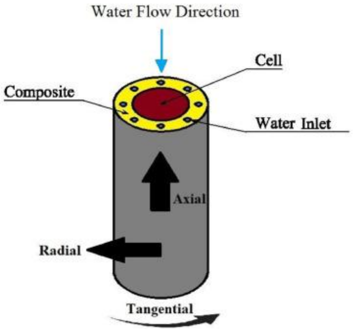

Author (year)	Battery type	Coolant	Type of Study	Findings	Configuration
Zhang et al. [265] (2020)	Prismatic $LiFePO_4$ battery	Heat pipe, Paraffin, Copper foam	Exp.	At an exceedingly high discharge rate of 5C, it is possible to control the maximum temperature difference within 5 °C. In addition, the system can significantly reduce the temperature disparity within a single cell. When compared to the maximum temperature reached in the baseline PCM based mode, the maximum temperature reached during the cycle testing is significantly lower, especially when the discharge rate is high.	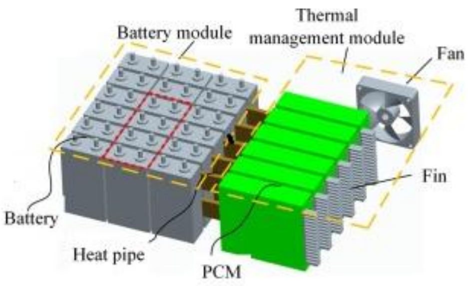
Li et al. [266] (2020)	18650 Li-ion battery	Air, Water, Paraffin, Copper foam	Exp. /Num.	Double-sided liquid cooling has superior temperature control, with the lowest battery temperature within the acceptable range. In natural convection, the maximum temperature surpassed 50 °C at 1395s with a heat input of 60 W (corresponding to a 4.5C rate for each battery). Comparatively, the T_{max} values for single-sided and double-sided liquid cooling are reduced to 43.40 °C and 37.13 °C, respectively.	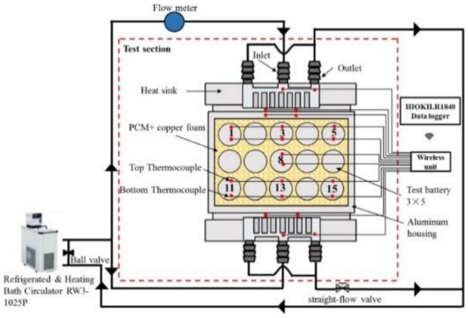

Author (year)	Battery type	Coolant	Type of Study	Findings	Configuration
Zhao et al. [267] (2019)	18650 Li-ion battery	Water, Paraffin, Copper foam	Num.	The battery's surface temperature can be sufficiently reduced by adding copper foam. Compared to a PCM-only module, the surface temperature of the battery decreases by 14 °C. After 1800s of operation, the module temperature is approximately 25 °C, indicating that the temperature of the battery pack is adequately controlled at the PCM melting point.	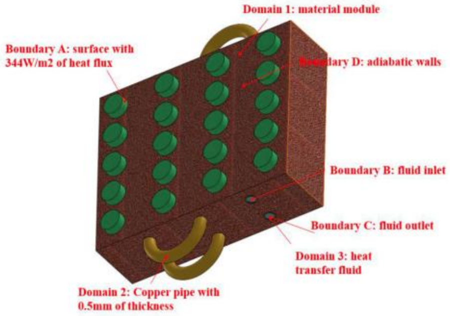
An et al. [268] (2019)	18650 Li-ion battery	Water, Paraffin (RT44HC), Expanded graphite (EG)	Num.	An increase in flow velocity improves the HBTMS's heat dissipation performance for the battery pack up to a velocity of 0.08 m/s, after which additional increases in flow velocity have little effect. Compared to the pure paraffin, the maximum temperature of the BTMS with a 6 wt% EG is reduced by 2.1 °C, and the temperature difference is only 2 °C.	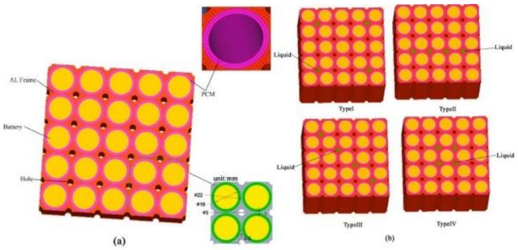
Jiang et al. [269] (2019)	18650 Li-ion battery	Thermoelectric Cooling, Paraffin, Copper foam	Exp.	Based on the highest cooling power or the lowest battery temperature, the optimal current is found experimentally to be around 6.0 to 6.5 A. At a battery heating capacity of 6 W, the thermoelectric cooling required 5335s for the battery's maximum temperature to reach 50 C, which is significantly longer than 1275s for liquid	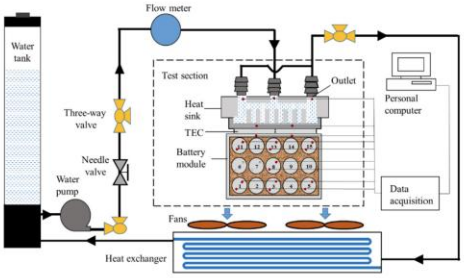

Author (year)	Battery type	Coolant	Type of Study	Findings	Configuration
				cooling and 930s for natural convection.	
Xie et al. [270] (2017)	Lithium titanate battery	Air, n-Eicosane paraffin, Copper foam	Exp. /Num.	Heat dissipation through phase change cooling is unaffected by changes in air flow rate or ambient temperature. Reducing the initial temperature of the battery during charge-discharge cycles is crucial for enhancing the thermal cycle characteristics of the HBTMS.	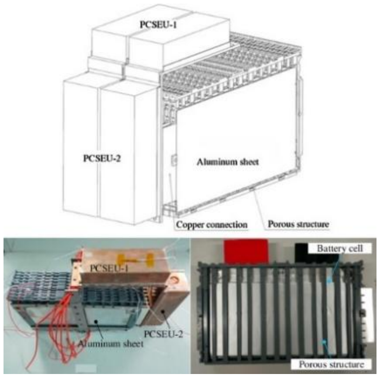
Shi et al. [271] (2017)	Lithium titanate battery	Air, n-Eicosane paraffin, Copper foam	Exp. /Num.	Reducing the convection thermal resistance or improving the conductivity of the phase change storage energy unit can significantly lower the battery temperature; the latter may be preferable because it does not require any additional energy to achieve the same result. Natural convection overheats at 42° C. Comparatively; the integrated thermal management system can effectively maintain a battery's temperature below 55 ° C with natural convection at 35 ° C and a modest airflow rate at 42 ° C.	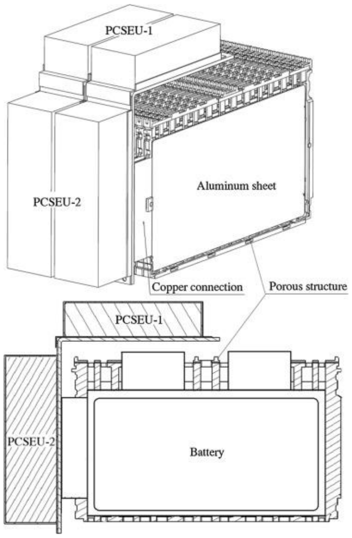

2.5 Conclusion

An effective BTMS is essential for ensuring safety, performance, longevity, and energy efficiency. Poor thermal management can lead to uneven temperature distribution, accelerated degradation, reduced charge and discharge efficiency, and, in extreme cases, thermal runaway. Therefore, understanding and mitigating battery heat generation and distribution through robust modelling and system design is critical. This chapter has reviewed the major heat generation mechanisms within batteries, highlighting the complexities associated with temperature gradients, entropy effects, and variable operational loads.

A substantial body of recent research has been dedicated to advancing BTMS through the integration of passive materials, notably PCM and porous structures such as metal foams and expanded graphite. PCM-based BTMSs present considerable potential for energy-efficient, passive thermal regulation, primarily by exploiting latent heat during phase transitions. Nonetheless, the inherently low thermal conductivity of PCMs significantly limits their standalone thermal performance. To address this shortcoming, porous media have been incorporated to develop CPCMs, through which thermal conductivity is markedly improved while structural integrity and latent heat storage capacity are preserved. In addition to enhancing conductive heat transfer, porous media also influence convective flow and thermal dispersion mechanisms, rendering them highly effective for augmenting both passive and active cooling strategies.

While recent advancements have greatly improved BTMS designs through passive and active strategies, limited work has addressed their integrated and optimised use in HBTMS configurations. In particular, the full potential of porous media, such as metal foams, remains underutilised when it comes to enhancing both conduction and convection within a single system. Prior investigations have primarily focused on traditional solid fins or the individual use of metal foams in either PCM-based or liquid-based systems. However, the superior thermal performance and energy density benefits offered by porous fins and layers have not been fully exploited. A relatively overlooked area is the integration of copper foam fins with PCMs and copper foam layers within liquid cooling channels, an approach that has the potential to greatly enhance heat transfer while reducing system weight and increasing energy density. Existing studies have largely not adequately considered the influence of structural characteristics such as porosity, pore density, and foam thickness, as well as the role of external conditions like ambient temperature and cyclic battery operation. The current study addresses these critical gaps by proposing a novel HBTMS configuration that simultaneously employs copper foam fins for improved conduction within PCM and copper foam layers for enhanced forced convection in liquid cooling. By systematically optimising the geometrical and structural parameters of the porous media, this research aims to deliver a more thermally efficient and compact HBTMS, advancing both the understanding and practical implementation of porous media in battery cooling technologies.

Building upon these principles, HBTMS that integrate active and passive methods have emerged as the most efficient and adaptable thermal control solutions. The incorporation of porous materials within HBTMS architectures amplifies their thermal responsiveness by improving heat transfer and facilitating more uniform temperature control. Despite challenges such as pressure drops and material compatibility, the optimal utilisation of metal foams and porous media presents a promising path toward the development of lightweight, high-performance thermal management systems. This chapter has systematically reviewed the fundamental principles, modelling approaches, and practical implementations of porous media across different BTMS configurations, highlighting their critical role in advancing efficient and reliable battery cooling strategies.

Chapter 3: Research Methodology

This chapter presents the comprehensive methodology employed to evaluate the thermal and structural performance of the proposed HBTMS. The chapter begins by introducing the research problem and the design features of the novel HBTMS, which integrates liquid cooling, PCM, and copper foam as both porous fins and layers to enhance heat dissipation and temperature uniformity. It then details the numerical modelling approach used to simulate transient heat generation within lithium-ion batteries, including the governing equations, initial and boundary conditions, and key assumptions underpinning the simulations. To optimise the system's design, a statistical approach based on Taguchi's design of experiments (DOE) is applied, and the significance of various influencing factors is assessed using analysis of variance (ANOVA). The chapter also includes mesh and time-step independence studies, along with validation of the numerical models against established experimental data, ensuring the reliability and accuracy of the computational results.

3.1 Problem Statement and Description of the Proposed HBTMS

The HBTMS proposed in this study integrates liquid cooling, PCM, and copper foam in the form of both porous fins and layers. As illustrated in Figure 3-1, the configuration comprises twelve 18650 lithium-ion batteries. Copper foam is employed as longitudinal porous fins surrounding each battery within the PCM housing and also as porous layers inserts inside the copper cooling tubes. Figure 3-1 (a) presents the key components of the system. Each battery is encased in an aluminium housing to prevent direct interaction with the PCM and to promote uniform heat distribution. Paraffin is selected as the PCM and filled into the housing. To improve its thermal conductivity, copper foam fins are embedded longitudinally, with PCM also occupying the foam's internal pores. Aluminium cooling plates with integrated copper tubes are introduced to regulate the paraffin's phase change, using water as the circulating coolant. The inclusion of copper foam layers within the tubes intensifies convective heat transfer, thus boosting overall cooling performance. Figure 3-1 (b) and (c) provide the detailed engineering drawing of the system, which are determined based on established literature common practice, manufacturing constraints of copper foam, and commercial specifications for copper tubes.

The material selection and design configuration of the proposed HBTMS were guided by the need to optimise thermal management while minimising overall system weight. Aluminium and copper foam were selected due to their high thermal conductivity and relatively low density, which support enhanced heat transfer and contribute to an improved energy density by reducing mass. This study focuses on a commercially available 18650 $LiNi_xCo_yMn_zO_2$ (NMC) lithium-ion battery, chosen for its superior energy density and widespread use in electric vehicles [76, 272]. The specifications and thermophysical properties of the NMC 18650 cell are summarised in Table 3-1. To streamline the numerical modelling while preserving accuracy, the battery is represented as a homogeneous cylindrical structure. This simplification is justified, as the internal components of cylindrical batteries have been shown to have a negligible effect on thermal behaviour [273]. It is noted, however, that the battery's thermal conductivity varies in the axial and radial directions due to anisotropic material composition.

Table 3-2 presents the thermophysical properties of all materials employed in this study, including aluminium alloy for the battery housings and cooling plates, copper foam used as both porous fins and layers, and paraffin selected as the PCM.

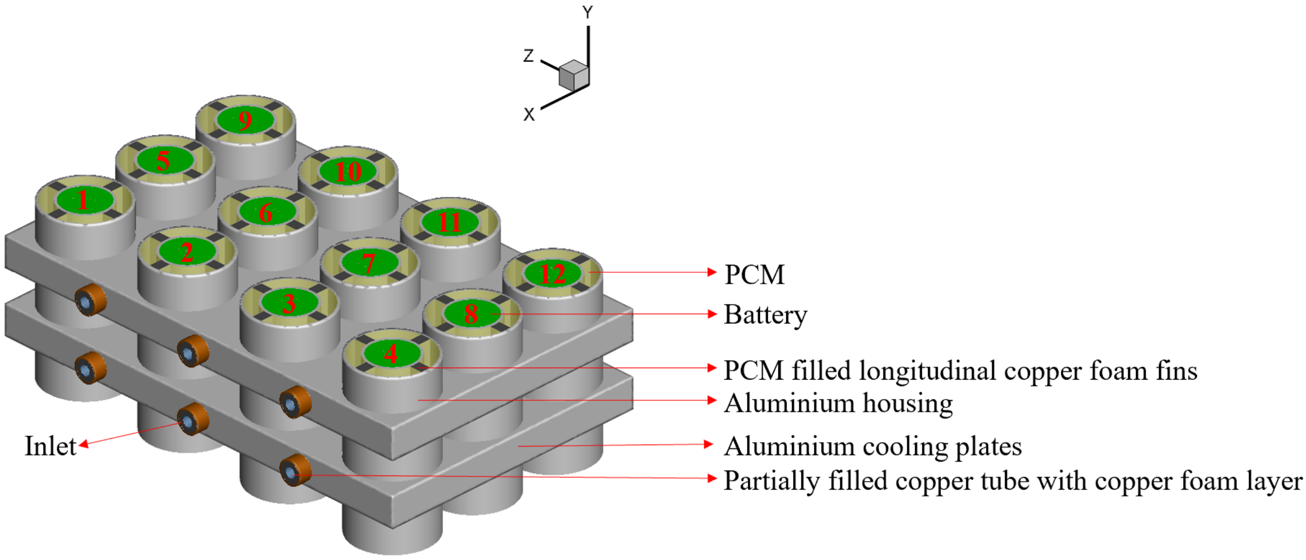

(a)

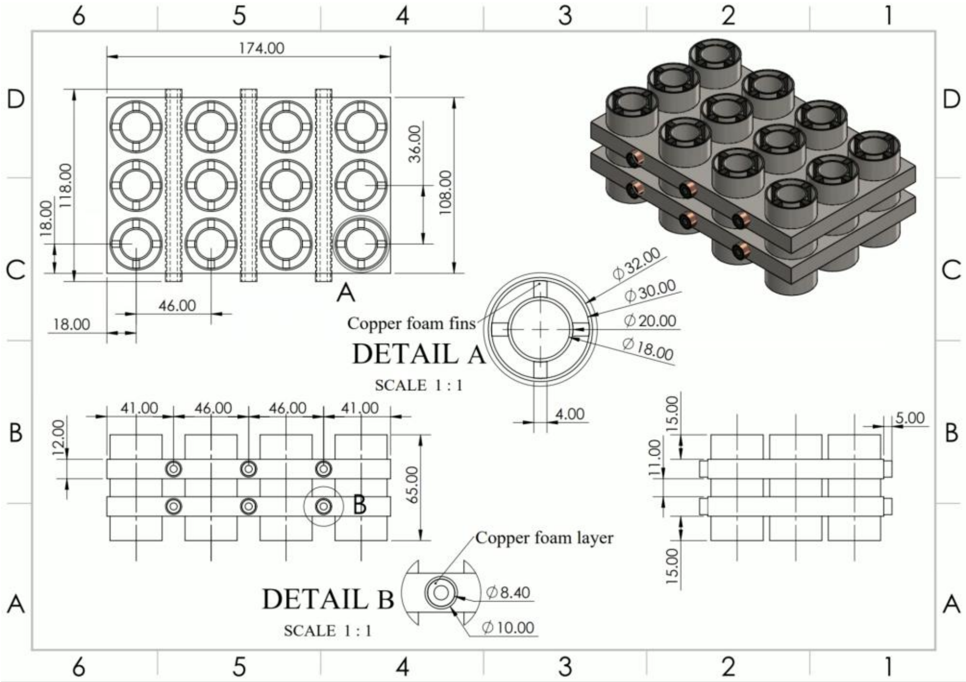

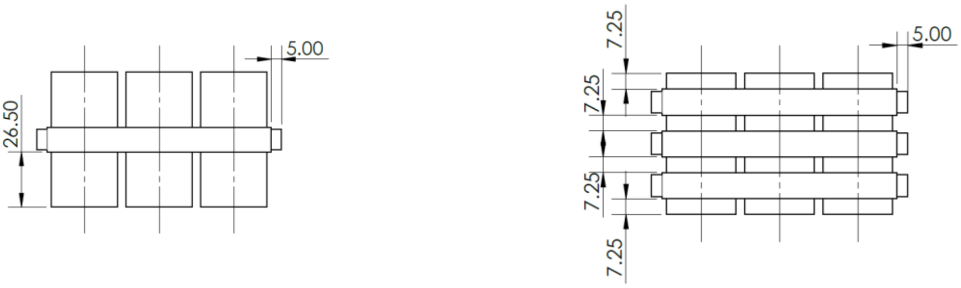

One cooling plate

Three cooling plates

(b)

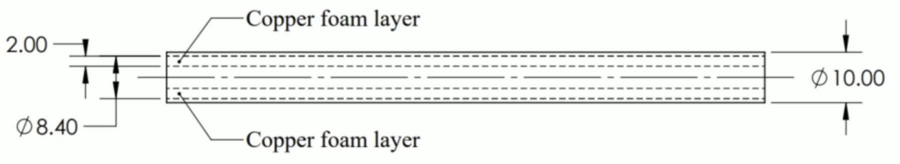

(c)

Figure 3-1. Proposed HBTMS (a) system components, (b) dimensional specifications for different number of cooling plates, and (c) dimensional specifications for copper tube with copper foam layer (DETAIL B) shown in mm.

Table 3-1. Specification and thermophysical properties of the battery [273]

Parameter	Value
Nominal voltage (V)	3.7
Nominal capacity (Ah)	2.6
Cell mass (kg)	0.0475
Thermal conductivity in the radial direction ($W\cdot m^{-1}\cdot K^{-1}$)	0.2
Thermal conductivity in the axial direction ($W\cdot m^{-1}\cdot K^{-1}$)	37.6
Specific heat capacity ($J\cdot kg^{-1}\cdot K^{-1}$)	1200.0

Table 3-2. Thermophysical properties of the materials [123, 274]

Materials	Properties	Value
Al alloy	Thermal conductivity ($W \cdot m^{-1} \cdot K^{-1}$)	167
Al alloy	Specific heat capacity ($J \cdot kg^{-1} \cdot K^{-1}$)	896
Al alloy	Density ($kg \cdot m^{-3}$)	2700
Copper	Thermal conductivity ($W \cdot m^{-1} \cdot K^{-1}$)	387.6
Copper	Specific heat capacity ($J \cdot kg^{-1} \cdot K^{-1}$)	386
Copper	Density ($kg \cdot m^{-3}$)	8900
Paraffin	Thermal conductivity ($W \cdot m^{-1} \cdot K^{-1}$)	0.2
Paraffin	Specific heat capacity ($J \cdot kg^{-1} \cdot K^{-1}$)	2000
Paraffin	Density ($kg \cdot m^{-3}$), solid	880
Paraffin	Density ($kg \cdot m^{-3}$), liquid	760
Paraffin	Solidus temperature (K)	311.15
Paraffin	Liquidus temperature (K)	316.15
Paraffin	Latent heat ($J \cdot kg^{-1}$)	174000
Paraffin	Dynamic viscosity ($Kg \cdot m^{-1} \cdot s^{-1}$)	0.02
Paraffin	Thermal expansion coefficient (K^{-1})	0.0001
Water	Thermal conductivity ($W \cdot m^{-1} \cdot K^{-1}$)	0.6
Water	Specific heat capacity ($J \cdot kg^{-1} \cdot K^{-1}$)	4182
Water	Density ($kg \cdot m^{-3}$), solid	998.2
Water	Dynamic viscosity ($Kg \cdot m^{-1} \cdot s^{-1}$)	0.001003

3.2 Numerical Modelling

3.2.1 Modelling of Transient Heat Generation in Batteries

For realistic application scenarios, the transient heat generation of the lithium-ion battery was considered. A lumped-capacitance model was employed to simulate the dynamic thermal behaviour, accounting for both resistive (Joule) and entropic heat generation mechanisms. The applicability of this model depends on the Biot number (Bi), calculated as $Bi = hL_b/k_b$, where h is the convective heat transfer coefficient, L_b is the characteristic length (defined as the ratio of the battery's volume to its surface area), and k_b is the thermal conductivity of the battery. The lumped-capacitance model is valid when the Biot number is less than 0.1 [275]. Under this assumption, the battery is treated as having spatially uniform thermophysical properties, and the heat generation rate is a function of the battery's temperature and current behaviour [276]. The total heat generation is described by the Bernardi equation [273]:

$$Q_t = Q_{irr} + Q_{rev} \tag{3-1}$$

$$Q_{irr} = I(E - V) = I^2 R_t \tag{3-2}$$

$$Q_{rev} = -T\Delta S\left(\frac{I}{nF}\right) = -I\left[T(\frac{dE}{dT})\right] \tag{3-3}$$

where the total heat generation Q_t within the battery comprises both irreversible heat Q_{irr}, reversible heat Q_{rev}. These components depend on key electrochemical and thermal parameters, including the open circuit voltage E, terminal voltage V, electric current I, temperature T, total internal resistance R_t, change in entropy ΔS, number of electrons n, Faraday's constant F, and the entropy coefficient $\frac{dE}{dT}$. Hybrid Pulse Power Characterization (HPPC) test [277] is commonly used to develop functions for the total internal resistance and the entropy coefficient. For this study, transient heat generation was modelled using the experimental data provided by [273, 278, 279], applying the aforementioned equations at discharge rates of 1C, 3C, and 5C. The discharge rate, or C-rate, is defined as the ratio of discharge current to the battery's nominal capacity [280], resulting in corresponding discharge durations of 3600, 1200, and 720 seconds, respectively.

The total internal resistance and entropy coefficient are calculated as defined in Table 3-3 and Equation (3-4), respectively [279].

Table 3-3. Total internal resistance at various temperatures [279]

Total internal resistance (R_t)	Temperature (K)
$166 - 1334 \times SOC + 6559 \times SOC^2 - 16531 \times SOC^3 + 22391 \times SOC^4 - 15496 \times SOC^5 + 4301 \times SOC^6$	293
$107 - 793 \times SOC + 4036 \times SOC^2 - 10514 \times SOC^3 + 14700 \times SOC^4 - 10480 \times SOC^5 + 2989 \times SOC^6$	303
$66 - 382 \times SOC + 1962 \times SOC^2 - 5181 \times SOC^3 + 7378 \times SOC^4 - 5365 \times SOC^5 + 1559 \times SOC^6$	313
$58 - 355 \times SOC + 1898 \times SOC^2 - 5121 \times SOC^3 + 7367 \times SOC^4 - 5374 \times SOC^5 + 1559 \times SOC^6$	323
$48 - 233 \times SOC + 1225 \times SOC^2 - 3263 \times SOC^3 + 4667 \times SOC^4 - 3406 \times SOC^5 + 992 \times SOC^6$	333

$$\frac{dE}{dT} = -0.355 + 2.154 \times SOC - 2.869 \times SOC^2 + 1.028 \times SOC^3 \tag{3-4}$$

where SOC is the state of charge of the battery.

Transient heat generation equations during discharge have been added as User Defined Function (UDF), which is presented in Appendix A. The heat generation per unit of the battery volume (q_b) is defined as follows:

$$q_b = \frac{Q_t}{Vol._{battery}} \tag{3-5}$$

Since heat generation during charging is significantly lower than during discharging, limited experimental studies have focused on it. For the specific lithium-ion battery investigated in this study, to the best of the author's knowledge, no reliable or validated transient heat generation data during charging was found in the literature. Therefore, constant heat generation values based on experimental data from [281] were adopted for various charging C-rates. These values are summarised in Table 3-4.

Table 3-4. 18650 lithium-ion battery heat generation during charge [281]

C rate	q_b (W.m^{-3})
1C	28773
2C	78957
3C	171075

3.2.2 Governing Equations, Boundary Conditions, and Assumptions

The enthalpy-porosity method was used to model the phase change behaviour of PCM, where the mushy region, representing the coexistence of solid and liquid phases, is treated as a porous domain. This approach incorporates the latent heat effects directly into the energy conservation equation, eliminating the need to explicitly track the phase boundary [282, 283]. In the case of pure PCM without copper foam, three distinct regions emerge during melting and solidification: solid, liquid, and mushy zones. Within the mushy region, the PCM is considered a porous medium, where the solid PCM serves as the matrix and the liquid portion occupies the pore space. In contrast, when simulating CPCMs integrated with copper foam, the liquid region is also represented as a porous medium, but with a porosity value different from that assigned to the mushy zone [264].

Copper foam was modelled as a porous medium using the Darcy–Brinkman–Forchheimer (DBF) approach. The local thermal equilibrium (LTE) model was applied to the copper foam fins surrounding the batteries, whereas the local thermal non-equilibrium (LTNE) model was employed for the copper foam layer inside the copper tubes to account for potential temperature differences between the solid and fluid phases.

To streamline the numerical simulations in this study, the following assumptions were adopted:

- The laminar flow of molten PCM is unsteady and incompressible.
- PCM phases are isotropic and homogeneous.
- The liquid PCM and water are Newtonian fluid.
- The Boussinesq approximation has been used to account for buoyancy forces in natural convection.
- Changes in volume during the PCM melting process and effects of viscous dissipation and radiation are negligible.
- The influence of thermal resistance between the zones' surfaces has been ignored.

- The copper foam structure is assumed to be homogeneous and isotropic.
- Thermal equilibrium is considered between PCM and copper foam fins.
- Thermal non equilibrium is considered between water and copper foam layers.

Considering the mentioned assumptions the governing equations for PCM and copper foam fins are as follows [284]:

Continuity:

$$\frac{\partial \rho_f}{\partial t} + \nabla . \rho_f \vec{V} = 0 \tag{3-6}$$

Momentum:

$$\frac{\rho_f}{\varepsilon}\frac{\partial \vec{V}}{\partial t} + \frac{\rho_f}{\varepsilon^2}(\vec{V}.\nabla)\vec{V} = -\nabla P + \frac{\mu_f}{\varepsilon}(\nabla^2 \vec{V}) - \rho_{f,ref}\beta_f \varepsilon (T - T_{ref})\vec{g} - \vec{S} - \vec{F} \tag{3-7}$$

where ρ is the density, ε is the porosity, $\vec{V}$ is the velocity vector, P is the pressure, μ is the dynamic viscosity, β is the thermal expansion coefficient, T is temperature, and $\vec{g}$ is the gravitational acceleration.

The source terms in the momentum equation represent the pressure losses associated with the phase change process and are defined using Darcy's damping law as follows [284]:

$$\vec{S} = A_m \frac{(1 - L_f)^2}{{L_f}^3 + 0.001}\vec{V} \tag{3-8}$$

where A_m is the mushy zone constant that has been considered to be 10^5 [274] and L_f is the liquid fraction.

In the governing equations for the PCM-only regions, or areas not containing copper foam fins, the porosity is assumed to be unity, and the momentum equation excludes source terms due to the absence of porous media. Furthermore, the latent heat of fusion L_f is defined as follows [285]:

$$L_f = \frac{\Delta H}{h_f} = \begin{cases} 0 & if\ T < T_s \\ \dfrac{T - T_{Solidus}}{T_{Liquidus} - T_{Solidus}} & T_s \le T \le T_l \\ 1 & if\ T > T_l \end{cases} \tag{3-9}$$

where ΔH is latent heat.

The total enthalpy is calculated as follows:

$$H = h + \Delta H \tag{3-10}$$

where h is the sensible enthalpy and defined as:

$$h = h_{ref} + \int_{T_{ref}}^{T} C_{p_f} dT \tag{3-11}$$

where h_{ref} is sensible enthalpy at reference temperature and C_p is the specific heat.

The last term on the right-hand side of the momentum equation, which is caused by the porous medium, is defined as:

$$\vec{F} = (\frac{\mu_f}{K} + \frac{\rho_f C|\vec{V}|}{\sqrt{K}})\vec{V} \tag{3-12}$$

where $|\vec{V}|$ is the magnitude of the velocity vector. In the above equations, the first term represents the viscous loss, and the second term represents the inertial loss. In these equations, K and C are permeability and inertial factor, respectively, and are given as [128]:

$$K = 0.00073(1-\varepsilon)^{-0.224} {d_f}^{-1.11} {d_p}^{3.11} \tag{3-13}$$

$$C = 0.0012(1-\varepsilon)^{-0.132} \left(\frac{d_f}{d_p}\right)^{-1.63} \tag{3-14}$$

where d_f and d_p are ligament diameter, pore size, respectively. They are defined as follows [286, 287]:

$$d_f = 1.18 d_p \sqrt{\frac{1-\varepsilon}{3\pi}} \tag{3-15}$$

$$d_p = 0.0224/\omega \tag{3-16}$$

where ω is the pore density as pores per inch (PPI).

Energy:

By considering LTE model, in which the PCM and copper foam fins are assumed to have the same temperature, the energy equation is given as [284]:

$$\frac{\partial \varepsilon \rho_f C_{p_f} T}{\partial t} + \nabla\left(\rho_f C_{p_f} \vec{V}.T\right) = \nabla(k_{eff} \nabla T) - S_L \tag{3-17}$$

where k_{eff} is the effective thermal conductivity and defined as follows [288]:

$$k_{eff} = (1-\varepsilon)k_s + \varepsilon k_f \tag{3-18}$$

where k is the thermal conductivity.

The last source term in the energy equation is defined as follows [289]:

$$S_L = \frac{\partial \varepsilon \rho_f L_f h_f}{\partial t} + \nabla(\rho_f \vec{V}.T L_f h_f) \tag{3-19}$$

where h_f is the latent heat of fusion.

The governing equations for the liquid-cooled region containing a copper foam layer, based on the LTNE model, are expressed as follows [290, 291]:

Continuity:

$$\frac{\partial \rho}{\partial t} + \nabla . \rho \vec{V} = 0 \tag{3-20}$$

Momentum:

Clear region:

$$\rho \frac{\partial \vec{V}}{\partial t} + \rho \nabla . \left(\vec{V} \vec{V} \right) = -\nabla P + \mu_f \left(\nabla^2 \vec{V} \right) \tag{3-21}$$

Porous region:

$$\rho \frac{\partial \vec{V}}{\partial t} + \frac{\rho}{\varepsilon} \nabla . \left(\vec{V} \vec{V} \right) = -\nabla P + \frac{\mu_f \left(\nabla^2 \vec{V} \right)}{\varepsilon} - \frac{\mu_f \vec{V}}{K} - \rho C_F \sqrt{\frac{1}{K}} \left| \vec{V} \right| \vec{V} \tag{3-22}$$

where C_F and K are the permeability of the porous media and the geometric function, respectively and can be expressed as [292]:

$$K = \frac{\varepsilon^3 d_p^2}{150(1-\varepsilon)^2} \tag{3-23}$$

$$C_F = \frac{1.75}{\sqrt{150} \varepsilon^{3/2}} \tag{3-24}$$

Energy:

Clear region:

$$\frac{\partial \left(\rho C_p T_f \right)}{\partial t} + \nabla \cdot \left(\rho C_p \vec{V} T_f \right) = \nabla \cdot \left(k_f \nabla T_f \right) \tag{3-25}$$

Porous region:

Solid phase:

$$\frac{\partial \left(\rho_s C_p T_s \right)}{\partial t} = \nabla \cdot \left(k_{s_{eff}} \nabla T_s \right) - h_{sf} a_{sf} \left(T_s - T_f \right) \tag{3-26}$$

Fluid phase:

$$\frac{\partial \left(\rho_f C_p T_f \right)}{\partial t} + \nabla \cdot \left(\frac{\rho_f C_p \vec{V} T_f}{\varepsilon} \right) = \nabla \cdot \left(k_{f_{eff}} \nabla T_f \right) + h_{sf} a_{sf} \left(T_s - T_f \right) \tag{3-27}$$

where $k_{s_{eff}}$ and $k_{f_{eff}}$ are effective thermal conductivity for solid and porous phase of the porous media, respectively, and defined as follows [176, 293, 294]:

$$k_{s_{eff}} = (1-\varepsilon)^{0.763} k_s \tag{3-28}$$

$$k_{f_{eff}} = \varepsilon k_f + k_{td} \tag{3-29}$$

where k_{td} is the thermal dispersion coefficient which is calculated as follows:

$$k_{td} = 0.025\rho_f C_p \sqrt{K}|\vec{V}| \tag{3-30}$$

h_{sf} and a_{sf} appearing in the energy equation are fluid-to-solid heat transfer coefficient and specific surface area [174, 295]:

$$h_{sf} = \left(\frac{k_f}{d_p}\right)^2 \left(1 + 1.1\left(\frac{C_{p_f}\mu_f}{k_f}\right)^{1/3}\right)\left(\frac{\rho_f|\vec{V}|d_p}{\mu_f}\right)^{0.6} \tag{3-31}$$

$$a_{sf} = \frac{6(1-\varepsilon)}{d_p} \tag{3-32}$$

Battery cell:

$$\rho_b c_{p_b}\frac{\partial T}{\partial t} = \nabla \cdot (k_b \nabla T) + q_b \tag{3-33}$$

Cooling plates:

$$\rho_s c_{p_s}\frac{\partial T}{\partial t} = \nabla \cdot (k_s \nabla T) \tag{3-34}$$

The initial condition for the HBTMS simulation was defined as follows:

$$T(x, y, z) = T_{amb}; t = 0 \tag{3-35}$$

where T_{amb} is the ambient temperature.

An adiabatic boundary condition was applied to the bottom surface of the HBTMS. A specified mass flow rate and inlet water temperature were imposed at the entry of the copper tubes containing copper foam layers, varying depending on the simulation case. Based on the geometrical dimensions presented in Figure 3-1 and the material properties outlined in

Table 3-2, the Reynolds number in the clear region of the copper tube was calculated to be 151.2, which is well below the laminar-to-turbulent transition threshold of 2000 [296]. Additionally, the permeability Reynolds number for the copper foam layer was found to be 0.123, far below the critical value of 100 for turbulent flow in porous media [37, 297]. As a result, laminar flow was assumed throughout all simulations. At the outlet, a pressure outlet boundary condition was set to atmospheric pressure. No-slip boundary conditions were applied at all wall surfaces. For all other external surfaces of the HBTMS, Robin boundary condition (third kind) was applied as follows:

$$-k_{wall}\frac{\partial T_{wall}}{\partial n} = h(T_{wall} - T_{amb}) \tag{3-36}$$

where h is the convection heat transfer coefficient and was considered to be 10 W·m^{-2}·K^{-1} [280] for air natural convection.

At the interface between solid and liquid phase of the porous media the following boundary conditions were considered for LTE and LTNE models.

LTE model [298]:

$$\begin{aligned}
\vec{V}\big|_{fluid} &= \vec{V}\big|_{porous} \\
\mu_f \frac{\partial \vec{V}}{\partial n}\bigg|_{fluid} &= \mu_{eff} \frac{\partial \vec{V}}{\partial n}\bigg|_{porous} \\
T_{fluid} &= T_{porous}, \\
k_f \frac{\partial T}{\partial n}\bigg|_{fluid} &= k_{eff} \frac{\partial T}{\partial n}\bigg|_{porous}
\end{aligned} \tag{3-37}$$

LTNE model [299]:

$$\begin{aligned}
\vec{V}\big|_{fluid} &= \vec{V}\big|_{porous} \\
\mu_f \frac{\partial \vec{V}}{\partial n}\bigg|_{fluid} &= \mu_{eff} \frac{\partial \vec{V}}{\partial n}\bigg|_{porous} \\
-k_f \frac{\partial T}{\partial n}\bigg|_{fluid} &= -k_{s_{eff}} \frac{\partial T}{\partial n}\bigg|_{porous} = q_{interface} \\
-k_f \frac{\partial T}{\partial n}\bigg|_{fluid} &= -k_{f_{eff}} \frac{\partial T}{\partial n}\bigg|_{porous} = q_{interface}
\end{aligned} \tag{3-38}$$

The governing equations were numerically solved using ANSYS FLUENT 23/R2, commercial CFD packages based on the finite volume method (FVM) as described by Patankar [300]. The solution employed specified initial and boundary conditions, with pressure–velocity coupling handled via the SIMPLE algorithm. Convective terms were discretised using a second-order upwind scheme, transient terms with a second-order implicit time integration scheme, and diffusion terms through spatial gradient reconstruction using the least squares cell-based method. Convergence criteria were set with residuals of 10^{-4} for continuity and momentum equations, and 10^{-6} for the energy equation. To manage the computational demands of the simulations, high-performance computing (HPC) resources were employed, with the system specifications detailed in Table 3-5. These resources enabled efficient handling of the complex and intensive simulations, while also providing a useful benchmark for future computational studies. On average, a single discharge simulation required 2 to 5 hours of wall-clock time, while a cyclic discharge–rest–charge simulation required 24 to 36 hours on 70 cores.

Table 3-5. Specifications of the HPC system used for numerical simulations.

Specification	Detail
Architecture	x86_64
CPU Operation Modes	32-bit, 64-bit
Total CPUs	72
Threads per Core	2
Cores per Socket	18
Sockets	2
NUMA Nodes	2
CPU Family	6
Model	85
Model Name	Intel(R) Xeon(R) Gold 6240 CPU @ 2.60GHz
CPU MHz	2600
Total RAM	187Gi
BogoMIPS	5200.00
Fluent solver Processes	70

3.3 Taguchi's Design of Experiments (DOE)

Among the diverse methodologies employed in Design of Experiments (DOE), the Taguchi method is distinguished by its structured and efficient approach to optimising product quality and performance while simultaneously reducing variability and resource utilisation. This technique employs orthogonal arrays to systematically organise experimental factors and their corresponding levels, thereby facilitating the simultaneous investigation of multiple parameters with a reduced number of experimental trials [301]. The method is especially esteemed for its capacity to generate reliable and interpretable results, improving product quality and enhancing robustness against external disturbances and noise factors [302].

The Taguchi method provides an effective framework for determining the optimal combination of factors influencing a given objective function. It streamlines the process of improving design quality, performance, and cost-effectiveness by enabling systematic experimentation through the use of orthogonal array designs. Meaningful results can be obtained with substantially fewer experimental trials through this approach, even in cases where extensive testing across all factor levels would typically be required by a full factorial design. While traditionally applied in experimental optimisation, the Taguchi method has increasingly been adopted in numerical and theoretical investigations in recent years [303]. In the present study, the Taguchi method was utilised to identify the most influential parameters governing the thermal performance of the HBTMS, as well as to quantify their relative contributions and establish a significance hierarchy.

In the Taguchi method, the selection of an appropriate orthogonal array is a crucial step, determined by the total degrees of freedom (DF) required for the experimental design. This total is obtained by summing the individual DF of each factor, where the DF for a given factor is calculated as one less than the number of its levels [303].

During the data analysis phase, the outcomes associated with the objective functions are converted into Signal-to-Noise (S/N) ratios, which serve to assess the degree to which the observed results deviate from or align with the expected performance derived from simulations [304]. Depending on the nature of the objective function, one of three S/N ratio formulations is applied: "lower-the-better," "higher-the-better," or "nominal-the-best" [303]. In this study, the primary response variables include maximum battery surface temperature ($T_{Max,Sur}$), maximum temperature difference within the battery module (ΔT_{Max}), performance evaluation criteria (PEC), and energy density (E_d). For Taguchi analysis of the $T_{Max,Sur}$, ΔT_{Max}, 1/ E_d, and the 1/ PEC lower-the-better option was considered to optimise the HBTMS for better thermal performance as the optimisation required minimising $T_{Max,Sur}$ and ΔT_{Max} while maximising E_d and PEC. The formula for the lower-the-better S/N ratio is [305]:

$$S/N = -10 \times \log_{10}\left(\frac{1}{n_{\mathrm{test}}}\sum_{\mathrm{i}=1}^{n_{\mathrm{test}}} y_{\mathrm{i}}^{2}\right) \tag{3-39}$$

The formula employs n_{test} to indicate the total number of test runs, while y_{i} denotes the value of the i^{th} performance parameter. In the context of this study, the y_{i} represent the $T_{Max,Sur}$, ΔT_{Max}, 1/ Ed, and 1/ PEC for each test.

3.4 ANOVA Technique

Analysis of Variance (ANOVA) is a widely used statistical method for evaluating the influence of various factors on a response variable by determining their contribution ratios and relative significance. It is commonly applied to identify which factors exert the most substantial effects on system performance [303]. Both the Taguchi method and ANOVA have found extensive application across numerous engineering disciplines, including manufacturing processes and heat transfer analysis [303, 304]. In the present study, the $T_{Max,Sur}$, ΔT_{Max}, 1/ Ed, and 1/ PEC was determined using the ANOVA technique. Within the ANOVA framework, the sum of squares (*SS*), degrees of freedom (*DF*), mean squares (*MS*), and contribution ratios ($\lambda_{\mathrm{factor}}$) for each factor are computed using the following equations [303, 304]:

$$SS = \frac{\sum \beta_{\mathrm{factor,i}}^{2}}{N_{\mathrm{rep.}}} - \frac{(\sum \beta_{\mathrm{i}})^{2}}{n_{\mathrm{test}}} \tag{3-40}$$

$$DF = L_{\mathrm{factor}} - 1 \tag{3-41}$$

$$MS = \frac{SS}{DF} \tag{3-42}$$

$$\lambda_{\text{factor}} = \frac{Adj\ SS}{Adj\ SS_{\text{total}}} \times 100 \tag{3-43}$$

where $\beta_{\text{factor,i}}$ denotes the cumulative S/N ratio at the i$^{\text{th}}$ level of a given factor, while β_{i} represents the individual S/N ratio at that level. $N_{\text{rep.}}$ indicates the number of repetitions for each level, and L_{factor} refers to the total number of levels associated with that factor. The term "factor" serves as a generic placeholder, to be replaced with specific identified input parameters being investigated. The adjusted sum of squares ($Adj\ SS$) reflects the sum of squares computed after excluding terms that are statistically insignificant. Similarly, the adjusted mean of squares ($Adj\ MS$) corresponds to the mean square value derived once these non-contributory terms have been removed from the response function [306].

3.5 Mesh Independence, Time-step Independence Studies, and Validation

The grid independence was assessed using the Grid Convergence Index (GCI) [307, 308]. The GCI for the computational grid is defined as follows:

$$GCI = F_s \frac{|\varepsilon_r|}{r^p - 1} \tag{3-44}$$

where F_s is a safety factor, the value is 1.25 for three grids comparisons. p is the rate of convergence, the theoretical value is 1.97 for a second-order method. The relative error ε_r is defined as:

$$\varepsilon_r = \frac{f_{i+1} - f_i}{f_i} \tag{3-45}$$

where $f_{\text{i}+1}$ and f_{i} are the solution values on the fine and coarse grids, respectively. In this context, these values represent the maximum temperature of the battery surface at the end of 5C discharge. The grid refinement ratio r_i is defined as:

$$r_{i,i+1} = \frac{h_i}{h_{i+1}} \tag{3-46}$$

$$h_i = \sqrt[3]{\frac{\sum_{i-1}^{N} \Delta V_i}{N}} \tag{3-47}$$

where h_i represents the average grid spacing, V_i denotes the volume of each grid cell, and N stands for the total number of grids.

Three types of grid densities and their corresponding GCI calculations are presented in Table 3-6. The GCI for 6612690 grid cells is below 3% which meets the grid convergence index criterion [309]. Also, the generated mesh for the HBTMS is shown in Figure 3-2.

Different time steps were studied to check time step independencies. Table 3-7 provides the maximum temperature of the battery surface at the end of 5C discharge for different time steps. As shown, a time step of 1 second was found to be appropriate for the current investigation.

Table 3-6. GCI analysis for different studied grids.

Grid number (N)	h_i	r	$(\boldsymbol{f_i})$ $T_{Max,Sur}$ (K)	$\boldsymbol{\varepsilon_r}$	GCI (%)
4944155	1	1.25	313.894287	0.052741	18.30
6612690	0.8	1.25	313.897891	0.003603	1.25
11642045	0.64	-	313.845152	-	-

Table 3-7. Different time steps for time step independency study

Time step (second)	$T_{Max,Sur}$ (K)	Error (%)
0.25	313.9788	-
0.5	313.9391	0.012635
1	313.8943	0.014271
2	313.7315	0.051876

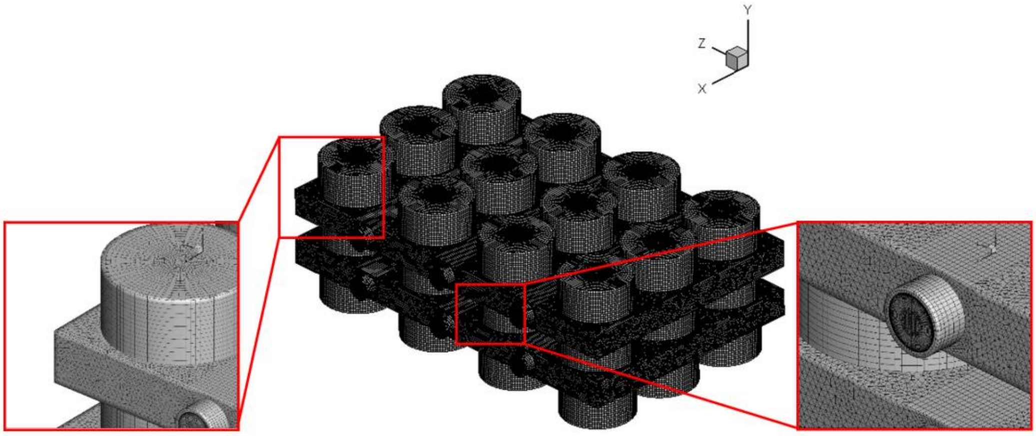

Figure 3-2. Generated mesh for the HBTMS

The numerical methods employed in this study were validated through comparisons with established experimental data. To verify the accuracy of the Bernardi model used for transient battery heat generation, a single-cell configuration was simulated in accordance with the experimental setup shown in Figure 3-3 (a). The ambient temperature was fixed at 298.15 K, consistent with the temperature chamber conditions reported in [273]. Natural convection boundary condition was applied on all external battery surfaces, using a constant convective heat transfer coefficient of 5 $W/m^2 \cdot K$.As presented in Figure 3-3 (b), the simulated battery surface temperatures were compared against experimental results from [273, 278, 279] for different discharge rates. The corresponding absolute error (K) and relative error (%) are shown in Figure 3-3 (c). The numerical results demonstrate good agreement with the experimental data. Additionally, the corresponding transient volumetric heat generation at various discharge rates are depicted in Figure 3-3 (d).

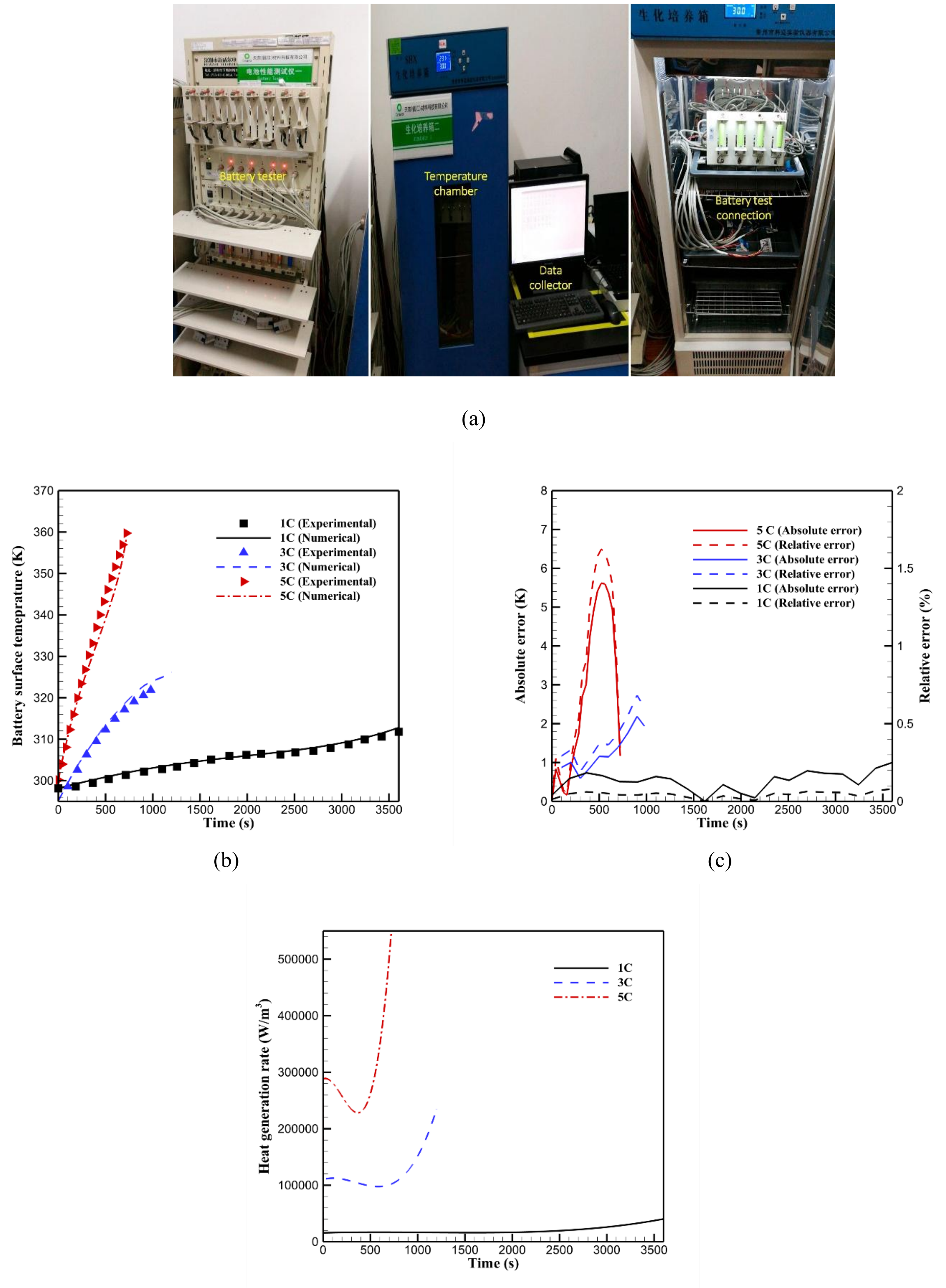

(a)

(b) (c)

(d)

Figure 3-3. Validation of the transient battery heat generation model: (a) experimental set up for battery thermal model validation [273] (b) comparison of present numerical and experimental battery surface temperatures [273, 278, 279], (c) absolute error (K) and relative error (%), and (d) corresponding transient volumetric heat generation at various discharge rates.

For the longitudinal copper foam fins applied within PCM, validation was conducted using the experimental and numerical study by Hu et al. [310] using both Local Thermal Equilibrium (LTE) and Local Thermal Non-Equilibrium (LTNE) models. The experimental set up by Hu et al. [310] is presented in Figure 3-4 (a), in which aluminium foam embedded with paraffin was investigated. As shown in Figure 3-4 (b), the experiment was replicated numerically by modelling the PCM-saturated foam (porosity 0.75 and pore density 10 PPI). A constant heat flux of 3500 W/m² was applied at the bottom surface, while symmetry and natural convection boundary conditions (5 W/m²·K) were imposed on the remaining boundaries. Figure 3-4 (c) presents the comparison between experimental temperature measurements and numerical obtained results using both LTE and LTNE models at measurement point 1. The associated absolute error (K) and relative error (%) are shown in Figure 3-4 (d). While both approaches accurately captured the thermal response of the composite PCM, the LTNE model exhibited slightly superior accuracy. Nevertheless, due to the slight difference in results and the significantly lower computational cost associated with the LTE model, the LTE approach was selected for simulating the behaviour of copper foam fins in this study.

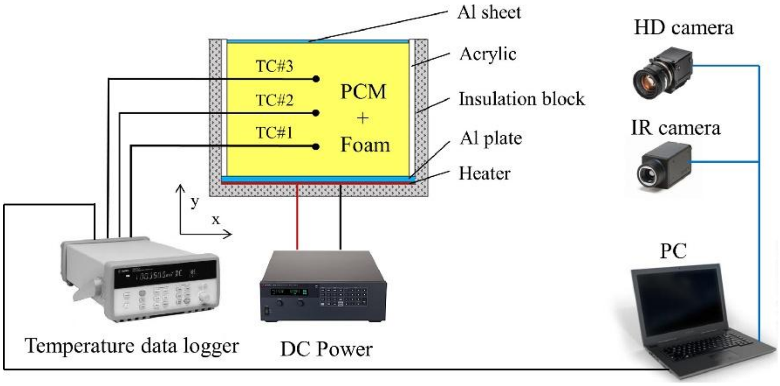

(a)

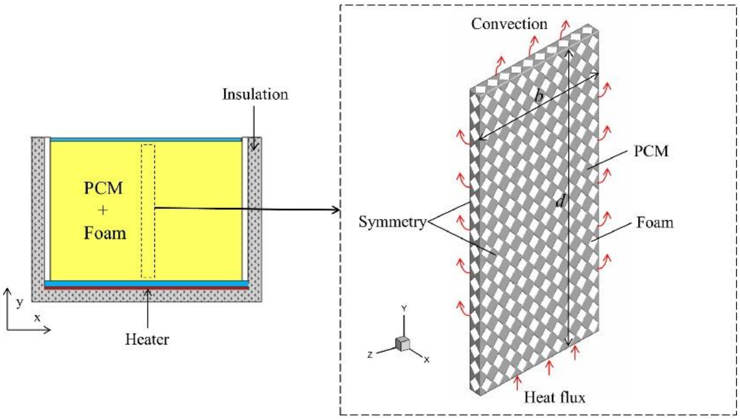

(b)

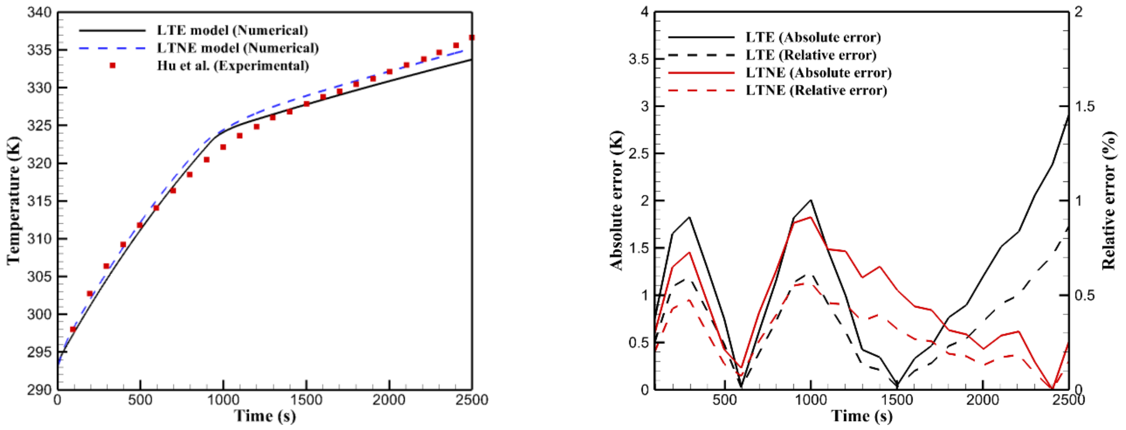

(c) (d)

Figure 3-4. Validation of PCM filled metal foam model based on the experimental and numerical study of Hu et al.[310]: (a) experimental setup with aluminium foam–paraffin composite, (b) corresponding numerical model and boundary conditions, (c) comparison of the present numerical results with experimental data, and (d) absolute error (K) and relative error (%).

To validate the liquid cooling performance in the proposed HBTMS, the numerical and experimental study by Xin et al. [278] was replicated. As depicted in Figure 3-5 (a), a liquid-cooled BTMS incorporating heat conducting blocks and water flow was investigated in the referenced study. The simulation was performed under transient heat generation conditions corresponding to a 3C discharge rate, with an inlet mass flow rate of 0.02 kg/s. Natural convection boundary condition was applied on all external surfaces, using a constant convective heat transfer coefficient of 5 W/m²·K. The comparison between the predicted and reported maximum battery surface temperatures is presented in Figure 3-5 (b) and the corresponding absolute error (K) and relative error (%) are shown in Figure 3-5 (c). The numerical results are in close agreement with the experimental data.

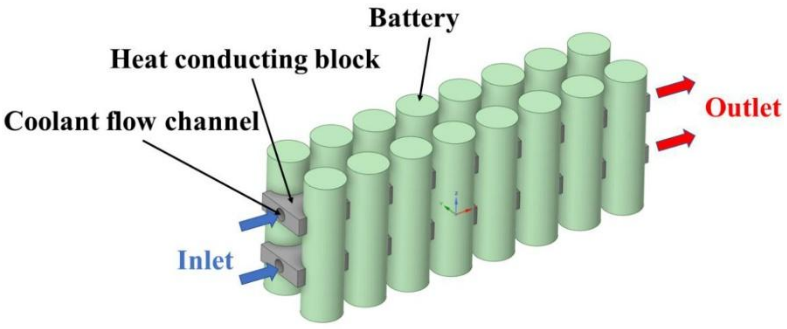

(a)

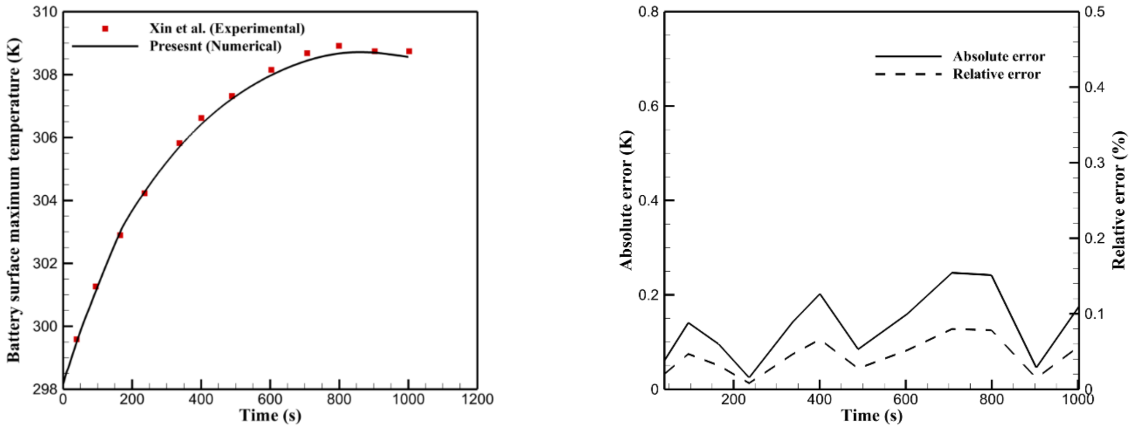

(b) (c)

Figure 3-5. Validation of the liquid cooling model against the experimental and numerical study of Xin et al. [278]: (a) liquid-cooled BTMS configuration, (b) comparison between the present numerical results and the reported maximum battery surface temperatures, and (c) absolute error (K) and relative error (%).

To validate the implementation of copper foam layers within copper tubes, the experimental study conducted by Amani et al. [311] was replicated numerically. As shown in Figure 3-6 (a), this study involved water flow through a copper tube embedded with copper foam (porosity 0.8 and pore density 10 PPI) subjected to a constant wall heat flux of 100 W/m^2. The numerical results of the average Nusselt number along the tube surface and the pressure drop were compared against the corresponding experimental results, as illustrated in

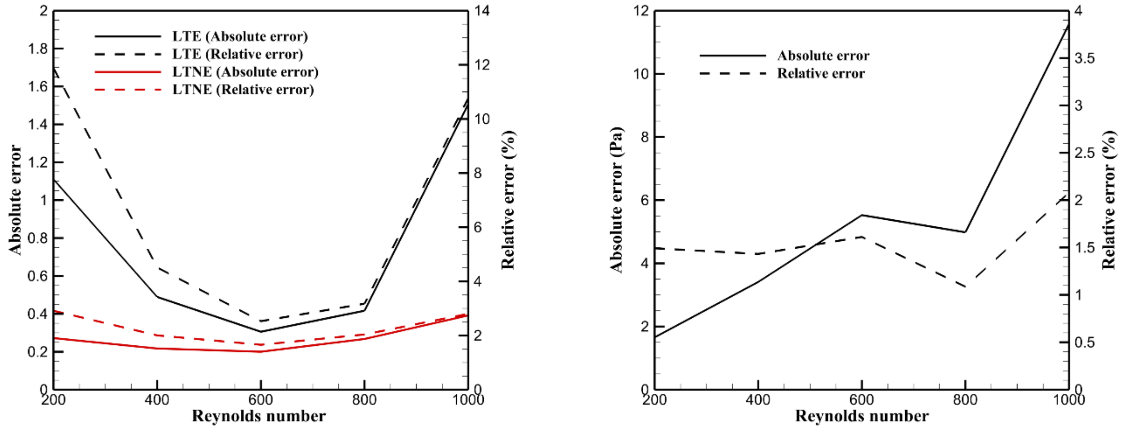

(d) (e)

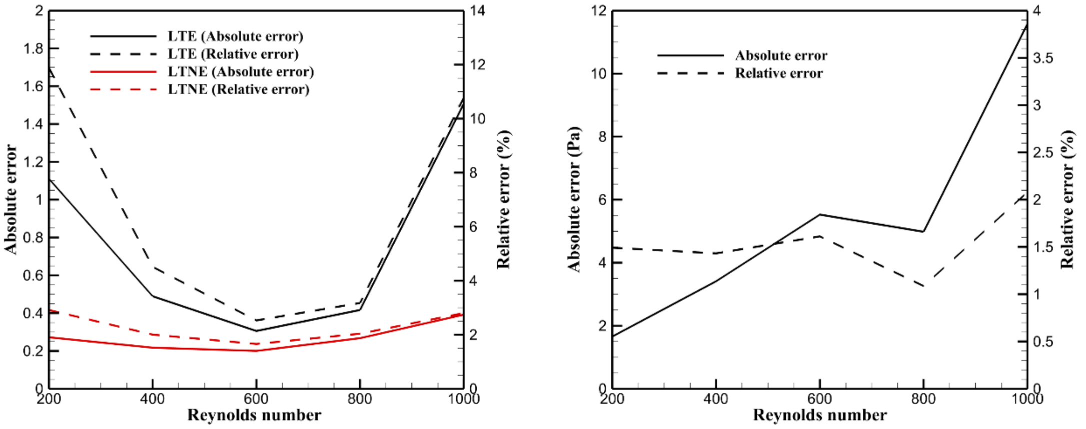

(d) (e)

Figure 3-6 (b) and (c), respectively. The associated absolute and relative errors are presented in

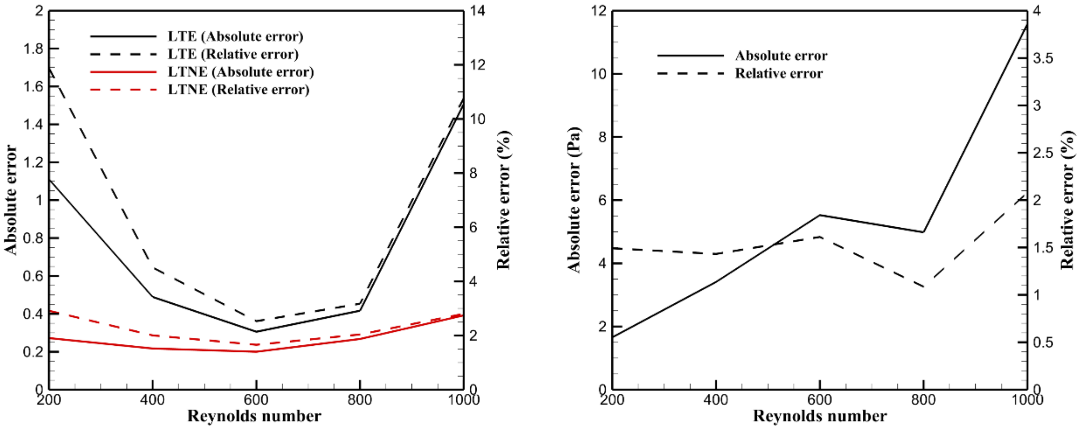

(d) (e)

Figure 3-6 (d) and (e). Simulations were performed using both the LTE and LTNE models; however, the LTNE model demonstrated superior agreement with the experimental data. Consequently, the LTNE approach was adopted for modelling the copper foam layer within the copper tube.

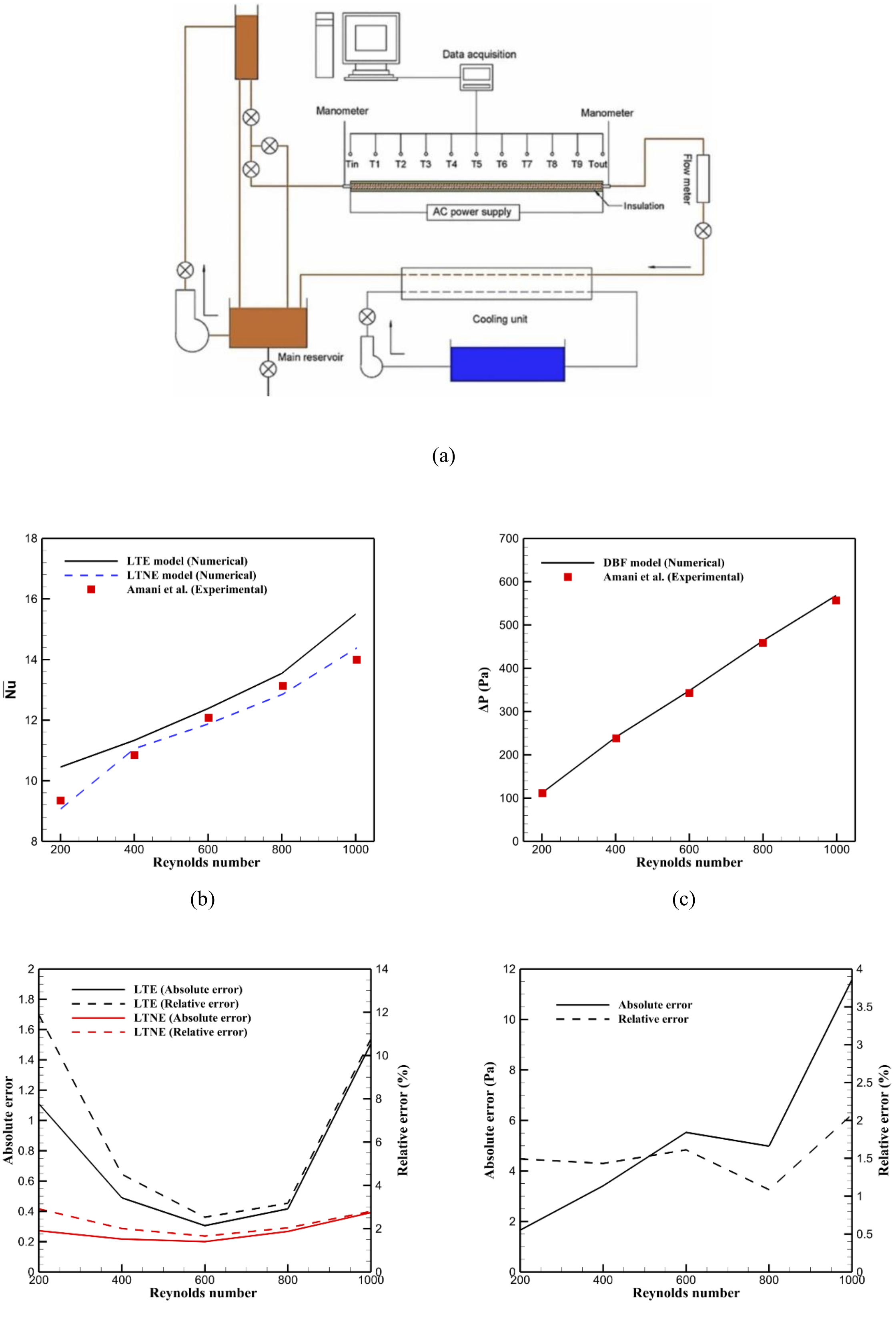

(a)

(b)

(c)

(d)

(e)

Figure 3-6. Validation of the copper foam filled tube model based on the experimental study of Amani et al. [311]: (a) experimental configuration of the copper foam filled tube; (b) comparison of average Nusselt number; (c) comparison of pressure drop; and (d, e) corresponding absolute error and relative error (%).

Chapter 4: Comparative Assessment and Parametric Study of the Proposed Copper Foam-Enhanced HBTMS

This chapter presents a comprehensive comparative and parametric investigation of the proposed hybrid battery thermal management system (HBTMS) enhanced with copper metal foam. The primary focus is to evaluate the system's thermal performance and identify the influence of key design and operational parameters under high discharge conditions.

The chapter begins with a comparison between the proposed HBTMS and conventional PCM-based systems, highlighting the advantages of integrating phase change materials, liquid cooling, and porous media. A series of parametric studies then follows, examining the effects of copper foam fin porosity and pore density, copper foam layer characteristics within the copper tubes, the quantity and thickness of copper foam fins, and the number of cooling plates. In addition, the impact of coolant inlet mass flow rate, inlet temperature, and ambient temperature on thermal regulation is assessed.

In each case, a single parameter is varied while keeping the others constant to isolate its effect on the behaviour of the system. The analysis includes detailed physical interpretations of the observed thermal and flow trends to provide a clearer understanding of the underlying mechanisms. This physical insight is essential for optimising the design, enhancing system efficiency, and supporting the development of lightweight and high-performance thermal management solutions for lithium-ion battery packs.

4.1 Comparison of the Proposed HBTMS with PCM Based BTMSs

The effectiveness of the proposed HBTMS, PCM with copper foam fins and liquid cooling with copper foam layers, was investigated under different discharge rates. This system was benchmarked against several BTMS configurations, including pure PCM, PCM with solid fins, PCM with copper foam fins without liquid cooling, and PCM with copper foam fins combined with liquid cooling. Transient heat generation was investigated at discharge rates of 1C, 3C, and 5C. Throughout the analysis, the porosity and pore density of the copper foam fins and layers were maintained at fixed values of 0.9 and 30 PPI [40], respectively.

To highlight the innovation of the proposed HBTMS, the performance of novel copper foam fins is first assessed by comparing them with configurations employing pure PCM and PCM with conventional solid fins, as illustrated in Figure 4-1 through Figure 4-7. Following this, the effects of integrating liquid cooling, both with and without a copper foam layer inside the copper tube, were evaluated against the baseline pure PCM across the same figures.

As illustrated in Figure 4-1, the maximum battery surface temperature ($T_{Max,Sur}$) in the pure PCM-based BTMS increases rapidly at the highest discharge rate, following three distinct thermal stages: before reaching the PCM solidus temperature (311.15 K), between the solidus and liquidus points (316.15 K), and beyond the liquidus point. These stages correspond to different thermal storage mechanisms within the PCM: sensible heat storage during the initial heating phase, latent heat absorption throughout the phase change, and further sensible heat accumulation after complete melting. At lower discharge rates, a similar temperature trend is observed; however, the temperature rise occurs in only two phases, as the PCM does not reach its liquidus temperature. This behaviour is attributed to the inherently low thermal conductivity of pure PCM.

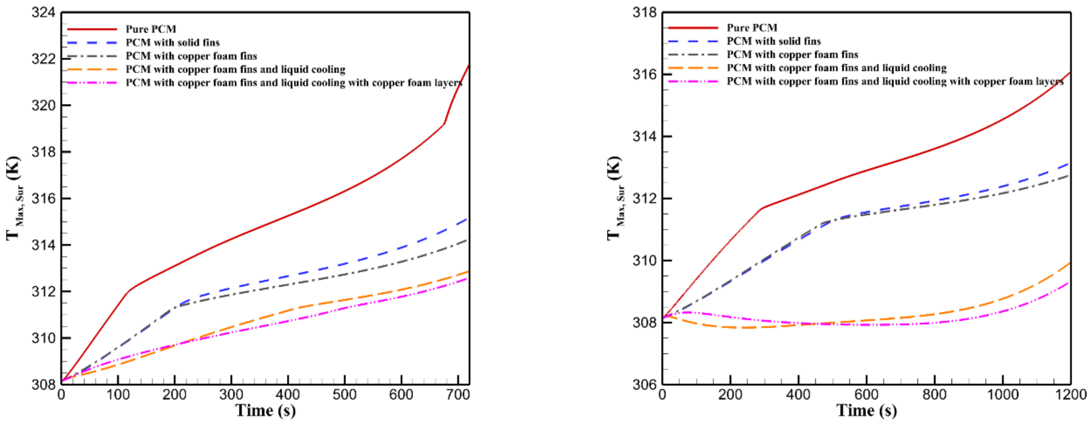

(a) 5C

(b) 3C

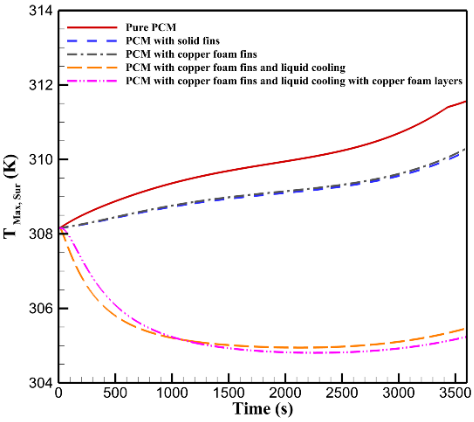

(c) 1C

Figure 4-1. Maximum battery surface temperature for different BTMS under various battery discharge rates: (a) 5C, (b) 3C, and (c) 1C.

As shown in Figure 4-2, for different discharge rates, a greater portion of PCM undergoes melting in the pure PCM compared to other configurations, with melting initiating almost immediately upon discharge. Further insights are provided by the contour plots in

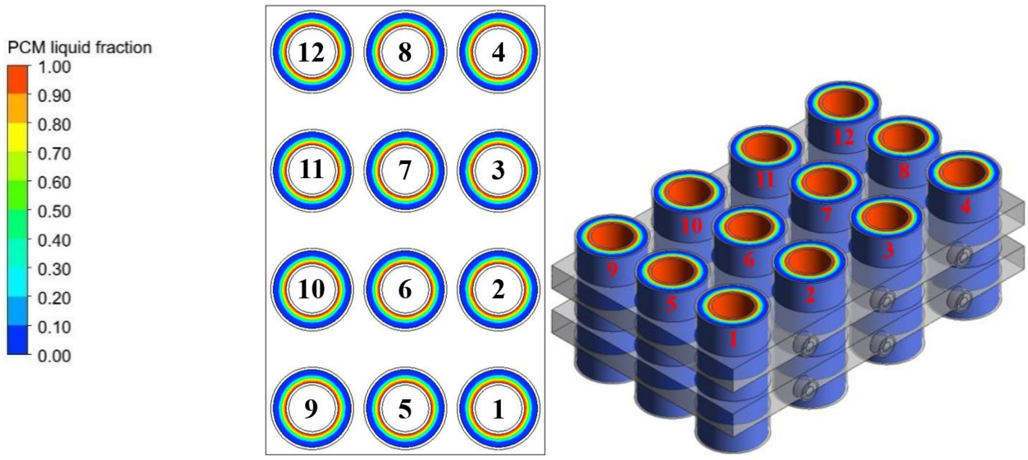

(a) Pure PCM

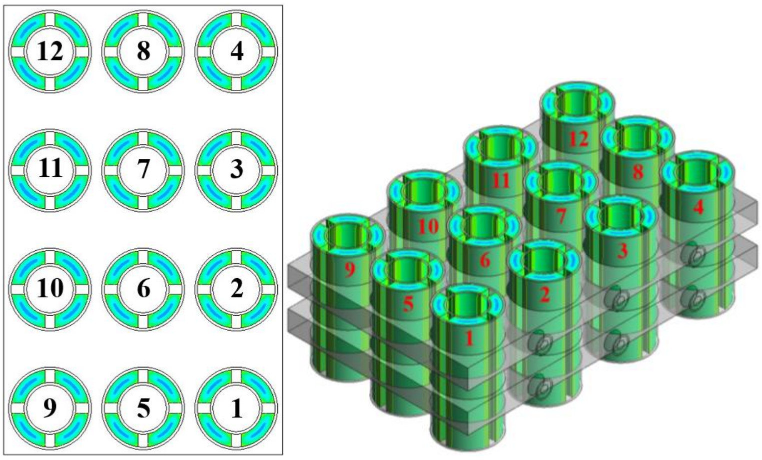

(b) PCM with solid fins

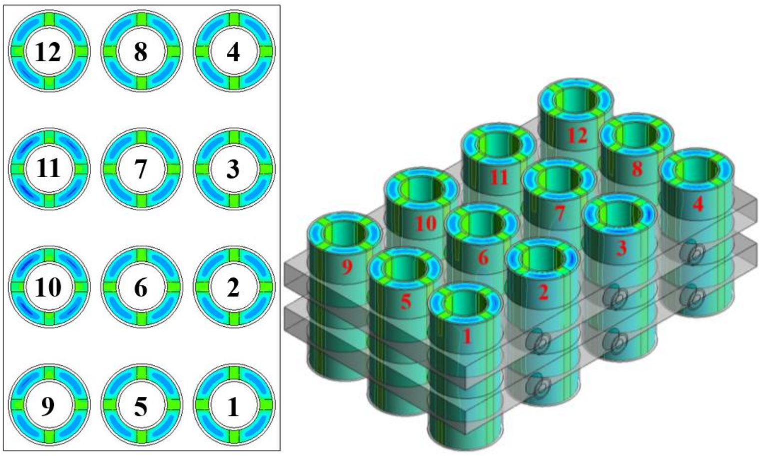

(c) PCM with copper foam fins

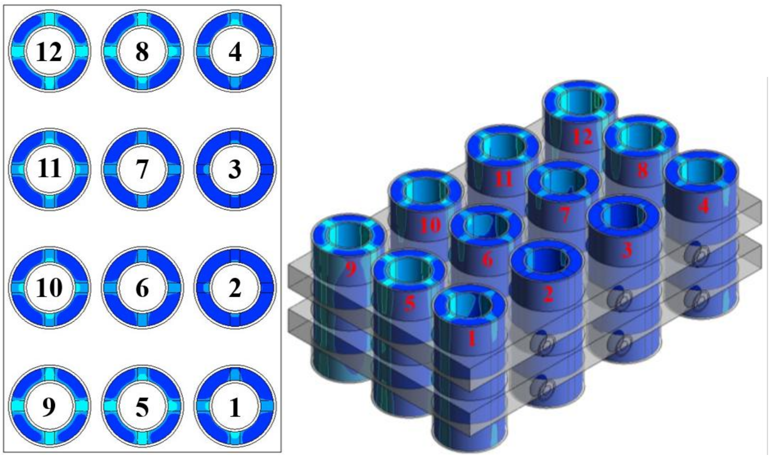

(d) PCM with copper foam fins and liquid cooling

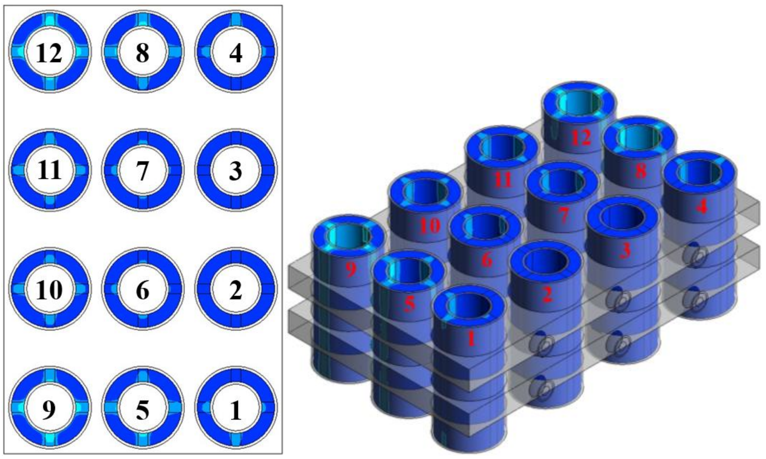

(e) PCM with copper foam fins and liquid cooling with copper foam layers

Figure 4-3 (a), which depict the PCM liquid fraction (L_f) distribution at the end of a 5C discharge. These plots reveal that the majority of the heat generated is dissipated through conduction and sensible heating, leading to melting concentrated around the battery housing. A thin molten layer forms around the battery due to the limited thermal conductivity, which acts as an insulating layer, restricting effective heat dissipation to the rest of the PCM volume.

These observations highlight a fundamental limitation of pure PCM in BTMS applications. While PCM can delay temperature rise due to its latent heat, the poor thermal conductivity significantly impedes its overall heat transfer effectiveness, especially at higher discharge rates or during extended operation. This underscores the necessity of developing HBTMS that integrate PCM with other thermal enhancement techniques to ensure reliable and safe thermal regulation.

To evaluate the effectiveness of the proposed HBTMS, two primary performance indicators were considered including $T_{Max,Sur}$ and L_f. As illustrated in Figure 4-1, the inclusion of fins, whether conventional longitudinal solid fins or the novel copper foam fins, demonstrably reduces $T_{Max,Sur}$ across different discharge rates. Considering the pure PCM as the baseline, the $T_{Max,Sur}$ at the end of discharge for 5C, 3C, and 1C were recorded as 321.77 K, 316.08 K, and 311.57 K, respectively. The addition of solid fins led to reductions in $T_{Max,Sur}$ by 6.6 K, 2.94 K, and 1.27 K for discharge rates of 5C, 3C, and 1C, respectively. Greater thermal performance was achieved with copper foam fins, with respective reductions of 7.52 K, 3.33 K, and 1.34 K under the same conditions.

The generated heat is transferred through conduction from the aluminium battery housing into the PCM and further through the PCM to the PCM housing in the HBTMS. The improved thermal performance is attributed to the addition of fins, which improves heat conduction by forming conduction paths within the PCM. In addition, the presence of fins significantly influences the extent and area of PCM melting. As shown in Figure 4-2 (a), the L_f value notably impacted by the presence of fins, with both fin types causing a similar delay in the onset of PCM melting. At the end of the 5C discharge rate, L_f for pure PCM reached nearly 0.3. With solid fins, L_f increased by 24%, rising to 0.36 due to better conduction. In contrast, PCM with copper foam fins showed a 14% reduction in L_f, decreasing to 0.25. A similar pattern was observed for the 3C discharge rate in Figure 4-2 (b), with less PCM melting due to lower transient heat generation. Nonetheless, at a 1C discharge rate, as depicted in Figure 4-2 (c), all the heat generated by the batteries was absorbed as sensible heat storage, preventing phase change.

When comparing the heat transfer mechanisms of solid and copper foam fins, both initially conduct the heat generated by the battery to the surrounding PCM housing. However, as depicted in Figure 4-2 (d), which presents the cross-sectional velocity field within the molten PCM, the onset of melting within the copper foam fins introduces buoyancy driven natural convection in addition to conduction. Although the velocity magnitude remains on the order of 10^{-7} m/s, indicating relatively weak flow, the low velocity magnitude is consistent with the restricted permeability of the foam matrix, which suppresses large scale convection while still promoting micro scale mixing. The interconnected porous network therefore facilitates localised circulation and enhances heat transfer in conjunction with the increased effective thermal conductivity of the copper foam. Furthermore, the high specific surface area of the porous structure provides a larger solid–liquid interfacial area for thermal exchange compared with solid fins. Consequently, as illustrated in Figure 4-1 (a) and (b), both fin types yield nearly identical maximum surface temperatures just before the onset of PCM melting, at 200 seconds for a 5C discharge and 480 seconds for a 3C discharge. Beyond this point, copper foam fins exhibit superior heat transfer performance.

As illustrated in the PCM liquid fraction contours in

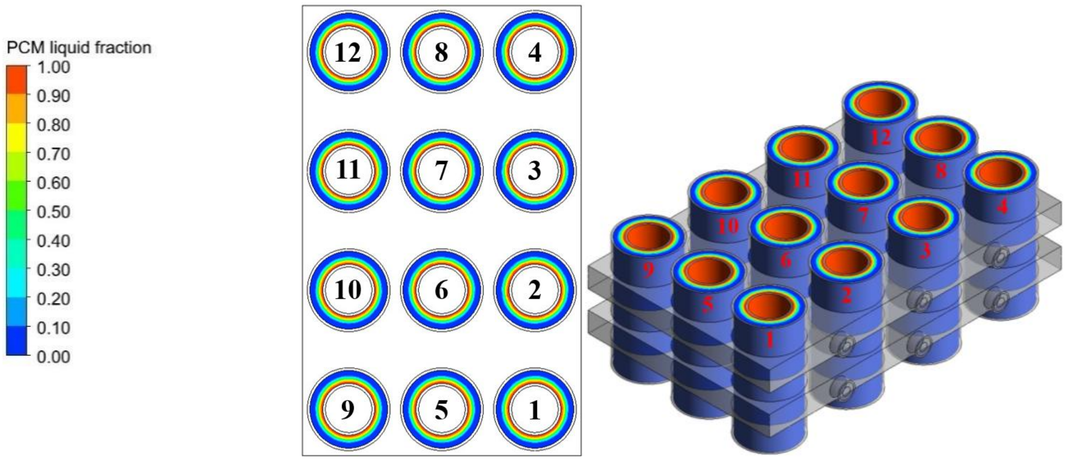

(a) Pure PCM

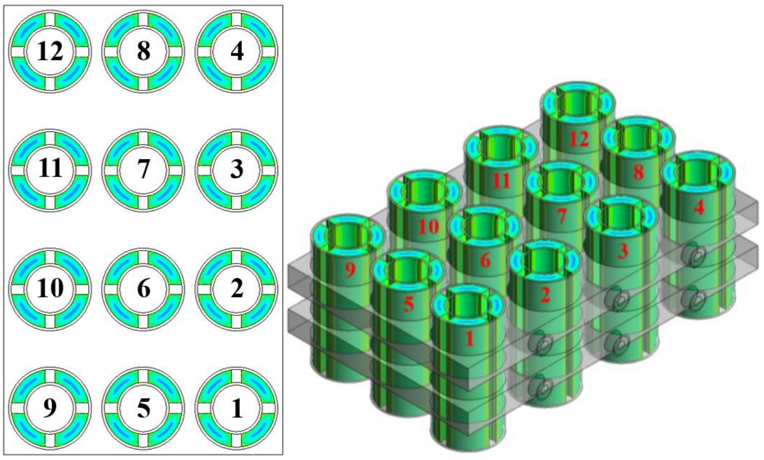

(b) PCM with solid fins

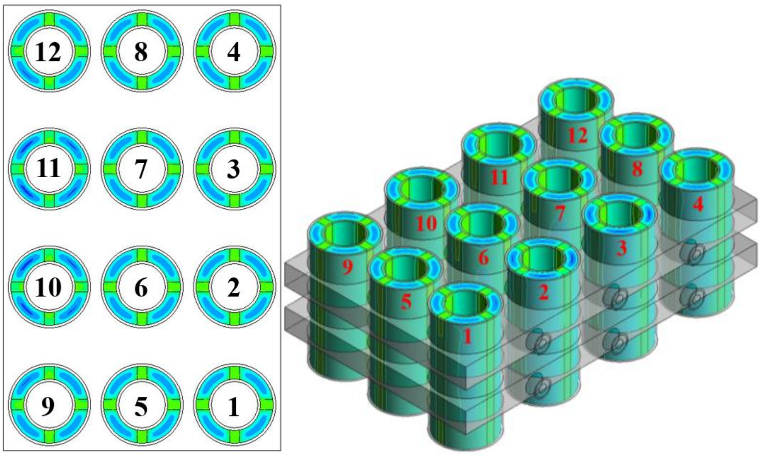

(c) PCM with copper foam fins

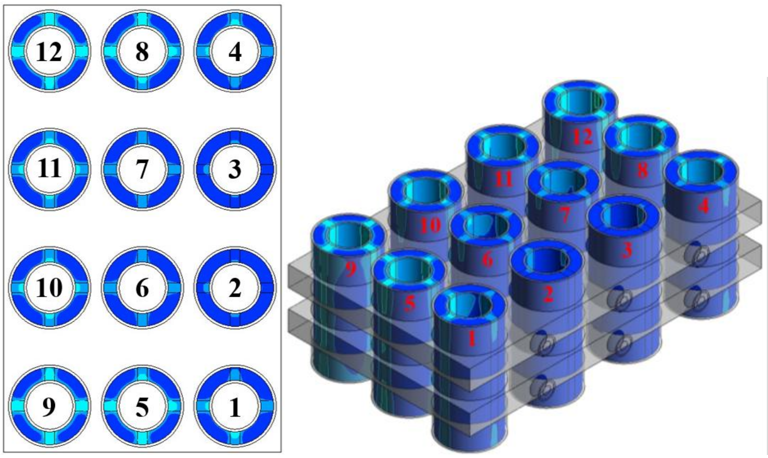

(d) PCM with copper foam fins and liquid cooling

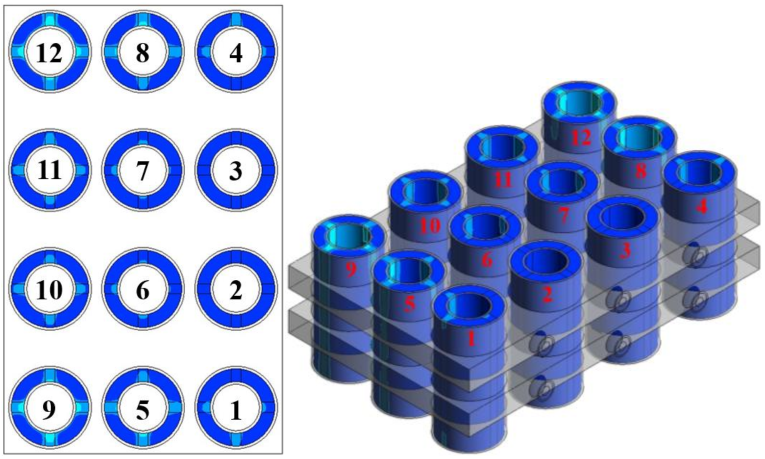

(e) PCM with copper foam fins and liquid cooling with copper foam layers

Figure 4-3 (a), (b), and (c), a smaller amount of PCM melted near the battery housing in configurations other than the pure PCM case. In the case of solid fins, heat is primarily transferred via conduction, resulting in localised heating around the fins and greater PCM melting in those regions and adjacent to the PCM housing. On the other hand, with copper foam fins, PCM melting mainly takes place within the porous structure and near the PCM housing. The copper foam fins serve as nucleation points for the phase change, which may lead to more uniform melting inside the pores. Therefore, the improved heat transfer in copper foam fins is due to a combination of increased surface area, enhanced convection from the movement of liquid PCM within the pores, and more even heat distribution throughout the PCM.

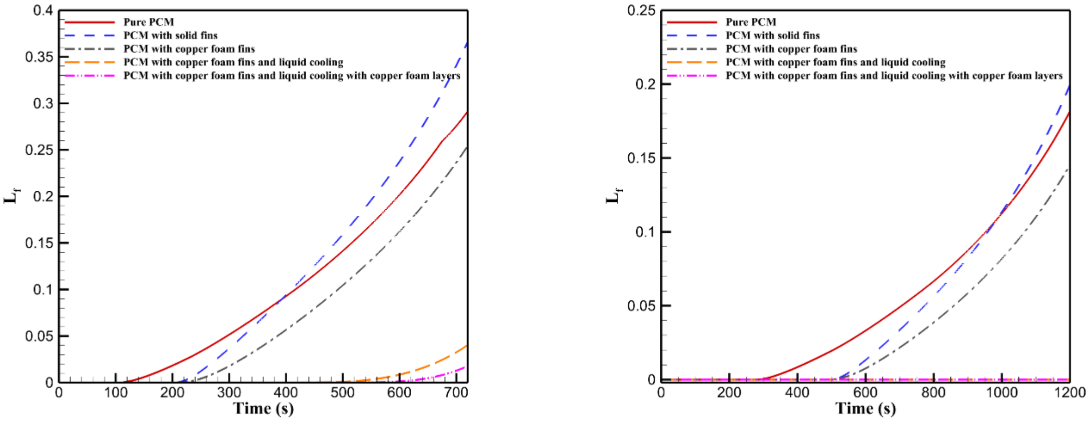

(a) 5C

(b) 3C

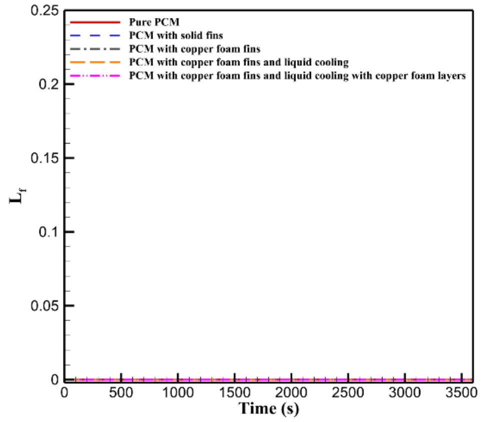

(c) 1C

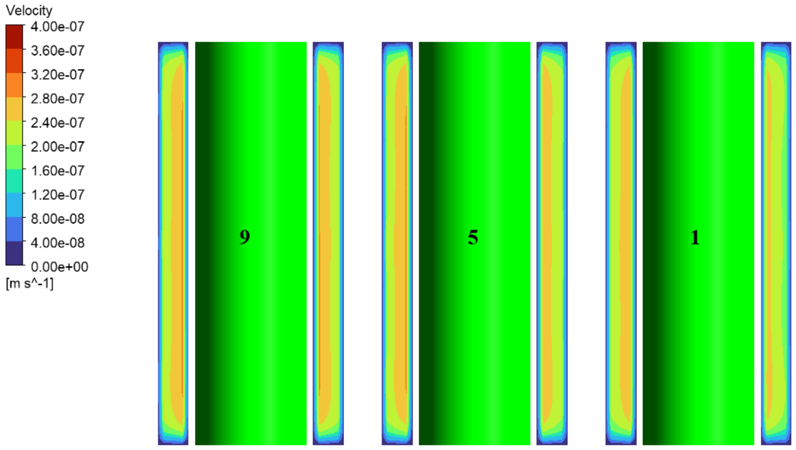

(d) Molten PCM velocity field

Figure 4-2. PCM liquid fraction for different BTMS under various battery discharge rates: (a) 5C, (b) 3C, (c) 1C, and (d) cross sectional velocity field of the molten PCM within the copper foam fins under natural convection.

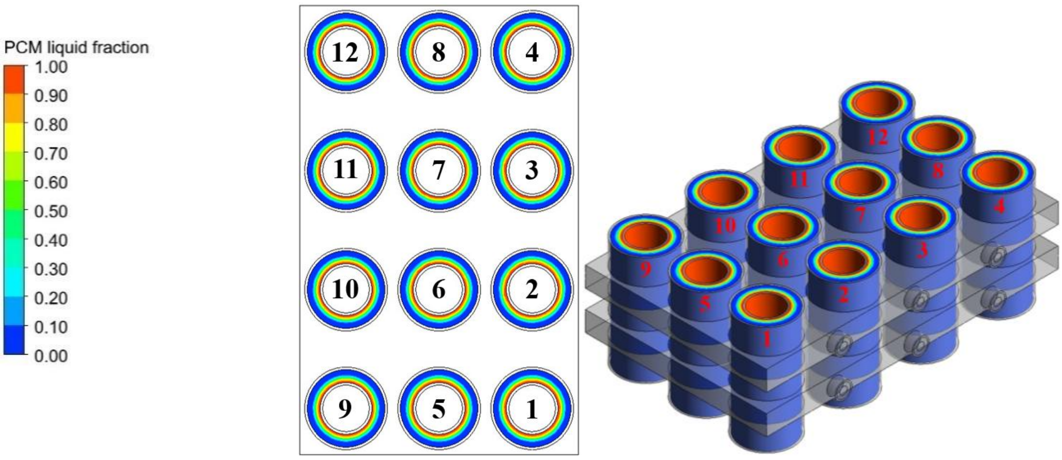

(a) Pure PCM

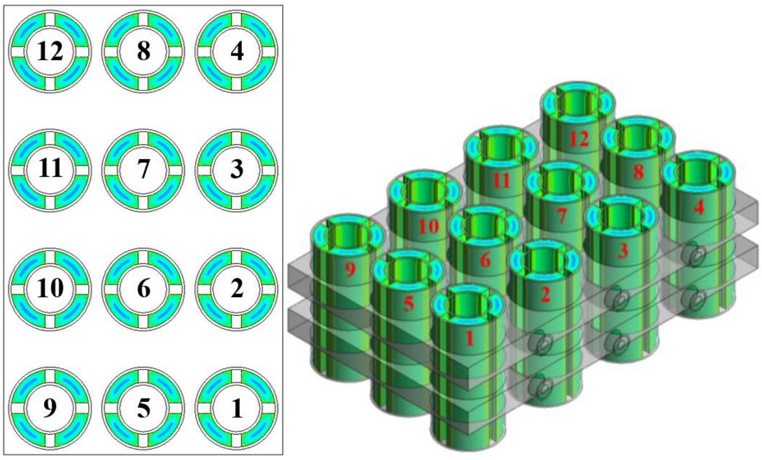

(b) PCM with solid fins

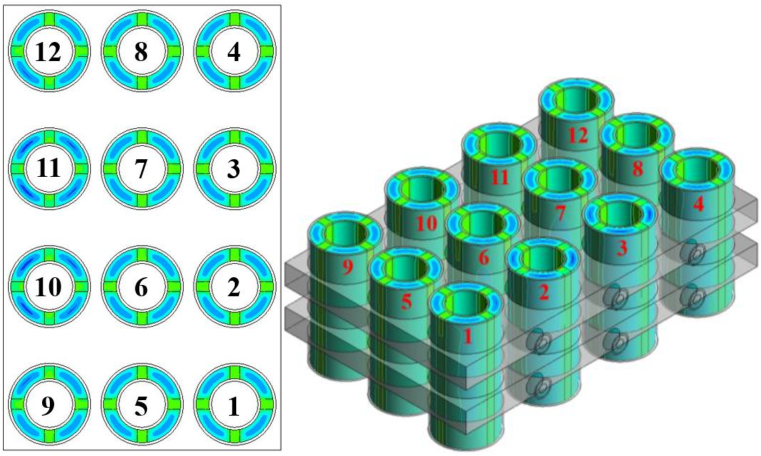

(c) PCM with copper foam fins

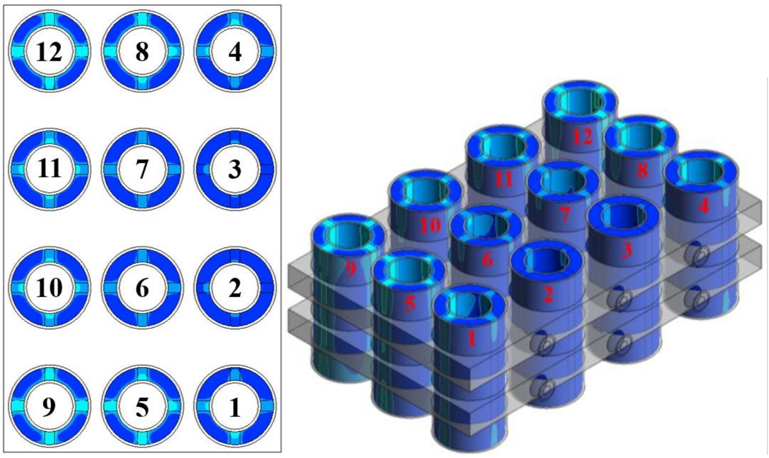

(d) PCM with copper foam fins and liquid cooling

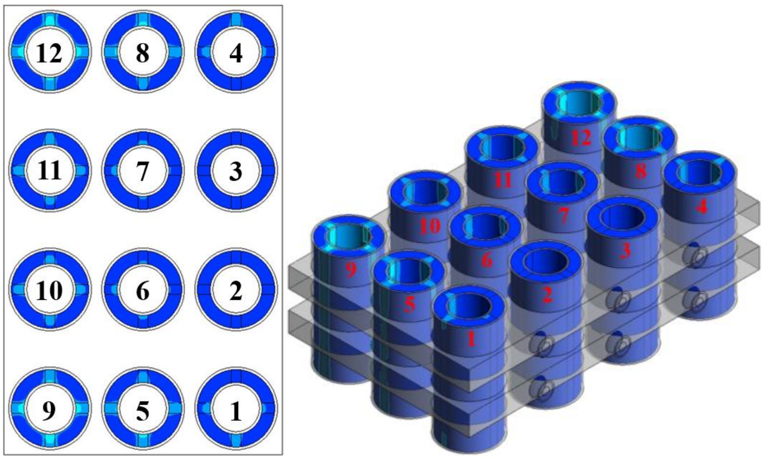

(e) PCM with copper foam fins and liquid cooling with copper foam layers

Figure 4-3. PCM liquid fraction contour plots for different BTMS at the end of the 5C discharge rate: (a) pure PCM, (b) PCM with solid fins, (c) PCM with copper foam fins, (d) PCM with copper foam fins and liquid cooling, and (e) PCM with copper foam fins, liquid cooling with copper foam layers.

The improved thermal performance of the HBTMS is indicated by the average Nusselt number on the battery's surface ($\overline{Nu}_b$), which is defined as follows [312]:

$$\overline{Nu}_b = \frac{q_{b,s} L_b}{\left(T_{b,sur} - T_{PCM,m}\right) K_{l,PCM}} \tag{4-1}$$

where $q_{b,s}$, L_b, $T_{b,sur}$, $T_{PCM,m}$, $K_{l,PCM}$ are heat flux on the battery surface, battery height, battery surface temperature, PCM melting temperature, and liquid PCM thermal conductivity, respectively.

Figure 4-4 presents the comparison of heat transfer enhancement based on the $\overline{Nu}_b$ for various BTMS configurations. For each configuration, the $\overline{Nu}_b$ increased sharply until the PCM began melting and the battery surface temperature surpassed the PCM's solidus temperature. After this phase, the $\overline{Nu}_b$ progressively declined until the discharge was completed. At higher discharge rates (3C and 5C), both solid and copper foam fin configurations demonstrated significantly higher $\overline{Nu}_b$ compared to the pure PCM case once melting had begun. Specifically, at the end of the 5C discharge, solid and copper foam fins led to $\overline{Nu}_b$ increases of 172% and 260%, respectively. Similarly, at 3C, the increases were 161% for solid fins and 231% for copper foam fins. However, as shown in Figure 4-4 (c), for the 1C discharge, where no phase change occurred, the pure PCM exhibited a higher $\overline{Nu}_b$. Moreover, when comparing all PCM-based BTMS configurations (pure PCM, PCM with solid fins, and PCM with copper foam fins) across discharge rates, a general trend was observed as lower discharge rates corresponded to higher $\overline{Nu}_b$. This behaviour is attributed to the extended discharge duration at lower C-rates, which allows the BTMS more time to dissipate the accumulated heat.

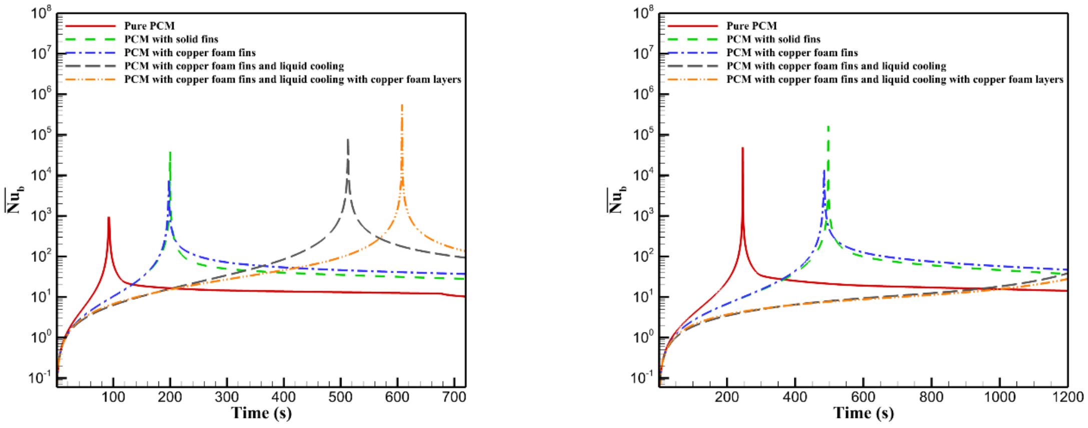

(a) 5C

(b) 3C

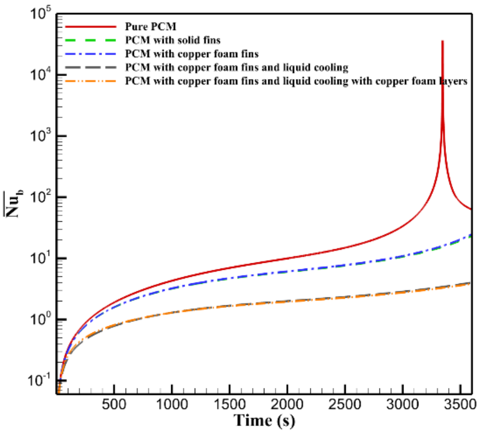

(c) 1C

Figure 4-4. Average Nusselt number on batteries surface for different BTMS under various battery discharge rates: (a) 5C, (b) 3C, and (c) 1C.

To further improve the performance of the BTMS, liquid cooling was integrated into the PCM with copper foam fins configuration. As illustrated in Figure 4-1, this combination resulted in a notable reduction in $T_{Max,Sur}$ when compared to the pure PCM. Specifically, reductions of 8.89 K, 6.14 K, and 6.10 K were observed for discharge rates of 5C, 3C, and 1C, respectively. Additional enhancement was achieved by incorporating a copper foam layer into the liquid cooling section, the HBTMS, combining PCM, copper foam fins, and liquid cooling with copper foam layers, further decreased $T_{Max,Sur}$ by 9.18 K, 6.75 K, and 6.33 K for the respective discharge rates. At the 1C discharge rate, the lower heat generation of the batteries led to $T_{Max,Sur}$ dropping even below the ambient temperature of 308.15 K. In this configuration, the generated heat, conducted to the cooling plates through the battery housing, PCM, copper foam fins, PCM housing, and cooling plates, was dissipated by forced convection due to the water flow in the copper tube. The presence of the copper foam layer also enhances the forced convection within the copper tube.

As illustrated in Figure 4-5 (a), the incorporation of a copper foam layer notably alters the parabolic velocity profile along the vertical axis at the centre of the copper tube. The copper foam layer introduces flow resistance, which reduces the local velocity within this region to below the average value. This added resistance also generates a sharper velocity gradient at the interface between the copper foam layer and the clear region, thereby enhancing mixing near the tube wall, an area characterised by the higher thermal conductivity of the copper foam layer. Within the central, more permeable region of the tube, the fluid velocity is approximately 1.75 times greater than that observed in the configuration without a copper foam layer.

The dimensionless temperature profile within the copper tube is defined as follows [313]:

$$\theta = \frac{k_{eff}\,(T - T_{w,tube})}{q_{w,\mathrm{tube}} D} \tag{4-2}$$

where $T_{w,tube}$ and $q_{w,\mathrm{tube}}$ are the copper tube wall temperature and heat flux, respectively. D is the diameter of the copper tube.

The temperature profile presented in Figure 4-5 (b) demonstrates the influence of the copper foam layer on temperature distribution within the copper tube. In the absence of a copper foam layer, the temperature profile remains continuous; however, with the introduction of the copper foam layer, a distinct discontinuity emerges. The higher temperature of the liquid phase within the copper foam layer, relative to the case without a copper foam layer, signifies improved heat extraction from the copper tube's surface. This improvement is attributed to the enhanced heat transfer area afforded by the copper foam's interconnected ligaments. Moreover, a noticeable temperature gradient between the solid and liquid phases inside the copper foam region is observed, primarily due to the much higher thermal conductivity of the copper foam compared to that of the flowing water. Additionally, the foam ligaments interfere with the development of the thermal boundary layer, further augmenting the overall heat transfer performance.

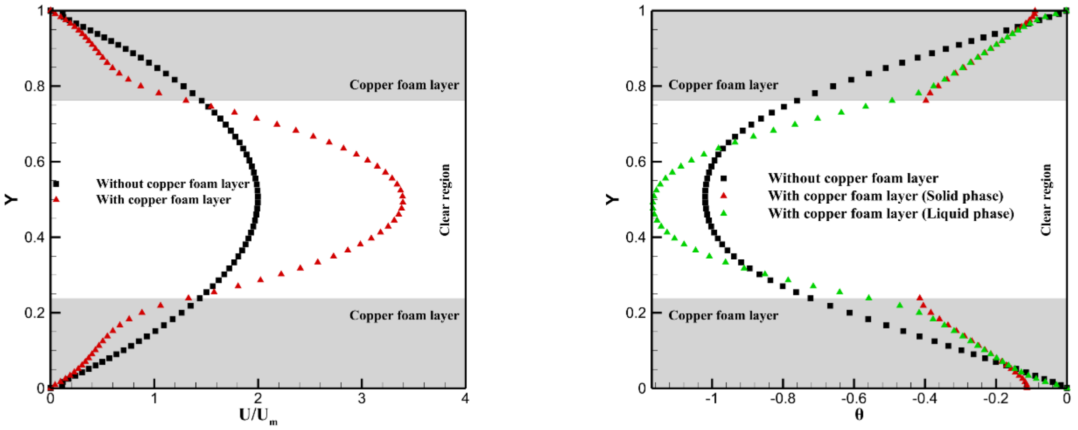

(a) (b)

Figure 4-5. Comparison of dimensionless (a) velocity and (b) temperature at the middle of the copper tube along the vertical axis with and without copper foam layer at the end of 5C discharge rate.

The integration of liquid cooling into the system significantly influences the PCM melting behaviour by notably delaying the onset of phase change. As illustrated in Figure 4-2, the L_f is substantially reduced across all HBTMS configurations incorporating liquid cooling. Specifically, under the 5C discharge rate, L_f decreased by approximately 86% for the configuration with liquid cooling alone and by 94% for the configuration with both liquid cooling and a copper foam layer, compared to the pure PCM. At lower discharge rates, the enhanced cooling efficiency prevented the PCM from reaching its melting point. Further insights can be drawn from the PCM liquid fraction contour plots in Figure 4-3 (a), (d), and (e), which show that during the 5C discharge, PCM melting was concentrated within the copper foam fins and around the battery housing. In contrast, PCM near the outer PCM housing remained largely solid due to the improved heat dissipation through the cooling plates. Batteries located closer to the liquid inlet, batteries 1 to 4, exhibited minimal PCM melting due to the lower coolant temperature. However, as water absorbed heat along the flow direction, its temperature increased, resulting in a greater extent of PCM melting for batteries 9 to 12. Moreover, batteries 2, 3, 6, 7, 10, and 11, surrounded by copper tubes embedded in the cooling plates, experienced reduced PCM melting, whereas batteries located along the outer sides of the module, which were less influenced by liquid cooling, exhibited more extensive PCM melting.

As illustrated in Figure 4-4 (a), under a 5C discharge rate, at the end of discharge, the HBTMS with liquid cooling and a copper foam layer, as well as the HBTMS with liquid cooling alone, increased the $\overline{Nu_b}$ by approximately 13 times and 9 times, respectively, compared to the pure PCM. Figure 4-4 (b) shows that under a 3C discharge rate, the improvement is approximately twofold and threefold, respectively. Therefore, it can be concluded that HBTMS with liquid cooling is particularly suitable for high discharge rates.

An effective BTMS must address not only the reduction of maximum temperature but also the control of maximum temperature variation to ensure uniform temperature distribution within the battery module and individual cells. Accordingly, the maximum temperature difference within the battery module (ΔT_{Max}) was selected as the second evaluation criterion. According to the literature, ΔT_{Max} should be kept below 5K [23, 24, 49]. As shown in Figure 4-6, ΔT_{Max} tends to increase with higher discharge rates in the enhanced HBTMS compared to the pure PCM. Based on the melting start time in Figure 4-2 for different discharge rates and various BTMSs, ΔT_{Max} typically decreased after the phase change began, particularly under higher discharge rates. For lower discharge rates, ΔT_{Max} showed minimal variation across different BTMS designs. Greater fluctuations in ΔT_{Max} were observed in the HBTMSs incorporating liquid cooling, with or without a copper foam layer; however, in all scenarios, ΔT_{Max} remained below the 5 K threshold. The observed temperature uniformity is primarily attributed to the aluminium housing design surrounding the battery cells, which interfaces with the cooling plates while preventing direct contact between the PCM and the battery cells, as well as direct contact between the fins and the cells that can cause overcooling at contact points and large local temperature gradients by improving lateral heat transfer. Additionally, as seen in the contour plots in Figure 4-7, this structural feature promotes a more even surface temperature distribution. The radial temperature gradient across the battery cells is linked to the inherently lower thermal conductivity in the radial direction compared to the axial.

In the context of EV applications, the temperature non-uniformity metric (ΔT_{Max}) is particularly important as it governs cell-to-cell performance dispersion, imbalance growth, and divergence in ageing rates across a module. The present results demonstrate that the proposed HBTMS maintains ΔT_{Max} within the uniformity target of below 5 K, indicating that the design is capable of limiting thermal mismatch under high-rate operation. From a scalability perspective, the external thermal boundaries applied directly correspond to the vehicle-level constraints that a battery module experiences in practice, namely the coolant-loop inlet temperature and flow capacity, together with the surrounding environment. Consequently, the trends reported here are transferable to EV modules by geometric replication of the cell-level unit and by preserving the same boundary-condition definitions at the module and cold plate interface.

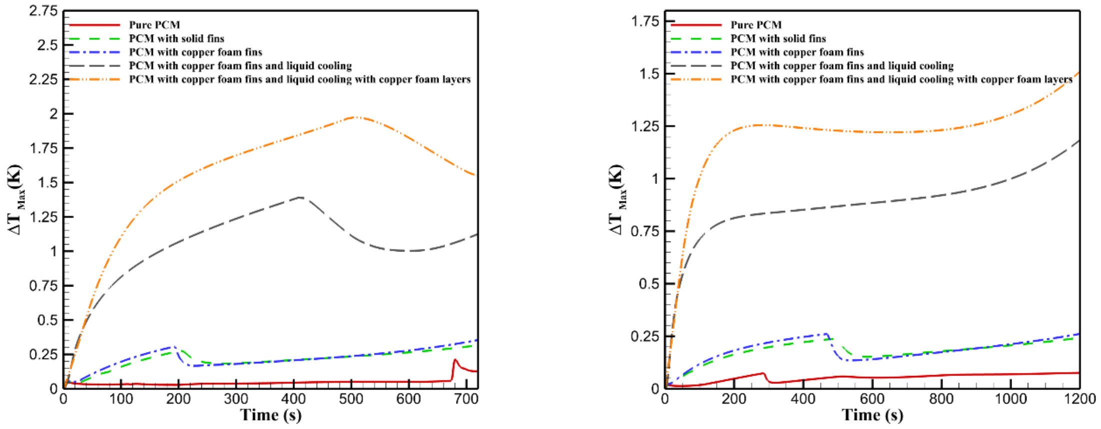

(a) 5C

(b) 3C

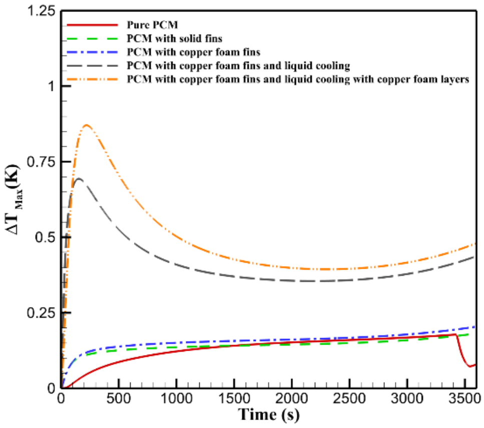

(c) 1C

Figure 4-6. Maximum temperature difference within the battery module for different BTMS under various battery discharge rates: (a) 5C, (b) 3C, and (c) 1C.

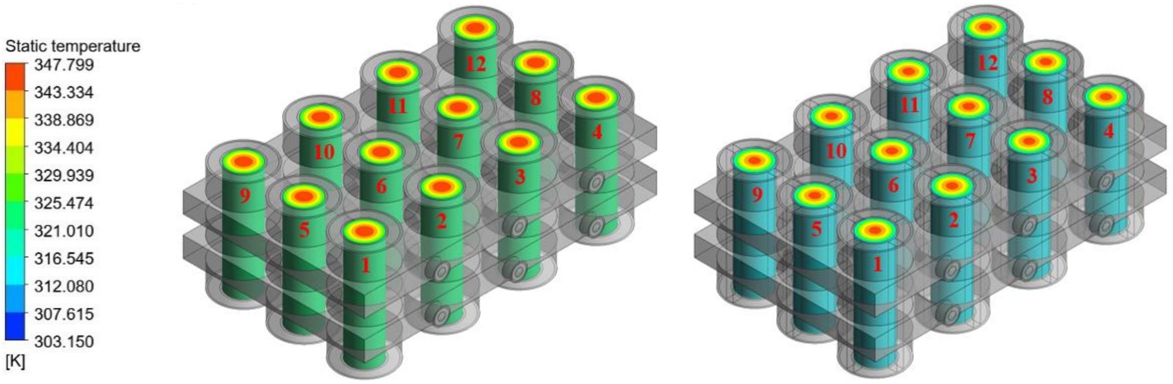

(a) Pure PCM

(b) PCM with solid fins

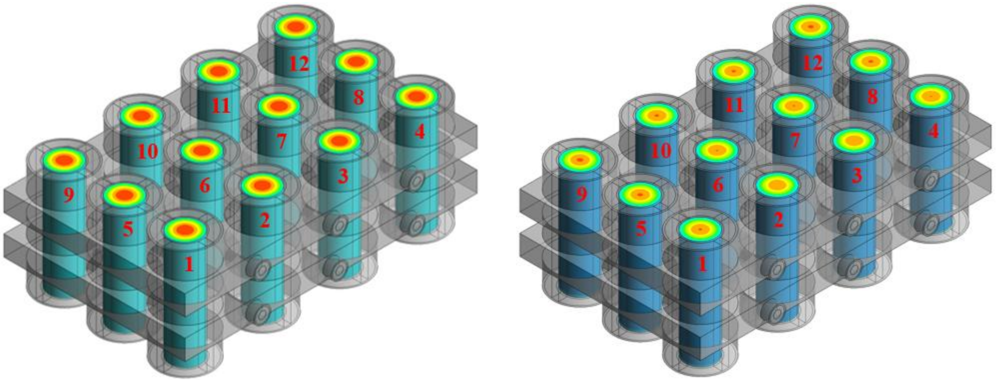

(c) PCM with copper foam fins

(d) PCM with copper foam fins and liquid cooling

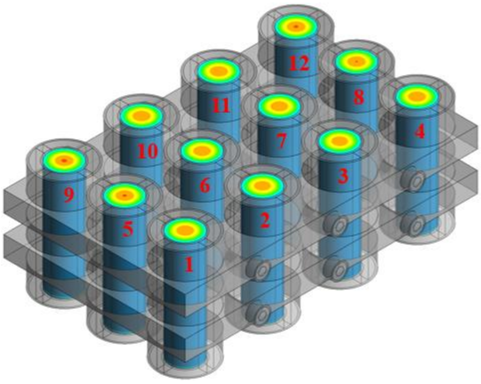

(e) PCM with copper foam fins and liquid cooling with copper foam layer

Figure 4-7. Static temperature contour plots for different BTMSs and HBTMS at the end of the 5C discharge rate: (a) pure PCM, (b) PCM with solid fins, (c) PCM with copper foam fins, (d) PCM with copper foam fins and liquid cooling, and (e) PCM with copper foam fins, liquid cooling with copper foam layers.

To comprehensively assess the performance of the proposed HBTMS, $T_{Max,Sur}$ and the battery maximum surface temperature difference ($\Delta T_{Max,b}$) at the end of discharge were evaluated for each battery under varying discharge rates, as illustrated in Figure 4-8. As shown, under different discharge rates, the battery cells located on the sides of the battery module (1, 4, 5, 8, 9, 12) consistently exhibited higher $T_{Max,Sur}$ compared to centrally positioned cells (2, 3, 6, 7, 10, 11). Figure 4-7 (e) demonstrates that the static temperature of cells near the inlet and at the centre of the module remained lower, whereas the highest core temperatures were recorded for batteries at the sides and in the last row. This pattern is attributed to the enhanced cooling effect experienced by centrally located cells, which are in closer proximity to the copper tubes embedded in the cooling plates. However, as the coolant travels along the copper tube, its capacity to absorb heat diminishes due to the rising inlet temperature. As a result, for all discharge rates, the highest and lowest $T_{Max,Sur}$ values were observed in batteries 12 and 2, respectively. In terms of $\Delta T_{Max,b}$, the proposed HBTMS successfully maintains the temperature variation across battery cells below 1 K, even under the highest discharge rate of 5C. At lower discharge rates, the temperature distribution becomes even more uniform, owing to the reduced rate of battery heat generation.

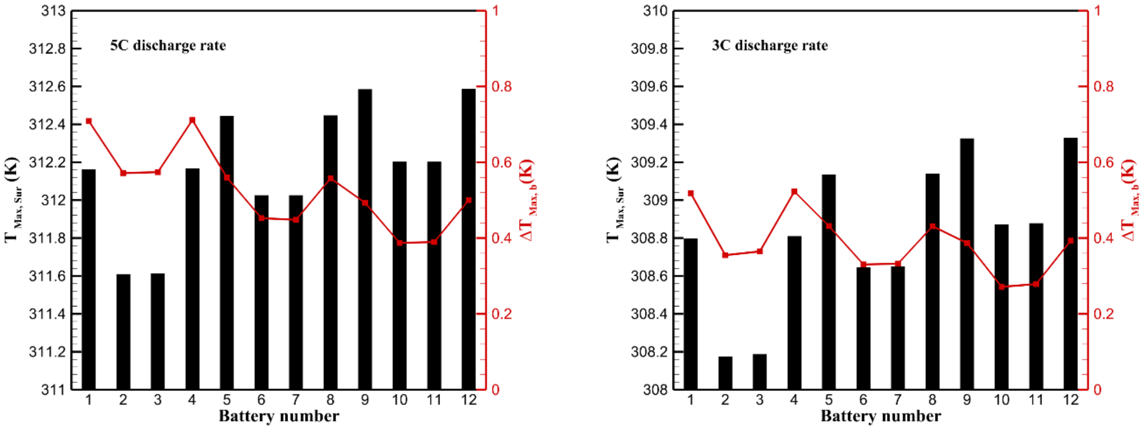

(a) 5C

(b) 3C

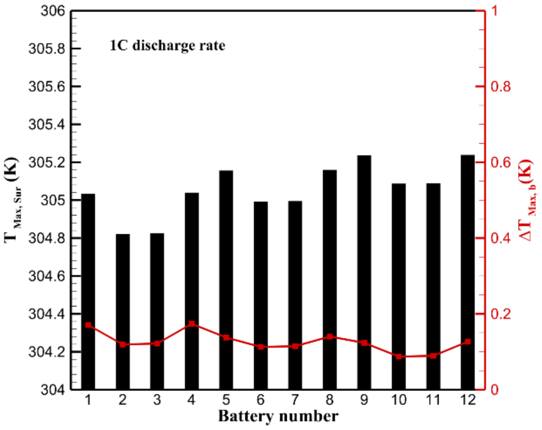

(c) 1C

Figure 4-8. $T_{Max,Sur}$, $\Delta T_{Max,b}$ at the end of discharge for the HBTMS under investigation for different discharge rates: (a) 5C, (b) 3C, and (c) 1C.

While the integration of fins into PCM enhances its thermal conductivity, it simultaneously leads to a reduction in the overall PCM volume within the BTMS.

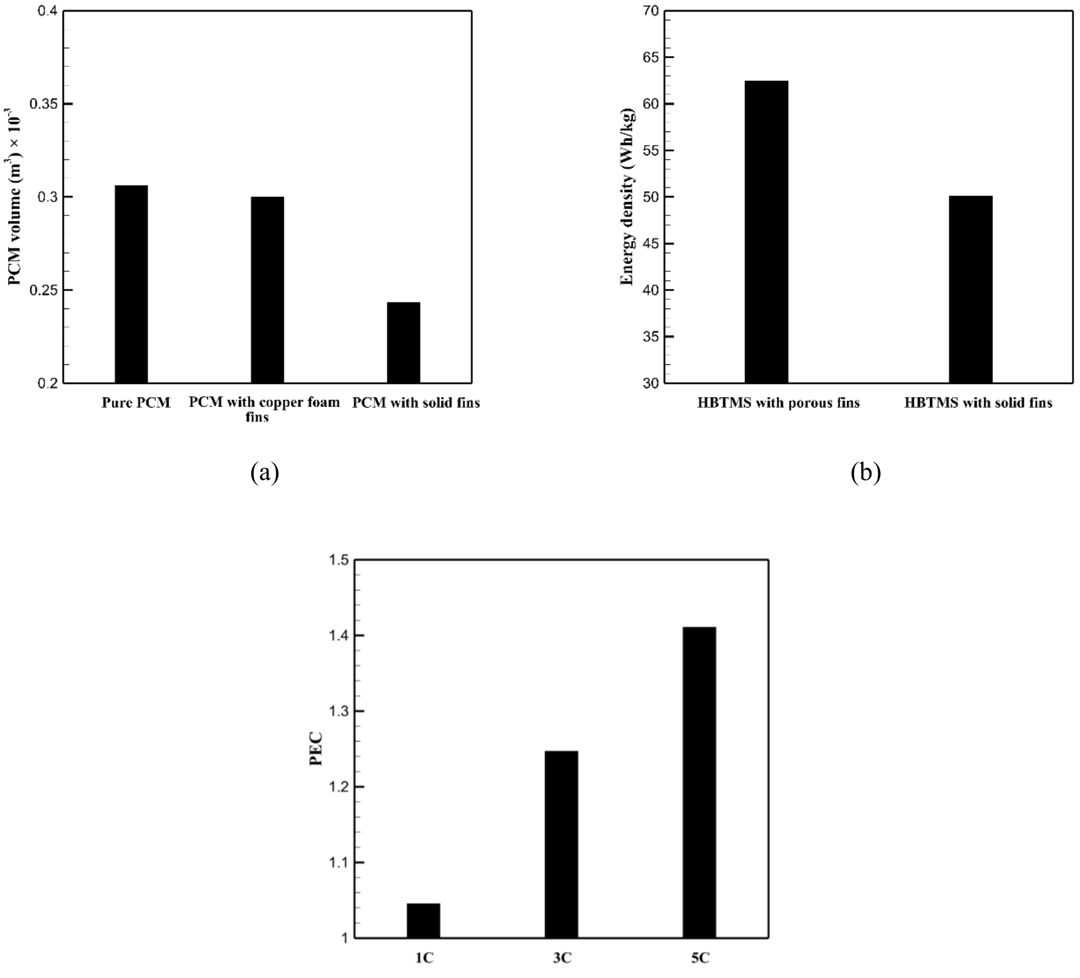

(a) (b)

(c)

Figure 4-9 (a) compares the PCM volume across configurations using pure PCM, PCM with solid fins, and PCM with copper foam fins. The results indicate that incorporating solid fins reduces the PCM volume by approximately 20%, whereas the use of copper foam fins leads to a significantly smaller reduction of only about 2%.

In this study, energy density is defined as a system-level gravimetric metric, calculated as the cell's nominal energy (UC_0) normalised by the mass of the HBTMS (m). It therefore quantifies the packaging mass penalty associated with the thermal management hardware, rather than the intrinsic electrochemical energy density of the cell. Since the nominal voltage and nominal capacity remain identical across the compared configurations, variations in energy density arise solely from differences in HBTMS mass [214]. The energy density is therefore expressed as:

$$E_d = \frac{UC_0}{m} \tag{4-3}$$

where E_d denotes the system-level gravimetric energy density (Wh/kg), U is the battery's nominal voltage (V), C_0 indicates the battery's nominal capacity (Ah), and m signifies the mass of the HBTMS (kg).

Considering the impact of fin type on HBTMS's energy density, as illustrated in Figure 4-9 (b), the porous structure of the fins results in a lower mass compared to conventional solid fins. This reduction in mass contributes to a significant improvement in energy density, with the HBTMS featuring copper foam fins achieving approximately 25% higher energy density than its counterpart with solid fins. Consequently, copper foam fins offer a distinct advantage over solid fins in terms of enhancing the system's energy density.

The incorporation of copper foam layers within the copper tube enhances the heat transfer rate; however, it also leads to an increase in pressure drop. As such, achieving an appropriate balance between these parameters is essential. To assess the heat transfer efficiency, the performance evaluation criterion (PEC) [314] , defined by Equation (4-4), was employed. The PEC quantifies the relative improvement in heat transfer by comparing the Nusselt number and pressure drop in liquid cooling systems with and without copper foam layers, while keeping all other geometrical features of the HBTMS unchanged. As illustrated in

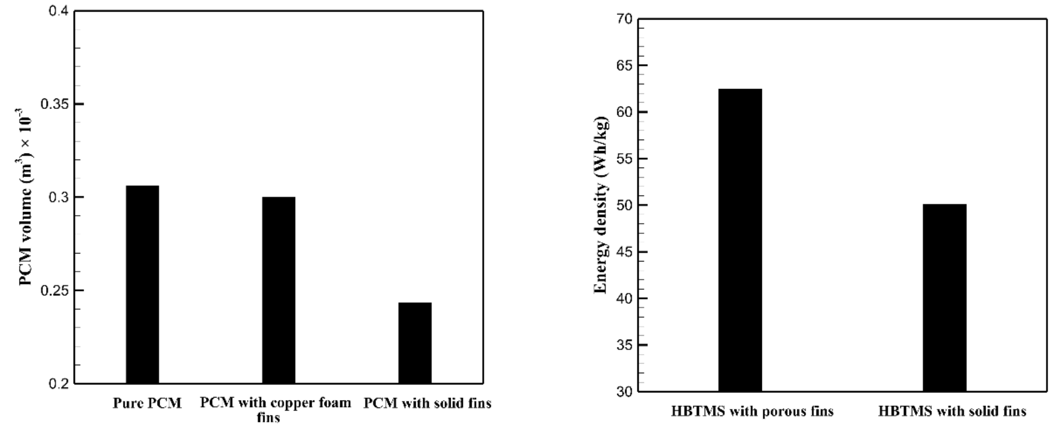

(a) (b)

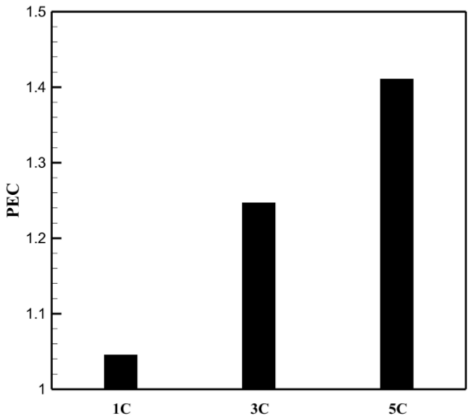

(c)

Figure 4-9 (c) and summarised in Table 4-1, PEC values across different discharge rates consistently exceed one, signifying that the improvement in heat transfer due to the copper foam layer surpasses the associated increase in pressure drop. This performance enhancement is particularly significant at higher discharge rates.

$$PEC = \frac{\overline{Nu}/\overline{Nu}_0}{(\overline{f_r}/\overline{f_r}_0)^{1/3}} \tag{4-4}$$

where $\overline{Nu}$ and $\overline{f_r}$ are the average Nusselt number for liquid cooling and friction factor, respectively, are defined as follows:

$$\overline{Nu} = \frac{\bar{h}D}{K_f} \tag{4-5}$$

where $\bar{h}$, D, and K_f represent the average convection heat transfer coefficient, copper tube inner diameter, and water thermal conductivity, respectively.

$$\overline{f_r} = \frac{\Delta P}{\rho_f U_{inlet}^2} \tag{4-6}$$

where ΔP, ρ_f, and U_{inlet} denote the pressure drop along the copper tube, water density, and inlet velocity, respectively.

Table 4-1. Performance Evaluation Criterion (PEC) values for different discharge rates.

Discharge rate	$\overline{\boldsymbol{Nu}}$	$\overline{\boldsymbol{Nu}_0}$	$\overline{\boldsymbol{f}_r}$	$\overline{\boldsymbol{f}_{r0}}$	$\boldsymbol{PEC}$
1C	4.14	2.8	1.21	0.43	1.05
3C	14.47	8.20	1.21	0.43	1.25
5C	27.15	13.60	1.21	0.43	1.41

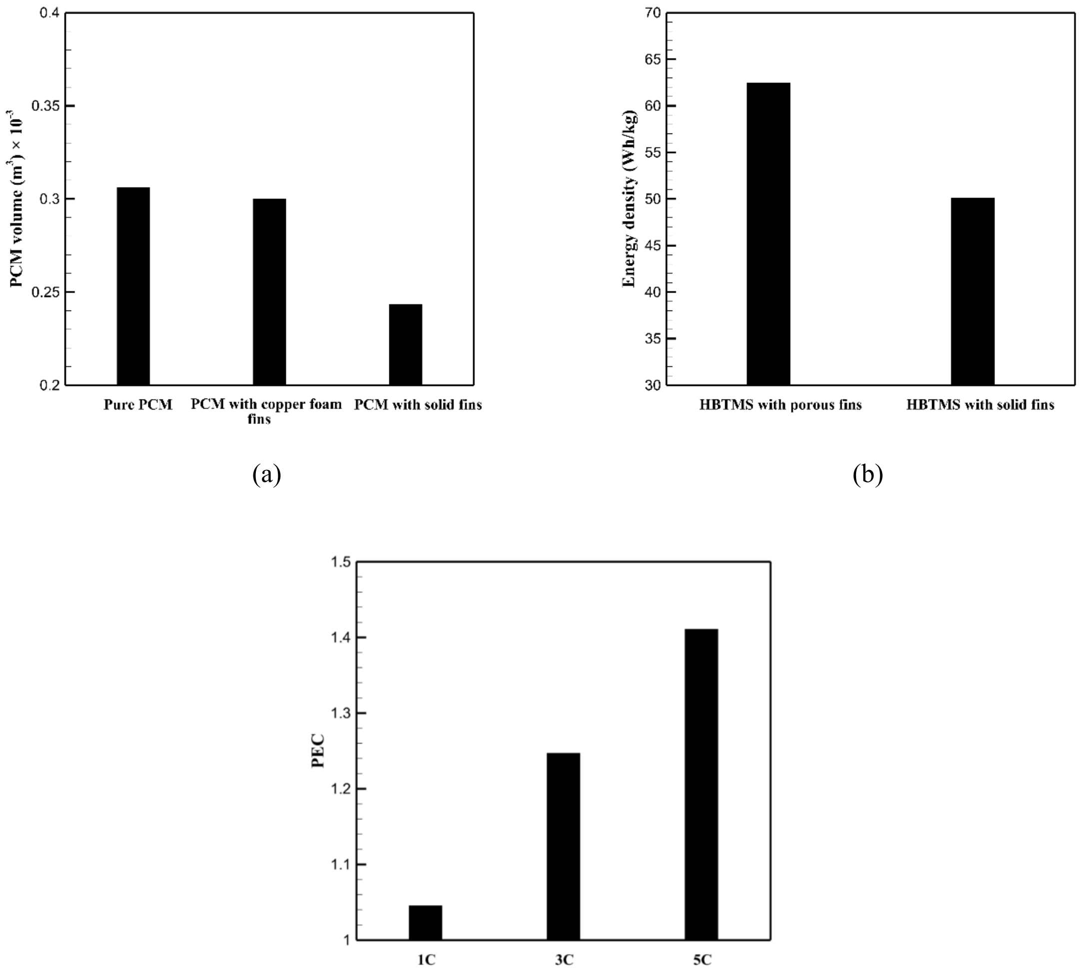

(a)

(b)

(c)

Figure 4-9. Comparison of HBTMS performance in terms of (a) the PCM volume in different fin configurations (b) energy density with different fin configurations and (c) PEC value at various discharge rates.

4.2 Copper Foam Fins Porosity and Pore Density

Porosity and pore density are key parameters of porous media that substantially affect both permeability and thermal performance. This section explores the impact of varying porosity levels (0.7, 0.8, and 0.9) and pore densities (20, 30, and 40 PPI) of the copper foam fins on the thermal behaviour and design efficiency of the proposed HBTMS during high 5C discharge. Throughout this investigation, the copper foam layers embedded within the copper tubes are kept at constant porosity and pore density values of 0.9 and 30 PPI, respectively. Four copper foam fins with thickness of 4 mm have been considered in each PCM housing. Two cooling plates with copper foam layer thickness of 2 mm within copper tubes have been considered with coolant inlet mass flow rate of 0.001 Kg/s and inlet temperature of 303.15 K. The ambient temperature is assumed to be 308.15 K.

As previously demonstrated, the incorporation of copper foam fins plays a crucial role in enhancing the thermal performance of the PCM by improving its effective thermal conductivity. The results illustrated in Figure 4-10 and Figure 4-11 demonstrate that porosity exerts a more pronounced influence on both $T_{Max,Sur}$ and L_f than pore density. As depicted in Figure 4-10 (a) reducing the porosity of the fins leads to a corresponding decrease in $T_{Max,Sur}$. Specifically, compared to a high porosity of 0.9, the $T_{Max,Sur}$ at the end of discharge is lowered by 0.18 K and 0.25 K for porosities of 0.8 and 0.7, respectively. This improvement is attributed to the increased copper content and reduced void space in lower porosity fins, which provide more effective heat conduction pathways within the PCM. In contrast, as shown in Figure 4-11 (a), higher porosity fins, characterised by larger voids, contain more PCM within the pores, resulting in higher L_f values. At the end of discharge, L_f is approximately 22% and 7% greater for porosities of 0.9 and 0.8, respectively, in comparison to a porosity of 0.7. Furthermore, the onset of PCM melting occurs earlier with lower porosity fins. For instance, under a 5C discharge rate, the melting process begins at 495 seconds for a porosity of 0.7, which is 22 and 31 seconds earlier than the onset times observed for porosities of 0.8 and 0.9, respectively, due to more effective heat conduction pathways.

The influence of pore density on system performance is illustrated in Figure 4-10 (b) and Figure 4-11 (b) which show that variations in pore density have a minimal effect on both $T_{Max,Sur}$ and L_f. As porosity was held constant, the total volume of metal remained unchanged across different pore densities. At a lower pore density of 20 PPI, there are fewer pores per unit length, requiring larger metal ligaments to maintain the same overall porosity. This configuration provides improved thermal conductivity due to the increased metal cross-sectional area. Conversely, at a higher pore density of 40 PPI, the PCM is distributed among a greater number of smaller pores, enhancing heat transfer through more extensive encapsulation. These competing effects, greater conduction paths at lower PPI and enhanced PCM distribution at higher PPI, tend to balance each other, resulting in a negligible net impact on both temperature and PCM melting behaviour. Furthermore, since porosity remains constant, the volume fraction of PCM does not vary across different pore density configurations.

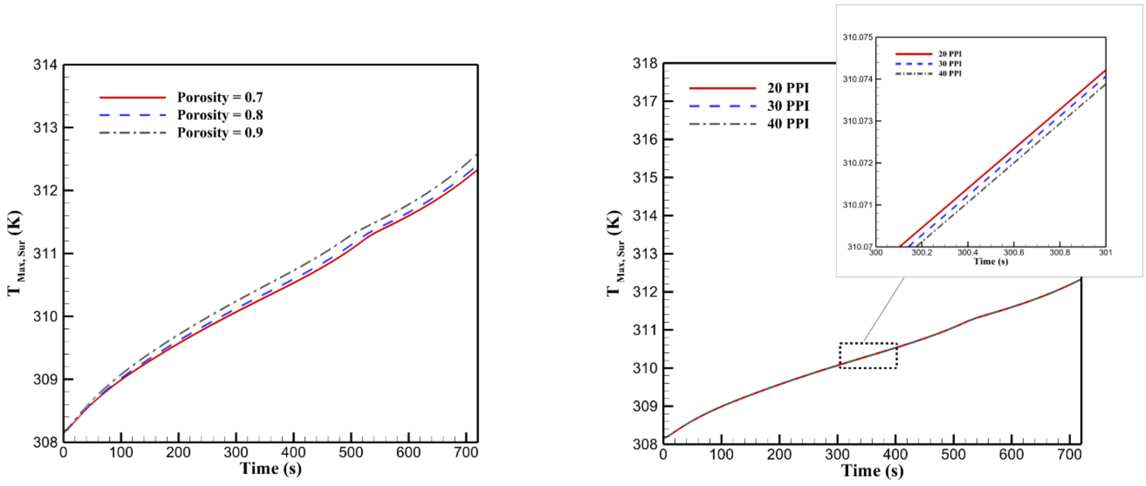

(a) (b)

Figure 4-10. Effect of copper foam fin properties on maximum battery surface temperature in terms of (a) porosity and (b) pore density.

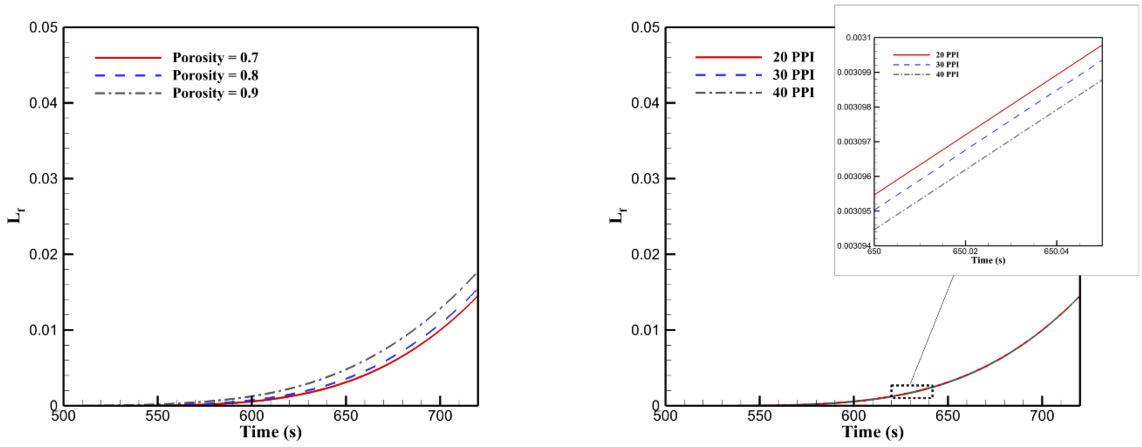

(a) (b)

Figure 4-11. Effect of copper foam fin properties on PCM liquid fraction in terms of (a) porosity and (b) pore density.

As depicted in Figure 4-12, the $\overline{Nu}_b$ is more strongly influenced by porosity than by pore density. Figure 4-12 (a) shows that following the onset of PCM melting lower porosity in the copper foam fins leads to a higher $\overline{Nu}_b$. This enhancement is attributed to improved thermal conduction and intensified pore-scale convection, both of which contribute to more effective heat transfer. By the end of the 5C discharge, the $\overline{Nu}_b$ increased by 33% and 52% for porosities of 0.8 and 0.7, respectively, in comparison to a porosity of 0.9. In contrast, as seen in Figure 4-12 (b), when porosity is held constant, changes in pore density have a negligible effect on the average Nusselt number. This outcome aligns with the previously observed minimal impact of pore density on PCM melting behaviour and battery surface temperature.

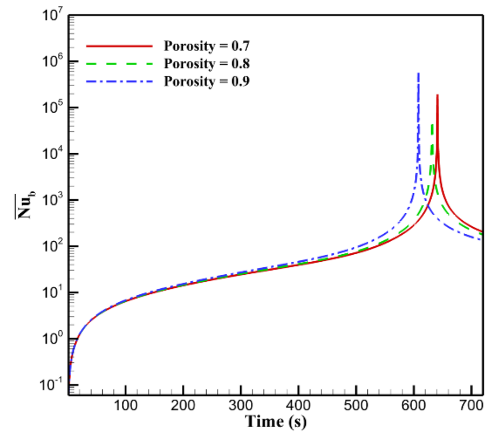

(a) (b)

Figure 4-12. Effect of copper foam fin properties on the average Nusselt number on the battery surface in terms of (a) porosity and (b) pore density.

At the end of the 5C discharge, the thermal state of individual battery cells within the module, illustrated in Figure 4-13, shows consistent trends in both $T_{Max,Sur}$ and $\Delta T_{Max,b}$ across different copper foam fin porosities, with lower values observed for the lower porosity of 0.7. Battery cells located near the inlet and toward the centre of the module exhibited lower $T_{Max,Sur}$ values. In contrast, higher $\Delta T_{Max,b}$ values were found in cells situated at the module's side, namely batteries 1, 4, 5, 8, 9, and 12, due to their reduced exposure to the effects of liquid cooling. Furthermore, as shown in Figure 4-13, variations in pore density had negligible influence on both $T_{Max,Sur}$ and $\Delta T_{Max,b}$, suggesting that pore density plays a limited role in affecting these thermal performance metrics.

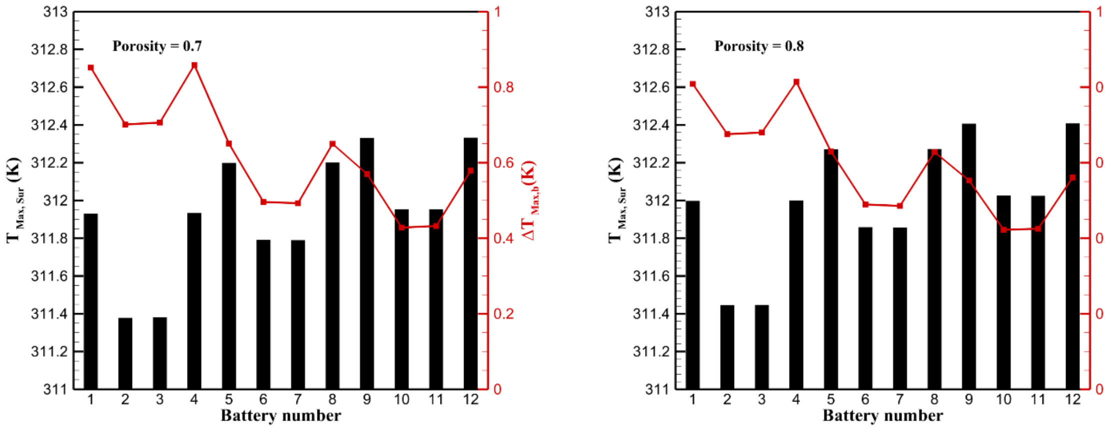

Porosity = 0.7 Porosity = 0.8

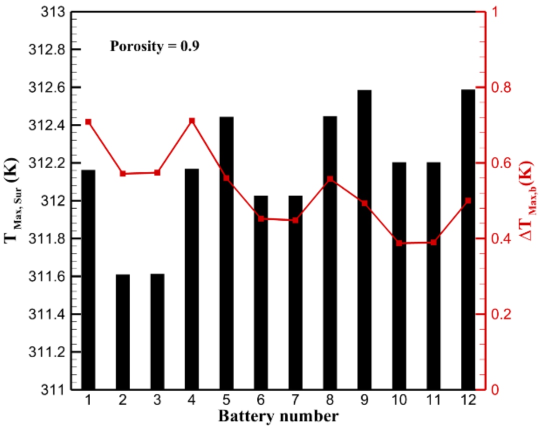

Porosity = 0.9
(a)

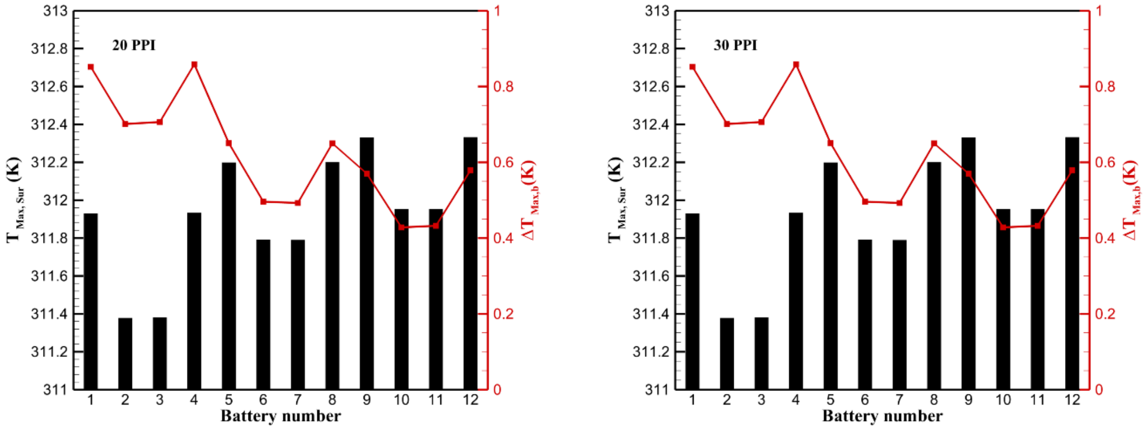

20 PPI 30 PPI

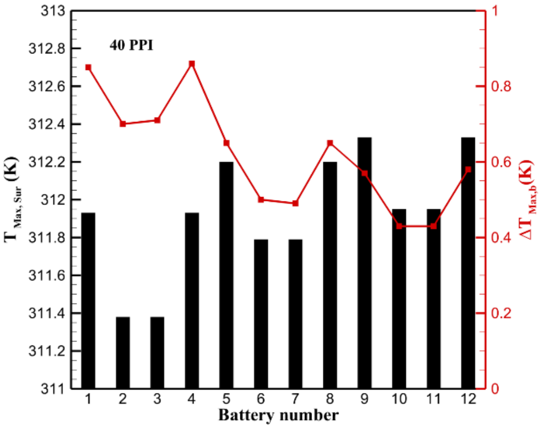

40 PPI
(b)

Figure 4-13. $T_{Max,Sur}$, $\Delta T_{Max,b}$ at the end of 5C discharge for the HBTMS with different copper foam fins' (a) porosity and (b) pore density.

With respect to the influence of copper foam fins' porosity on PCM volume, Figure 4-14 (a) indicates that an increase in porosity slightly raises the PCM volume, as higher porosity levels provide more void space to accommodate PCM. Relative to a porosity of 0.7, PCM volume increased by approximately 4% and 25% for porosities of 0.8 and 0.9, respectively. Conversely, as shown in Figure 4-14 (b), the energy density of the system is more substantially affected by porosity. Lower porosity fins contain a greater amount of copper, which contributes to higher system weight due to copper's higher density, thus reducing energy density. Consequently, adopting copper foam fins with higher porosity, when compared to a porosity of 0.7, leads to an increase in energy density of about 3% and 6% for porosities of 0.8 and 0.9, respectively.

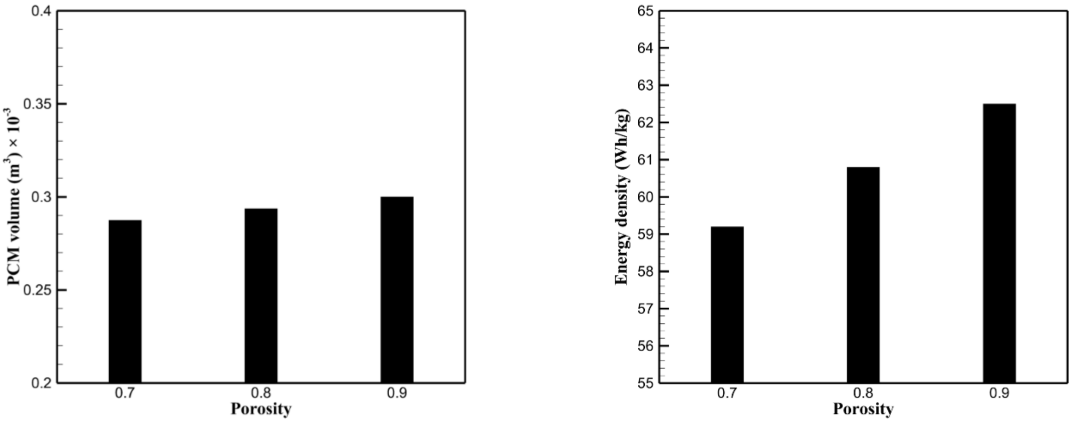

(a) (b)

Figure 4-14. Comparison of (a) PCM volume and (b) energy density for HBTMS with different copper foam fins' porosity.

4.3 Copper Foam Layer Porosity and Pore Density Within the Copper Tube

As established in the preceding sections, the HBTMS configuration incorporating liquid cooling with a copper foam layer demonstrated superior effectiveness. Accordingly, this section focuses on investigating the influence of the copper foam layer's properties within the copper tube, specifically porosity (0.7, 0.8, and 0.9) and pore density (20, 30, and 40 PPI), on the system's cooling performance during high 5C discharge. For the purpose of this analysis, the porosity and pore density of the copper foam fins were maintained at constant values of 0.9 and 30 PPI, respectively. Four copper foam fins with thickness of 4 mm have been considered in each PCM housing. Two cooling plates with copper foam layer thickness of 2 mm within copper tubes have been considered with coolant inlet mass flow rate of 0.001 Kg/s and inlet temperature of 303.15 K. The ambient temperature is assumed to be 308.15 K.

As illustrated in Figure 4-15 (a), in contrast to the effect observed with copper foam fins (Figure 4-10 (a)), increasing the porosity of the copper foam layer results in a reduction in the

$T_{Max,Sur}$. At the end of the 5C discharge, $T_{Max,Sur}$ is reduced by approximately 0.1 K and 0.16 K for porosities of 0.8 and 0.9, respectively, compared to a porosity of 0.7. A higher porosity introduces more voids within the copper foam, which, as shown in Figure 4-16 (a) facilitates greater penetration and flow of the cooling fluid through the copper foam layer. Consequently, as more liquid permeates the copper foam, the velocity of the fluid in the clear region of the copper tube decreases. Compared to a porosity of 0.7, the maximum dimensionless velocity in the clear region drops by approximately 42% and 50% for porosities of 0.8 and 0.9, respectively. The enhanced fluid penetration at higher porosities promotes increased mixing near the copper tube wall, thereby improving convective heat transfer. The comparison of dimensionless temperature profiles for the solid phase at various porosities, shown in Figure 4-16 (b) reveals that the lower porosity of 0.7 results in a higher solid-phase temperature due to the improved effective thermal conductivity of the denser porous matrix. However, the dimensionless temperature of the liquid phase within the copper foam layer is highest at a porosity of 0.9, indicating more effective heat removal from the copper tube surface at higher porosity levels.

Local Nusselt number in the copper foam layer is defined as follows [315]:

$$Nu = -\frac{D}{(T_{Solid\ phase} - T_{bulk})}\frac{\partial T}{\partial y}\bigg|_{w} \tag{4-7}$$

The aforementioned enhancement in heat transfer is reflected in the local Nusselt number in the copper foam layer due to improved convection along the copper foam layer, as shown in Figure 4-16 (c), the local Nusselt number increases by approximately 24% and 73% for porosities of 0.8 and 0.9, respectively, compared to a porosity of 0.7. This improvement facilitates more effective heat transfer generated by the battery to the cooling fluid, thereby contributing to the reduction of $T_{Max,Sur}$.

The influence of pore density variations in the copper foam layers on $T_{Max,Sur}$ is illustrated in Figure 4-15 (b). In contrast to porosity, higher pore density leads to an increase in $T_{Max,Sur}$. During the discharge, the maximum difference in $T_{Max,Sur}$ for 30 PPI and 40 PPI compared to 20 PPI was 0.14 K and 0.25 K, respectively. However, this difference is primarily observed before the onset of PCM melting. After approximately 500 seconds, copper foam layers with varying pore densities yield nearly identical $T_{Max,Sur}$ values.

This behaviour can be explained by the fact that, at constant porosity, higher pore densities result in smaller pore sizes, which impede the flow of cooling fluid through the copper foam layer. As highlighted in Figure 4-17 (a) the dimensionless velocity within the copper foam layer decreases with increasing pore density, with the 40 PPI configuration exhibiting a lower velocity than the 20 PPI case. Additionally, as observed for porosity, the fluid velocity in the clear region of the copper tube increases with higher pore density. Figure 4-17 (b) indicates that the restricted flow reduces the efficiency of heat transfer from the battery to the coolant, leading to elevated surface temperatures. Despite the increase in available surface area associated with higher pore density, the diminished fluid flow reduces the overall effectiveness of convective heat transfer.

Moreover, Figure 4-17 (b) indicates that changes in pore density exert minimal influence on the local temperature distribution, particularly in the clear region of the copper tube. While the 20 PPI copper foam layer achieves a higher heat transfer rate owing to enhanced fluid penetration, it provides a smaller effective heat transfer area than the 40 PPI configuration, due to the lower number of pores within the same length. These competing effects result in only a limited difference in the local temperature. As shown in Figure 4-17 (c), variations in pore density induce only slight changes in the local Nusselt number along the copper foam layer. Although increasing pore density at constant porosity maintains similar heat conduction pathways, it reduces convective heat transfer owing to decreased permeability. Consequently, the local Nusselt number diminishes with higher pore density.

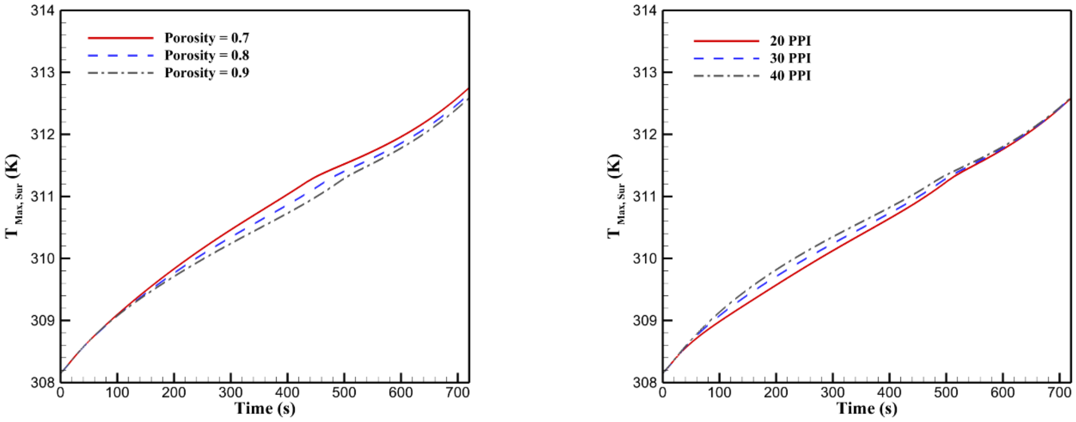

(a) (b)

Figure 4-15. Effect of copper foam layer properties on maximum battery surface temperature in terms of (a) porosity and (b) pore density.

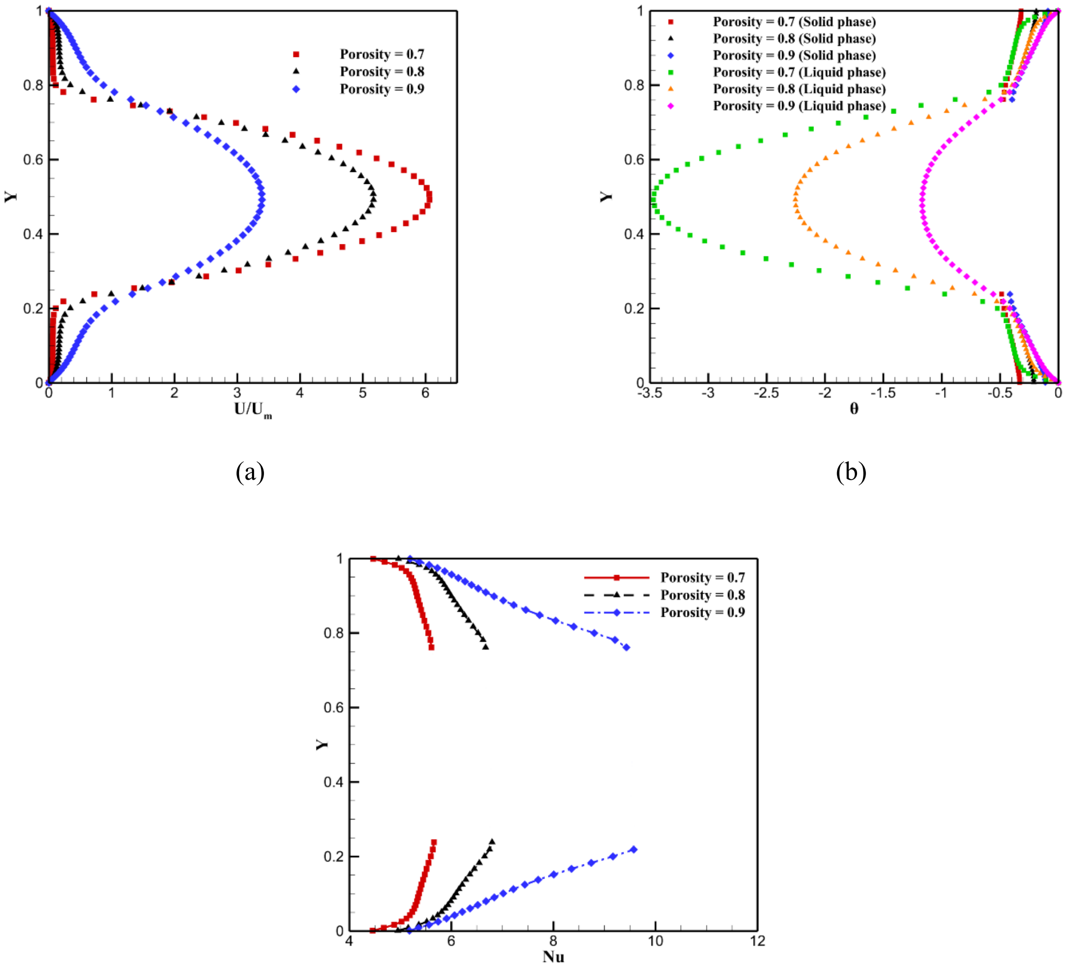

(a) (b)

(c)

Figure 4-16. Effect of copper foam layer porosity on (a) dimensionless velocity, (b) dimensionless temperature, and (c) local Nusselt number at the middle of the copper tube along the vertical axis at the end of 5C discharge rate.

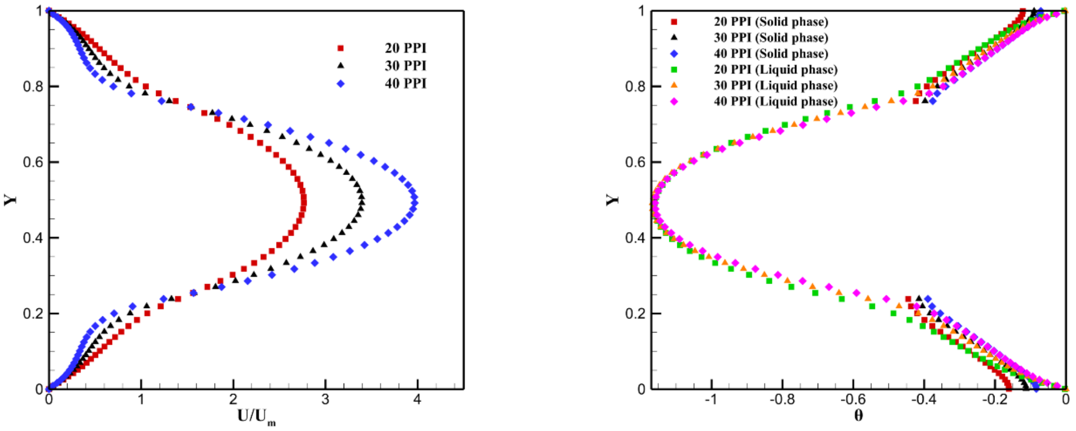

(a) (b)

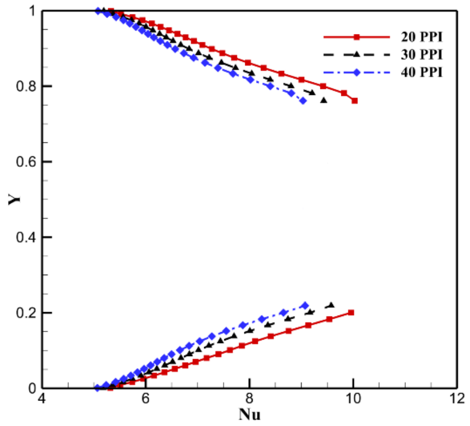

(c)

Figure 4-17. Effect of copper foam layer pore density on (a) dimensionless velocity, (b) dimensionless temperature, and (c) local Nusselt number at the middle of the copper tube along the vertical axis at the end of 5C discharge rate.

As depicted in Figure 4-18, porosity variations in the copper foam layers exhibit a more substantial influence on the L_f than changes in pore density. Reduction in the heat transfer enhancement capability of the copper foam layers in the copper tube leads to increased heat absorption by the PCM, resulting in more pronounced PCM melting. Figure 4-18 (a) demonstrates that the onset of PCM melting is significantly affected by porosity of the copper foam layer in the copper tube; relative to a porosity of 0.7, melting was delayed by 58 seconds and 34 seconds for porosities of 0.8 and 0.9, respectively. In contrast, an inverse trend was observed with changes in pore density, where higher pore densities led to an earlier initiation of PCM melting.

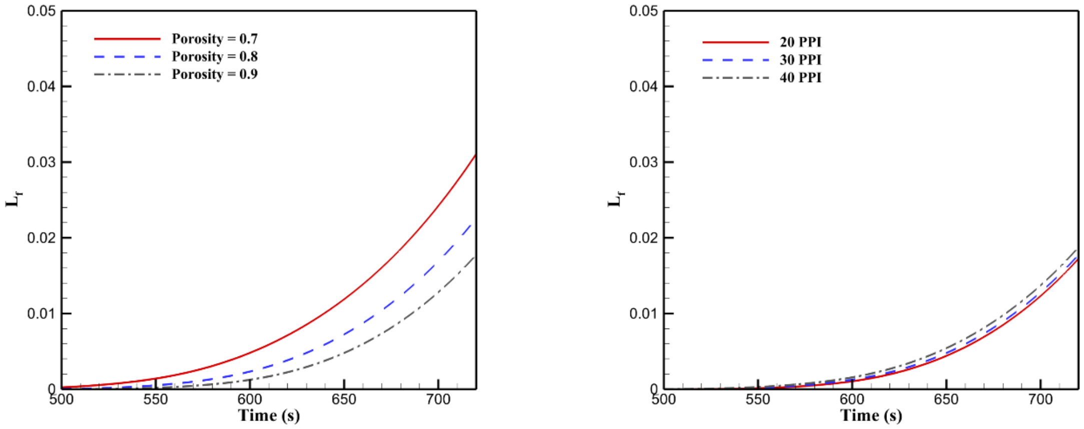

(a) (b)

Figure 4-18. Effect of copper foam layer properties on PCM liquid fraction in terms of (a) porosity and (b) pore density.

Figure 4-19 illustrates the influence of the copper foam layers' porosity and pore density on the $\overline{Nu}_b$. As depicted, higher porosity enhances heat transfer performance, resulting in increased Nusselt numbers, particularly after the initiation of PCM melting. At the end of discharge, porosities of 0.9 and 0.8 yield approximately 31% and 16% higher Nusselt numbers, respectively, compared to a porosity of 0.7. In contrast, pore density exhibits a weaker effect on the Nusselt number, which shows a decreasing trend with increasing pore density. Specifically, at the end of the discharge, the $\overline{Nu}_b$ declines by roughly 1% and 3% for pore densities of 30 PPI and 40 PPI, respectively, in comparison to 20 PPI.

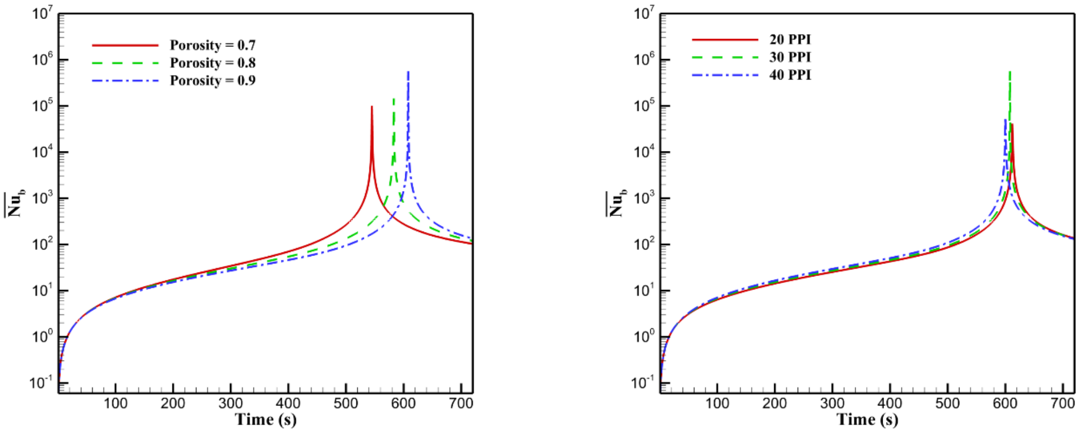

(a) (b)

Figure 4-19. Effect of copper foam layer properties on the average Nusselt number on the battery surface in terms of (a) porosity and (b) pore density.

Figure 4-20 presents the $T_{Max,Sur}$ and $\Delta T_{Max,b}$ values for individual battery cells at the end of the 5C discharge. As in earlier observations, the central battery cells, located adjacent to the liquid cooling tube, exhibit lower $T_{Max,Sur}$. In contrast, batteries 9 and 12, positioned in the last row, experience the highest $T_{Max,Sur}$. Regarding $\Delta T_{Max,b}$, battery cells situated along the sides of the module display greater temperature difference. This trend remains consistent across various porosity and pore density configurations, underscoring that the thermal performance of battery cells is more strongly influenced by their location within the module and the local cooling conditions than by variations in the copper foam layer structure.

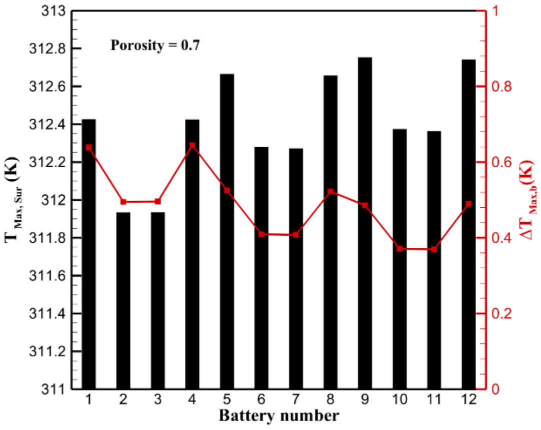

Porosity = 0.7

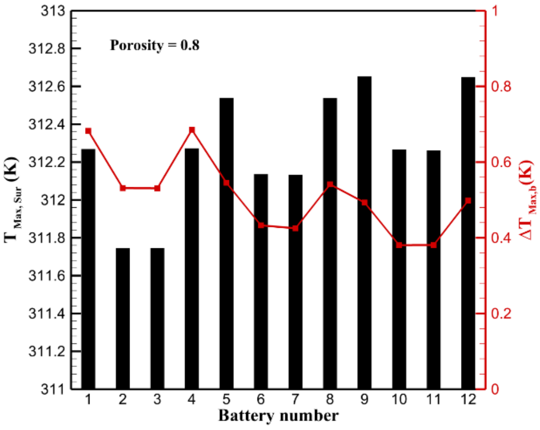

Porosity = 0.8

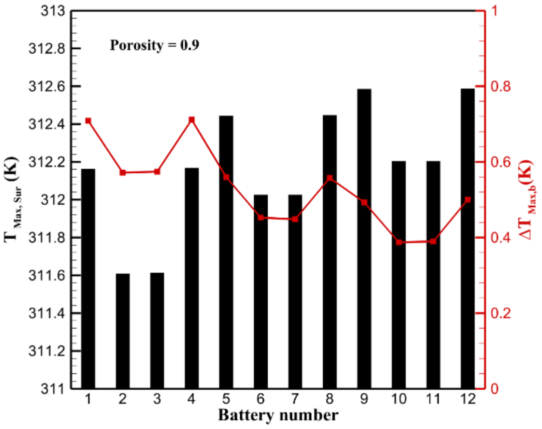

Porosity = 0.9

(a)

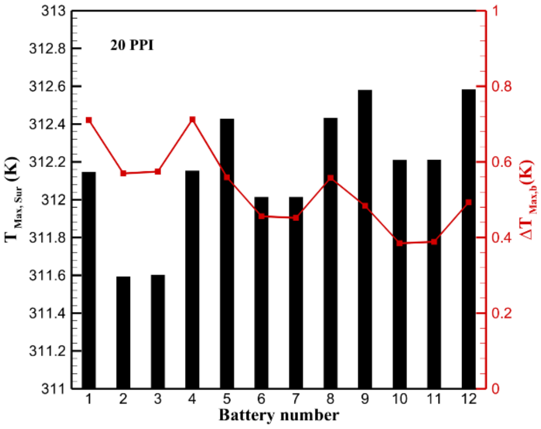

20 PPI

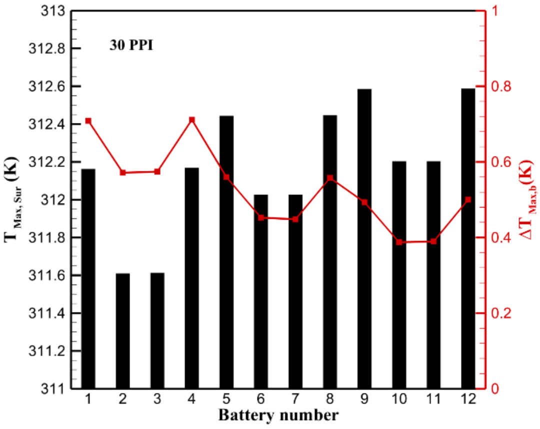

30 PPI

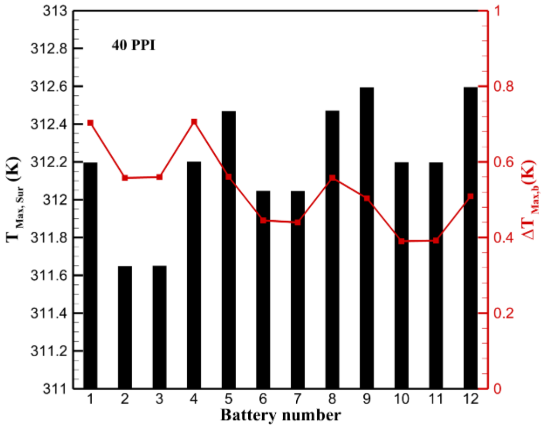

40 PPI

(b)

Figure 4-20. $T_{Max,Sur}$, $\Delta T_{Max,b}$ for the HBTMS with different copper foam layers' (a) porosity and (b) pore density at the end of 5C discharge rate.

To evaluate the trade-off between the increased pressure drop and enhanced heat transfer provided by the copper foam layers within the copper tube, the PEC values for various porosities and pore densities are presented in Figure 4-21. At a lower porosity of 0.7, as shown in Figure 4-21 (a), the elevated pressure drop exceeds the benefits of improved heat transfer, resulting in a PEC value below one. This outcome suggests that employing copper foam layers with low porosity is suboptimal. In contrast, for higher porosities of 0.8 and 0.9, the PEC values increase by 53% and 114%, respectively, relative to a porosity of 0.7, and exceed unity, indicating more favourable performance. At a fixed copper foam layer porosity of 0.9, as illustrated in Figure 4-21 (b), the maximum PEC value is observed at a pore density of 30 PPI, approximately 12% and 8% higher than those for 20 PPI and 40 PPI, respectively. These findings highlight that optimising the combination of pore density and porosity within the copper foam layer can effectively balance pressure loss and heat transfer enhancement.

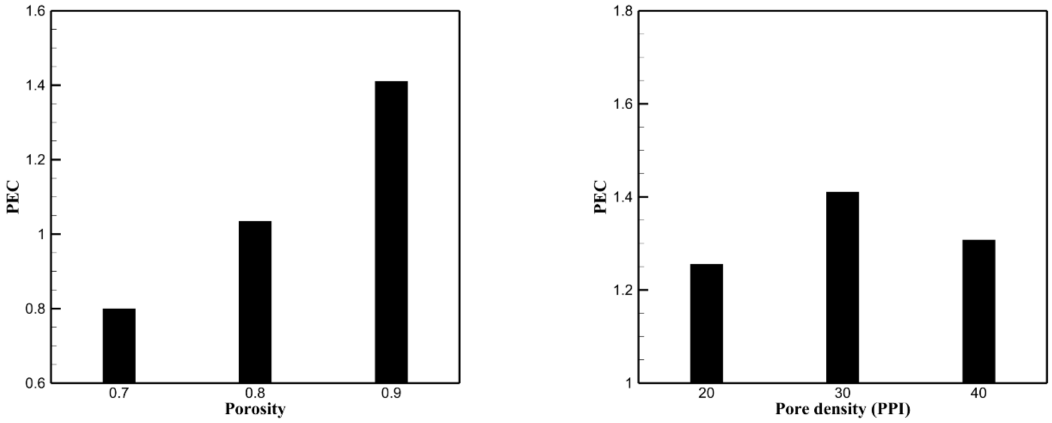

(a) (b)

Figure 4-21. Effect of copper foam layer properties on PEC in terms of (a) porosity and (b) pore density at the end of 5C discharge rate.

As shown in Figure 4-22, the energy density of the system increases proportionally with the porosity of the copper foam layers. Increasing the porosity from 0.7 to 0.8 and 0.9 leads to improvements in energy density of approximately 1.3% and 2.8%, respectively. This improvement is attributed to the greater void volume associated with higher porosity, which reduces the total system weight. As the mass decreases without affecting the energy storage capability, the energy density correspondingly improves.

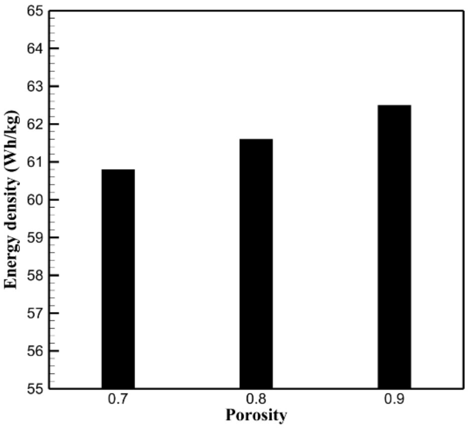

Figure 4-22. Comparison of energy density for HBTMS with different copper foam layers' porosity.

In practical applications, the limited influence of pore density on thermal performance indicates that the choice of metal foams with different pore densities, when porosity is held constant, is more likely governed by considerations such as mechanical integrity, ease of fabrication, and cost-effectiveness, rather than thermal efficiency [316]. Although copper foam fins with lower porosity typically offer improved thermal conductivity and thus enhanced heat transfer, those with higher porosity are generally preferred for their capacity to elevate energy density, an important criterion for effective system design. The marginal decrease in thermal performance associated with higher porosity is compensated by the benefits of reduced system weight and increased energy efficiency. Similarly, copper foam layers with higher porosity facilitate better coolant flow and more effective heat dissipation, whereas higher pore density, while increasing surface area, may impede fluid flow and marginally diminish heat transfer efficiency. Therefore, achieving an optimal balance between porosity and pore density in the copper foam layer is essential for maximising system performance. Based on the results obtained, copper foam layers with higher porosity are recommended due to their superior energy density and enhanced thermal regulation, making them especially suitable for applications where both performance and efficiency are paramount.

4.4 Quantity of Copper Foam Fins and Thickness

This section investigates the impact of varying the quantity of copper foam fins (4, 6, and 8) with a fixed thickness of 4 mm, as well as the effect of different copper foam fin thicknesses (2, 4, and 6 mm) for a constant fin quantity of 4, on the thermal behaviour and design efficiency of the proposed HBTMS during high 5C discharge. Throughout this study, the porosity and pore density for both the copper foam fins and the copper foam layers within the copper tubes are maintained at constant values of 0.9 and 30 PPI, respectively. Two cooling plates are configured with copper foam layers of 2 mm thickness inside the copper tubes. The coolant inlet mass flow rate and temperature are fixed at 0.001 kg/s and 303.15 K, respectively, while the ambient temperature is also maintained at 308.15 K.

The influence of the quantity and thickness of copper foam fins on the $T_{Max,Sur}$ during the 5C discharge is presented in Figure 4-23. As shown in Figure 4-23 (a), increasing either the quantity or the thickness of the copper foam fins leads to a reduction in $T_{Max,Sur}$. Compared to the case with pure PCM, where $T_{Max,Sur}$ reaches 321.77 K, the addition of 4, 6, and 8 copper foam fins results in reductions of 2.85%, 2.94%, and 3.06%, respectively. Similarly, as illustrated in Figure 4-23 (b), increasing the thickness of the copper foam fins also enhances thermal performance. For fin thicknesses of 2, 4, and 6 mm, $T_{Max,Sur}$ is reduced by 2.65%, 2.85%, and 2.93%, respectively, compared to the pure PCM. The observed improvements are attributed to the increased heat transfer surface area provided by additional or thicker fins, which facilitates enhanced thermal conduction. This improvement is particularly significant due to the inherently low thermal conductivity of PCM. Furthermore, the presence of copper foam fins with higher quantity or thickness promote pore-scale convection after the onset of PCM melting, thereby further enhancing the thermal performance of the HBTMS.

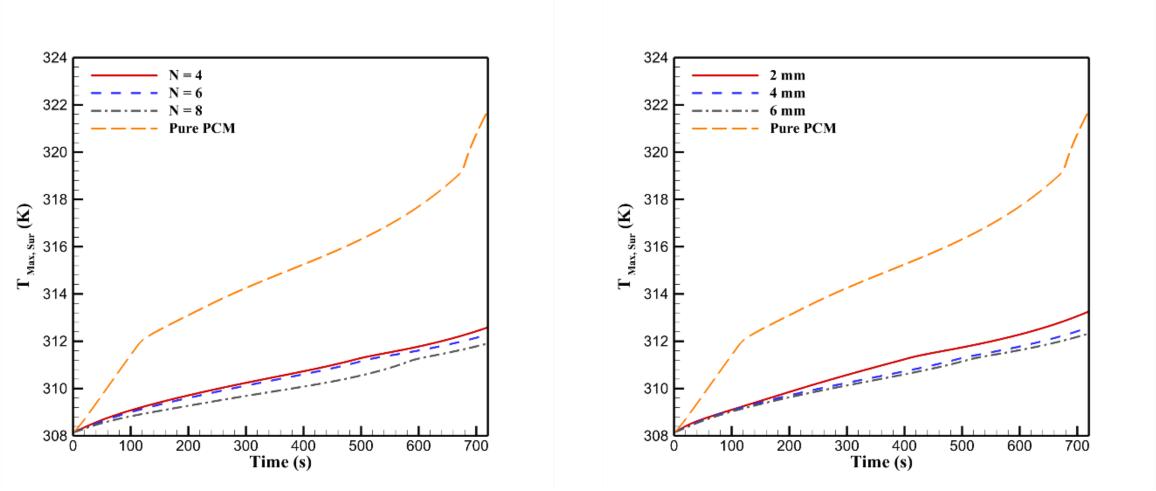

(a) (b)

Figure 4-23. Impact of the different (a) quantity and (b) thickness of copper foam fins on batteries maximum surface temperature.

As illustrated in Figure 4-24 and Figure 4-25, the PCM melting pattern is significantly influenced by both the quantity and thickness of copper foam fins. According to Figure 4-24 (a), introducing copper foam fins caused a noticeable delay in the onset of PCM melting. Compared to the pure PCM, the initiation of melting was delayed by 382 s, 394 s, and 469 s when using 4, 6, and 8 copper foam fins, respectively. Additionally, L_f at the end of discharge was reduced by 93.92%, 88.97%, and 94.47% for 4, 6, and 8 copper foam fins, respectively, compared to pure PCM. This behaviour can be explained by the dual role of copper foam fins in heat conduction and PCM melting. Increasing the quantity of fins from 4 to 6 enhances the effective thermal conductivity of the system, allowing more uniform heat distribution and thus promoting greater PCM melting. However, when 8 fins are employed, the rate of heat conduction to the PCM housing increases significantly. As a result, a larger portion of the generated heat is conducted directly to the PCM housing rather than being absorbed by the PCM to undergo the phase change process. This phenomenon is further evidenced by the PCM liquid fraction contour plots in Figure 4-25 (a) to (c). A considerable amount of PCM melting is observed around batteries 9 and 12 when 6 fins are used (Figure 4-25 (b)). In contrast, increasing the fin quantity to 8 reduces PCM melting around the batteries in the first row (batteries 1 to 4), where no PCM melting occurs, as shown in Figure 4-25 (c). This is attributed to the improved heat conduction through the additional fins, which conduct heat more efficiently to the cooling plates. Furthermore, the batteries positioned in the first row benefit from their proximity to the coolant inlet, where lower inlet temperatures contribute to enhanced cooling performance.

Similar to the effect of the quantity of copper foam fins, the thickness of the fins also plays a significant role in influencing PCM melting behaviour, as illustrated in Figure 4-24 (b). Compared to pure PCM, the onset of PCM melting was delayed by 293 s, 382 s, and 393 s when using copper foam fins with thicknesses of 2 mm, 4 mm, and 6 mm, respectively. Additionally, the L_f at the end of discharge decreased by 82.36%, 93.91%, and 88.86% for 2 mm, 4 mm, and 6 mm fins, respectively. As depicted in Figure 4-25 (d), the melting pattern for 2 mm thick copper foam fins are not confined to the PCM located within the fins. Due to the limited conduction path provided by the thin fins, the generated heat is not effectively transferred to the PCM housing. Consequently, PCM melting extends beyond the fins to the region surrounding the battery housing, forming an unfavourable melting pattern. This leads to the accumulation of melted PCM in areas that act as thermal insulation rather than contributing to heat absorption. This phenomenon is particularly noticeable around batteries 9 to 12. With increased fin thickness, as shown in Figure 4-25 (e) and (f), PCM melting becomes more localised within the fins, and no melting is observed around the battery housing, even for cells in the last row. Furthermore, Figure 4-24 (b) reveals that at the end of discharge, a greater amount of PCM has melted in the 6 mm fin configuration compared to the 4 mm. However, the 4 mm thick fins appear to offer better thermal performance overall, achieving a more favourable balance between the heat conducted through the fins and the heat absorbed by the PCM. In contrast, with the 6 mm thick fins, the increased contact area between the copper foam and PCM facilitates enhanced heat absorption, resulting in more PCM melting, particularly near the outer side of the battery module, as confirmed by the PCM liquid fraction contours in Figure 4-25 (e) and (f).

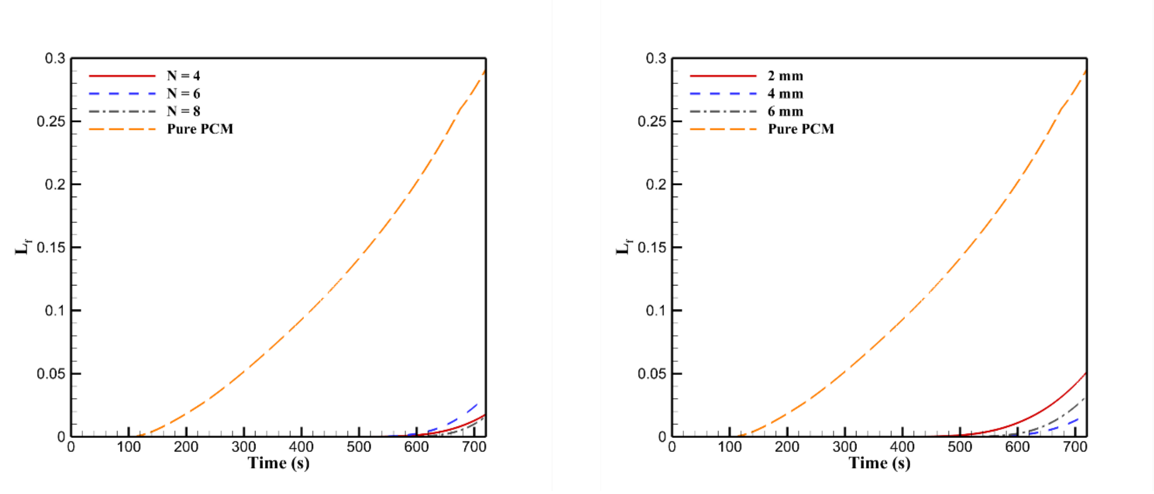

(a) (b)

Figure 4-24. Impact of the different (a) quantity and (b) thickness of copper foam fins on PCM liquid fraction.

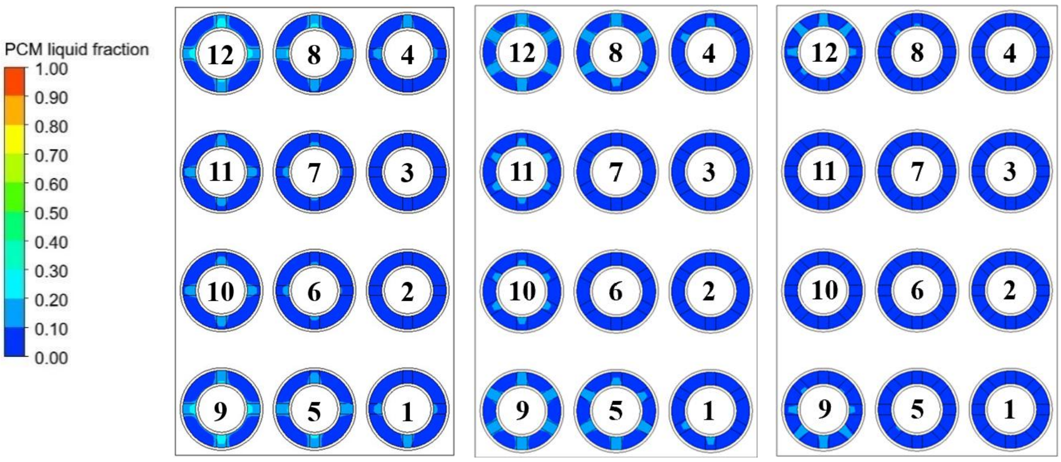

(a) 4 fins (b) 6 fins (c) 8 fins

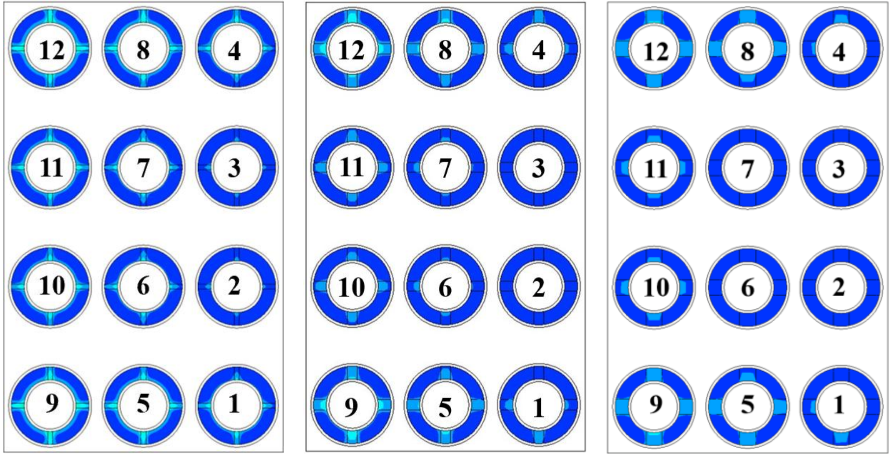

(d) 2 mm (e) 4 mm (f) 6 mm

Figure 4-25. PCM liquid fraction contour plots for the HBTMS at the end of the 5C discharge, showing the effect of copper foam fin quantity with (a) 4 fins, (b) 6 fins, and (c) 8 fins, and fin thickness with (d) 2 mm, (e) 4 mm, and (f) 6 mm.

The influence of varying copper foam fins quantity and thickness on the thermal performance of the HBTMS, in terms of the $\overline{Nu_b}$, is illustrated in Figure 4-26. As shown in Figure 4-26 (a), the inclusion of copper foam fins delays the occurrence of the peak in $\overline{Nu_b}$ during discharge, compared to the case with pure PCM. This delay is attributed to the postponed onset of PCM melting when copper foam fins are employed, which results in the battery surface temperature rising beyond the PCM melting temperature at a later stage. At the end of the discharge, $\overline{Nu_b}$ is significantly enhanced relative to pure PCM. Specifically, improvements of 13.11, 19.61, and 144.06 times are observed for systems incorporating 4, 6, and 8 copper foam fins, respectively. A similar effect, as illustrated in Figure 4-26 (b), was observed for copper foam fins of varying thicknesses. Due to enhanced conduction and pore scale convection provided by thicker fins, the $\overline{Nu_b}$ increased significantly compared to pure PCM, with values rising by 6.88, 13.12, and 18.45 times by the end of discharge, respectively.

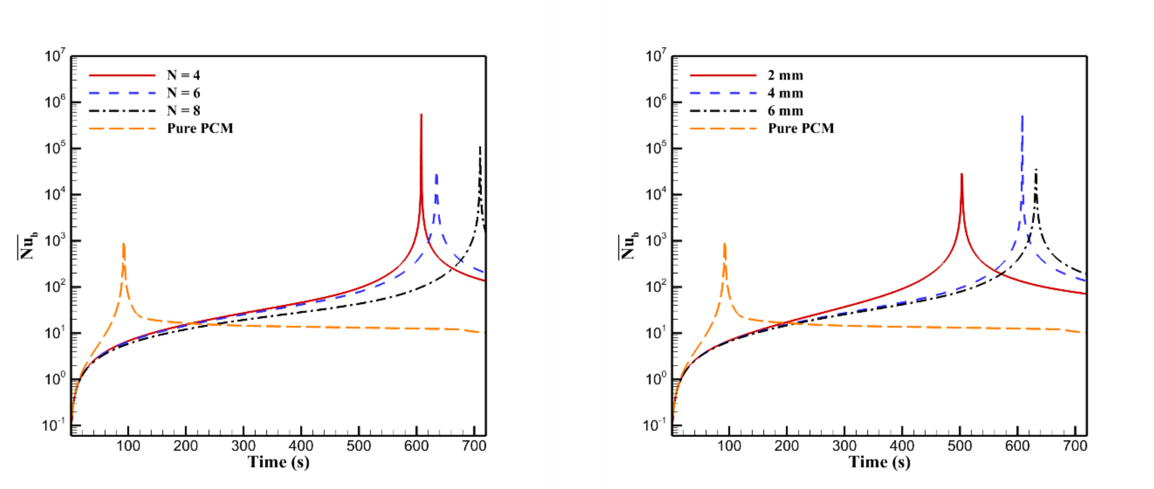

(a) (b)

Figure 4-26. Battery surface average Nusselt number for HBTMS with different (a) quantity and (b) thickness of copper foam fins.

The ΔT_{Max} for varying numbers and thicknesses of copper foam fins is presented in Figure 4-27. Referring to the PCM melting onset shown in Figure 4-24, Figure 4-27 (a) illustrates that for different numbers of copper foam fins, ΔT_{Max} generally increases during discharge until the onset of PCM melting. The highest ΔT_{Max} of 2.1 K is observed for the configuration with 8 fins, attributed to the delayed melting of the PCM in this case. However, this temperature difference reduces to 1.4 K by the end of the discharge. Among the investigated configurations, the case with 6 copper foam fins demonstrates the most thermal uniformity, with a peak ΔT_{Max} of 1.75 K at 508 s, which declines to 1.2 K by the end of discharge. In contrast, the configuration with 4 copper foam fins shows a higher ΔT_{Max} of 1.5 K at the end of the discharge. In terms of copper foam fin thickness, Figure 4-27 (b) shows that the 2 mm configuration exhibits less pronounced variations in ΔT_{Max} during discharge, reaching a peak of 1.4 K at 417 s, which decreases to 1.2 K by the end of the discharge. This smoother thermal behaviour is consistent with the greater PCM melting observed in Figure 4-24 (b). Conversely, the 4 mm configuration results in the highest ΔT_{Max} during discharge, peaking at 2 K at 506 s and settling at 1.6 K by the end of the discharge. These observations are closely linked to the PCM melting pattern, the development of effective conduction paths, and the enhancement of pore scale convection. They underscore the critical role of managing PCM melting dynamics through the combined application of copper foam fins and liquid cooling to optimise the thermal performance of the HBTMS.

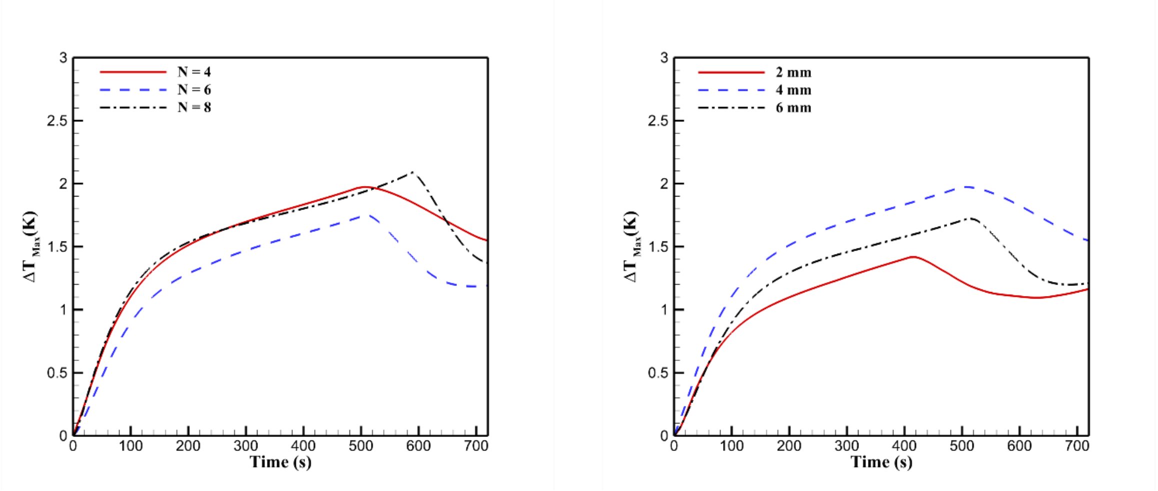

(a) (b)

Figure 4-27. Maximum temperature difference within the battery module for HBTMS with different (a) quantity and (b) thickness of copper foam fins.

The battery level thermal performance of the HBTMS, in terms of each battery's $T_{Max,Sur}$ and $\Delta T_{Max,b}$, is presented in Figure 4-28 for various copper foam fins quantity and thicknesses at the end of the 5C discharge. As shown in Figure 4-28 (a), (b), and (c), increasing the quantity of copper foam fins generally results in a reduction in $\Delta T_{Max,b}$ across all batteries. The lowest $\Delta T_{Max,b}$ values were observed for batteries 2 and 3, which are surrounded by copper tubes embedded in the cooling plates and positioned near the coolant inlet. In contrast, the highest $\Delta T_{Max,b}$ values were recorded for batteries 9 and 12, located on the outer side of the last row. These cells are exposed to the elevated coolant temperatures after it has passed through upstream batteries, and they are cooled predominantly from only one side by the copper tubes. A similar trend is observed for different copper foam fin thicknesses, as depicted in Figure 4-28 (e), (f), and (g). Increasing the fin thickness results in a reduction in $\Delta T_{Max,b}$ for each battery, with the lowest and highest values recorded for batteries 2 and 3, and 9 and 12, respectively. As shown in Figure 4-28, for all copper foam fin configurations, the $\Delta T_{Max,b}$ remains below 1 K. The highest $\Delta T_{Max,b}$ values are observed for batteries 1 and 4 in the first row. Although these batteries benefit from the relatively low inlet coolant temperature, their placement at the sides of the battery module results in only one side being adjacent to the copper tubes, leading to more pronounced temperature differences. With increasing the copper foam fins quantity, $\Delta T_{Max,b}$ is highest in the first row and decreases progressively in the second and third rows, owing to the rise in coolant temperature along the copper tube from inlet to outlet. This effect is particularly evident in the configuration with 8 copper foam fins, where $\Delta T_{Max,\,b}$ exceeds 0.8 K in the first row but drops below 0.6 K in the subsequent rows. The enhanced conduction pathways provided by the increased quantity of fins allow the heat generated by the first-row batteries to be transferred more effectively to the housing and cooling plates, where it is dissipated by the liquid cooling system. A similar fluctuation pattern in $\Delta T_{Max,b}$ is observed across different fin thicknesses, with a slight increase in $\Delta T_{Max,b}$ for thicker fins. Additionally, for all copper foam fins quantity and thicknesses, batteries 2, 3, 6, 7, 10, and 11, each of which is enclosed on both sides by copper tubes in the cooling plates, exhibit similar $\Delta T_{Max,b}$ values. This consistency is attributed to the symmetrical cooling effect provided by the HBTMS liquid cooling system on both sides of these batteries.

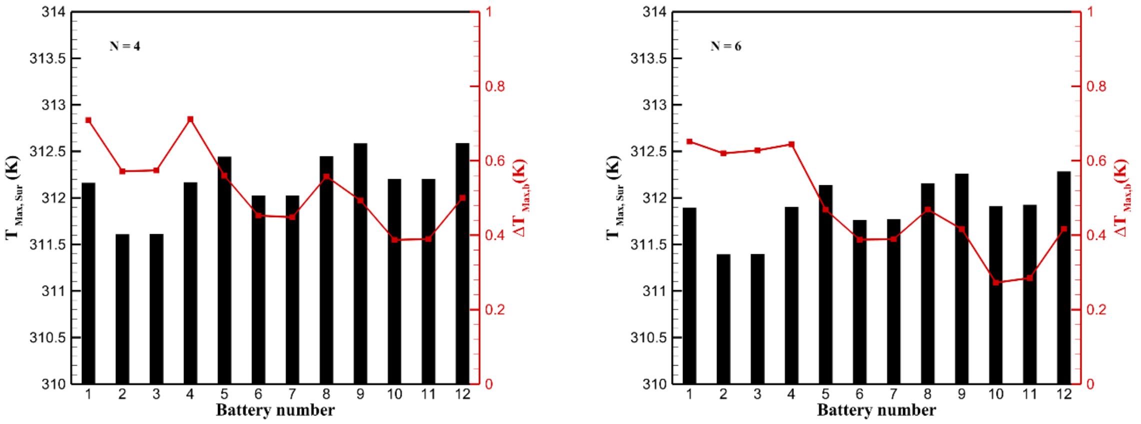

(a) 4 fins

(b) 6 fins

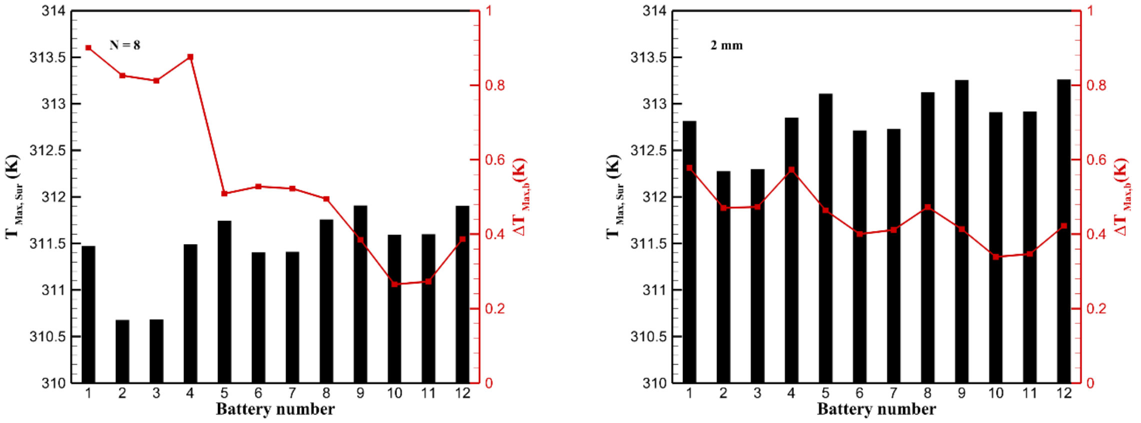

(c) 8 fins

(d) 2 mm

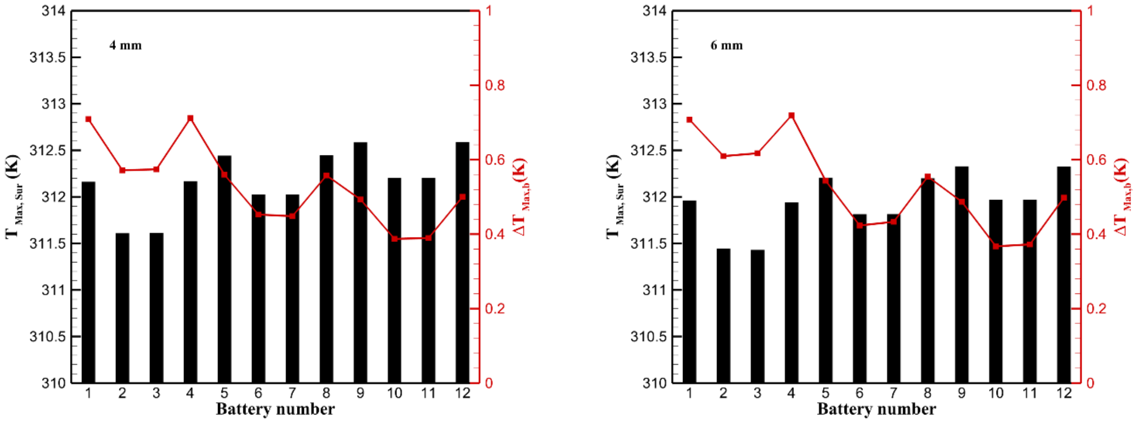

(e) 4 mm (f) 6 mm

Figure 4-28. $T_{Max,Sur}$, $\Delta T_{Max,b}$ for the HBTMS at the end of the 5C discharge rate, showing the effect of copper foam fin quantity with (a) 4 fins, (b) 6 fins, and (c) 8 fins, and fin thickness with (d) 2 mm, (e) 4 mm, and (f) 6 mm.

The impact of varying copper foam fins quantity and thickness on the energy density of the HBTMS is illustrated in Figure 4-29. As the quantity or thickness of the copper foam fins increases, the volume of copper foam used also increases, which in turn raises the overall weight of the system. This added weight adversely affects the system's energy density. Specifically, employing eight copper foam fins results in a 2.72% reduction in energy density compared to the configuration with four fins. Similarly, increasing the fin thickness from 2 mm to 6 mm leads to a 2.68% decrease in energy density. These findings highlight the trade-off between thermal performance enhancement and energy density, underscoring the importance of optimising fin geometry to achieve an effective balance between cooling efficiency and system mass.

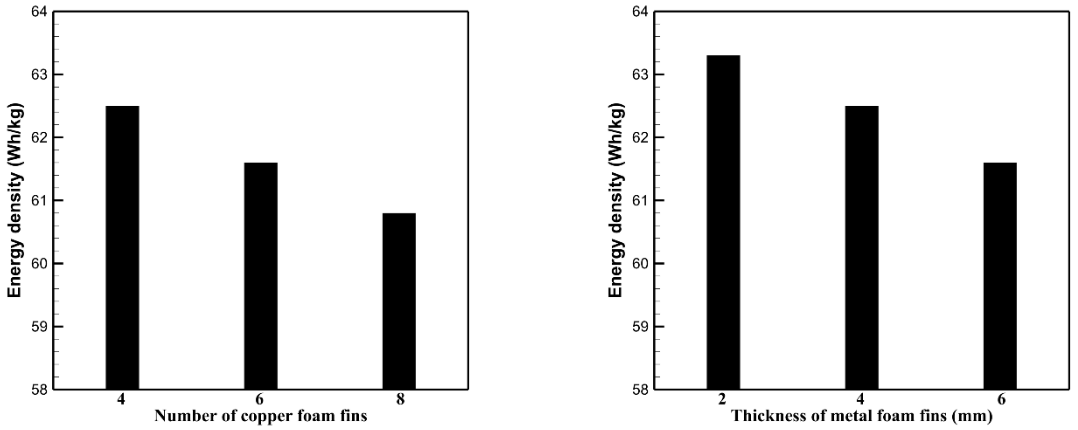

(a) (b)

Figure 4-29. Energy density of the HBTMS with different (a) quantity and (b) thickness of copper foam fins.

4.5 Number of the Cooling Plates

This section investigates the effect of varying the number of cooling plates (1, 2, and 3) in the proposed HBTMS during high 5C discharge, as well as the role of incorporating copper foam layers within the copper tubes at a constant thickness of 2 mm. The porosity and pore density of both the copper foam fins and the copper foam layers are fixed at 0.9 and 30 PPI, respectively. Each PCM housing includes four copper foam fins with a thickness of 4 mm. The coolant inlet mass flow rate is set to 0.001 kg/s, with an inlet temperature of 303.15 K, and the ambient temperature is maintained at 308.15 K.

The influence of varying the number of cooling plates, with and without copper foam layers, on the $T_{Max,Sur}$ is illustrated in Figure 4-30 (a) and compared against the baseline pure PCM. As indicated, in the pure PCM configuration, $T_{Max,Sur}$ rises sharply during the 5C discharge, reaching approximately 322 K at the end of 5C discharge. This temperature increase is attributed to the inherently low thermal conductivity of the pure PCM, which leads to heat accumulation around the battery surfaces and the formation of a melted PCM layer near the battery housing (as shown in Figure 4-31 (a)). This molten layer, having low thermal conductivity, acts as an insulating layer. To mitigate this effect, the implementation of the HBTMS, with or without copper foam layers, substantially reduces $T_{Max,Sur}$. Specifically, Figure 4-30 (a) shows that introducing HBTMS achieves temperature reductions of 8.46 K, 9.19 K, and 9.68 K for systems with one, two, and three cooling plates without copper foam layers, respectively. Additionally, comparing configurations with and without copper foam layers shows reductions of 2.76%, 3.24%, and 3.43% in $T_{Max,Sur}$ for one, two, and three cooling plates, respectively, due to the presence of the copper foam layer. Notably, a comparison between the configuration with two cooling plates with copper foam layers and that with three cooling plates without copper foam layers yields nearly equivalent $T_{Max,Sur}$ values of 312.58 K and 312.41 K at the end of 5C discharge, respectively. These findings highlight that integrating copper foam layers can reduce the number of required cooling plates while maintaining equivalent thermal performance.

The number of cooling plates plays a crucial role in determining the extent and distribution of PCM melting in the HBTMS, as well as influencing the L_f, due to the enhanced convective heat transfer within the cooling plates. As illustrated in Figure 4-30 (b), the addition of cooling plates without copper foam layers substantially reduced the amount of molten PCM by 66.06%, 93.91%, and 97.51% for configurations with one, two, and three cooling plates, respectively, when compared to the pure PCM configuration. Moreover, incorporating copper foam layers within the copper tubes further decreased the L_f, with the most notable reduction occurring in the single cooling plate configuration. Specifically, as shown in Figure 4-30 (b), L_f was reduced by 32.36%, 9.01%, and 6.83% for systems with one, two, and three cooling plates, respectively, in comparison to their counterparts without copper foam layers. Additionally, as shown in Figure 4-30 (b), the introduction of HBTMS with cooling plates considerably delayed the onset of PCM melting. For instance, in the configuration with three cooling plates with copper foam layers, PCM melting commenced at 618 seconds, whereas in the pure PCM, melting began much earlier, at 113 seconds.

PCM liquid fraction contour plots at the end of 5C discharge, shown in Figure 4-31, highlight distinct differences between pure PCM and the HBTMS configurations. In contrast to the extensive melting observed in pure PCM, especially around the battery housing, the HBTMS exhibits more confined and localised PCM melting, predominantly occurring within the pores of the copper foam fins. This behaviour is attributed to the enhanced thermal conductivity of the PCM provided by the copper foam structure, which promotes melting within the fins. Furthermore, the inclusion of additional cooling plates, particularly those incorporating copper foam layers, substantially reduces the overall extent of PCM melting. For instance, in the configuration with a single cooling plate without copper foam layers (Figure 4-31 (c)), PCM melting extends beyond the fins and is evident around both the battery and PCM housing. Conversely, as illustrated in Figure 4-31 (b), (d), and (f), the addition of copper foam layers improves heat conduction from the battery housing through the PCM, fins, and PCM housing, facilitating more efficient heat removal by forced convection in the copper tubes and thereby decreasing PCM melting. Similarly, increasing the number of cooling plates, regardless of the presence of copper foam layers, leads to a further reduction in PCM melting, with the remaining melted PCM confined primarily to the high-conductivity fin pores. Additionally, as observed in Figure 4-31, less PCM is melted around batteries 1 to 4, especially batteries 2 and 3, due to their direct exposure to the copper tubes, which enhances local heat extraction. However, as water progresses through the copper tubes toward the outlet and accumulates heat, its cooling capacity diminishes. As a result, greater PCM melting is seen around batteries in the last row, particularly batteries 9 and 12 located on the outer side, with residual melting observed even in the three cooling plate configuration.

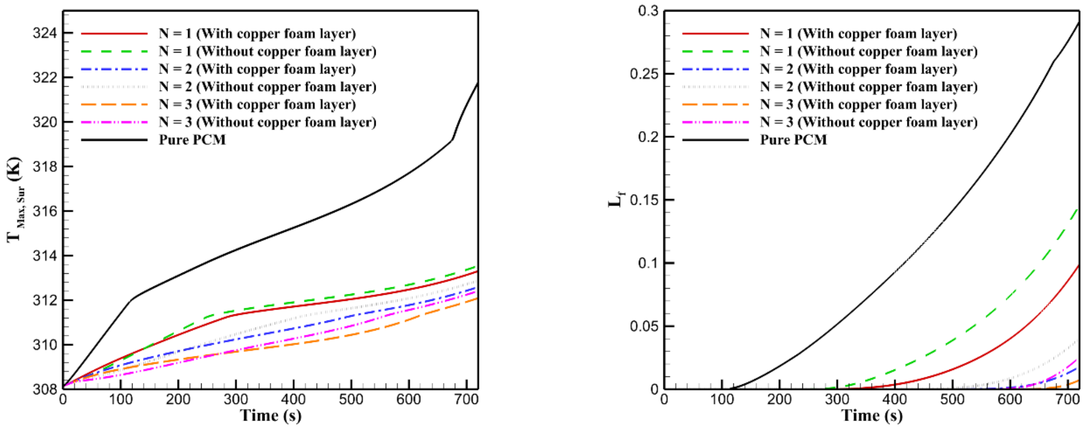

(a) (b)

Figure 4-30. Impact of the different number of cooling plates on (a) batteries maximum surface temperature and (b) PCM liquid fraction.

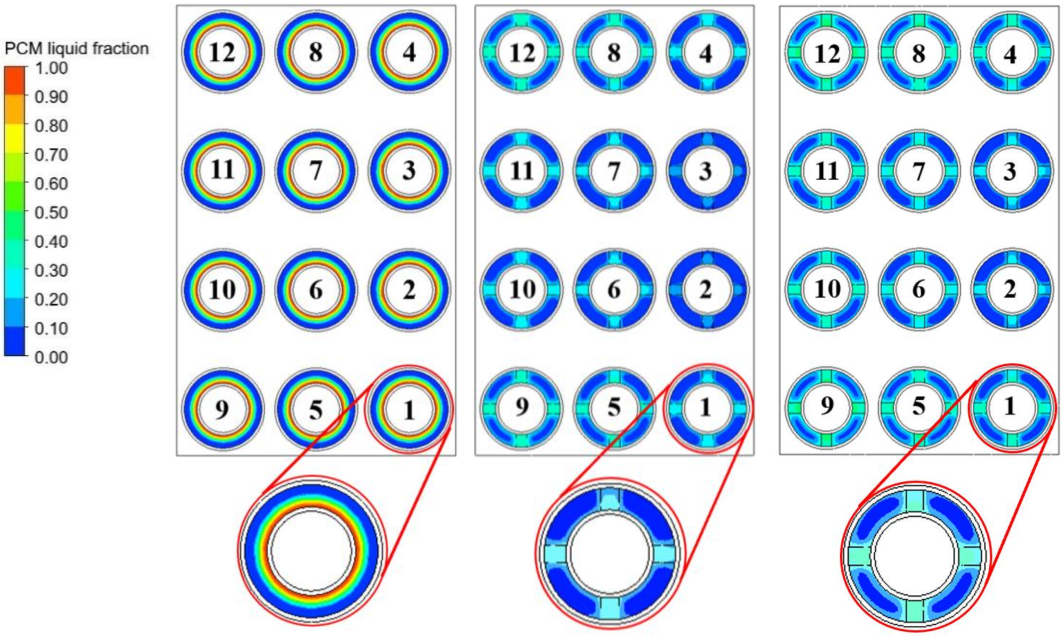

(a) Pure PCM

(b) One cooling plate with copper foam layers

(c) One cooling plate without copper foam layers

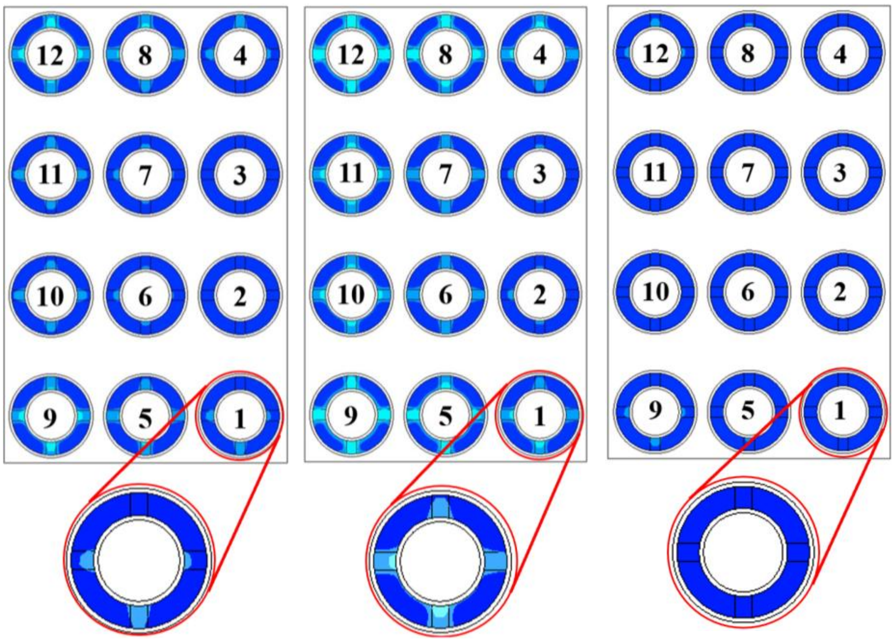

(d) Two cooling plates with copper foam layers

(e) Two cooling plates without copper foam layers

(f) Three cooling plates with copper foam layers

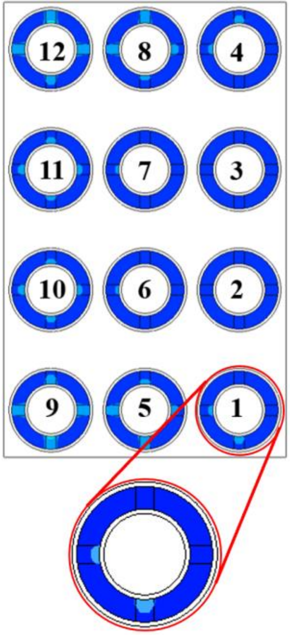

(g) Three cooling plates without copper foam layers

Figure 4-31. PCM liquid fraction contour plots for pure PCM and HBTMS with different number of cooling plates at the end of 5C discharge: (a) pure PCM, (b) one cooling plate with copper foam layers, (c) one cooling plate without copper foam layers, (d) two cooling plates with copper foam layers, (e) two cooling plates without copper foam layers, (f) three cooling plates with copper foam layers, and (g) three cooling plates without copper foam layers.

To evaluate the thermal performance improvement offered by the HBTMS, the $\overline{Nu_b}$ is presented in Figure 4-32. A substantial increase in $\overline{Nu_b}$ was observed compared to pure PCM, with values rising by approximately 7, 13, and 33 times for HBTMS configurations incorporating one, two, and three cooling plates with copper foam layers, respectively. This enhancement is primarily attributed to the integration of longitudinal copper foam fins within the PCM and the utilisation of liquid cooling via copper tubes equipped with copper foam layers. These features collectively enhance heat transfer by providing conductive pathways, facilitating both natural and forced convection, and increasing the effective heat transfer surface area. Furthermore, the presence of the copper foam layers notably modifies the velocity and temperature profiles inside the copper tubes, thereby enhancing fluid mixing and intensifying convective heat transfer near the tube walls.

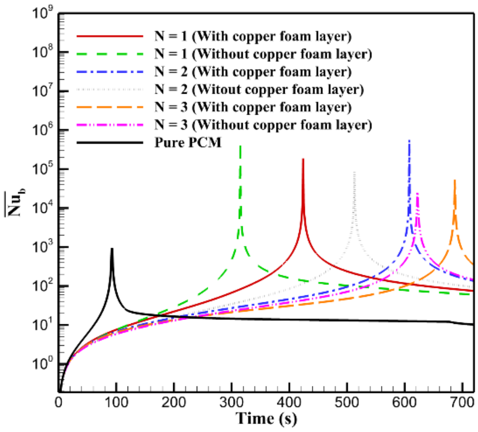

Figure 4-32. Battery surface average Nusselt number for pure PCM and HBTMS with different number of cooling plates at the end of 5C discharge.

Each battery's $T_{Max,Sur}$ and $\Delta T_{Max,b}$ for both the HBTMS and pure PCM are presented in Figure 4-33, with corresponding static temperature contour plots shown in Figure 4-34. As illustrated in Figure 4-33 (a), under pure PCM, all battery cells reached a similarly elevated $T_{Max,Sur}$ of approximately 322 K, with $\Delta T_{Max,b}$ maintained at around 0.65 K. This nearly uniform temperature distribution, also evident in Figure 4-34 (a), results from the aluminium housing surrounding each battery, which promotes radial heat conduction and contributes to a relatively even temperature distribution. The application of the HBTMS with three cooling plates, as shown in Figure 4-33 (b) reduced $T_{Max,Sur}$ across all battery cells. Due to the influence of the liquid cooled plates, batteries positioned on the sides of the module (1, 4, 5, 8, 9, and 12) experienced higher $T_{Max,Sur}$ compared to centrally located cells (2, 3, 6, 7, 10, and 11). As depicted in Figure 4-34 (b), lower static temperatures were observed in batteries near the coolant inlet and the centre of the module, whereas the highest core temperatures appeared on the side and last row cells. This distribution is attributed to the improved cooling efficacy provided by proximity to copper tubes and the copper foam layer enhanced liquid cooling. Regarding $\Delta T_{Max,b}$, unlike the uniformity in the pure PCM, some variations were noted in the HBTMS case, with a maximum of around 0.7 K in batteries 1 and 4, which are more exposed to one side cooling. Nonetheless, this remains well below the 5 K threshold suggested in the literature. Despite this variation, Figure 4-34 (b), demonstrates that the HBTMS achieves a nearly uniform surface temperature with a marked reduction compared to pure PCM. Such thermal uniformity is critical to optimising battery performance and longevity, as it minimises thermal stress and reduces the likelihood of temperature induced degradation or imbalance across the battery module.

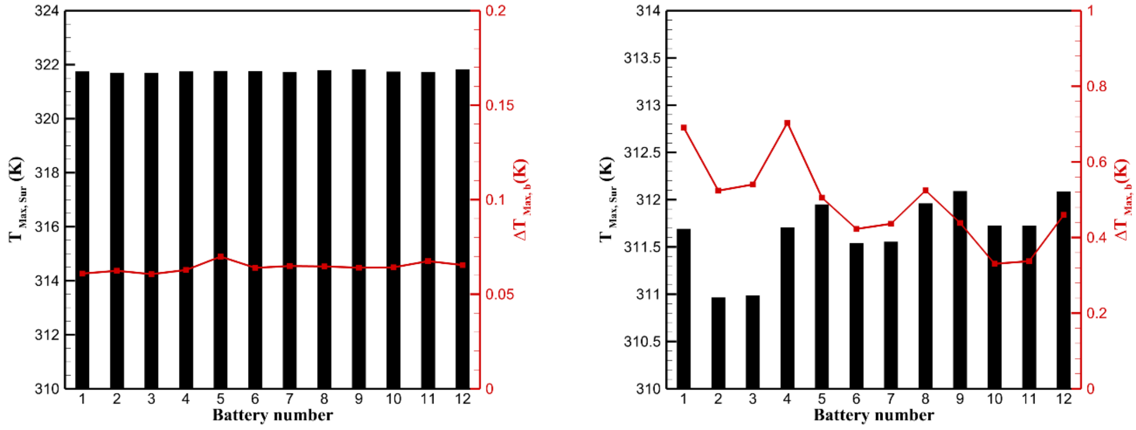

(a) Pure PCM (b) Three cooling plates with copper foam layers

Figure 4-33. Comparison of the $T_{Max,Sur}$ and $\Delta T_{Max,b}$ of the (a) pure PCM and (b) HBTMS with three cooling plates with copper foam layers at the end of 5C discharge.

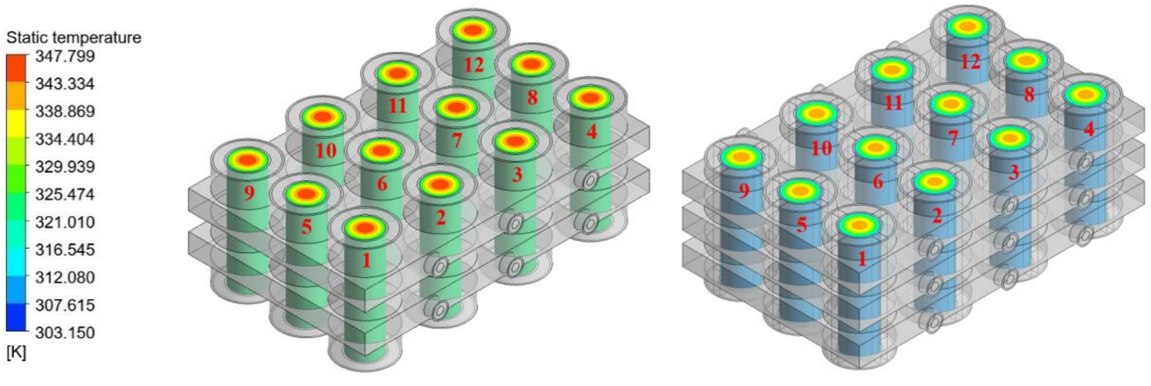

(a) Pure PCM (b) Three cooling plates with copper foam layers

Figure 4-34. Comparison of the static temperature contour plots of (a) pure PCM and (b) HBTMS with three cooling plates with copper foam layers at the end of 5C discharge.

As illustrated in Figure 4-35, the number of cooling plates has a notable influence on the energy density of the HBTMS due to the added mass. When comparing systems with an equal number of cooling plates, the inclusion of copper foam layers slightly lowers energy density; however, the additional mass contributed by the metal foam is minimal relative to that of full cooling plates. Considering that the HBTMS configuration with three cooling plates without copper foam layers performs comparably to the configuration with two cooling plates incorporating copper foam layers in terms of $T_{Max,Sur}$ (Figure 4-30 (a)), $\overline{Nu_b}$ (Figure 4-32), and PCM melting (Figure 4-31), the two cooling plates configuration with copper foam layers is favoured. This setup achieves an 11% enhancement in energy density, demonstrating that the inclusion of metal foam effectively compensates for the reduced cooling surface area. Consequently, this results in a lighter, more energy efficient system without compromising thermal reliability or operational effectiveness.

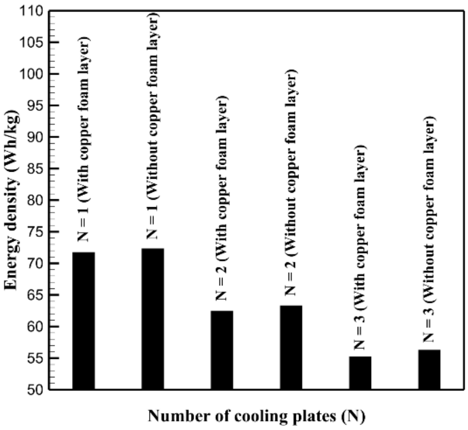

Figure 4-35. Energy density of the HBTMS with different number of cooling plates with or without copper foam layers.

4.6 Copper Foam Layers Thickness

In this section, the impact of varying copper foam layer thicknesses (0, 1, 2, 2.5, 3, and 4.2 mm) within the copper tubes on the thermal behaviour and design efficiency of the proposed HBTMS during high 5C discharge have been investigated. Throughout this study, the porosity and pore density of both the copper foam fins, and the copper foam layers are kept constant at 0.9 and 30 PPI, respectively. Four copper foam fins with a thickness of 4 mm have been considered in each PCM housing. A coolant inlet mass flow rate of 0.001 kg/s and an inlet temperature of 303.15 K are applied. The number of cooling plates is fixed at two, and the ambient temperature is maintained at 308.15 K.

The influence of various copper foam layer thicknesses on $T_{Max,Sur}$ is illustrated in Figure 4-36 (a). Compared to the copper tube without a copper foam layer, a reduction in $T_{Max,Sur}$ was observed when the tube was partially filled with copper foam. As the thickness increased, the interconnected pores of the foam provided additional surface area for heat exchange and disrupted the developing thermal boundary layer, thereby enhancing the overall active heat removal from the system. However, when the copper foam layer thickness reached 4.2 mm, resulting in a fully filled tube, convection was hindered by the elevated flow resistance, and conduction through the foam ligaments became the dominant heat transfer mechanism. Consequently, $T_{Max,Sur}$ reaches 313.69 K at the end of the 5C discharge for the 4.2 mm thickness. Reductions in thickness to 0, 1, 2, 2.5, and 3 mm led to corresponding decreases in $T_{Max,Sur}$ by 0.8, 0.82, 1.11, 1.25, and 1.45 K, respectively. As the forced convection heat transfer rate is influenced by variations in copper foam layer thickness, a greater amount of PCM is melted in the fully filled tube, with the L_f peaking at 0.19 by the end of the 5C discharge, as shown in Figure 4-36 (b). When thicknesses of 0, 1, 2, 2.5, and 3 mm are applied, L_f reduces by 79.21%, 65.44%, 90.82%, 89.21%, and 94.7%, respectively. Furthermore, the onset of PCM melting is delayed by 159, 178, 262, 304, and 341 seconds, respectively, for these thicknesses compared to the fully filled tube.

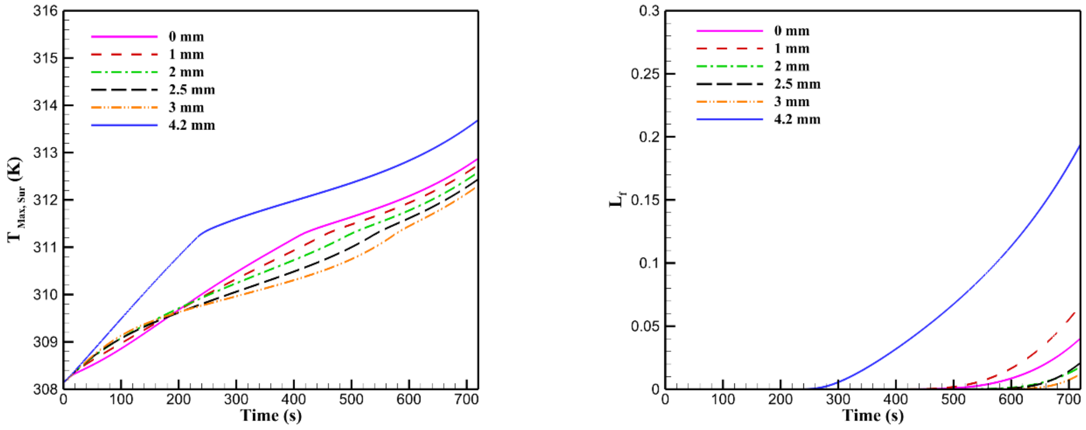

(a) (b)

Figure 4-36. Impact of the copper foam layer thickness on (a) batteries maximum surface temperature and (b) PCM liquid fraction.

Each battery's $T_{Max,Sur}$ and $\Delta T_{Max,b}$ under various copper foam layer thicknesses is presented in Figure 4-37 at the end of 5C discharge. Improved overall cooling performance was consistently observed for the partially filled copper tubes, as indicated by lower $T_{Max,Sur}$ across the module. The highest $T_{Max,Sur}$ was recorded on batteries 9 and 12, positioned on the side of the last row, where the effectiveness of liquid cooling is diminished due to prior heat absorption along the flow path. The lowest $\Delta T_{Max,b}$ was achieved by the fully filled copper tube, with values predominantly between 0.3 and 0.5 K, as shown in Figure 4-37 (f). This result is attributed to the dominance of conductive heat transfer in the fully packed foam, which reduces temperature gradients but constrains convective heat removal by the coolant. As the copper foam layer thickness increases from 0 to 3 mm, $T_{Max,Sur}$ also increases, though it remained below 1 K. Additionally, it was noted that the increase in thickness predominantly affected $\Delta T_{Max,b}$ on batteries 1 to 4 in the first row, where the highest cooling efficiency is achieved due to their proximity to the inlet section of the cooling plates.

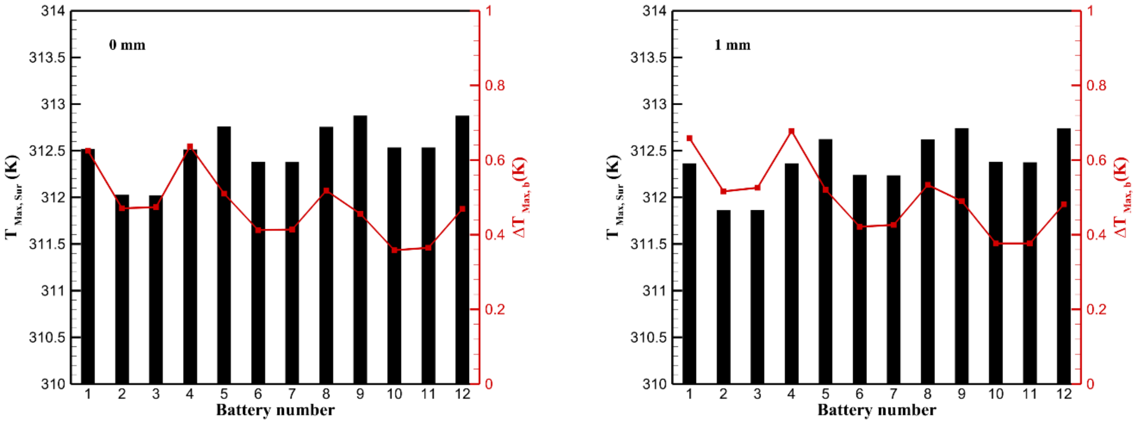

(a) 0 mm

(b) 1 mm

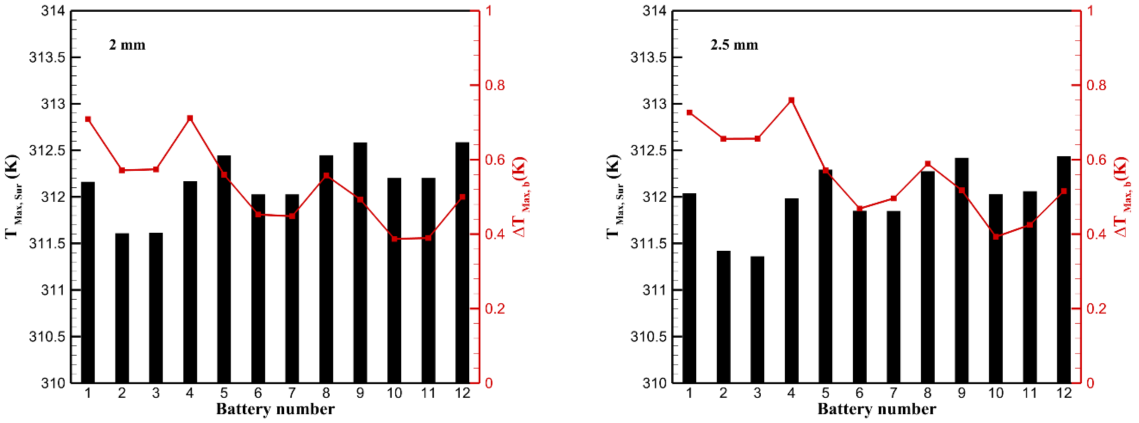

(c) 2 mm

(d) 2.5 mm

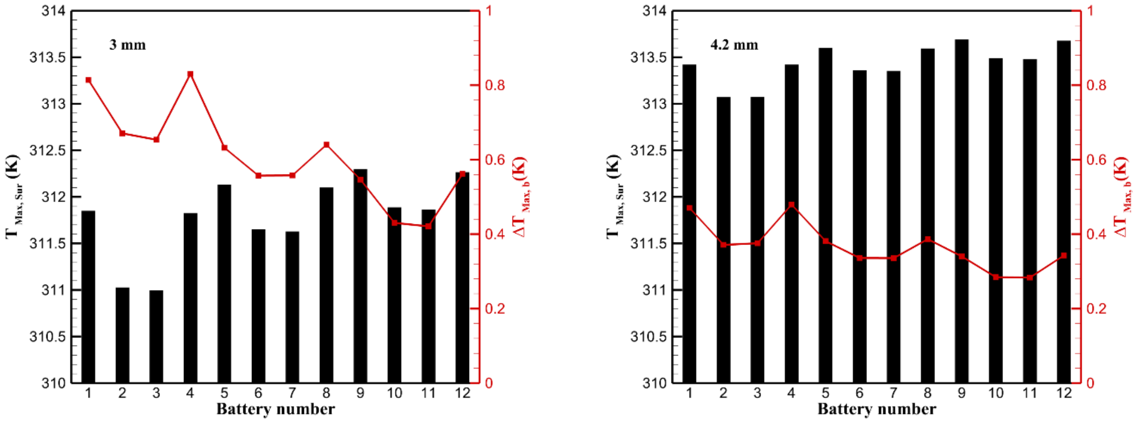

(e) 3 mm (f) 4.2 mm

Figure 4-37. Comparison of the $T_{Max,Sur}$ and $\Delta T_{Max,b}$ of the HBTMS at the end of the 5C discharge rate, showing the effect of copper foam layer thickness with (a) 0 mm, (b) 1 mm, (c) 2 mm, (d) 2.5 mm, (e) 3 mm, and (f) 4.2 mm.

The influence of different copper foam layer thicknesses on the $\overline{Nu_b}$ is depicted in Figure 4-38. As shown, $\overline{Nu_b}$ peaked at different stages of discharge primarily due to the delayed onset of PCM melting and the battery surface temperature surpassing the PCM's solidus temperature. In the case where the copper tube is completely filled with copper foam, the lowest $\overline{Nu_b}$ value of 42.7 was observed at the end of the 5C discharge. In contrast, the use of partially filled tubes leads to a notable enhancement in $\overline{Nu_b}$. Specifically, improvements by factors of 2.18, 2.10, 3.16, 4.10, and 6.49 are achieved for copper foam layer thicknesses of 0, 1, 2, 2.5, and 3 mm, respectively, when compared to the fully filled configuration.

This enhancement is attributed to the influence of copper foam layer thickness on the dimensionless velocity and temperature profiles within the copper tube, as depicted in Figure 4-39. As shown in Figure 4-39 (a), the dimensionless velocity within the copper foam region is notably lower than in the clear region, and the uniform velocity profile in either a fully filled or clear tube is markedly disrupted by the inclusion of a partial copper foam layer. This disruption results from increased flow retardation and induced mixing due to the inertial and viscous forces generated by the solid framework of the copper foam. The porous structure near the tube wall introduces additional resistance, decreasing local fluid velocity within the foam, while simultaneously deflecting more flow into the clear central region, thereby elevating the maximum velocity in that domain. This redistribution of flow creates a steeper velocity gradient, which in turn intensifies forced convection at the interface between the copper foam layer and the clear region. Additionally, partially filling the tube mitigates the substantial pressure drop typically associated with fully packed configurations.

Similarly, as demonstrated in Figure 4-39 (b), the uniform dimensionless temperature distribution observed in a clear copper tube and the consistent solid–liquid phase temperatures in a fully filled tube are noticeably affected by the presence of partially inserted copper foam layer. This influence is primarily due to the copper foam layer's effect on both conductive and convective heat transfer mechanisms within the tube. The improvements in conduction and convection are largely driven by the copper foam layer's capacity to promote fluid mixing, increase the effective thermal conductivity of the coolant, and establish a thinner hydrodynamic boundary layer, thereby lowering the thermal resistance. Moreover, with increasing copper foam layer thickness, the development of the thermal boundary layer becomes more pronounced, driven by the intensification of velocity and temperature gradients near the interface between the porous region and the tube wall. Thicker copper foam layers thus further enhance heat transfer performance by reinforcing these gradients and providing stronger interaction between conductive and convective processes at the interface.

Furthermore, as depicted in Figure 4-39 (b), increasing the thickness of the metal foam promotes the development of the thermal boundary layer near the inner wall of the copper tube. However, beyond a critical thickness, the benefits of improved conduction are offset by reduced coolant flow, indicating diminishing returns. Consequently, the optimal copper foam layer thickness is identified as the one that effectively augments local mixing and heat transfer while avoiding excessive deceleration of fluid flow. It is also observed that the solid phase temperature rises with varying foam thicknesses, reaching its peak at a 2 mm thickness, which highlights the improved conductive heat transfer near the tube wall. Additionally, a temperature discontinuity emerges at the interface between the copper foam layer and the clear region, as well as between the solid and liquid phases within the copper foam layer. This discontinuity is attributed to the increased coolant velocity at the interface, which intensifies forced convection at the boundary between the copper foam and clear regions.

The elevated fluid temperature observed at the core of the copper tube, particularly for metal foam thicknesses greater than 1 mm, indicates enhanced heat transfer and more efficient heat removal from the tube wall. However, as shown in Figure 4-39 (b), for a 1 mm copper foam layer, the maximum fluid temperature at the core of the tube is lower than that of the clear tube, resulting in a reduced $\overline{Nu_b}$ as presented in Figure 4-38. Moreover, as illustrated in Figure 4-39 (a), the dimensionless fluid velocity at the tube's core increases with copper foam layer thickness up to 2.5 mm, reaching a maximum value of 3.68. When the thickness is further increased to 3 mm, the core velocity declines to 3.37, which is marginally lower than that observed for the 2 mm case (3.39). This reduction in velocity is attributed to the copper foam layer occupying a larger portion of the tube's cross-section. Given the porosity of 0.9 and pore density of 30 PPI, a greater volume of fluid is diverted into the copper foam layer, thereby reducing the peak velocity in the clear region. This observation is consistent to the results reported in the literature [317-319] and highlights the significant influence of copper foam layer thickness on heat transfer performance, as evident in the trends of $T_{Max,Sur}$ and $\overline{Nu_b}$.

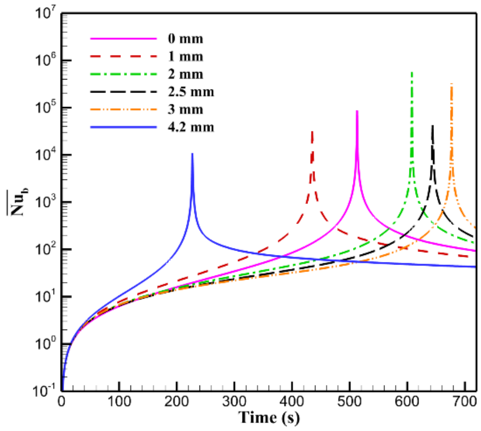

Figure 4-38. Batteries surface average Nusselt number for HBTMS with different copper foam layer thickness at the end of 5C discharge.

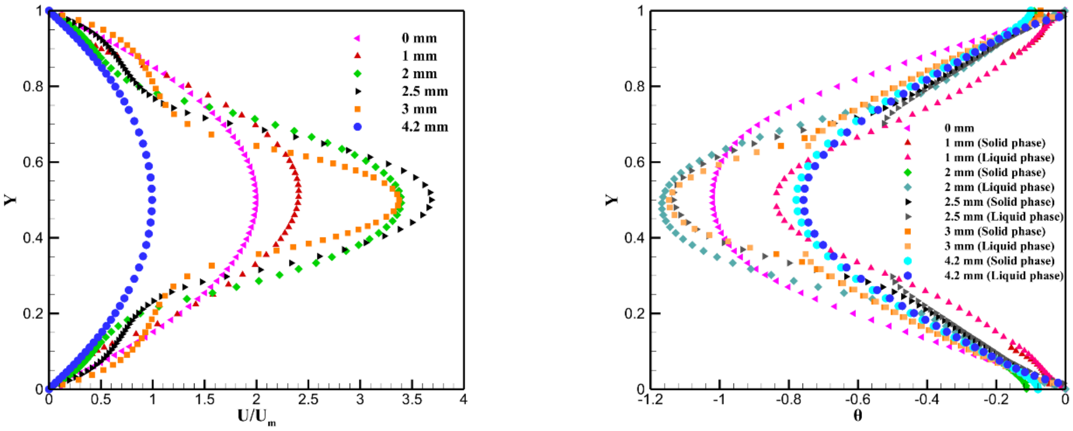

(a) (b)

Figure 4-39. (a) Dimensionless velocity and (b) temperature within the copper tube with different copper foam layer thickness at the end of 5C discharge.

The PEC values for various copper foam layer thicknesses are presented in Figure 4-21. A PEC value below one signifies that the increase in pressure drop outweighs the heat transfer enhancement, as is the case for the fully filled copper tube, which exhibits a low PEC value of 0.11. In contrast, for partially filled copper tubes, all considered thicknesses yield PEC values greater than one, indicating superior thermal performance relative to the fully filled configuration. Among these, the 2 mm copper foam layer thickness achieves the highest PEC value, identifying it as the optimal configuration. While increasing foam thickness can further enhance conduction by promoting the development of the thermal boundary layer near the tube wall, this benefit is counteracted by a pronounced decline in coolant flow, thereby reducing convective heat transfer, especially at the copper foam and clear region interface. At the 2 mm thickness, the porous ligaments effectively support enhanced local mixing and conduction without imposing excessive flow resistance, which would otherwise compromise convection and increase pressure drop. Consequently, a copper foam layer thickness of 2 mm provides an optimal trade-off between heat transfer improvement and pressure drop, with the maintained porosity of 0.9 also supporting a high system energy density.

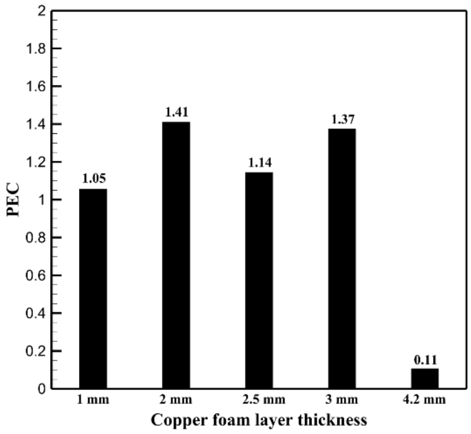

Figure 4-40. Impact of copper foam layer thickness on PEC.

4.7 Liquid Cooling Inlet Mass Flow Rate and Temperature

In this section, the impact of varying coolant inlet mass flow rates and inlet temperatures on the thermal behaviour and design efficiency of the proposed HBTMS during high 5C discharge is investigated. Different inlet mass flow rates (0.0002, 0.001, and 0.002 kg/s) are studied while maintaining a constant inlet temperature of 303.15 K. Additionally, the effect of varying inlet temperatures (298.15, 303.15, and 308.15 K) is examined with a fixed mass flow rate of 0.001 kg/s. Throughout this study, the porosity and pore density of both the copper foam fins and the copper foam layers are kept constant at 0.9 and 30 PPI, respectively. Four copper foam fins with a thickness of 4 mm are considered in each PCM housing. The copper tubes within the two cooling plates incorporate copper foam layers with a thickness of 2 mm. The ambient temperature is maintained at 308.15 K.

The performance of the proposed HBTMS under varying inlet mass flow rates and temperatures, in terms of the $T_{Max,Sur}$ during 5C discharge, is shown in Figure 4-41. As depicted in Figure 4-41 (a), increasing the inlet mass flow rate significantly reduced the $T_{Max,Sur}$, as higher flow rates enhance forced convection within the copper tubes. For configurations without copper foam layers, compared to the pure PCM, $T_{Max,Sur}$ decreased by 7.95 K, 8.89 K, and 9.33 K for inlet mass flow rates of 0.0002 kg/s, 0.001 kg/s, and 0.002 kg/s, respectively. The inclusion of copper foam layers within the copper tubes further augmented forced convection. As a result, $T_{Max,Sur}$ reductions of 8.13 K, 9.18 K, and 9.82 K were achieved for the same respective flow rates, compared to pure PCM. Notably, a comparison between the $T_{Max,Sur}$ values for 0.002 kg/s without a copper foam layer and 0.001 kg/s with a copper foam layer shows a minimal difference of only 0.15 K at the end of discharge. This finding indicates that incorporating copper foam layers allows for a lower coolant flow rate while maintaining nearly equivalent thermal performance, thus offering an efficient means of reducing pumping power without compromising cooling effectiveness.

Similarly, decreasing the inlet coolant temperature, as shown in Figure 4-41 (b), improves the thermal performance of the HBTMS by increasing the coolant's capacity to absorb heat via the cooling plates. In the configurations without copper foam layers, compared to pure PCM, $T_{Max,Sur}$ was reduced by 10.01 K, 8.89 K, and 8.02 K for inlet temperatures of 298.15 K, 303.15 K, and 308.15 K, respectively, by the end of the discharge. Additional improvement was achieved by incorporating copper foam layers within the copper tubes. Under these conditions, $T_{Max,Sur}$ decreased by 10.69 K, 9.18 K, and 8.24 K for the same respective inlet temperatures.

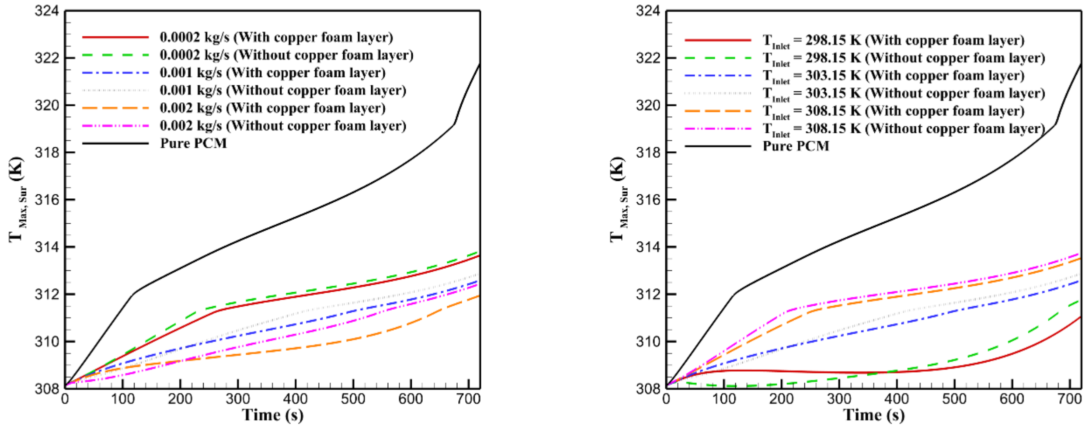

(a) (b)

Figure 4-41. Impact of the liquid cooling inlet (a) mass flow rate and (b) temperature on batteries maximum surface temperature.

Since variations in the inlet mass flow rate or temperature directly influence the active cooling part of the HBTMS, they also affect the extent and distribution of PCM melting, as illustrated in Figure 4-42 and Figure 4-43. As shown in Figure 4-42, increasing the inlet mass flow rate led to a significant reduction in PCM melting compared to the pure PCM. This enhancement is attributed to the increased effective thermal conductivity of the PCM surrounding the batteries, achieved through the integration of copper foam fins, as well as the intensified forced convection within the copper tubes. These effects promote more efficient heat transfer to the coolant, reducing the reliance on latent heat absorption by the PCM during the phase change process. Therefore, compared to pure PCM, L_f decreased by factors of 2.15 and 16.45 for inlet mass flow rates of 0.0002 kg/s and 0.001 kg/s, respectively. At the highest flow rate of 0.002 kg/s, the PCM melting was nearly negligible, with a recorded L_f value of only 0.0012 at the end of the 5C discharge.

A similar trend was observed with a reduction in the inlet temperature, which enhanced the active cooling effectiveness of the HBTMS and reduced the amount of heat available for PCM phase change. As depicted in Figure 4-42 (b), compared to pure PCM, L_f declined by factors of 2.21 and 16.45 for inlet temperatures of 308.15 K and 303.15 K, respectively. At the lowest inlet temperature of 298.15 K, the active cooling dominated to such an extent that the PCM remained entirely in its solid state throughout the 5C discharge.

As shown in Figure 4-42, the onset of PCM melting is significantly influenced by both the inlet mass flow rate and inlet temperature due to their direct impact on the active cooling capacity of the HBTMS. In particular, Figure 4-42 (a) demonstrates that increasing the inlet mass flow rate delays the onset of melting by 149 seconds and 382 seconds for flow rates of 0.0002 kg/s and 0.001 kg/s, respectively, when compared to the pure PCM. A comparable effect was observed in Figure 4-42 (b), where reducing the inlet temperature also postpones PCM melting. Delays of 138 seconds and 382 seconds were recorded for inlet temperatures of 308.15 K and 303.15 K, respectively.

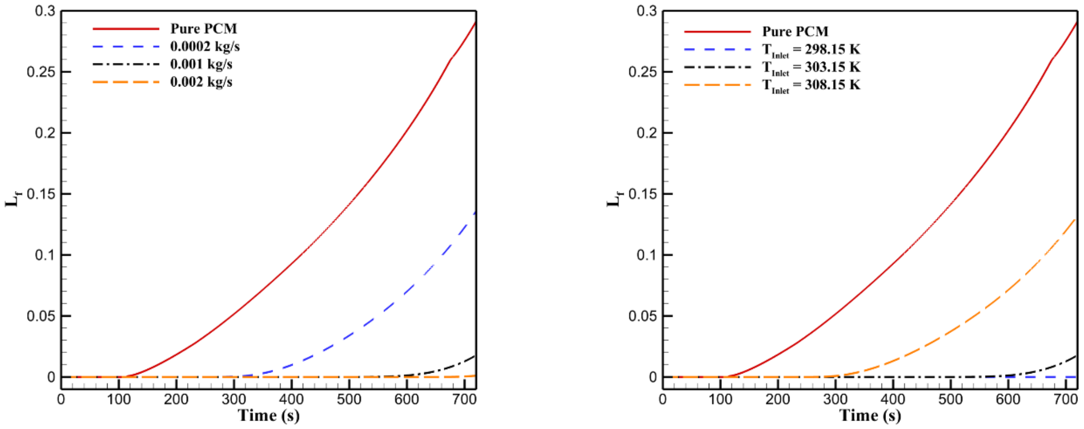

(a) (b)

Figure 4-42. Impact of the liquid cooling inlet (a) mass flow rate and (b) temperature on PCM liquid fraction.

As illustrated in Figure 4-43 (a) to (c), at a low inlet mass flow rate of 0.0002 kg/s, significant PCM melting occurs by the end of discharge, primarily within the copper foam fins and in the regions surrounding the batteries and PCM housing. As the inlet mass flow rate increases to 0.001 kg/s, the extent of PCM melting decreases considerably, particularly around the cells in the first row, including batteries 2 and 3. At the highest mass flow rate of 0.002 kg/s, only minimal PCM melting was observed, confined to the copper foam fins around batteries 9 and 12. In contrast, increasing the inlet temperature, as shown in Figure 4-43 (d) to (f), results in greater PCM melting. At an inlet temperature of 303.15 K, melting initiates from the last row, particularly around batteries 9 and 12. At the highest inlet temperature of 308.15 K, melted PCM is observed throughout the battery module, extending beyond the copper foam fins and progressively increasing from the first to the last row. These observations underscore the critical importance of optimising both the inlet mass flow rate and temperature to effectively utilise the PCM's latent heat for thermal regulation.

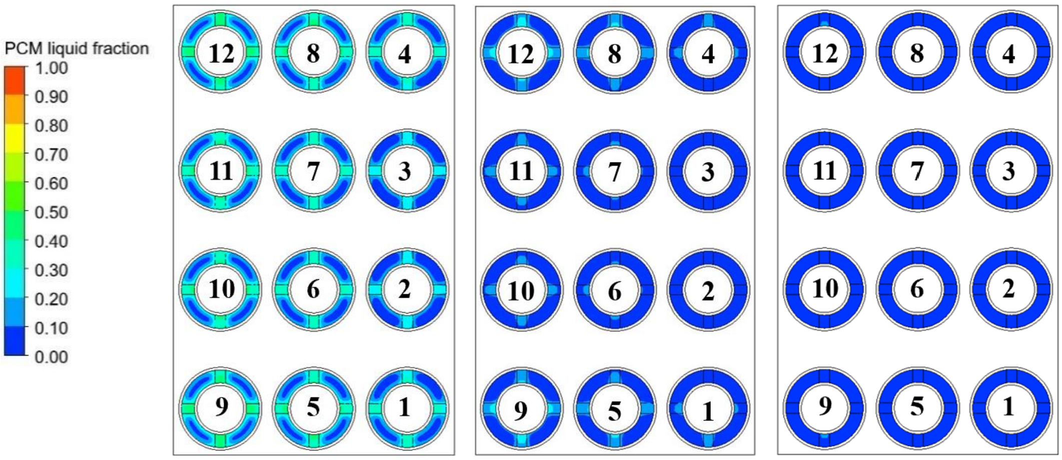

(a) 0.0002 kg/s (b) 0.001 kg/s (c) 0.002 kg/s

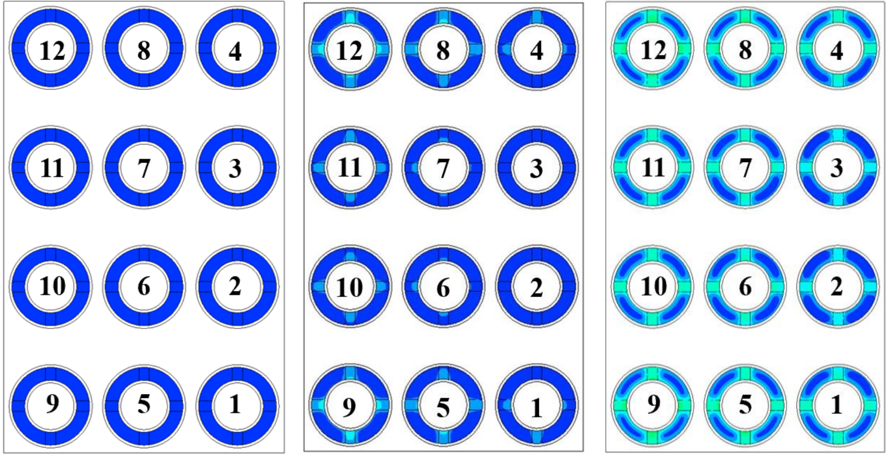

(d) 298.15 K (e) 303.15 K (f) 308.15 K

Figure 4-43. PCM liquid fraction contour plots for the HBTMS at the end of the 5C discharge rate, showing the effect of liquid cooling inlet mass flow rate with (a) 0.0002 kg/s, (b) 0.001 kg/s, and (c) 0.002 kg/s, and inlet temperature with (d) 298.15 K, (e) 303.15 K, and (f) 308.15 K.

The influence of varying inlet mass flow rates and temperatures on the $\overline{Nu_b}$ is demonstrated in Figure 4-44. As shown in Figure 4-44 (a), $\overline{Nu_b}$ increases significantly with higher inlet mass flow rates, both with and without the copper foam layers. In all cases, except at the mass flow rate of 0.001 kg/s, a peak in $\overline{Nu_b}$ was observed when the battery surface temperature surpasses the PCM solidus temperature. At the end of discharge, and compared to the pure PCM, the $\overline{Nu_b}$ increased by approximately 4.72, 9.04, and 15.04 times for inlet mass flow rates of 0.0002 kg/s, 0.001 kg/s, and 0.002 kg/s, respectively, in the absence of copper foam layers. With the inclusion of copper foam layers, further enhancement is achieved, resulting in improvements of 5.18, 13.11, and 204.85 times, respectively, for the same mass flow rates. These findings highlight the significant contribution of both increased coolant flow and the presence of copper foam layers in enhancing forced convection within the system.

As illustrated in Figure 4-44 (b), a similarly significant influence of inlet temperature on the $\overline{Nu_b}$ was observed. The improvement in active cooling due to lower inlet temperatures results in enhanced heat transfer. For cases without copper foam layers, $\overline{Nu_b}$ increased by approximately 30.39, 9.04, and 4.73 times compared to pure PCM for inlet temperatures of 298.15 K, 303.15 K, and 308.15 K, respectively. When copper foam layers are included, further enhancements were achieved, with $\overline{Nu_b}$ increasing by 7.26, 13.11, and 5.37 times, respectively, for the same inlet temperatures. Notably, the lower enhancement at 298.15 K for the case with copper foam layers, compared to its counterpart without copper foam layers, is attributed to the fact that the battery surface temperature remains below the PCM solidus temperature by the end of discharge, thereby limiting the contribution of latent heat absorption and associated convective enhancement.

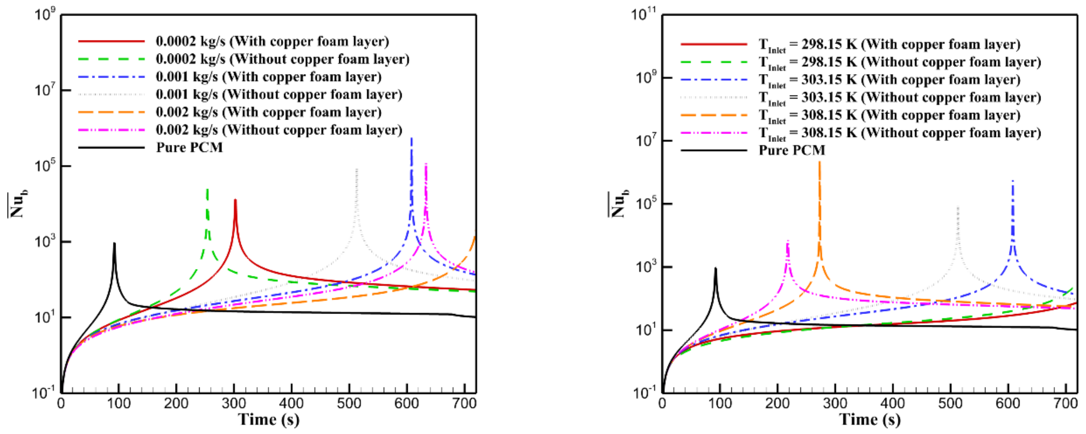

(a) (b)

Figure 4-44. Impact of the liquid cooling inlet (a) mass flow rate and (b) temperature on battery surface average Nusselt number.

$T_{Max,Sur}$ and $\Delta T_{Max,b}$ values for each battery cell at the of the discharge for different inlet mass flow rate and temperature is demonstrated in Figure 4-45. As shown in Figure 4-45 (a) to (c), increasing the inlet mass flow rate leads to a noticeable reduction in $T_{Max,Sur}$, particularly for batteries 2 and 3, which are most affected by proximity to the coolant inlet. However, $\Delta T_{Max,b}$ exhibits an increasing trend with higher inlet flow rates. At lower mass flow rates, as seen in Figure 4-45 (a), the variation in $\Delta T_{Max,b}$ is minimal, remaining below 0.5 K, with the highest values observed on batteries 1 and 4. This is attributed to the fact that these batteries are being exposed to liquid cooling on only one side. As the mass flow rate increases, the temperature of the coolant rises along the length of the copper tube, further amplifying the cooling imbalance. Consequently, $\Delta T_{Max,b}$ increases to values exceeding 0.6 K and 0.9 K for flow rates of 0.001 kg/s and 0.002 kg/s, respectively, with the most pronounced differences occurring on batteries 1 and 4. In contrast, in terms of the inlet temperature impact on $T_{Max,Sur}$ and $\Delta T_{Max,b}$, as depicted in Figure 4-45 (d) to (f), by increasing the inlet temperature while higher $T_{Max,Sur}$ values were recorded particularly on batteries 9 and 12, $\Delta T_{Max,b}$ found to be reduced. The $\Delta T_{Max,b}$ values exceeding 1 K on batteries 1 and 4 at an inlet temperature of 298.15 K are reduced to below approximately 0.5 K when the inlet temperature is increased to 308.15 K.

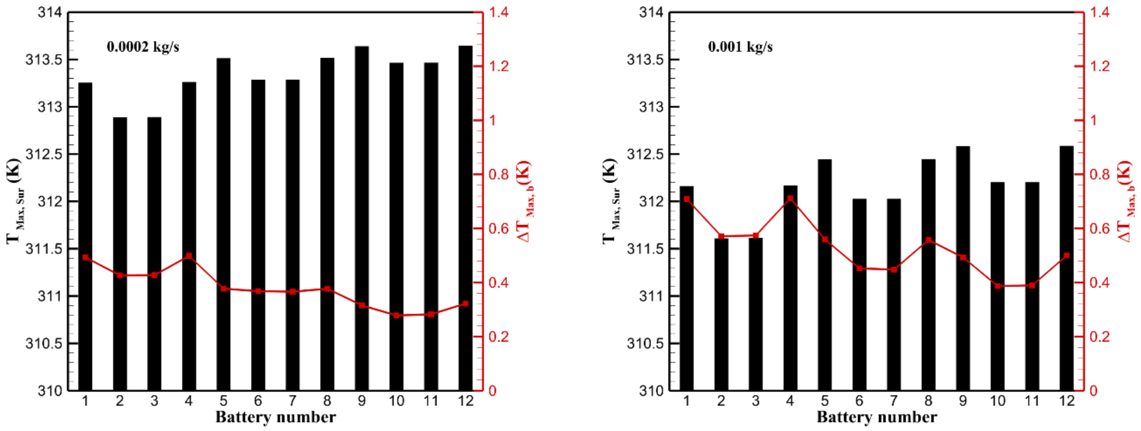

(a) 0.0002 kg/s

(b) 0.001 kg/s

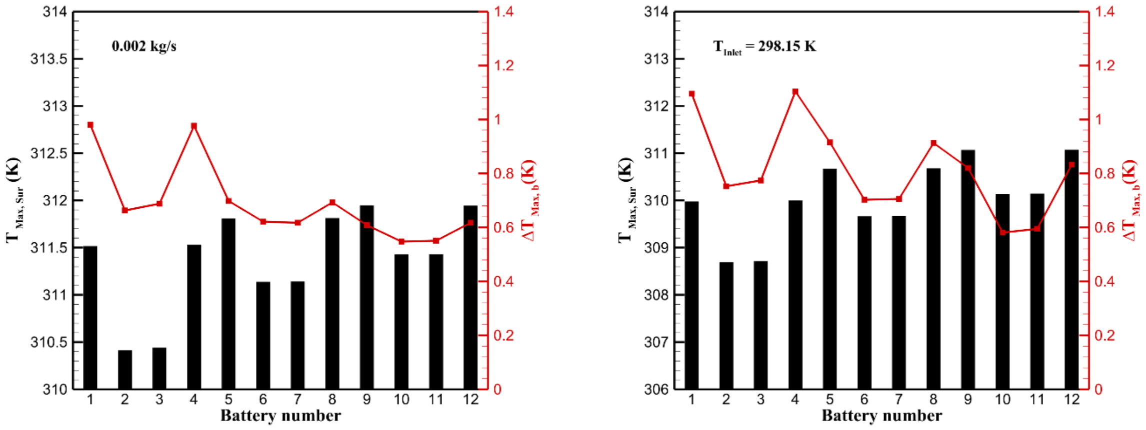

(c) 0.002 kg/s

(d) 298.15 K

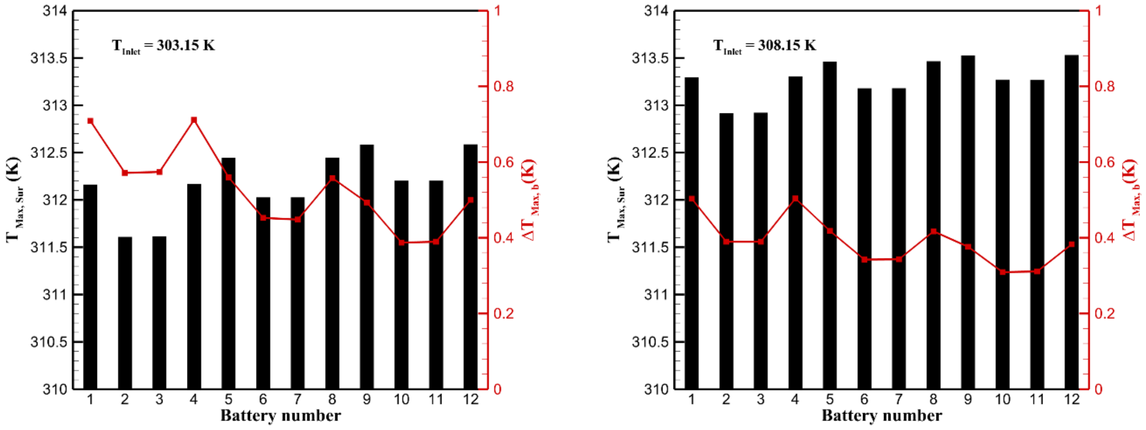

e) 303.15 K

(f) 308.15 K

Figure 4-45. $T_{Max,Sur}$ and $\Delta T_{Max,b}$ for the HBTMS at the end of the 5C discharge rate, showing the effect of liquid cooling inlet mass flow rate with (a) 0.0002 kg/s, (b) 0.001 kg/s, and (c) 0.002 kg/s, and inlet temperature with (d) 298.15 K, (e) 303.15 K, and (f) 308.15 K.

The impact of varying inlet mass flow rate and temperature on the PEC value is illustrated in Figure 4-46. As can be seen in Figure 4-46 (a) although an increase in inlet mass flow rate leads to a higher pressure drop, the overall performance benefit from enhanced forced convection within the copper tubes outweighs this drawback, resulting in higher PEC values. Specifically, compared to the low inlet mass flow rate of 0.0002 kg/s, the PEC value increased by 7.6% and 16.8% for flow rates of 0.001 kg/s and 0.002 kg/s, respectively. In contrast, Figure 4-46 (b), demonstrates that at a constant inlet mass flow rate of 0.001 kg/s, and consequently constant pressure drop, increasing the inlet temperature adversely affects the forced convection performance. As a result, compared to an inlet temperature of 298.15 K, the PEC value decreased by 19.4% and 26.8% for inlet temperatures of 303.15 K and 308.15 K, respectively.

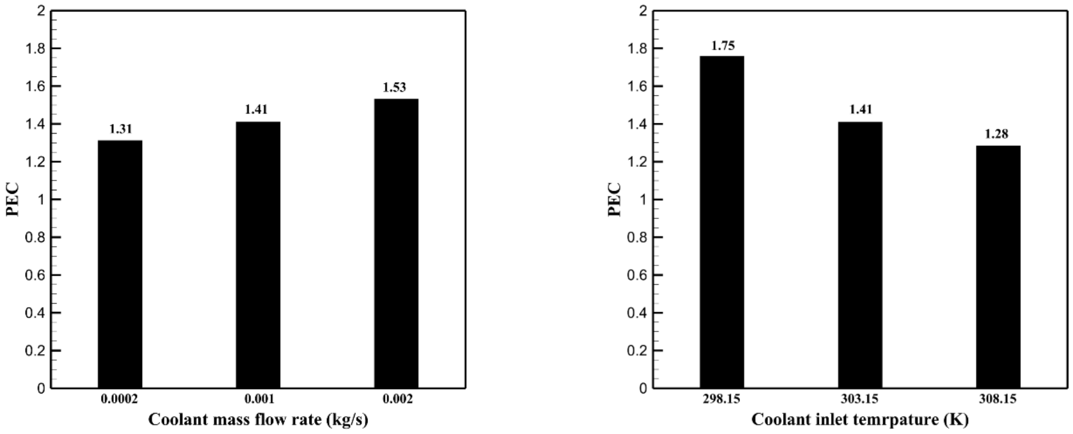

(a) (b)

Figure 4-46. Impact of the liquid cooling inlet (a) mass flow rate and (b) temperature on PEC.

For EV integration, variations in coolant inlet temperature and mass flow rate can be interpreted as vehicle-level boundary conditions that reflect the capability of the low temperature thermal loop. The present parametric results therefore provide design relevant guidance on the robustness of the HBTMS to realistic operating envelopes, including elevated ambient temperature and less favourable coolant conditions. In scaling from a single repeating unit to a module or pack, the dominant additional consideration is coolant distribution uniformity across parallel flow paths; nevertheless, the local thermal response of each cell–PCM–copper foam structure remains governed by the same boundary definitions adopted here. Accordingly, these results can be applied to EV-scale systems by ensuring that the pack manifold and cold-plate design deliver comparable inlet conditions (temperature and mass flow) to each module, thereby preserving the demonstrated thermal margins and temperature uniformity.

4.8 Ambient Temperature

In this section, the impact of varying ambient temperatures (303.15, 308.15, 313.15, and 318.15 K) on the thermal behaviour and design efficiency of the proposed HBTMS during high 5C discharge is investigated. Throughout this study, the porosity and pore density of both the copper foam fins, and the copper foam layers are kept constant at 0.9 and 30 PPI, respectively. Four copper foam fins with a thickness of 4 mm are considered in each PCM housing. The copper tubes within the two cooling plates incorporate copper foam layers with a thickness of 2 mm. A constant coolant inlet mass flow rate of 0.001 kg/s and an inlet temperature of 303.15 K are applied.

The influence of ambient temperature, a key parameter in HBTMSs employing PCM, on the performance of the proposed HBTMS in terms of $T_{Max,Sur}$ and L_f during high 5C discharge rate is illustrated in Figure 4-47. As shown in Figure 4-47 (a), $T_{Max,Sur}$ increases more rapidly at lower ambient temperatures, with rises of 8.67 K and 4.44 K recorded at 303.15 K and 308.15 K, respectively. In contrast, at higher ambient conditions of 313.15 K and 318.15 K, the variation in $T_{Max,Sur}$ during discharge is significantly lower, limited to just 1.7 K and 1.5 K, respectively. This behaviour is explained by the phase state of the PCM. At ambient temperatures below its solidus point (311.15 K), the PCM remains solid initially and only partially melts during discharge, as indicated in Figure 4-47 (b), where the maximum L_f reaches 0.02 due to effective heat removal by the cooling plates. Conversely, at higher ambient temperatures, the PCM is already partially melted at the start of discharge, which allows for more effective thermal management throughout the cycle. These findings emphasise the necessity of hybrid cooling strategies in PCM based BTMSs, not only to enhance thermal conductivity via embedded copper foam fins but also to incorporate reliable external cooling mechanisms such as cooling plates, especially under elevated ambient temperature conditions.

To offer a more comprehensive understanding of the PCM melting behaviour, liquid fraction contour plots at the end of the 5C discharge are illustrated in Figure 4-48. At the lowest ambient temperature of 303.15 K, the PCM surrounding the batteries remains entirely in the solid phase, indicating that the temperature was effectively maintained below the solidus point. As the ambient temperature rises to 308.15 K, melting begins primarily within the copper foam fins, driven by enhanced conduction, while the cooling plates significantly influence batteries 1 to 4 in the first row near the coolant inlet. At 313.15 K, a broader melting of the PCM was observed both within the fins and around batteries 9 to 12, with a relatively uniform melting profile, except for batteries 2 and 3, which benefit from proximity to the cooling inlet, reducing their local PCM melting.

At the highest ambient temperature of 318.15 K, PCM is fully melted around all battery cells; nevertheless, the HBTMS still effectively manages the temperature rise. As shown in Figure 4-47 (a), at ambient temperatures of 313.15 K and 318.15 K, the system maintains $T_{Max,Sur}$ nearly constant and close to the ambient, illustrating effective thermal control. Furthermore, Figure 4-47 (b), demonstrates that at 318.15 K, partial recovery of PCM from the melted state was observed, while at 313.15 K, the liquid fraction remains stable at approximately 0.4, reflecting the system's ability to maintain a controlled and consistent thermal response across a range of ambient conditions.

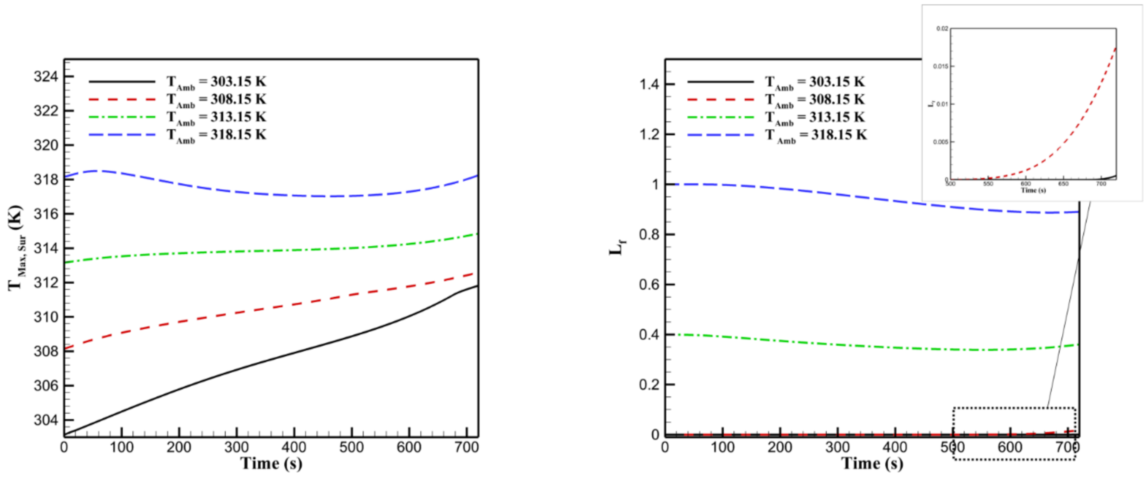

(a) (b)

Figure 4-47. Impact of the ambient temperature on (a) batteries maximum surface temperature and (b) PCM liquid fraction

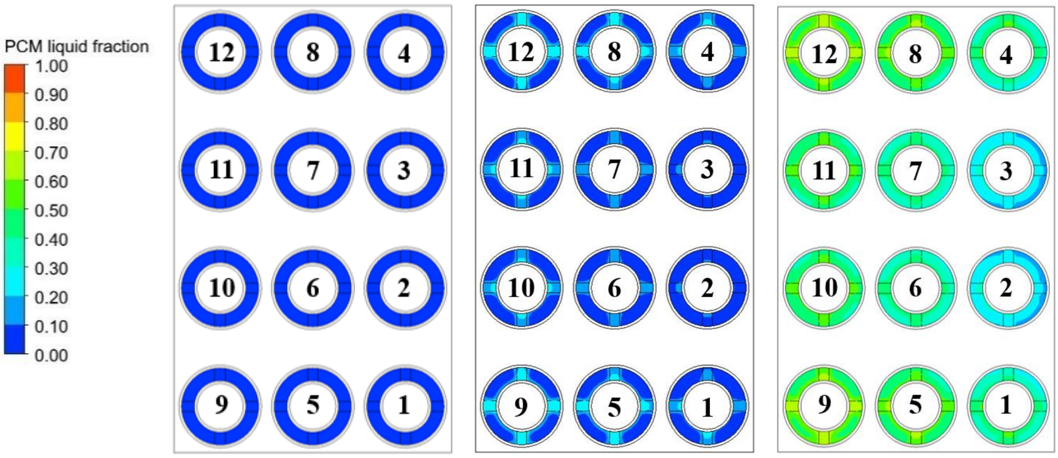

(a) T_{Amb} = 303.15 K (b) T_{Amb} = 308.15 K (c) T_{Amb} = 313.15 K

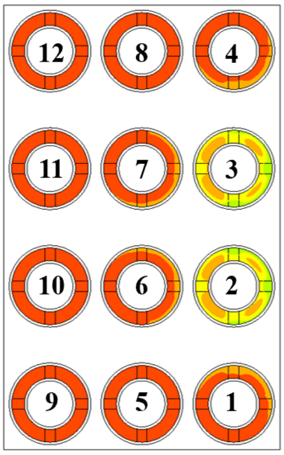

(d) T_{Amb} = 318.15 K

Figure 4-48. PCM liquid fraction contour plots at different ambient temperatures at the end of the 5C discharge: (a) T_{Amb} = 303.15 K, (b) T_{Amb} = 308.15 K, (c) T_{Amb} = 313.15 K, and (d) T_{Amb} = 318.15 K.

The variation of the $\overline{Nu}_b$ under different ambient temperatures is presented in Figure 4-49. At the lowest ambient temperature of 303.15 K, where the PCM remains fully solid and the battery surface temperature does not exceed the PCM melting point, $\overline{Nu}_b$ exhibited a steady increase throughout the discharge process. As the ambient temperature rises to 308.15 K, $\overline{Nu}_b$ reached a peak as the surface temperature approached the PCM solidus temperature and then declined to 135 by end of the 5C discharge. At higher ambient temperatures, 313.15 K and 318.15 K, where the PCM is partially melted at the beginning of the discharge, $\overline{Nu}_b$ exhibited a smoother and more stable trend. Specifically, at 313.15 K, by 500 seconds, $\overline{Nu}_b$ stabilised around 40.8, maintained this level for the remainder of the discharge. This behaviour results from a thermal balance between the heat conducted through the battery housing and into the PCM structure, including the fins, housing, and cooling plates, and the heat removed via forced convection through the copper tubes enhanced by copper foam layers. As evidenced in Figure 4-47 (b), this balance is reflected with a relatively constant L_f throughout the discharge. At the highest ambient temperature of 318.15 K, a similar pattern was observed. $\overline{Nu}_b$ maintained a quasi-steady behaviour during the last 20 seconds of discharge, reaching a value of approximately 20.2.

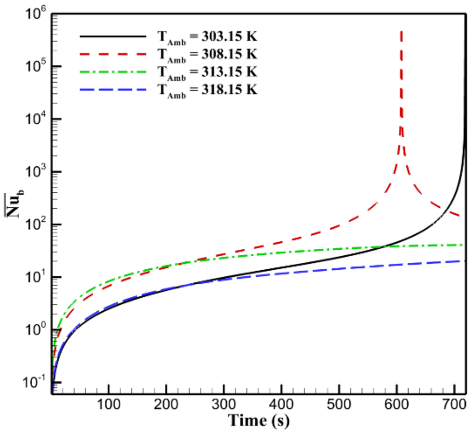

Figure 4-49. Batteries surface average Nusselt number for HBTMS at different ambient temperatures at end of the 5C discharge.

Figure 4-50 presents the $T_{Max,Sur}$ and $\Delta T_{Max,b}$ across individual battery cells at varying ambient temperatures. As the ambient temperature increased, a rise in $T_{Max,Sur}$ was observed, consistently with batteries 9 and 12 exhibiting the highest temperatures, and batteries 2 and 3 the lowest. An upward trend in $\Delta T_{Max,b}$ was also recorded, with the largest values typically occurring on battery 4. Notably, at 308.15 K, $\Delta T_{Max,b}$ decreased by approximately 28% compared to 303.15 K, which is attributed to greater PCM melting at the higher ambient condition. At elevated ambient temperatures of 313.15 K and 318.15 K, the maximum $\Delta T_{Max,b}$ values on battery 4 reached 1 K and 1.2 K, respectively, well below the critical threshold of 5 K. The total temperature variation across all batteries (ΔT_{Max}) in the module remained within acceptable limits, measured as 1.3 K, 1.27 K, 2.1 K, and 3.43 K for ambient conditions of 303.15 K, 308.15 K, 313.15 K, and 318.15 K, respectively. These results underscore that the integration of PCM with longitudinal copper foam fins, combined with copper tube based liquid cooling enhanced by copper foam layers, effectively controls the maximum cell temperatures and ensures thermally uniform operation, even under elevated ambient temperatures.

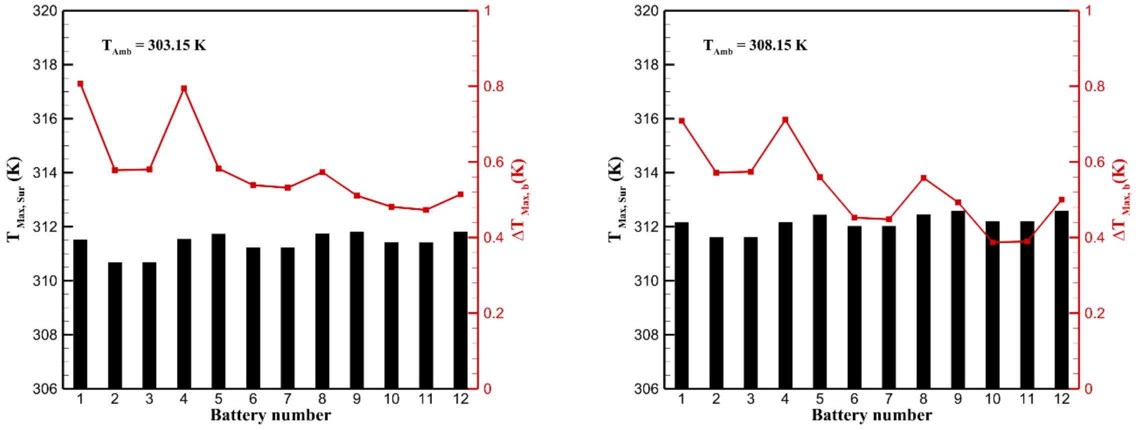

(a) T_{Amb} = 303.15 K (b) T_{Amb} = 308.15 K

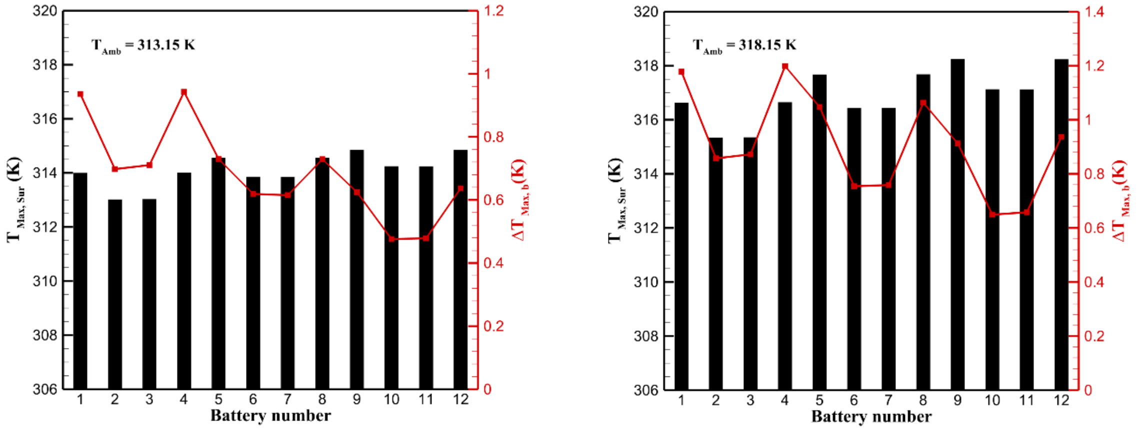

(c) T_{Amb} = 313.15 K (d) T_{Amb} = 318.15 K

Figure 4-50. $T_{Max,Sur}$ and $\Delta T_{Max,b}$ for the HBTMS at the end of the 5C discharge rate for different ambient temperatures: (a) T_{Amb} = 303.15 K, (b) T_{Amb} = 308.15 K, (c) T_{Amb} = 313.15 K, and (d) T_{Amb} = 318.15 K.

Chapter 5: Multi-Objective Optimisation and Performance Evaluation of the Proposed HBTMS

This chapter presents a detailed statistical investigation and optimisation of the proposed HBTMS by examining the collective impact of multiple design and operational parameters. Building upon the insights gained through the comparative and parametric analysis in the previous chapter, this study employs statistical methods to identify the most influential factors and determine their optimal levels for enhanced system performance.

The analysis is structured to provide a comprehensive understanding of how each design and operational variable affects the thermal behaviour and overall performance of the system. In addition to single-objective optimisation, a multi-objective approach is also adopted to identify a balanced configuration that satisfies multiple objectives simultaneously. This integrated evaluation highlights the trade-offs involved in system design and supports the development of an optimised HBTMS that offers improved thermal management, structural efficiency, and energy performance. Throughout the chapter, physical interpretations of observed trends are provided to explain the underlying mechanisms behind the statistical results, supporting a more informed and robust design process.

5.1 Taguchi Design of Experiments for Multi-Parameter Analysis of HBTMS

As shown in Table 5-1, the statistical analysis based on the Taguchi method involved 11 different factors, including the number of cooling plates, ambient temperature, coolant temperature, inlet mass flow rate, copper foam fin thickness, copper foam fins quantity, copper foam fin porosity, copper foam fin pore density, copper foam layer porosity, copper foam layer pore density, and copper foam layer thickness. These factors were systematically varied across three levels to investigate their impact on system performance. Considering 11 factors at three levels, an L27 (3^11) orthogonal array was developed using the Taguchi method in the Minitab software. As detailed in Table 5-2, this array was utilised to explore various HBTMS configurations while identifying the minimum number of required cases for an efficient analysis.

Table 5-1. Factors and levels used in Taguchi method analysis.

Factors	Level 1	Level 2	Level 3
Number of cooling plates	1	2	3
Ambient temperature (K)	308.15	313.15	318.15
Coolant temperature (K)	298.15	303.15	308.15
Inlet mass flow rate (kg/s)	0.0002	0.001	0.002
Copper foam fin thickness (mm)	2	4	6
Copper foam fin quantity	4	6	8
Copper foam fin porosity	0.7	0.8	0.9
Copper foam fin pore density (PPI)	20	30	40
Copper foam layer thickness (mm)	2	2.5	3
Copper foam layer porosity	0.7	0.8	0.9
Copper foam layer pore density (PPI)	20	30	40

Table 5-2. L27 orthogonal array based on the Taguchi method.

Case	Number of cooling plates	Ambient temperature (K)	Coolant temperature (K)	Inlet mass flow rate (kg/s)	Copper foam fin thickness (mm)	Copper foam fin quantity	Copper foam fin porosity	Copper foam fin pore density (PPI)	Copper foam layer porosity	Copper foam layer pore density (PPI)	Copper foam layer thickness (mm)
1	1	308.15	298.15	0.0002	2	4	0.7	20	0.7	20	2
2	1	308.15	298.15	0.0002	4	6	0.8	30	0.8	30	2.5
3	1	308.15	298.15	0.0002	6	8	0.9	40	0.9	40	3
4	1	313.15	303.15	0.001	2	4	0.7	30	0.8	30	3
5	1	313.15	303.15	0.001	4	6	0.8	40	0.9	40	2
6	1	313.15	303.15	0.001	6	8	0.9	20	0.7	20	2.5
7	1	318.15	308.15	0.002	2	4	0.7	40	0.9	40	2.5
8	1	318.15	308.15	0.002	4	6	0.8	20	0.7	20	3
9	1	318.15	308.15	0.002	6	8	0.9	30	0.8	30	2
10	2	308.15	303.15	0.002	2	6	0.9	20	0.8	40	2
11	2	308.15	303.15	0.002	4	8	0.7	30	0.9	20	2.5
12	2	308.15	303.15	0.002	6	4	0.8	40	0.7	30	3
13	2	313.15	308.15	0.0002	2	6	0.9	30	0.9	20	3
14	2	313.15	308.15	0.0002	4	8	0.7	40	0.7	30	2
15	2	313.15	308.15	0.0002	6	4	0.8	20	0.8	40	2.5
16	2	318.15	298.15	0.001	2	6	0.9	40	0.7	30	2.5
17	2	318.15	298.15	0.001	4	8	0.7	20	0.8	40	3
18	2	318.15	298.15	0.001	6	4	0.8	30	0.9	20	2
19	3	308.15	308.15	0.001	2	8	0.8	20	0.9	30	2
20	3	308.15	308.15	0.001	4	4	0.9	30	0.7	40	2.5
21	3	308.15	308.15	0.001	6	6	0.7	40	0.8	20	3
22	3	313.15	298.15	0.002	2	8	0.8	30	0.7	40	3
23	3	313.15	298.15	0.002	4	4	0.9	40	0.8	20	2
24	3	313.15	298.15	0.002	6	6	0.7	20	0.9	30	2.5
25	3	318.15	303.15	0.0002	2	8	0.8	40	0.8	20	2.5
26	3	318.15	303.15	0.0002	4	4	0.9	20	0.9	30	3
27	3	318.15	303.15	0.0002	6	6	0.7	30	0.7	40	2

Based on the developed L27 (3^11) orthogonal array, 27 different HBTMS cases were simulated at a high 5C discharge rate. The results (response variables) at the end of the discharge (720 s) are presented in Table 5-3. The results include the maximum battery surface temperature ($T_{Max,Sur}$), maximum temperature difference within the battery module (ΔT_{Max}), performance evaluation criteria (PEC), reciprocal of performance evaluation criteria (1/PEC), energy density (E_d), reciprocal of energy density ($1/E_d$), and PCM liquid fraction (L_f). These results were systematically analysed to identify the most influential parameters affecting the proposed HBTMS and to optimise its design in terms of both thermal performance and energy density.

As depicted in Table 5-3, the lowest $T_{Max,Sur}$ of 311.3737 K was observed in case 12 for the HBTMS with two cooling plates, four copper foam fins (porosity of 0.8 and pore density of 40 PPI) with thickness of 6 mm, copper foam layer (porosity of 0.7 and pore density of 30 PPI) with thickness of 3 mm at ambient temperature of 308.15 K and water inlet with mass flow rate of 0.002 kg/s at 303.15 K. This low $T_{Max,Sur}$, as shown in Figure 5-1 (c), was achieved due to the highest mass flow rate and metal foam layer thickness among different cases which improves the convective cooling within the copper tubes. Also, the highest thickness of the copper foam fins that has been considered in this case has enhanced the conduction within the PCM. Given the substantial influence of ambient temperature on HBTMS performance, the lowest value among the different simulation cases was selected for analysis. Moreover, the lowest L_f was also observed in this case with the value of 1.48×10^{-6} and as illustrated in Figure 5-1 (d), the PCM has remained unmelted around the batteries as the battery surface temperature is close to the PCM melting temperature of 311.15 K. This phenomenon is attributed to the highest mass flow rate in the liquid cooling system, the greatest copper foam fin thickness, and the low ambient temperature. These factors enhanced heat dissipation from the system, reducing heat storage within the PCM and consequently lowering the thermal load on the HBTMS.

The highest $T_{Max,Sur}$ of 322.9469 K was achieved in case 7 for the HBTMS with one cooling plate, four copper foam fins (porosity of 0.7 and pore density of 40 PPI) with thickness of 2 mm, copper foam layer (porosity of 0.9 and pore density of 40 PPI) with thickness of 2.5 mm at ambient temperature of 318.15 K and water inlet with mass flow rate of 0.002 kg/s at 308.15 K. As depicted in Figure 5-1 (a), $T_{Max,Sur}$ is mostly evident on the batteries 1, 4, 5, 8, 9, and 12 which are further away from the copper tubes. This $T_{Max,Sur}$ is a result of considering HBTMS with one cooling plate at the highest ambient and water inlet temperature along with the lowest quantity and thickness of copper foam fins among the different cases. In this case the HBTMS experienced high thermal load due to high ambient temperature and as shown in Figure 5-1 (b), the highest L_f was recorded for this case and the PCM is fully melted as the ambient temperature is 7 K higher than the PCM melting temperature. In this case as the PCM latent heat was fully utilised and due to thermal saturation [43], it was not able to absorb more heat through its latent heat. Also, the liquid cooling was not able to extract the generated heat effectively to prevent complete melting of PCM even at the highest mass flow rate since the inlet temperature was assumed to be high. This phenomenon, referred to as premature melting [304, 320], can be avoided by improving the design of the HBTMS at high operational temperatures.

The lowest ΔT_{Max} of 0.5843, according to Table 5-3, was observed in case 13 for the HBTMS involving two cooling plates, six copper foam fins (porosity of 0.9 and pore density of 30 PPI) with thickness of 2 mm, copper foam layer (porosity of 0.9 and pore density of 20 PPI) with thickness of 3 mm at ambient temperature of 313.15 K and water inlet with mass flow rate of 0.0002 kg/s at 308.15 K. Although liquid cooling systems are highly effective in dissipating heat, they suffer from the drawback of rising coolant temperature along the cooling channels, particularly at high flow rates, which leads to a nonuniform temperature distribution. In this case relatively low mass flow rate of the water contributes to achieving more uniform temperature which is evident in static temperature contour plots in Figure 5-1 (e). Also, as the PCM L_f has reached 0.6528, it has not been fully melted. As shown in Figure 5-1 (f) the PCM was mostly melted within the copper foam fins. When the PCM is partially melted and undergoing phase transition, its thermal regulation capability becomes more dominant, thereby contributing to enhanced temperature uniformity. In contrast the highest ΔT_{Max} of 4.5866, still blow the threshold of 5 K, was recorded in case 22 for the HBTMS involving three cooling plates, eight copper foam fins (porosity of 0.8 and pore density of 30 PPI) with thickness of 2 mm, copper foam layer (porosity of 0.7 and pore density of 40 PPI) with thickness of 3 mm at ambient temperature of 313.15 K and water inlet with mass flow rate of 0.002 kg/s at 298.15 K. As shown in Figure 5-1 (g), the temperature difference on the batteries' surfaces could be observed especially on batteries 2 and 3 close to the cooling plates inlet. Cooling with high mass flow rate and very low inlet temperature compared to ambient temperature with three cooling plates in this case has caused unfavourable temperature gradient on the batteries. Also, in contrast to case 13, as depicted in Figure 5-1 (g), the PCM is just melted around the batteries

9 to 12 on the last row, indicating that in this the latent heat of the PCM was not effectively utilised.

The Highest PEC value of 1.91 was recorded in case 18 for the HBTMS involving two cooling plates, four copper foam fins (porosity of 0.8 and pore density of 30 PPI) with thickness of 6 mm, copper foam layer (porosity of 0.9 and pore density of 20 PPI) with a thickness of 2 mm at ambient temperature of 318.15 K and water inlet with mass flow rate of 0.001 kg/s at 298.15 K. In this case the pressure drop was minimised due to the lowest copper foam layer thickness and highest porosity at moderate mass flow rate among other simulated cases. Also, the generated heat was transferred effectively by the copper foam fins with the highest thickness to the copper tubes with the lowest inlet temperature. Therefore, in this case the effective forced convection has been provided by the partially filled copper tubes with minimum pressure drop leading to the highest PEC value. In contract the lowest PEC value of 0.4078 was observed in case 22 for the HBTMS including three cooling plates, eight copper foam fins (porosity of 0.8 and pore density of 30 PPI) with a thickness of 2 mm, copper foam layer (porosity of 0.7 and pore density of 40 PPI) with a thickness of 3 mm at ambient temperature of 313.15 K and water inlet with mass flow rate of 0.002 kg/s at 298.15 K. The low PEC value in this case is the result of the highest thickness for copper foam layer with the lowest porosity at the highest inlet mass flow rate leading to the highest pressure drop which outweigh the heat transfer enhancement offered by copper foam layer insertion in the copper tubes.

In terms of the E_d, the highest value of 74.9 was achieved in case 7 for the HBTMS with one cooling plate, four copper foam fins (porosity of 0.7 and pore density of 40 PPI) with a thickness of 2 mm, copper foam layer (porosity of 0.9 and pore density of 40 PPI) with a thickness of 2.5 mm, as this case involves the lowest cooling plate number, fin quantity and fin thickness and high porosity of the copper foam layer. The lowest energy density value of 45.5 was recorded in case 27 for the HBTMS with three cooling plate, six copper foam fins (porosity of 0.7 and pore density of 30 PPI) with a thickness of 6 mm, copper foam layer (porosity of 0.7 and pore density of 40 PPI) with a thickness of 2 mm. In this case, the increased system weight is primarily due to the high number of cooling plates, each incorporating the maximum quantity of copper foam fins with the lowest porosity in both the fins and the copper foam layers.

Table 5-3. Results of simulations for different cases based on L27 orthogonal array.

Case	$T_{Max,Sur}$ (K)	ΔT_{Max} (K)	PEC	1/PEC	E_d (Wh.kg^{-1})	$1/E_d$ (kg.Wh^{-1})	L_f
1	313.9159	1.0689	1.3348	0.7491	72.8	0.0137	0.1825

Case	$T_{Max,Sur}$ (K)	ΔT_{Max} (K)	PEC	1/PEC	E_d (Wh.kg^{-1})	$1/E_d$ (kg.Wh^{-1})	L_f
2	313.1753	1.1032	1.2831	0.7793	69.8	0.0143	0.1687
3	313.8055	1.7866	1.1481	0.8709	70.2	0.0142	0.2975
4	315.1933	2.4667	1.3724	0.7286	73.1	0.0136	0.3930
5	315.2415	1.1828	1.1941	0.8373	70.5	0.0141	0.5814
6	315.0219	2.4853	0.6621	1.5103	69.1	0.0144	0.4801
7	322.9469	3.0728	1.1891	0.8409	74.9	0.0133	1
8	317.8275	3.7208	0.9771	1.0234	69	0.0144	0.8740
9	321.0093	3.1112	1.3695	0.7301	70	0.0142	0.9996
10	312.2005	1.4355	1.6579	0.6031	62	0.0161	0.0043
11	312.2411	0.9696	1.2137	0.8238	54.8	0.0182	0.0389
12	311.3737	2.6836	0.8209	1.2181	57.6	0.0173	1.48×10^{-6}
13	316.1688	0.5843	1.2894	0.7755	62.6	0.0159	0.6528
14	315.2296	0.6051	1.4787	0.6762	53.6	0.0186	0.6179
15	315.5884	0.7704	1.4426	0.6931	58.2	0.0171	0.6029
16	316.9885	2.9921	0.6876	1.4542	60.8	0.0164	0.7697
17	316.0834	3.7835	1.3181	0.7587	53.9	0.0185	0.6618
18	315.5619	3.4334	1.9125	0.5228	59.1	0.0169	0.6033
19	313.4588	0.5979	1.1808	0.8468	52.1	0.0191	0.0072
20	313.0146	0.7339	0.6952	1.4382	51.2	0.0195	0.0072
21	312.396	0.7467	1.2958	0.7717	45.9	0.0217	0.0073
22	311.8159	4.5866	0.4078	2.4517	49.8	0.0200	0.0072
23	312.3606	2.6788	1.2828	0.7795	52.4	0.0190	0.0072
24	312.6778	2.2751	1.1477	0.8712	46.9	0.0213	0.0072
25	320.8838	1.8304	1.2206	0.8192	51	0.0196	0.0072
26	321.2677	1.8471	1.1425	0.8752	53.1	0.0188	0.0072
27	320.1197	1.8658	1.3114	0.7625	45.5	0.0219	0.0072

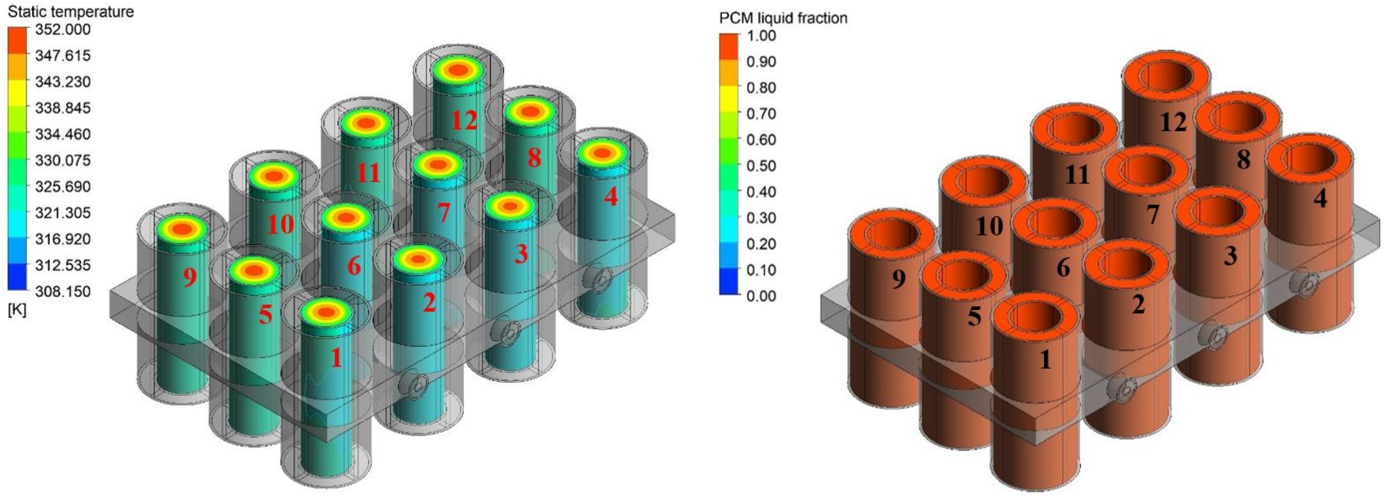

(a) (b)

Case 7

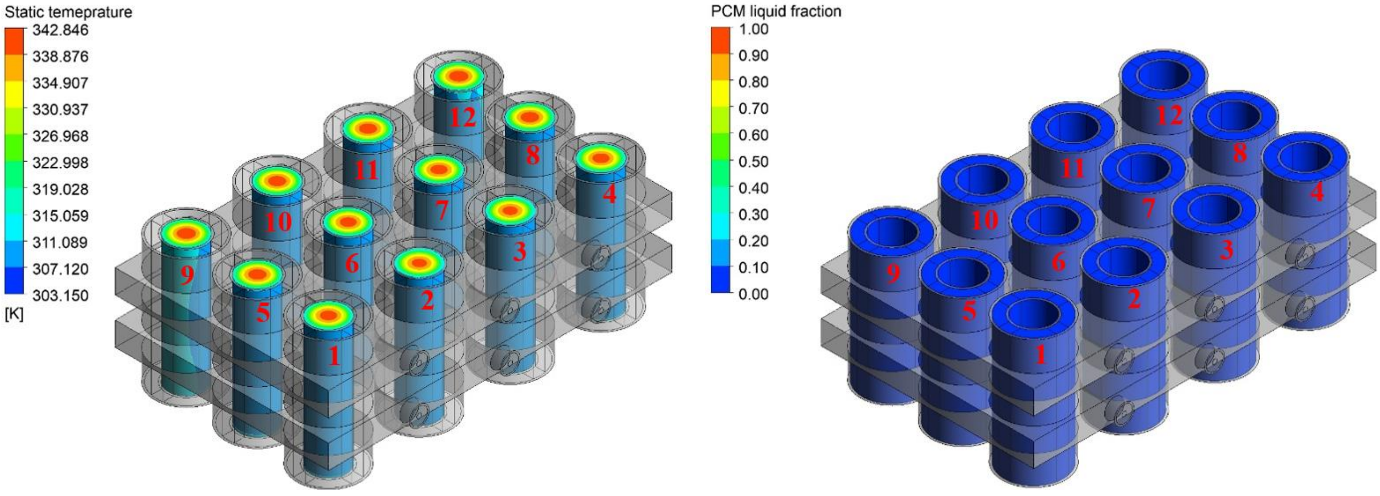

(c) (d)

Case 12

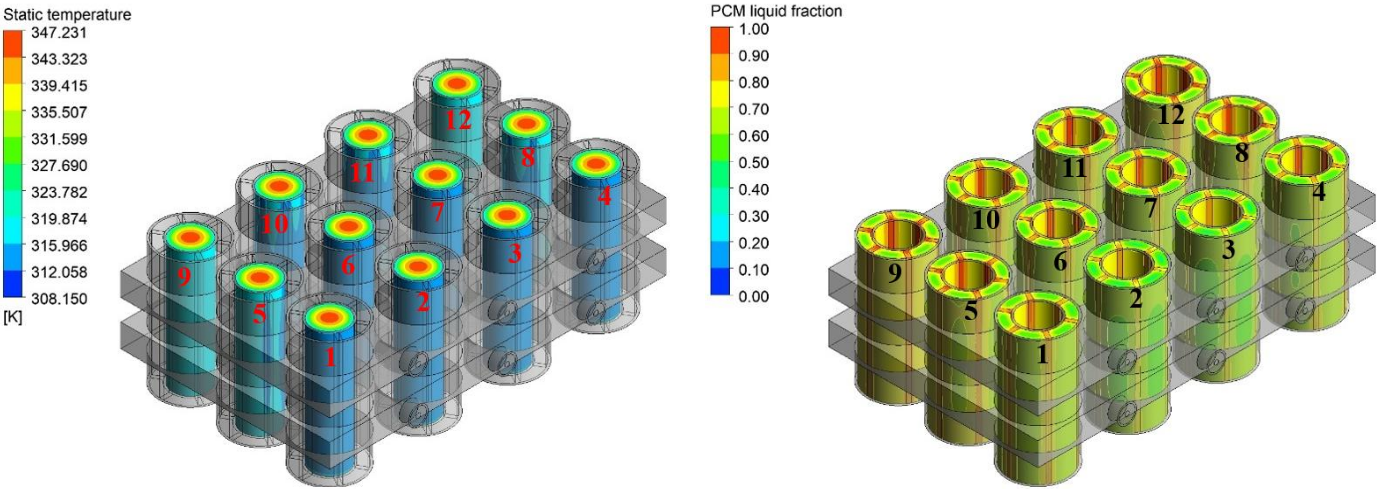

(e) (f)

Case 13

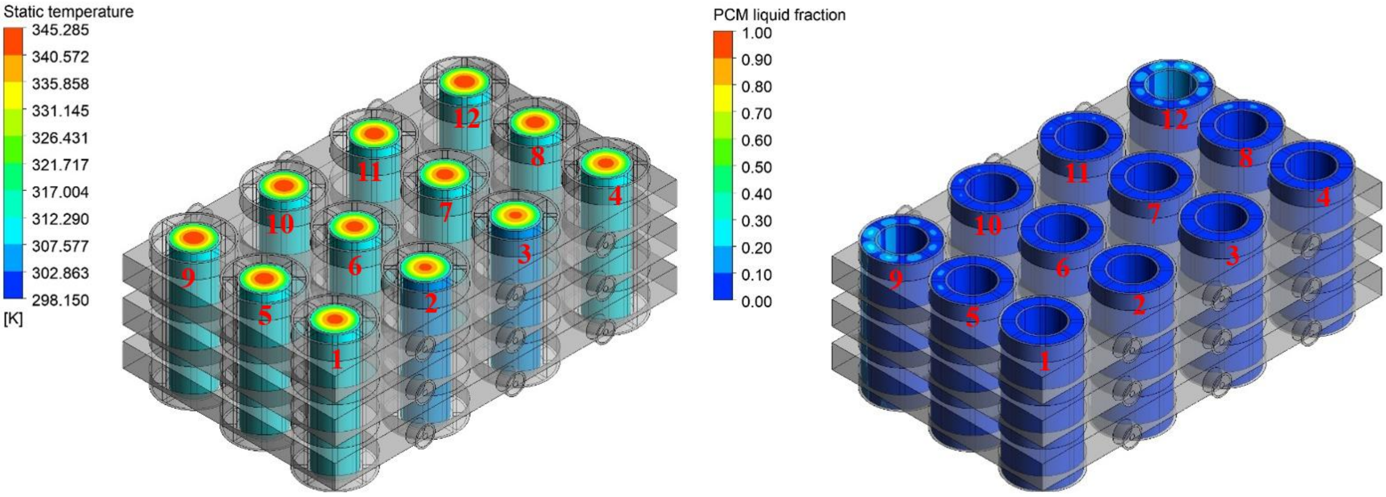

(g) (h)

Case 22

Figure 5-1. Static temperature and PCM liquid fraction contour plots at the end of the 5C discharge for different cases.

5.2 Multi-Response Statistical Analysis for HBTMS Optimisation via Taguchi and ANOVA

To provide a clear picture of the impact of the investigated factors, the Taguchi and ANOVA methods were utilised, for each of the primary response variables of $T_{Max,Sur}$, ΔT_{Max}, PEC, and E_d. For Taguchi analysis of the $T_{Max,Sur}$ and ΔT_{Max} the lower-the-better option was considered to optimise the HBTMS for better thermal performance. However, for improved PEC and E_d higher-the-better approach was followed to provide an effective design.

The results as the Taguchi response signal-to-noise (S/N) table offer a comprehensive analysis of the relative influence of each investigated factor on the selected response variables. Specifically, the level values correspond to the mean (S/N) ratios obtained for each distinct factor level, wherein higher S/N ratios indicate improved system performance or reduced variability in the measured response. Additionally, the Delta values, calculated as the difference between the maximum and minimum mean S/N ratios across the levels for each individual factor, serve as quantitative indicators of factor sensitivity or significance. Consequently, factors demonstrating larger Delta values are identified as having a more pronounced effect on the response of interest, whereas those with lower Delta values display limited influence. The associated parameter rankings, derived directly from the Delta values, facilitate prioritisation of influential factors, thereby guiding targeted optimisation strategies and subsequent system design enhancements [302].

Analysis of variance (ANOVA) represents a robust statistical methodology for determining the relative significance and contribution of individual factors towards a selected response variable. An ANOVA typically includes several essential elements, such as degrees of freedom (DF), adjusted sum of squares (Adj SS), adjusted mean squares (Adj MS), F-values, p-values, and percentage contributions. The adjusted sum of squares quantifies the extent of variability attributable to each factor, whilst the mean square indicates the variability explained per degree of freedom. The F-value is obtained by comparing the variance explained by a particular parameter to the residual error variance, with higher values denoting greater statistical significance, and is expressed as:

$$F_i = \frac{\text{Adj MS}_i}{Error} \tag{5-1}$$

Complementarily, the p-value explicitly determines the statistical significance of parameters, with values below a predefined significance threshold (typically 0.05) indicating a meaningful effect on system performance. The p-value is computed as the upper-tail probability of the F distribution with the corresponding degrees of freedom. Moreover, percentage contribution offers quantitative insight into each factor's relative influence, facilitating clear differentiation between highly influential and comparatively minor factors. Consequently, ANOVA is instrumental in systematically identifying and ranking parameters, thereby guiding targeted optimisation efforts and informed decision-making within performance-driven design processes [306].

5.2.1 Impact Assessment of Design and Operational Parameters on $T_{Max,Sur}$

Mean values of $T_{Max,Sur}$ for each factor and level are depicted in Figure 5-2. With respect to the quantity of cooling plates, the lowest mean $T_{Max,Sur}$ of 314.6 K was achieved when using two plates. This outcome reflects an optimal balance in PCM latent heat utilisation. Specifically, employing a single plate leads to significant PCM melting during discharge, whereas employing three plates results in negligible melting, both of which adversely affect the cooling performance of the system [304]. In contrast, with two plates, the PCM melting remains confined to the pores of the copper foam fins, thereby promoting considerable heat transfer enhancement via conduction within the fins and pore-scale convection and mixing.

Ambient temperature has a similarly pronounced influence on the mean of $T_{Max,Sur}$. The minimum mean $T_{Max,Sur}$ of 312.8 K was observed at 308.15 K, which is below the solidus temperature of the PCM (311.15 K). As a result, the PCM remains in a solid state at the onset of discharge. When the ambient temperature rises to 318.15 K, the mean $T_{Max,Sur}$ increases by 6.4 K. At elevated ambient temperatures, the HBTMS experiences a higher thermal load and reduced convective heat transfer due to the diminished temperature gradient between the system and its surroundings. Moreover, since the initial temperature of the system at the beginning of discharge is higher than the PCM solidus temperature, part of the PCM is already melted resulting in a portion of its latent heat capacity being unusable for subsequent cooling.

A lower coolant inlet temperature likewise was found to be beneficial for reducing the mean of $T_{Max,Sur}$ achieving the minimum value of 314 K at ambient temperature of 298.15 K. Increasing the inlet temperature from 298.15 K to 303.15 K led to 1.9 K rise in mean of $T_{Max,Sur}$. However, a further increase of 5 K in inlet temperature yielded only a modest increase of 0.5 K in the mean of $T_{Max,Sur}$. This diminishing effect can be attributed to the dominant impact of lower inlet temperature on the PCM melting pattern within the HBTMS.

With regard to coolant mass flow rate, higher flow rates generally enhance convective heat transfer and consequently lower the mean of $T_{Max,Sur}$. Notably, raising the mass flow rate from 0.0002 kg/s to 0.001 kg/s reduces the mean of $T_{Max,Sur}$ by 1.9 K, reaching a minimum value of 314.8 K. However, further increasing the flow rate to 0.002 kg/s results in a slight 0.1 K rise. This can be attributed to a reduction in the PCM cooling effectiveness at higher flow rates, where the phase change is delayed, negatively impacting the utilisation of PCM latent heat capacity for cooling.

Regarding the effect of copper foam fin thickness, it can be concluded that increased fin thickness enhances conductive heat transfer pathways within the PCM, thereby reducing the mean of $T_{Max,Sur}$. Thickness of 4 mm facilitates improved conduction pathways within the PCM, yielding a minimum mean of $T_{Max,Sur}$ of 315.2 K. Nevertheless, further increasing the thickness to 6 mm does not appreciably reduce the mean of $T_{Max,Sur}$, as it simultaneously reduces the PCM volume, thereby limiting the system's passive cooling capacity. The influence of the quantity of copper foam fins is similarly limited, with the mean of $T_{Max,Sur}$ values varying by only 0.3–0.4 K. The minimum mean $T_{Max,Sur}$ of 315.2 K was attained when employing four copper foam fins. Porosity and pore density of the copper foam fins each contribute to a fluctuation of less than 1 K in the mean $T_{Max,Sur}$. The minimum mean $T_{Max,Sur}$ of 315 K and 315.3 K were obtained at porosity of 0.8 and pore density of 20 PPI, respectively. Although copper foam fin parameters significantly influence PCM melting behaviour, their overall impact on HBTMS performance, as measured by mean $T_{Max,Sur}$, is modest. Thus, optimal values for these parameters should be determined based on other critical performance criteria, such as energy density.

For the copper foam layer, increasing the porosity from 0.7 to 0.9 leads to an almost linear rise in the mean $T_{Max,Sur}$ from 315 K to 315.9 K. By contrast, the pore density of the copper foam layer yields a maximum variation of 0.4 K when increased from 20 PPI to 40 PPI, indicating a limited effect on the system's cooling performance. Altering the layer thickness similarly induces changes below 0.6 K, with the lowest mean $T_{Max,Sur}$ of 315.1 K observed at 3 mm. Given that copper foam layer parameters demonstrated limited influence on the mean $T_{Max,Sur}$, these parameters need to be optimised based on other important performance indicators, such as energy density and PEC.

Based on the Taguchi main-effect analysis, the optimum combination of factors for minimising the mean of $T_{Max,Sur}$ is as follows: two cooling plates, an ambient temperature of 308.15 K, a coolant temperature of 298.15 K, an inlet mass flow rate of 0.001 kg/s, a copper foam fin thickness of 4 mm, six copper foam fins, a copper foam fin porosity of 0.8 with a pore density of 30 PPI, and a copper foam layer characterised by 0.7 porosity, 20 PPI, and 3 mm thickness. This particular set of design and operational conditions delivers the most effective thermal management configuration by aiming to achieve the lowest mean of $T_{Max,Sur}$.

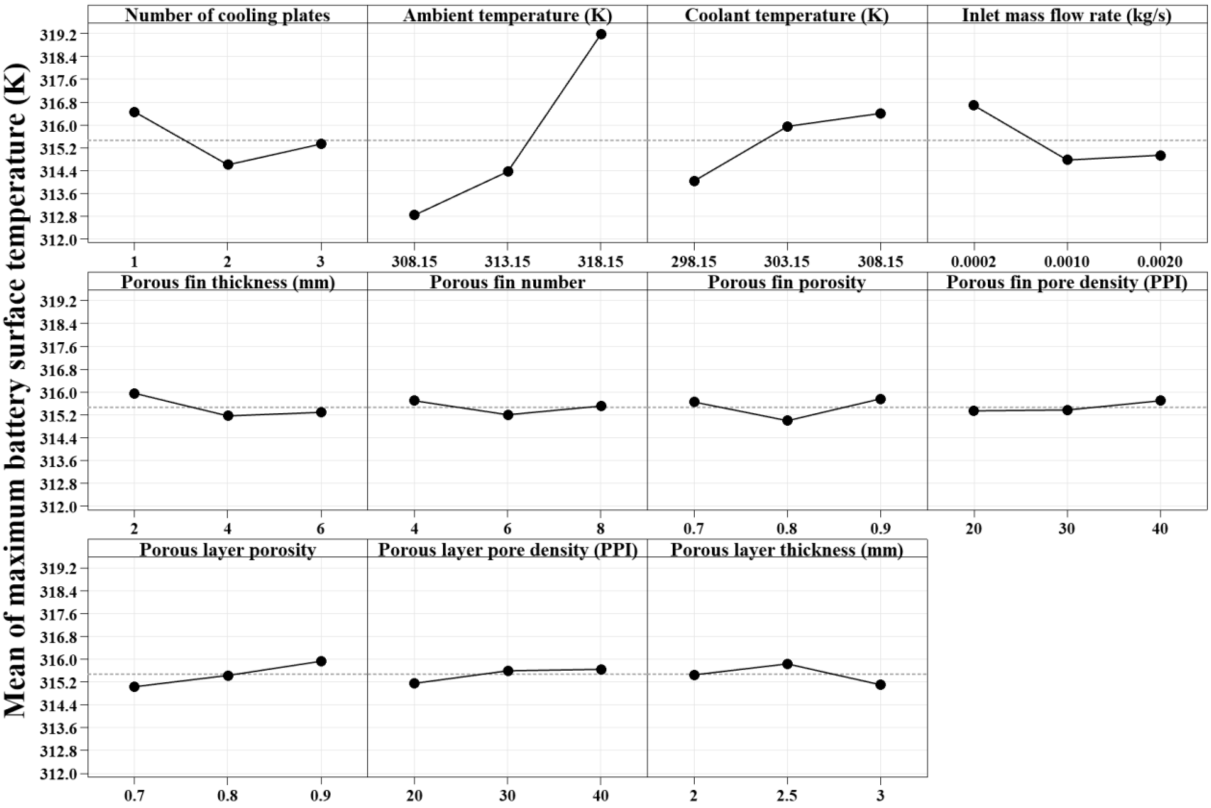

Figure 5-2. Mean of maximum battery surface temperature ($T_{Max,Sur}$) for various factors and levels at the end of the 5C discharge rate.

Table 5-4 summarises the S/N ratios for $T_{Max,Sur}$ across three levels of each factor, along with the corresponding Delta and rank. Notably, ambient temperature exhibits the largest Delta value of 0.17, indicating its dominant influence on the $T_{Max,Sur}$. Coolant temperature with Delta value of 0.06 and inlet mass flow rate with Delta value of 0.05 follow in importance, signifying that both maintaining an appropriate coolant temperature and ensuring sufficient coolant flow are crucial for effective thermal management. The number of cooling plates is ranked fourth by Delta value of 0.05, showing a similar magnitude of effect as inlet mass flow rate but slightly less influence based on the ranking criteria. In contrast, factors related to the copper foam fin design including thickness, number, porosity, and pore density and the copper foam layer properties such as porosity, pore density, and thickness exhibit smaller Delta values in the range of 0.01 to 0.02, suggesting relatively lower impacts on $T_{Max,Sur}$. Nevertheless, these factors still contribute to overall performance, especially when considering additional metrics such as material constraints or energy density. Overall, based on the obtained Taguchi results, controlling ambient temperature, coolant temperature, and coolant flow rate emerges as the most effective strategy for minimising $T_{Max,Sur}$, while fine-tuning the remaining parameters can further optimise system performance.

Table 5-4. Response table for signal to noise ratios (S/N) for each level of factors for maximum battery surface temperature ($T_{Max,Sur}$).

Level	Number of cooling plates	Ambient temperature (K)	Coolant temperature (K)	Inlet mass flow rate (kg/s)	Copper foam fin thickness (mm)	Copper foam fin quantity	Copper foam fin porosity	Copper foam fin pore density (PPI)	Copper foam layer porosity	Copper foam layer pore density (PPI)	Copper foam layer thickness (mm)
1	-50.01	-49.91	-49.94	-50.01	-49.99	-49.98	-49.98	-49.98	-49.97	-49.97	-49.98
2	-49.96	-49.95	-49.99	-49.96	-49.97	-49.97	-49.97	-49.98	-49.98	-49.98	-49.99
3	-49.97	-50.08	-50.00	-49.96	-49.97	-49.98	-49.99	-49.98	-49.99	-49.98	-49.97
Delta	0.05	0.17	0.06	0.05	0.02	0.01	0.02	0.01	0.02	0.01	0.02
Rank	4	1	2	3	6	10	7	11	5	9	8

Table 5-5 presents the ANOVA results for $T_{Max,Sur}$, highlighting the relative importance and statistical significance of each investigated factor. The ambient temperature emerges as the most influential parameter, with the largest Adj SS of 197.487 and the highest percentage contribution of 70.80 %, confirming its dominant impact on the thermal performance. This effect is underscored by a very high F-value of 223.58 and a p-value of less than 0.001, indicating strong statistical significance at the conventional 0.05 level. Subsequently, the coolant temperature emerges as the next most significant factor, accounting for 10.13 % of the total variation. The inlet mass flow rate follows with 7.23%, while the number of cooling plates contributes 5.64 %. All four of these factors exhibit p-values below 0.05, confirming that each has a statistically significant effect on $T_{Max,Sur}$. In contrast, parameters associated with the copper foam fin and copper foam layer design such as thickness, number, porosity, pore density each exhibit comparatively small percentage contributions ranging from 0.25% to 1.30% and higher p-values that exceed the 0.05 threshold, signifying modest or statistically non-significant effects on the $T_{Max,Sur}$. Notably, the error term accounts for a minimal 0.63% of the total variance, suggesting that the selected factors collectively explain the vast majority of variations in $T_{Max,Sur}$. The rankings derived from ANOVA closely match those obtained from the Taguchi analysis for the $T_{Max,Sur}$. Both methods indicate that ambient temperature has the most significant influence, followed by coolant temperature, inlet mass flow rate, and the number of cooling plates. Similarly, parameters related to the copper foam structure exhibit consistent but modest contributions under the conditions investigated.

Table 5-5. ANOVA analysis results for maximum battery surface temperature ($T_{Max,Sur}$).

Source	DF	Adj SS	Adj MS	F-Value	p-Value	Contribution (%)
Number of cooling plates	2	15.734	7.8670	17.81	0.010	5.640316

Source	DF	Adj SS	Adj MS	F-Value	p-Value	Contribution (%)
Ambient temperature (K)	2	197.487	98.7437	223.58	0.000	70.79504
Coolant temperature (K)	2	28.259	14.1293	31.99	0.003	10.13027
Inlet mass flow rate (kg/s)	2	20.164	10.0818	22.83	0.006	7.22838
Copper foam fin thickness (mm)	2	3.271	1.6354	3.70	0.123	1.172586
Copper foam fin quantity	2	1.111	0.5553	1.26	0.377	0.398271
Copper foam fin porosity	2	3.088	1.5438	3.50	0.132	1.106985
Copper foam fin pore density (PPI)	2	0.695	0.3476	0.79	0.515	0.249143
Copper foam layer porosity	2	3.626	1.8132	4.11	0.107	1.299847
Copper foam layer pore density (PPI)	2	1.329	0.6643	1.50	0.326	0.476419
Copper foam layer thickness (mm)	2	2.426	1.2131	2.75	0.178	0.869671
Error	4	1.767	0.4417			0.633433
Total	26	278.956				100

5.2.2 Impact Assessment of Design and Operational Parameters on ΔT_{Max}

The impact of various factors and their respective levels on mean of ΔT_{Max} is presented in Figure 5-3. As shown, increasing the number of cooling plates initially reduces the mean ΔT_{Max}, dropping from 2.22 K to 1.90 K when two plates are employed. This improvement is likely due to enhanced forced convection introduced by multiple cooling plates within the HBTMS. However, further increasing the number of cooling plates beyond two resulted in negligible additional improvement.

Similar to the trend observed for the mean $T_{Max,Sur}$, the mean ΔT_{Max} increased substantially from 1.2 K at an ambient temperature of 308.15 K to 2.85 K at 318.15 K. Higher ambient temperatures impose an increased thermal load on the HBTMS, thereby limiting its temperature management capability. This effect is partly due to the increased melting of the PCM at the start of the discharge, given that the PCM's latent heat is vital in achieving uniform temperature distribution. In contrast, elevating coolant inlet temperature from the baseline value of 298.15 K by 10 K resulted in a reduction of the mean ΔT_{Max} by 1.08 K, achieving the lowest value of 1.55 K. This outcome arises from the particular layout of the HBTMS, wherein the batteries located close to the inlet benefit most from the coolant's high cooling capacity at lower temperatures, while its effectiveness diminishes as it flows in the copper tubes, resulting in greater temperature difference between the first and last rows of batteries. Moreover, as the inlet mass flow rate increases, the mentioned discrepancy in HBTMS cooling becomes more pronounced. As shown, raising the inlet mass flow rate by a factor of ten, from 0.0002 kg/s to 0.002 kg/s, elevated the mean ΔT_{Max} by 115 %, reaching 2.73 K. Consequently, both inlet mass flow rate and temperature contribute markedly to the melting distribution of PCM, especially affecting thermal behaviour in the last rows of batteries.

In terms of copper foam fin thickness, increasing the thickness up to 4 mm reduced the mean ΔT_{Max} to 1.85 K, by providing more robust conduction pathways for initial PCM melting, which primarily occurs within the copper foam fin pores. However, further increasing the thickness beyond 4 mm elevated the mean ΔT_{Max} to 2.13 K, potentially due to a decrease in the overall PCM volume and, consequently, a reduction in passive cooling capacity. Similarly, the quantity of copper foam fins influenced the mean ΔT_{Max}, with the lowest value of 1.77 K achieved using six fins, whereas considering eight fins led to a higher value of 2.20 K, likely attributable to excessive PCM melting and associated thermal gradients. In terms of copper foam fin porosity, the minimum mean ΔT_{Max} was achieved at a porosity of 0.7, attributed to enhanced conduction heat transfer within the PCM. Increasing the porosity to 0.8 weakens conductive heat transfer, increasing the mean ΔT_{Max} up to 2.20 K, whereas at 0.9, more PCM is accommodated in the pores, and pore scale convection of the melted PCM alongside conduction results in reducing the mean ΔT_{Max} to 1.96 K. By contrast, pore density exhibited only minor fluctuations below 0.1 K, with 40 PPI producing the lowest mean ΔT_{Max} of 1.95 K. Hence, while the quantity and thickness of fins predominantly improve overall heat conduction and PCM melting patterns, the porosity and pore density further refine temperature uniformity through a balance of conduction and pore-scale convection.

Copper foam layer porosity was observed to have a linear influence on the mean ΔT_{Max}. The lowest mean ΔT_{Max} of 1.75 K was observed at a porosity of 0.9, highlighting enhanced convection within the copper tubes at higher porosity. Variations in the copper foam layer pore density had minimal impact on mean ΔT_{Max}, with fluctuations limited to 0.1 K, similar to the copper foam fin pore density. However, unlike the copper foam fin pore density, the lowest mean ΔT_{Max} for the copper foam layer pore density occurred at the lowest pore density of 20 PPI. Furthermore, increasing the copper foam layer thickness to 2.5 mm from the initial value of 2 mm resulted in minor variations of the mean ΔT_{Max} below 0.1 K initially. Nevertheless, by further increasing of the thickness as the forced convection cooling impact becomes more dominant on the first row of the batteries in the module, the mean of ΔT_{Max} was increased by 0.67 K, reaching the maximum value of 2.47 K.

Based on the obtained results, the combination of the factors minimising the mean ΔT_{Max} corresponds to the following factor levels: three cooling plates, 308.15 K ambient temperature, 308.15 K coolant temperature, inlet mass flow rate of 0.0002 kg/s, six copper foam fins with thickness of 4 mm, 0.7 porosity and 40 PPI pore density, copper foam layer with thickness of 2 mm, 0.9 porosity and 20 PPI pore density. Although ambient temperature and flow rate rank as the most critical factors, fine-tuning the copper foam fin and layer properties provides additional improvements in temperature uniformity.

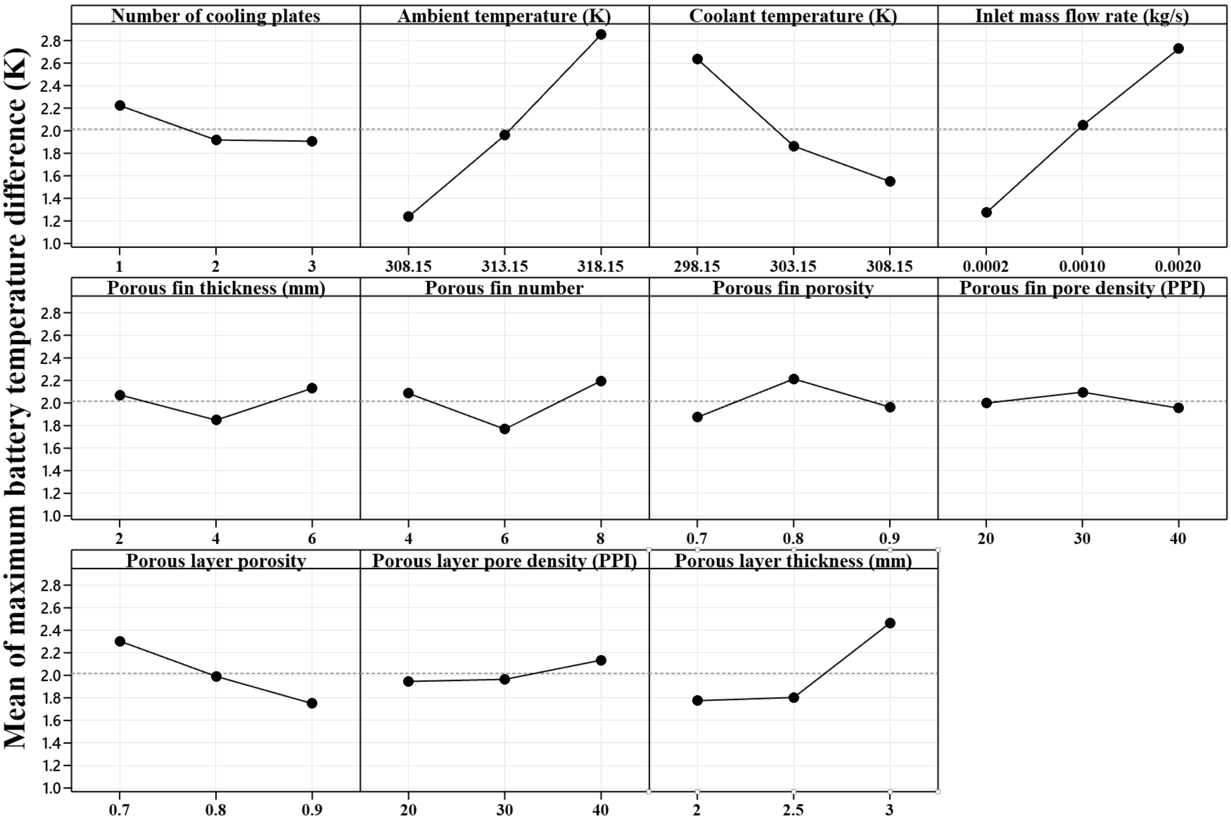

Figure 5-3. Mean of maximum temperature difference within the battery module (ΔT_{Max}) for various factors and levels at the end of the 5C discharge rate.

Table 5-6 presents the S/N ratios for ΔT_{Max} across three levels of each factor, along with each Delta values and overall rank. Ambient temperature with a Delta value of 7.84 was found to be the most influential parameter, indicating that lower ambient temperatures, such as 308.15 K, are most effective at minimising ΔT_{Max}. Inlet mass flow rate followed with a Delta of 6.69, suggesting that a minimal flow rate of 0.0002 kg/s provides greater temperature uniformity. Coolant temperature ranked third, with a Delta value of 6.35, highlighting that a moderate coolant temperature of 308.15 K could reduce temperature gradients.

Among the middle-ranked parameters, copper foam layer thickness has a Delta value of 2.76 and is ranked fourth, indicating that a thinner layer of 2 mm supports more uniform heat distribution. The number of cooling plates holds the subsequent standing with a Delta of 2.52, showing that employing three plates balances cooling without introducing high temperature difference. Copper foam layer porosity features a Delta of 2.17, reinforcing that higher porosity of 0.9 further enhances thermal uniformity. Copper foam fin thickness with a Delta of 1.99 and a rank of 7, achieves optimal performance at 4 mm, while the quantity of copper foam fins by a Delta of 1.62 and a rank of 8, indicates that six fins enhance temperature uniformity. Copper foam fin porosity follows with a Delta of 1.07 and a rank of 9, providing uniformity at lower porosity of 0.7. Copper foam layer pore density has a Delta of 0.85 and is ranked tenth, implying a slight advantage at 20 PPI, whereas copper foam fin pore density, with a Delta of 0.10 and the lowest rank of 11, found to have only a minimal effect on the maximum temperature difference within the battery module.

Overall, external and operational parameters, notably ambient temperature, coolant flow conditions, and coolant temperature, dominate the control of ΔT_{Max}. Conversely, fin related, and copper foam layer characteristics provide more subtle refinements, collectively contributing to enhanced thermal uniformity within the battery module.

Table 5-6. Response table for signal to noise ratios (S/N) for each level of factors for maximum temperature difference within the battery module (ΔT_{Max}).

Level	Number of cooling plates	Ambient temperature (K)	Coolant temperature (K)	Inlet mass flow rate (kg/s)	Copper foam fin thickness (mm)	Copper foam fin quantity	Copper foam fin porosity	Copper foam fin pore density (PPI)	Copper foam layer porosity	Copper foam layer pore density (PPI)	Copper foam layer thickness (mm)
1	-6.07	-0.91	-7.46	-1.24	-4.46	-5.15	-3.90	-4.48	-5.50	-4.10	-3.43
2	-3.54	-3.87	-4.96	-4.36	-3.53	-3.52	-4.97	-4.47	-4.69	-4.47	-3.91
3	-3.91	-8.75	-1.11	-7.93	-5.53	-4.86	-4.66	-4.58	-3.33	-4.96	-6.19
Delta	2.52	7.84	6.35	6.69	1.99	1.62	1.07	0.10	2.17	0.85	2.76
Rank	5	1	3	2	7	8	9	11	6	10	4

Table 5-7 summarises the analysis of ANOVA results for ΔT_{Max}, illustrating the influence of each factor on the maximum battery temperature difference. Ambient temperature emerges as the dominant parameter, contributing approximately 34.48 %, with a high F-value of 59.96 and a highly significant p-value of 0.001. Inlet mass flow rate follows with a 27.84 % contribution and p-value of 0.002, indicating that the rate at which coolant circulates significantly affects temperature uniformity. Coolant temperature, accounting for 16.43 % of the variation with p-value of 0.004, likewise plays a major role in minimising thermal discrepancies. Copper foam layer thickness contributes 8.08 % and p-value of 0.016, making it statistically significant for ensuring even temperature distribution, whereas copper foam layer porosity, at 4.08 % and p-value of 0.048, has a moderate yet meaningful impact. The remaining factors, including the number of cooling plates, copper foam fin thickness, fin quantity, and related structural parameters, each has less than 3 % of the total variability and exhibit non-significant p-values above 0.05. Notably, these ANOVA findings align closely with the

Taguchi S/N analysis results. Similarly, these findings underscore the critical importance of controlling ambient temperature, coolant characteristics, and key copper foam layer properties to mitigate ΔT_{Max}.

Table 5-7. ANOVA analysis results for maximum temperature difference within the battery module (ΔT_{Max}).

Source	DF	Adj SS	Adj MS	F-Value	p-Value	Contribution (%)
Number of cooling plates	2	0.5764	0.28820	2.94	0.164	1.688134
Ambient temperature (K)	2	11.7728	5.88639	59.96	0.001	34.47965
Coolant temperature (K)	2	5.6117	2.80586	28.58	0.004	16.4353
Inlet mass flow rate (kg/s)	2	9.5069	4.75343	48.42	0.002	27.84338
Copper foam fin thickness (mm)	2	0.3975	0.19876	2.02	0.247	1.16418
Copper foam fin quantity	2	0.8868	0.44338	4.52	0.094	2.59722
Copper foam fin porosity	2	0.5578	0.27888	2.84	0.171	1.63366
Copper foam fin pore density (PPI)	2	0.0944	0.04722	0.48	0.650	0.276474
Copper foam layer porosity	2	1.3921	0.69606	7.09	0.048	4.07712
Copper foam layer pore density (PPI)	2	0.1954	0.09769	1.00	0.446	0.572279
Copper foam layer thickness (mm)	2	2.7598	1.37990	14.06	0.016	8.082778
Error	4	0.3927	0.09817			1.150122
Total	26	34.1442				100

5.2.3 Impact Assessment of Design and Operational Parameters on PEC

Figure 5-4 illustrates the influence of various factors and levels on the PEC. Variations in the number of cooling plates directly affect the rate at which heat is conducted to the copper tubes and subsequently dissipated via forced convection. The optimal thermal performance, indicated by the highest mean PEC value of 1.31, was achieved using two cooling plates. This outcome is attributed to the effective balance achieved with two plates, promoting efficient latent heat utilisation of the PCM and ensuring adequate PCM melting within the copper foam fins to facilitate pore scale convection heat transfer toward the copper tubes. However, increasing the number of cooling plates beyond this optimum reduces PCM melting due to diminished latent heat utilisation, resulting in a significant decline in the mean PEC to 1.07.

Ambient temperature exhibited a varying influence on the system's thermal performance, as indicated by the mean PEC values. At the lower ambient temperature of 308.15 K, a mean PEC of 1.18 was recorded. This value decreased slightly to 1.14 when the ambient temperature increased to 313.15 K, a reduction attributed to more extensive PCM melting, which diminished the contribution of passive cooling relative to active cooling within the HBTMS. However, upon further increasing the ambient temperature to 318.15 K, the mean PEC rose again to 1.23. At this higher temperature, the PCM melting intensifies, reducing the available latent heat capacity for passive cooling and thereby increasing heat conduction toward the cooling plates. Consequently, the system becomes more reliant on active cooling through the cooling plates, leading to enhanced overall heat transfer performance and a corresponding rise in the mean PEC value.

Coolant inlet temperature exhibited only a minor influence on the mean PEC, with maximum variation of 0.04. Conversely, the inlet mass flow rate significantly influenced PEC, primarily due to its direct relationship with the pressure drop within the copper tubes. As depicted, increasing the inlet mass flow rate from 0.0002 kg/s to 0.002 kg/s reduced the mean PEC value by approximately 14.5 %, reaching its minimum of 1.12. This substantial decline underscores the critical trade-off between enhanced convective cooling performance and increased pressure drop, reflected clearly in the considerable reduction of PEC at higher mass flow rates.

Increasing the copper foam fin thickness positively influenced the PEC value, with the mean PEC rising progressively as thickness increased from 2 mm to 6 mm, reaching a maximum mean value of 1.23. This enhancement results from improved conduction paths provided by thicker fins, enabling more efficient heat transfer to the cooling tubes. Conversely, increasing the quantity of copper foam fins exhibited an opposite effect. As the quantity of fins increased from four to eight, the system experienced a reduction in PEC, dropping by approximately 11% to a mean value of 1.12. This reduction is likely due to an increased amount of PCM melting within numerous fins, which adversely affected the balance between passive and active cooling, resulting in diminished active cooling portion. Additionally, increasing copper foam fin porosity also showed a declining trend in the mean PEC value. Higher porosity fins decreased the effective thermal conductivity with the conduction paths provided by fins within the PCM, thereby reducing conductive heat transport within the PCM and limiting overall PEC performance. Specifically, mean PEC decreased progressively as porosity increased, highlighting reduced conduction effectiveness at higher porosities. Conversely, copper foam fin pore density exhibited minimal influence on the PEC, with fluctuations limited to about 0.06. The highest mean PEC value was observed at 20 PPI, indicating only minor improvements associated with lower pore densities.

The copper foam layer characteristics also demonstrated a noticeable impact on the PEC value, particularly concerning porosity, pore density, and layer thickness. An intermediate porosity of 0.8 provided the highest mean PEC value of 1.31, indicating an optimal balance between convective heat transfer and pressure drop. Conversely, lower porosity of 0.7 resulted in a substantial decrease in PEC to an unfavourable value of 0.93, which is below 1, suggesting significantly increased flow resistance and pressure drop, while higher porosity of 0.9 moderately reduced PEC to 1.26. The mean PEC exhibited a slight downward trend as the pore density of the copper foam layer increased. Specifically, increasing the pore density from 20 PPI to 40 PPI reduced the mean PEC by approximately 0.06, representing a decline of about 7%. The highest PEC value of 1.24 was recorded at a pore density of 20 PPI. Copper foam layer thickness significantly influenced PEC, with a pronounced 25% reduction observed as the thickness increased from 2 mm to 2.5 mm, corresponding to the lowest PEC value of 1.06. This decrease is attributed to increased pressure drop within the copper foam layers. However, further increasing the thickness to 3 mm slightly improved PEC, possibly due to reduced flow resistance as the coolant was forced into the clear region of the copper tubes.

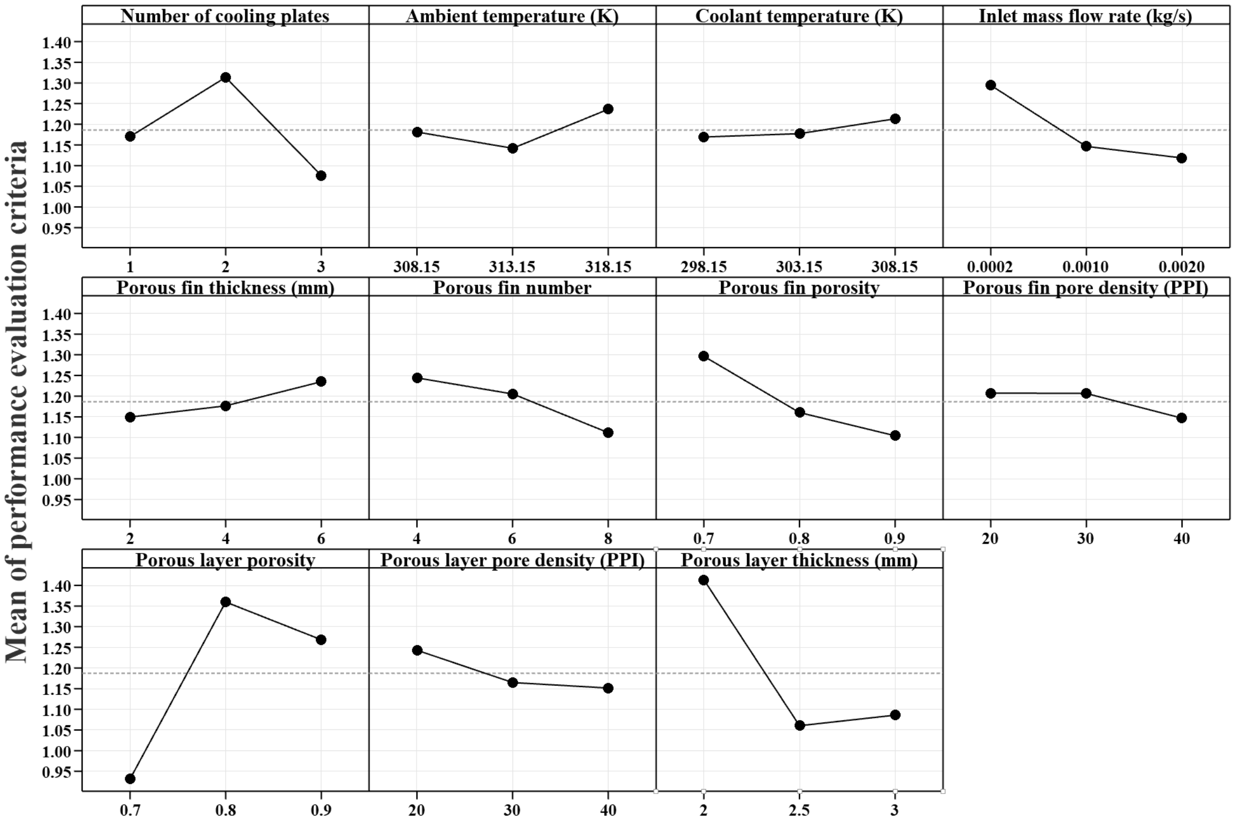

Figure 5-4. Mean of performance evaluation criteria (PEC) for various factors and levels at the end of the 5C discharge rate.

Table 5-8 presents the S/N ratios for the PEC across three levels of each factor, along with their corresponding Delta values and overall rank. Copper foam layer porosity emerged as the most influential parameter, with the highest Delta value of 3.91, indicating that a porosity level of 0.8 maximises PEC. Copper foam layer thickness follows closely with a Delta value of 2.74, showing that a thinner layer of 2 mm enhances performance. The number of cooling plates is the third most significant factor, with a Delta of 1.84, highlighting that employing two cooling plates optimises convection heat transfer efficiency along with pressure drop in the copper tubes.

Among the moderately impactful factors, copper foam fin porosity ranks fourth with a Delta of 1.80, indicating that a lower porosity of 0.7 leads to improved PEC. Inlet mass flow rate ranks fifth, with a Delta of 1.77, emphasising that a lower flow rate of 0.0002 kg/s enhances system performance. The quantity of copper foam fins follows, with a Delta of 1.20, highlighting that a reduced fin quantity contributes positively to PEC. Ambient temperature has a lower degree of influence, standing in the seventh position with a Delta of 1.00, where a higher temperature of 318.15 K presents minor improvements.

Among the least significant factors, copper foam layer pore density has a Delta of 0.97 and ranks eighth, suggesting that a lower pore density of 20 PPI is slightly preferable. Copper foam fin thickness, with a Delta of 0.86, is considered the ninth most significant factor, where an optimal thickness of 6 mm. Coolant temperature follows in the tenth position with a Delta of 0.79, indicates that a moderate temperature of 308.15 K is slightly beneficial. Finally, copper foam fin pore density has the lowest Delta value of 0.44 and ranks eleventh, implying a negligible effect on PEC.

Overall, copper foam layer characteristics and cooling plate configuration are the most dominant factors affecting PEC, followed by flow rate and copper foam fin properties, which provide moderate improvements. Coolant-related parameters and fin pore density exhibit minimal influence, suggesting that their impact on PEC is relatively limited. These findings indicate that optimising copper foam layer porosity, thickness, and the number of cooling plates is crucial for enhancing PEC, while adjustments to coolant conditions and fin pore density play a more secondary role.

Table 5-8. Response table for signal to noise ratios (S/N) for each level of factors for performance evaluation criteria (PEC).

Level	Number of cooling plates	Ambient temperature (K)	Coolant temperature (K)	Inlet mass flow rate (kg/s)	Copper foam fin thickness (mm)	Copper foam fin quantity	Copper foam fin porosity	Copper foam fin pore density (PPI)	Copper foam layer porosity	Copper foam layer pore density (PPI)	Copper foam layer thickness (mm)
1	1.18	1.20	0.69	2.21	0.61	1.56	2.23	1.39	-1.27	1.60	2.91
2	1.99	0.56	1.15	0.67	1.24	1.41	0.67	0.95	2.64	1.10	0.16
3	0.15	1.56	1.48	0.44	1.47	0.36	0.43	0.98	1.95	0.63	0.25
Delta	1.84	1.00	0.79	1.77	0.86	1.20	1.80	0.44	3.91	0.97	2.74
Rank	3	7	10	5	9	6	4	11	1	8	2

Table 5-9 presents the results of the ANOVA for the PEC, identifying the statistical significance and contribution of each factor to the overall system performance. Among all factors, copper foam layer porosity is identified as the most influential parameter, contributing 35.18% to PEC variation. This factor exhibits a high F-value of 10.76 and a p-value of 0.025, indicating strong statistical significance. Copper foam layer thickness follows as the second most impactful parameter, with a 26.68% contribution, an F-value of 8.16, and a p-value of 0.039, confirming its significant effect on PEC. Together, these two parameters account for over 60% of the total contribution, underscoring their critical role in optimising PEC.

The number of cooling plates ranks third in terms of influence, contributing 9.82% to PEC variation, though its p-value of 0.160 suggests that its impact is not statistically significant. Similarly, copper foam fin porosity and inlet mass flow rate contribute 6.68% and 6.15%, respectively, with moderate F-values of 2.04 and 1.88, though their p-values remain above 0.05, indicating that their effects do not reach statistical significance. The number of copper foam fins, with a contribution of 3.19%, also demonstrate a minor but noticeable impact.

The remaining factors including ambient temperature, coolant temperature, copper foam fin thickness, copper foam fin pore density, and copper foam layer pore density exhibit low contributions, all below 2%, with correspondingly low F-values and high p-values. This suggests that their impact on PEC is minimal and statistically insignificant. The error term accounts for 6.54% of the total variation, indicating that the studied cases adequately capture most of the influential factors.

The ANOVA results align closely with the Taguchi analysis, both identifying copper foam layer porosity and thickness as the most influential factors in optimising PEC. While the Taguchi method ranked the number of cooling plates as the third most impactful parameter, ANOVA assigns it a similar contribution but without statistical significance. Additionally, both analyses suggest that copper foam fin porosity and inlet mass flow rate have moderate influence, though ANOVA deems their effects statistically inconclusive. Conversely, parameters such as ambient temperature, coolant temperature, and copper foam fin pore density exhibit minimal impact in both methods, reinforcing their limited role in PEC enhancement.

Table 5-9. ANOVA analysis results for performance evaluation criteria (PEC).

Source	DF	Adj SS	Adj MS	F-Value	p-Value	Contribution (%)
Number of cooling plates	2	0.25731	0.128655	3.00	0.160	9.81983
Ambient temperature (K)	2	0.04059	0.020295	0.47	0.654	1.549053
Coolant temperature (K)	2	0.00986	0.004931	0.12	0.894	0.376291
Inlet mass flow rate (kg/s)	2	0.16110	0.080552	1.88	0.266	6.148128

Source	DF	Adj SS	Adj MS	F-Value	p-Value	Contribution (%)
Copper foam fin thickness (mm)	2	0.03441	0.017204	0.40	0.694	1.313203
Copper foam fin quantity	2	0.08368	0.041839	0.98	0.452	3.193515
Copper foam fin porosity	2	0.17513	0.087563	2.04	0.245	6.68356
Copper foam fin pore density (PPI)	2	0.02172	0.010859	0.25	0.788	0.82891
Copper foam layer porosity	2	0.92183	0.460916	10.76	0.025	35.18019
Copper foam layer pore density (PPI)	2	0.04412	0.022062	0.51	0.632	1.68377
Copper foam layer thickness (mm)	2	0.69916	0.349582	8.16	0.039	26.68234
Error	4	0.17139	0.042848			6.540829
Total	26	2.62031				100

5.2.4 Impact Assessment of Design and Operational Parameters on E_d

The influence of the investigated factors and their levels on the mean E_d is illustrated in Figure 5-5. As shown, the substantial weight of the cooling plates leads to a significant reduction in energy density as their number increases. Specifically, when three cooling plates are used, the mean E_d decreases by 30% compared to a single cooling plate, reaching a minimum value of 49.77. In contrast, external factors such as ambient temperature, coolant inlet temperature, and inlet mass flow rate do not affect the system's weight, resulting in a relatively constant mean E_d.

In terms of copper foam fin thickness, increasing it from 2 mm to 6 mm led to a 7% reduction in the maximum mean E_d, decreasing from 62.12 to a minimum of 58.06. This reduction is attributed to the added weight of thicker copper foam fins. Similarly, increasing the quantity of copper foam fins in the system resulted in a 5% decline in mean E_d. However, as porosity increased, the copper volume within the fins decreased at a constant overall volume, leading to a 6% improvement in mean E_d, reaching a maximum of 61.27 at a porosity of 0.9. In contrast, variations in pore density, while maintaining a constant porosity, did not affect the system's weight, resulting in a nearly constant mean E_d.

Similar to fin porosity, higher porosity in copper foam layers contributed to an improvement in mean E_d. Copper foam layers with a porosity of 0.9 enhanced mean E_d by 3% compared to the porosity of 0.7. Variations in pore density within the copper foam layer resulted in nearly identical mean E_d values, as the system's weight remains unaffected by this factor. In contrast to copper foam fin thickness, changes in copper foam layer thickness had a limited impact on mean E_d, with a maximum variation of only 0.3.

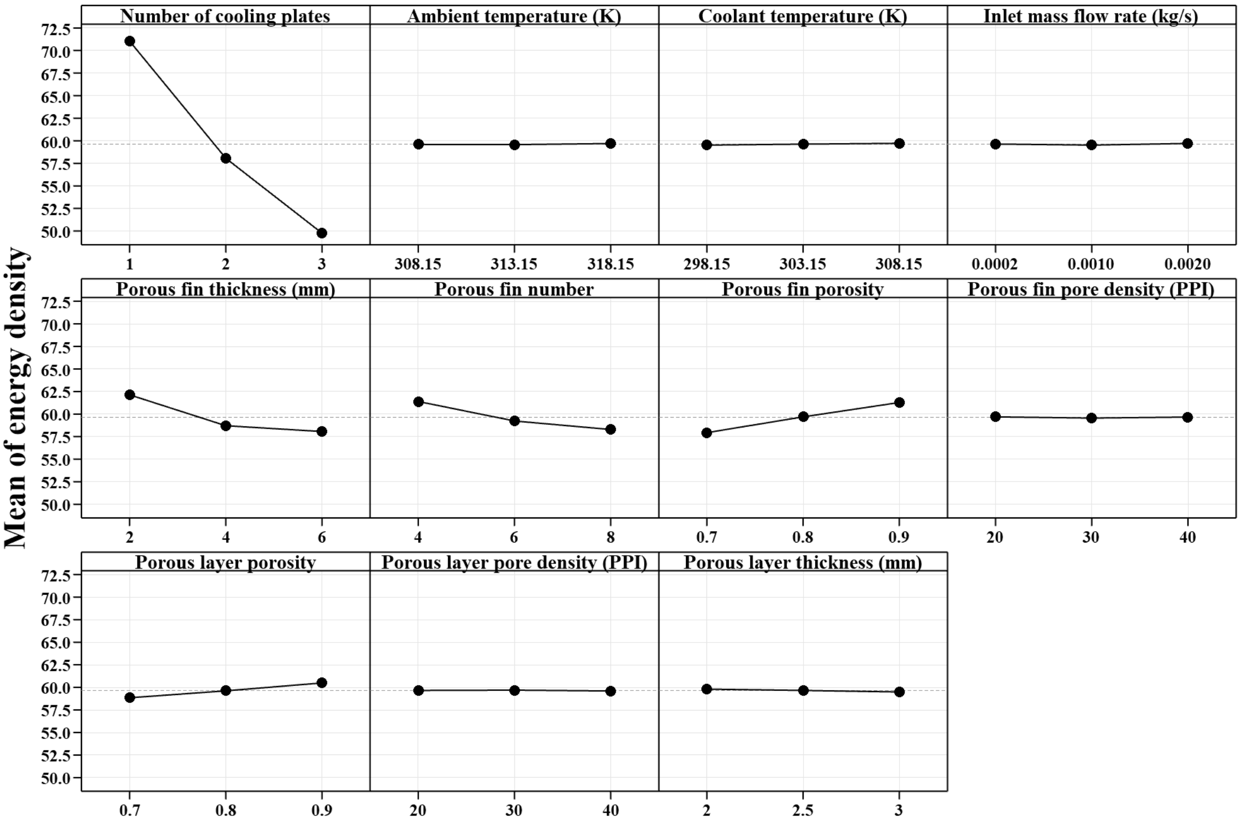

Figure 5-5. Mean of energy density (E_d) for various factors and levels at the end of the 5C discharge rate.

Table 5-10 presents the response table of S/N ratios for the E_d, highlighting the influence of various factors on system performance. Among the analysed parameters, the number of cooling plates emerges as the most influential factor, with the highest Delta value of 3.10. The results indicate that an increase in the number of cooling plates leads to a reduction in the S/N ratio, suggesting a negative impact on E_d. The second most significant factor is copper foam fin thickness, with a Delta value of 0.61, followed closely by copper foam fin porosity, with a Delta value of 0.59. Meanwhile, higher copper foam fin porosity appears to improve E_d up to a certain level, but excessive porosity may compromise structural stability and thermal performance. The copper foam fin quantity, with a Delta value of 0.44, is another moderately influential factor, implying that an increase in the quantity of fins can influence E_d; however, its effect is less pronounced than that of cooling plates, fin thickness, or porosity. Similarly, copper foam layer porosity, with a Delta value of 0.25, demonstrates a moderate impact, indicating that variations in porosity within the copper foam layer contribute to minor changes in E_d. Other copper foam layer properties, such as copper foam layer thickness, with a Delta value of 0.05, and copper foam layer pore density, with a Delta value of 0.04, exhibit a relatively small effect on E_d.

In contrast, the cooling-related parameters, including ambient temperature, coolant temperature, and inlet mass flow rate, exhibit the lowest Delta values, ranging from 0.01 to 0.02, ranking them as the least influential factors. Unlike their significant role in controlling battery surface temperature, these parameters appear to have a negligible impact on E_d. This suggests that while cooling conditions are crucial for thermal management, E_d is predominantly influenced by structural and material characteristics rather than by variations in temperature or flow conditions.

Overall, the findings indicate that E_d optimisation should prioritise structural modifications, particularly the number of cooling plates, copper foam fin thickness, and porosity, rather than relying on cooling parameters. The minimal impact of coolant temperature and mass flow rate suggests that improvements in E_d can be achieved without significant modifications to the cooling system, thereby focusing design efforts on material selection and structural enhancements. These insights provide valuable guidance for optimising thermal management strategies while maintaining high efficiency in battery cooling applications.

Table 5-10. Response table for signal to noise ratios (S/N) for each level of factors for energy density (E_d).

Level	Number of cooling plates	Ambient temperature (K)	Coolant temperature (K)	Inlet mass flow rate (kg/s)	Copper foam fin thickness (mm)	Copper foam fin quantity	Copper foam fin porosity	Copper foam fin pore density (PPI)	Copper foam layer porosity	Copper foam layer pore density (PPI)	Copper foam layer thickness (mm)
1	37.03	35.40	35.39	35.41	35.77	35.67	35.09	35.43	35.29	35.41	35.43
2	35.27	35.40	35.41	35.39	35.30	35.32	35.44	35.39	35.40	35.42	35.41
3	33.93	35.41	35.42	35.42	35.15	35.23	35.68	35.40	35.53	35.38	35.38
Delta	3.10	0.01	0.02	0.02	0.61	0.44	0.59	0.04	0.25	0.04	0.05
Rank	1	11	10	9	2	4	3	7	5	8	6

Table 5-11 presents the ANOVA results for E_d, identifying the statistical significance and contribution of various parameters. The results clearly indicated that the number of cooling plates is the most influential factor, contributing 91.39% to the total variance in E_d, with an extremely high F-value of 11742.56 and a p-value of 0.000. This dominant influence suggests that changes in the number of cooling plates have the most significant impact on E_d, making it the primary parameter to optimise for improved energy density. This result aligns closely with the Taguchi analysis, where the number of cooling plates also had the highest Delta value.

Beyond the number of cooling plates, copper foam fin thickness, copper foam fin porosity, and copper foam fin quantity emerged as the next most influential factors, with much smaller contributions compared to cooling plates. Copper foam fin thickness contributes 3.80%

to the total variance, while copper foam fin porosity and copper foam fin quantity contribute 2.21% and 2.01%, respectively, all with p-values of 0.000, indicating their statistical significance. These findings are in agreement with the Taguchi analysis, which also ranked copper foam fin thickness, porosity, and fin quantity as the next most impactful factors after the number of cooling plates.

The copper foam layer porosity also exhibits a statistically significant effect, though its impact is considerably smaller, contributing only 0.54% to the total variance, with a p-value of 0.001. This suggests that while copper foam layer porosity may play a minor role in energy density optimisation, its effect is not as critical as the copper foam fin parameters. The Taguchi analysis similarly ranked copper foam layer porosity lower in importance, further validating this observation.

In contrast, several parameters including ambient temperature, coolant temperature, and inlet mass flow rate were found to have no statistically significant impact on E_d, with p-values exceeding 0.05 and individual contributions below 0.01%. The ANOVA results confirm that E_d is largely independent of thermal conditions. This aligns with the Taguchi findings, where ambient temperature, coolant temperature, and mass flow rate had the lowest Delta values, reinforcing their negligible impact on E_d. The consistency between these two statistical approaches strongly suggests that cooling system modifications should not be prioritised for energy density optimisation.

Similarly, copper foam fin pore density, copper foam layer pore density, and copper foam layer thickness exhibit insignificant effects on E_d, with each factor contributing less than 0.02% to the total variance. These parameters also ranked among the least influential in the Taguchi analysis, confirming that modifications to copper foam layer characteristics do not substantially influence E_d.

The combination of ANOVA and Taguchi analysis provides strong validation for these conclusions, ensuring the reliability of the results. The findings guide the design of battery cooling systems, suggesting that prioritising the number of cooling plates and fine-tuning copper foam fin characteristics are the most effective strategies for enhancing E_d, while modifications to cooling parameters and copper foam layer properties offer minimal benefits.

Table 5-11. ANOVA analysis results for energy density (E_d).

Source	DF	Adj SS	Adj MS	F-Value	p-Value	Contribution (%)
Number of cooling plates	2	2070.17	1035.08	11742.56	0.000	91.39137
Ambient temperature (K)	2	0.08	0.04	0.43	0.676	0.003532

Source	DF	Adj SS	Adj MS	F-Value	p-Value	Contribution (%)
Coolant temperature (K)	2	0.18	0.09	1.03	0.437	0.007946
Inlet mass flow rate (kg/s)	2	0.17	0.08	0.94	0.464	0.007505
Copper foam fin thickness (mm)	2	85.99	43.00	487.78	0.000	3.796183
Copper foam fin quantity	2	45.45	22.72	257.78	0.000	2.006472
Copper foam fin porosity	2	50.04	25.02	283.82	0.000	2.209106
Copper foam fin pore density (PPI)	2	0.09	0.05	0.52	0.629	0.003973
Copper foam layer porosity	2	12.19	6.09	69.13	0.001	0.538149
Copper foam layer pore density (PPI)	2	0.04	0.02	0.21	0.822	0.001766
Copper foam layer thickness (mm)	2	0.44	0.22	2.47	0.200	0.019425
Error	4	0.35	0.09			0.015451
Total	26	2265.17				100

5.3 Multi-Objective Optimisation and Evaluation of HBTMS Design Parameters

In order to study the influence of different factors simultaneously on the response variables, Taguchi analysis was caried out on $T_{Max,Sur}$, ΔT_{Max}, 1/PEC, and $1/E_d$ based on lower-the-better option. The "mean of means" method serves as a comprehensive measure for evaluating performance across multiple response variables, providing a structured approach to analysing complex systems with numerous performance criteria. This technique involves calculating the average of the mean responses for each factor level across all response variables, thereby facilitating a clearer assessment and comparison of different factor levels. By aggregating data in this manner, decision-making in multi-objective optimisation scenarios is simplified, and the most effective factor settings can be identified more efficiently. The magnitude of the mean of means, whether higher or lower, indicates the collective influence of a factor level on all response variables simultaneously. Previous studies have demonstrated that this approach enhances the ability to determine factor levels that produce the most favourable overall performance [321, 322]. It is particularly valuable in engineering and quality improvement research, where the simultaneous optimisation of multiple criteria is essential.

As depicted in Figure 5-6, for different number of cooling plates, the minimum value of mean of means was observed for two cooling plates. As discussed in individual optimisation, two cooling plates provide a balanced heat transfer performance by effectively controlling PCM melting and enabling active cooling for the HBTMS. This configuration significantly contributes to minimising $T_{Max,Sur}$ and ΔT_{Max}, and improving the PEC. Additionally, maintaining a moderate number of two cooling plates ensures an acceptable E_d while enhancing thermal performance. Regarding ambient temperature, the optimal case was achieved at the lowest ambient temperature of 308.15 K, as the reduced thermal load on the HBTMS facilitates better thermal management by lowering maximum temperature and improving temperature uniformity. Furthermore, active cooling was found to be more effective at lower ambient temperatures, leading to enhanced PEC value. Similarly, the lowest coolant inlet temperature of 298.15 K yielded superior thermal performance by minimising $T_{Max,Sur}$ and ΔT_{Max}, and 1/PEC, as the cooling capability of the HBTMS is enhanced. For the inlet mass flow rate, a moderate value of 0.001 kg/s was found to be optimal, as it improves thermal performance in terms of $T_{Max,Sur}$ and ΔT_{Max} while controlling the pressure drop to enhance PEC.

A moderate fin thickness of 4 mm was found to be more effective in enhancing conduction within the PCM, leading to optimised $T_{Max,Sur,}$ ΔT_{Max}, and PEC. Additionally, an optimised structural design could be achieved to maximise E_d. Similarly, a design incorporating a moderate quantity of six copper foam fins was identified as optimal, achieving the best performance in terms of $T_{Max,Sur,}$ ΔT_{Max}, and PEC by optimising conduction paths within the PCM while maintaining a lightweight structure to enhance E_d. The mean of means value exhibited minor variations across different copper foam fin porosities, with a maximum fluctuation of 0.1. The minimum value was recorded at a porosity of 0.8, as this configuration provided the highest conduction within the PCM, resulting in optimised $T_{Max,Sur,}$ ΔT_{Max}, and PEC. However, this type of copper foam fin slightly increased the overall system weight. A similar trend was observed for copper foam fin pore density, with maximum variations of 0.01, and the minimum value recorded at a pore density of 20 PPI.

Limited impact of copper foam layer porosity on the mean of means value was observed, with a moderate porosity of 0.8 leading to the optimised case. Similarly, the pore density of the copper foam layer demonstrated minimal influence, with variations of up to 0.1, and a low pore density of 20 PPI was identified as the optimal configuration. Since an increased copper foam layer thickness result in a higher pressure drop within the system and reduces the active cooling capability of the HBTMS, a copper foam layer thickness of 2 mm was determined to be the optimised design.

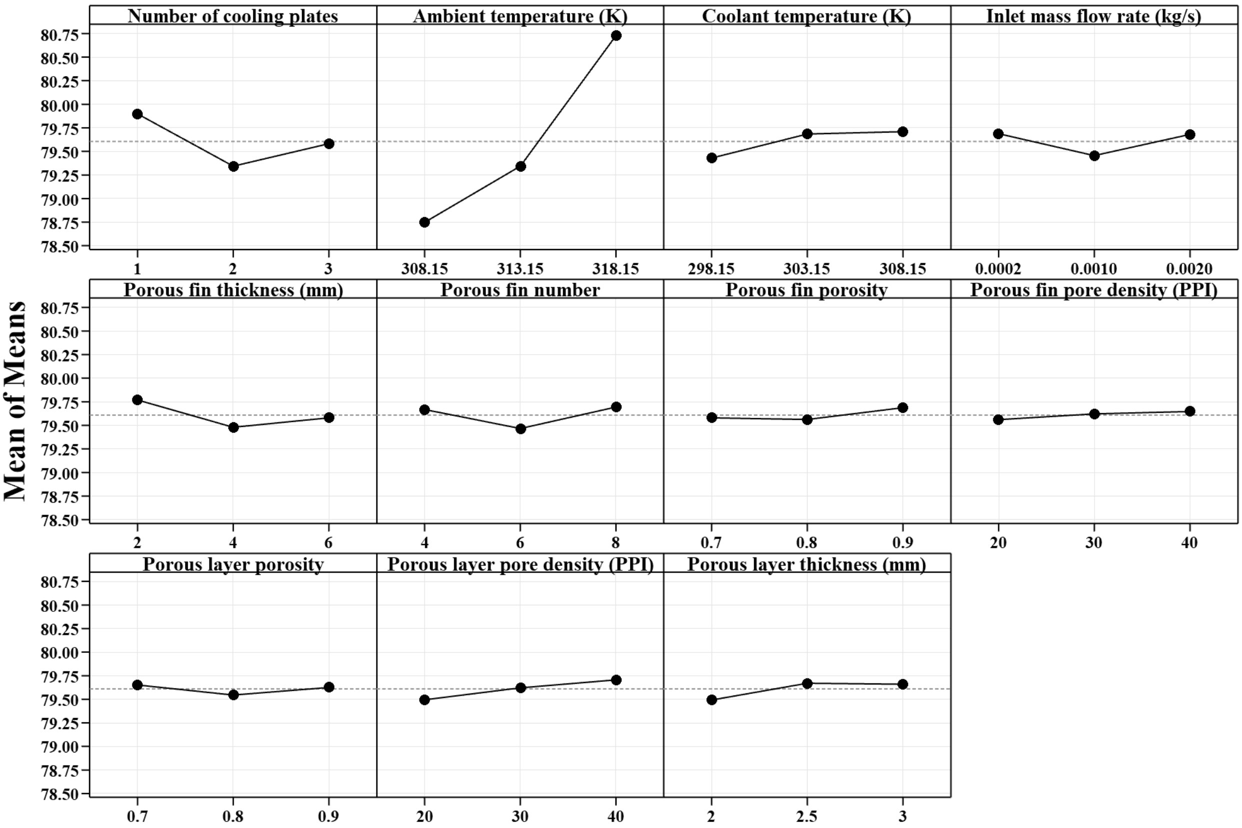

Figure 5-6. Mean of means for various factors and levels at the end of the 5C discharge rate.

Table 5-12 summarises the Taguchi S/N ratios for the "mean of means," evaluating the overall system response to each investigated factor across three distinct levels. Among the tested parameters, ambient temperature emerges as the most influential factor, exhibiting the largest Delta value of 0.17. This finding highlights the critical role of ambient temperature in determining the overall thermal performance of the battery system, with lower ambient temperatures generally improving system effectiveness. Following this, coolant temperature and inlet mass flow rate exhibit moderate yet notable impacts, with Delta values of 0.06 and 0.05, respectively, underscoring the importance of carefully controlling coolant conditions to optimise thermal management. Similarly, the number of cooling plates demonstrates a moderate influence with Delta value of 0.05, reinforcing that an optimal number of cooling plates contributes meaningfully to system performance. Conversely, parameters relating to porous structures such as copper foam layer porosity (Delta = 0.02), copper foam fin thickness (Delta = 0.02), copper foam fin porosity (Delta = 0.02), copper foam layer thickness (Delta = 0.02), copper foam layer pore density (Delta = 0.01), copper foam fin quantity (Delta = 0.01), and copper foam fin pore density (Delta = 0.01), showed comparatively minor influences. These results indicate that the porous media properties primarily serve to fine-tune the system's thermal performance, whereas external conditions including ambient temperature, coolant temperature, and inlet mass flow rate, represent the most critical parameters for overall optimisation.

Table 5-12. Response table for signal to noise ratios (S/N) for each level of factors for mean of means.

Level	Number of cooling plates	Ambient temperature (K)	Coolant temperature (K)	Inlet mass flow rate (kg/s)	Copper foam fin thickness (mm)	Copper foam fin quantity	Copper foam fin porosity	Copper foam fin pore density (PPI)	Copper foam layer porosity	Copper foam layer pore density (PPI)	Copper foam layer thickness (mm)
1	-43.99	-43.89	-43.92	-43.99	-43.97	-43.96	-43.96	-43.95	-43.95	-43.95	-43.96
2	-43.93	-43.93	-43.97	-43.94	-43.95	-43.95	-43.95	-43.96	-43.96	-43.96	-43.97
3	-43.95	-44.06	-43.98	-43.94	-43.95	-43.96	-43.97	-43.96	-43.97	-43.96	-43.95
Delta	0.05	0.17	0.06	0.05	0.02	0.01	0.02	0.01	0.02	0.01	0.02
Rank	4	1	2	3	6	10	7	11	5	9	8

In practical battery packs, additional thermal hardware can reduce the cell-to-pack ratio, and therefore any improvement in thermal control must be balanced against geometric and manufacturing constraints. The present multi-objective optimisation explicitly reflects this EV-relevant trade-off by simultaneously targeting temperature control and energy density related constraints, thereby discouraging solutions that achieve cooling improvements only through disproportionate increases in structural or coolant-side complexity. Consequently, the optimal configuration can be regarded as a scalable module-level design rule. It provides a repeatable architecture that may be deployed across multiple cells and cooling plates, provided that the same external boundary conditions (coolant inlet temperature and flow capacity, and ambient environment) are maintained at the module level.

Chapter 6: Cyclic Performance of the Proposed HBTMS

In this chapter the cyclic thermal performance of the proposed HBTMS has been investigated under repeated charging and discharging conditions. Recognising the critical importance of thermal stability over extended operational periods, a comprehensive comparative analysis is conducted between the HBTMS and pure PCM. The evaluation encompasses three distinct cycling scenarios. Particular attention is paid to the evolution of performance parameters across cycles to assess heat accumulation, thermal uniformity, and latent heat recovery.

To facilitate a detailed understanding, temperature and liquid fraction contour plots are also presented, enabling visualisation of thermal gradients and PCM saturation patterns within the system. Through this systematic assessment, the chapter aims to validate the long-term effectiveness, repeatability, and thermal resilience of the HBTMS under varying operational conditions.

6.1 Cyclic Charge and Discharge Performance of the HBTMS

In this section, the performance of the HBTMS over 5 cycles of discharge, rest and charge has been evaluated and compared against pure PCM. The optimised HBTMS configuration identified in the previous chapter has been adopted for these cyclic performance studies. This configuration comprises two cooling plates, an ambient temperature of 308.15 K, a coolant temperature of 303.15 K, and an inlet mass flow rate of 0.001 kg/s. Additionally, the system includes six copper foam fins with a thickness of 4 mm, a porosity of 0.8, and a pore density of 20 PPI, as well as a copper foam layer characterised by a thickness of 2 mm, a porosity of 0.8, and a pore density of 20 PPI. The specific C-rates for discharge and charge, along with the rest durations, are summarised in Table 6-1. Given that the highest heat generation occurs during the discharge phase, a high discharge rate of 5C has been selected for all cycle scenarios. The rest periods are defined in accordance with common practice in the literature [116, 323, 324], providing sufficient time for the battery to cool before the subsequent charging phase. For safety reasons, the maximum charging rate is limited to 3C, as recommended in prior studies [281].

Table 6-1. Specifications of the investigated cycles

Cycle type	Discharge rate	Rest time (s)	Charge rate
I	5C	300	1C
II	5C	300	2C
III	5C	300	3C

6.1.1 Type I Cycles

As depicted in Figure 6-1 (a), under Type I cycles, the pure PCM system reached $T_{Max,Sur}$ of 321.821 K at the end of the first cycle's discharge phase. This temperature subsequently decreased during the rest and charging phases due to the lower heat generation associated with 1C charging, in contrast to the 5C discharge. Figure 6-1 (b) demonstrates that during the first cycle, the PCM melted to L_f value of approximately 0.44, and then partially solidified by the end of the cycle, reaching L_f of about 0.32. This indicates that the latent heat capacity consumed during the first cycle was not fully recovered. In contrast, the HBTMS recorded a $T_{Max,Sur}$ that was 9.6 K lower than that of the pure PCM at the end of the first cycle's discharge. Due to the lower heat generation rate of the 1C charging phase and the enhanced heat removal capability of the HBTMS, $T_{Max,Sur}$ decreased significantly during the rest and charging stages, dropping even below the ambient temperature of 308.15 K by the end of the first cycle. As illustrated in Figure 6-1 (b) and Figure 6-2 (c), the HBTMS resulted in a lower degree of PCM melting during the first cycle, and the melted PCM was fully solidified by the end of the cycle, demonstrating complete restoration of the latent heat capacity.

As illustrated in Figure 6-1 (a), the pure PCM exhibits a progressive increase in $T_{Max,Sur}$ across successive Type I cycles, reaching values of 321.821 K, 327.017 K, 329.490 K, 330.656 K, and 331.219 K from the first to the fifth cycle, respectively. The safety threshold of 323.15 K is exceeded during the second cycle, with the $T_{Max,Sur}$ rising to approximately 8 K above the limit in later cycles. Additionally, as shown in Figure 6-1 (b), the PCM undergoes melting during each cycle but fails to fully solidify by the end of the rest and charging phases. In the final two cycles, the PCM becomes fully melted and saturated by the end of discharge. Over the five Type I cycles, the L_f peaks at approximately 0.74, indicating only partial restoration of the latent heat capacity. This incomplete phase change, as depicted in Figure 6-2 (d) and (h), leads to localised melting around the battery cells. The resulting heat accumulation and elevated temperatures are primarily attributed to the PCM's low thermal conductivity and inadequate post cycle cooling.

In contrast, as shown in Figure 6-1 (a), the HBTMS maintains a consistent pattern for $T_{Max,Sur}$ across multiple cycles, effectively preventing heat accumulation. This stability is also reflected in the PCM melting and solidification behaviour illustrated in Figure 6-1 (b). The $T_{Max,Sur}$ of 312.215 K at the end of the first cycle slightly decreases to 312.183 K in subsequent cycles, due to the lower initial temperatures in cycles two to five, which fall below the ambient temperature as the initial temperature in the first cycle. This contrasts with the pure PCM, where the initial temperature of each cycle progressively increases, particularly during the first two cycles. Compared to the safety limit of 323.15 K, the HBTMS consistently maintains $T_{Max,Sur}$ approximately 11 K lower, indicating effective and reliable thermal management even over extended cycles. Furthermore, as shown in Figure 6-2 (a) and (e), the temperature difference between the battery core and surface remains stable at less than 5 K after both the first and fifth cycles, highlighting the system's thermal uniformity. The effective temperature control achieved by the HBTMS is due to enhanced PCM thermal conductivity via embedded copper foam fins, which expand the active phase change region, and improved heat extraction through the copper foam layers in copper tubes. Additionally, as demonstrated in Figure 6-1 (b) and Figure 6-2 (c) and (g), unlike the pure PCM, in which the liquid fraction increases by approximately 30% with each cycle, the HBTMS enables complete PCM solidification at the end of each cycle. This ensures full recovery of the latent heat capacity and supports stable, repeatable phase change behaviour. In better words, HBTMS facilitates reversible and stable phase change dynamics along with continued phase change participation which results in considerable thermal sustainability, long-term durability of the system.

The performance of the HBTMS and the pure PCM in terms of the ΔT_{Max} is compared in Figure 6-1 (c). As illustrated, both systems exhibit fluctuations in ΔT_{Max} across the cycles; however, in all cases, the values remain well below the safety threshold of 5 K. For the pure PCM, ΔT_{Max} shows a gradual increase over successive cycles, reaching a peak value of approximately 2 K during the last two cycles. This increase corresponds to the progressive saturation of the PCM, which limits the active melting region, as shown in Figure 6-1 (b). In contrast, the HBTMS exhibits a consistent ΔT_{Max} pattern across all cycles, with a stable peak value of 2 K. This repeatable behaviour reflects the stable and reversible phase change dynamics of the PCM in the HBTMS configuration, as also demonstrated in Figure 6-1 (b). Notably, each HBTMS cycle features two distinct ΔT_{Max} peaks. The first occurs immediately after the discharge phase, where the highest heat generation rate was observed and the effectiveness of liquid cooling varies across battery locations. A slight decrease follows during the rest period, when heat generation ceases and the HBTMS remains active in cooling. As charging begins, ΔT_{Max} increases again due to continued, though lower, heat generation.

However, the HBTMS effectively mitigates this rise, leading to a gradual reduction in ΔT_{Max} through the charging phase and into the end of the cycle. Furthermore, both systems achieve a similar minimum ΔT_{Max} value of approximately 0.5 K at the end of each cycle.

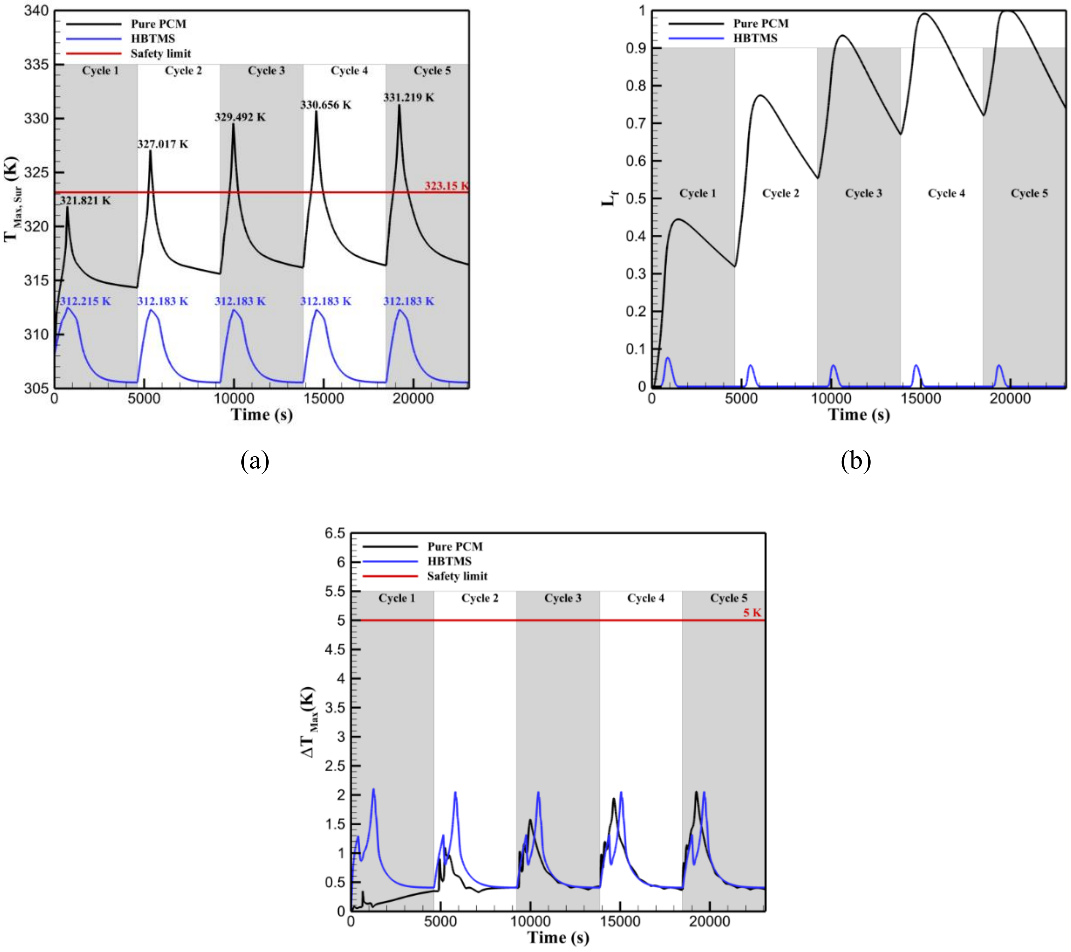

(a)

(b)

(c)

Figure 6-1. Performance of the HBTMS under Type I cycles in terms of (a) maximum battery surface temperature, (b) PCM liquid fraction, and (c) maximum temperature difference within the battery module.

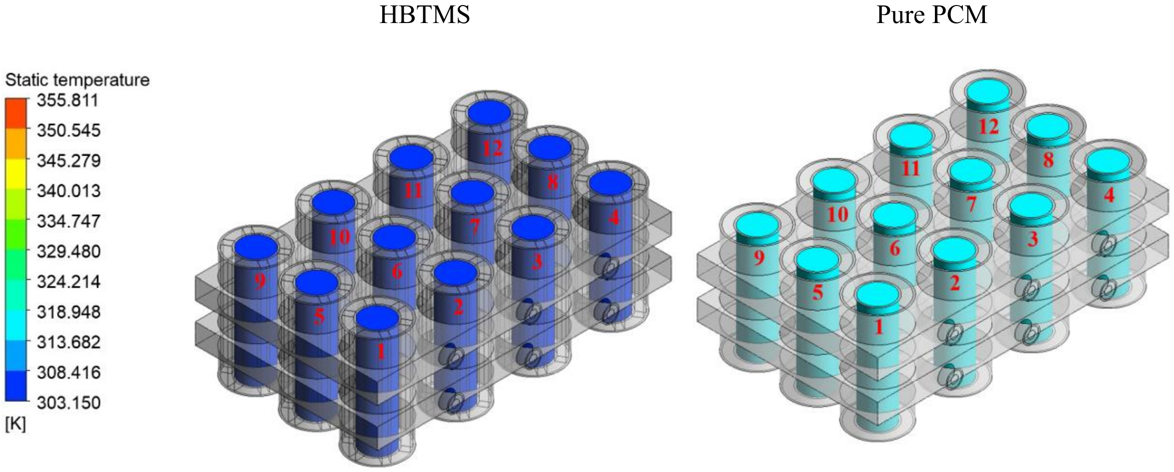

(a) (b)

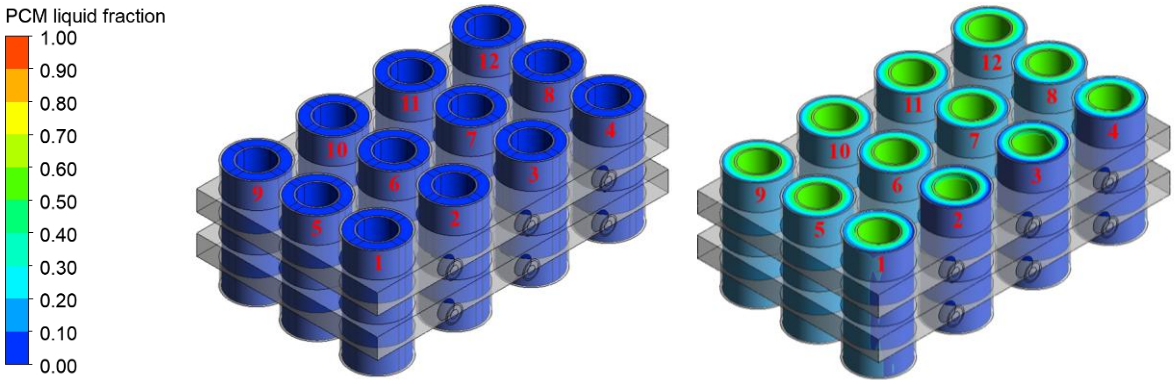

(c) (d)

First Cycle

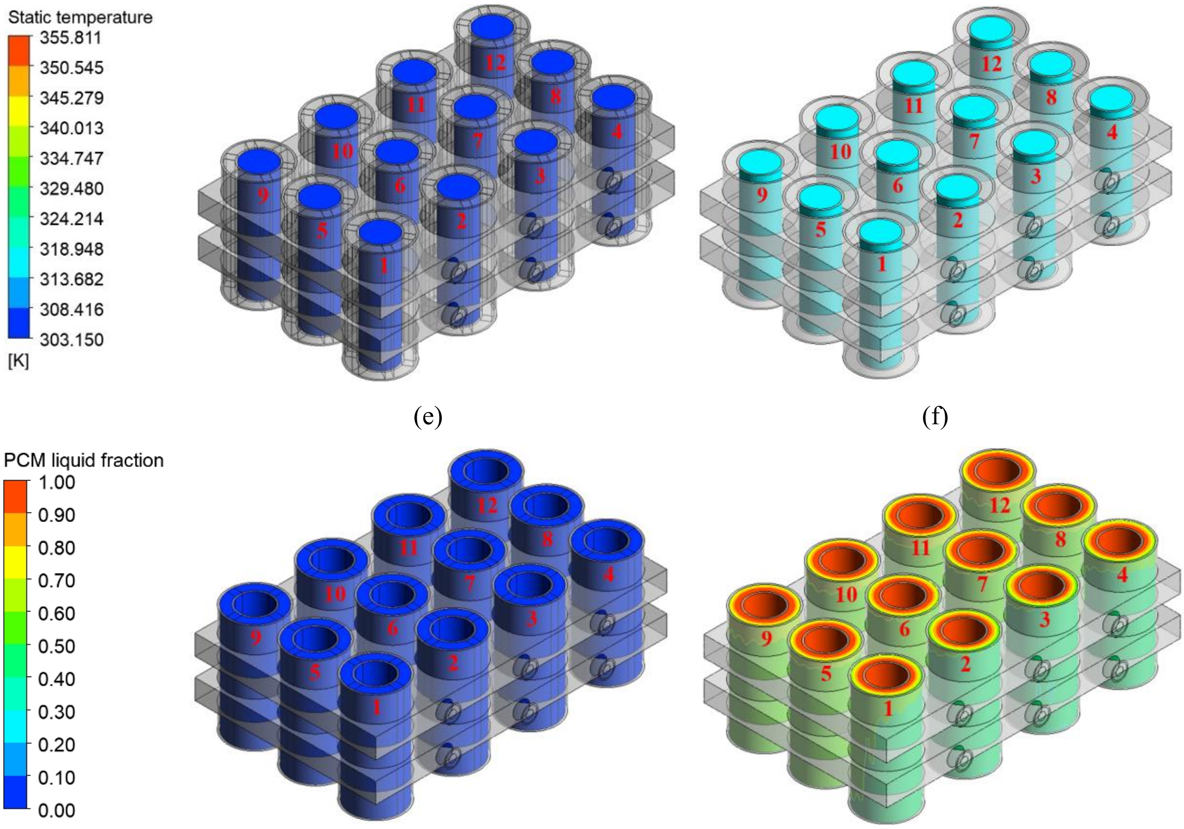

(g) (h)

Fifth Cycle

Figure 6-2. Static temperature and PCM liquid fraction contour plots of the HBTMS and pure PCM under Type I cycles at the end of the first and fifth cycle.

6.1.2 Type II Cycles

The performance of the HBTMS under Type II cycles is illustrated in Figure 6-3 and compared with that of the pure PCM. As shown in Figure 6-3 (a), similar to the Type I cycles, the pure PCM reaches a $T_{Max,Sur}$ approximately 1.33 K below the safety limit by the end of the first discharge. A subsequent temperature drop is also observed during the rest period.

However, during the 2C charging phase, the temperature decline is less pronounced compared to the 1C charging in Type I cycles. Owing to the higher heat generation rate associated with 2C charging, $T_{Max,Sur}$ of around 317 K was maintained. This behaviour indicates a thermal balance between the heat generated and the heat dissipation within the pure PCM. Additionally, as shown in Figure 6-3 (b) and the liquid fraction contour plot at the end of the first cycle in Figure 6-4 (d), the PCM is not fully melted and L_f reached approximately 0.59. This represents a 90% increase compared to the maximum L_f observed under Type I cycles for pure PCM, reflecting the greater thermal load in Type II cycles. For the HBTMS, a similar $T_{Max,Sur}$ of 312.215 K is observed by the end of the first discharge, which is 10.9 K below the safety limit. Notably, during both the rest and 2C charging phases, $T_{Max,Sur}$ continues to decline and even drops below the ambient temperature, despite the higher heat generation compared to the 1C charging in Type I cycles. However, a comparison of the static temperature contours in Figure 6-2 (a) and Figure 6-4 (a) reveals a slight increase in the battery core temperature under Type II cycles relative to Type I, attributable to the increased thermal load. Nevertheless, the HBTMS exhibits a similar PCM phase change pattern during the first Type II cycle as in Type I, with complete solidification of the PCM by the end of the cycle. This indicates full restoration of the PCM's latent heat capacity, confirming the system's capacity to manage elevated thermal loads while maintaining stable and reversible thermal behaviour.

As depicted in Figure 6-3 (a), during successive Type II cycles, the $T_{Max,Sur}$ under pure PCM increases rapidly, reaching values of 321.821 K, 330.411 K, 336.898 K, 338.749 K, and 339.024 K at the end of discharge in the first through fifth cycles, respectively. Compared to the Type I cycles (Figure 6-1 (a)), these values represent temperature increases of 3.394 K, 7.406 K, 8.093 K, and 7.805 K during the second to fifth cycles, respectively. Notably, the safety limit of 323.15 K is first exceeded during the discharge phase of the second cycle. Although $T_{Max,Sur}$ temporarily drops below the safety limit by the end of the second cycle, it consistently exceeds the limit in the subsequent three cycles. The enhanced heat generation during 2C discharge in Type II cycles intensifies the heat accumulation issue, making the limitations of pure PCM more pronounced. As shown in Figure 6-3 (b), the PCM undergoes continuous melting without a solidification stage, becoming fully saturated early in the third cycle's discharge phase, an observation supported by the liquid fraction contour plots in Figure 6-4 (d) and (h). In contrast, the HBTMS maintains superior thermal stability throughout all cycles. As shown in Figure 6-3 (a), the maximum $T_{Max,Sur}$ remains nearly constant, reaching 312.262 K from the second to the fifth cycle, only a minor increase of 0.04 K from the first cycle and still 10.88 K below the safety limit. Compared to Type I cycles, the maximum $T_{Max,Sur}$ increases by only 0.08 K, further underscoring that the system is significantly less sensitive to cycle type under HBTMS operation. A comparison of the static temperature contour plots by the end of the first and fifth cycles (Figure 6-4 (a) and (e)) reveals that HBTMS maintains a nearly identical temperature distribution across both the battery surface and core. In contrast, for the pure PCM, a comparison of Figure 6-4 (b) and (f) highlights a substantial temperature increase by the fifth cycle, particularly at the battery core. The PCM phase change patterns further confirm these observations. As shown in Figure 6-3 (b), the HBTMS supports a repeatable melting and solidification cycle, allowing full restoration of the PCM's latent heat capacity. This is evidenced by the liquid fraction contour plots, where complete solidification is evident at the end of the fifth cycle for the HBTMS (Figure 6-4 (g)). Conversely, for the pure PCM, the PCM remains fully melted at the end of the fifth cycle (Figure 6-4 (h)), indicating ineffective thermal recovery.

In terms of ΔT_{Max}, Figure 6-3 (c) depicts that both systems maintain ΔT_{Max} below the safety limit of 5 K under Type II cycles, despite observable fluctuations. For the pure PCM, ΔT_{Max} increases over the first three cycles, reaching a peak of approximately 1.5 K during the third cycle. After the PCM becomes fully melted, ΔT_{Max} slightly decreases to around 1.3 K. Compared to Type I cycles, greater thermal uniformity was observed in the pure PCM under Type II cycles, due to increased PCM melting driven by the higher heat generation associated with 2C charging. In comparison, the HBTMS exhibits a similar trend to that observed in Type I cycles, with a slight upward shift of approximately 0.5 K. A consistent maximum ΔT_{Max} of around 2.5 K is recorded at the end of the discharge phase in each cycle. Notably, by the end of each cycle, the HBTMS demonstrates lower ΔT_{Max} values than the pure PCM, indicating superior thermal uniformity. This performance is attributed to the higher heat generation during the 2C charging stages and the enhanced thermal regulation capabilities of the HBTMS. Moreover, while the range of ΔT_{Max} variation for the HBTMS across cycles is approximately 1.5 K, it remains significantly narrower, around 0.4 K, for the pure PCM. This variation is likely due to the spatial differences in liquid cooling effectiveness within the HBTMS, where batteries positioned in the first row benefit more from lower inlet temperatures, particularly during the rest and charging stages.

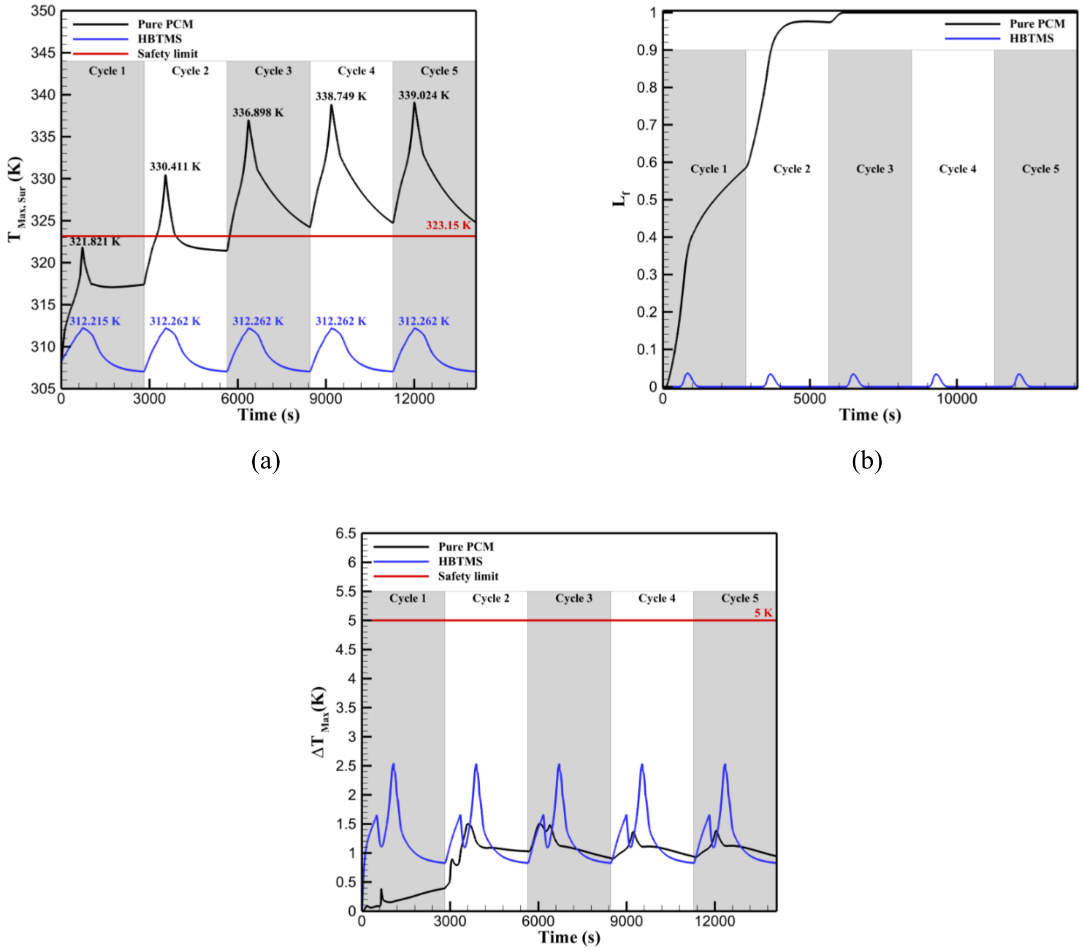

(a) (b)

(c)

Figure 6-3. Performance of the HBTMS under Type II cycles in terms of (a) maximum battery surface temperature, (b) PCM liquid fraction, and (c) maximum temperature difference within the battery module.

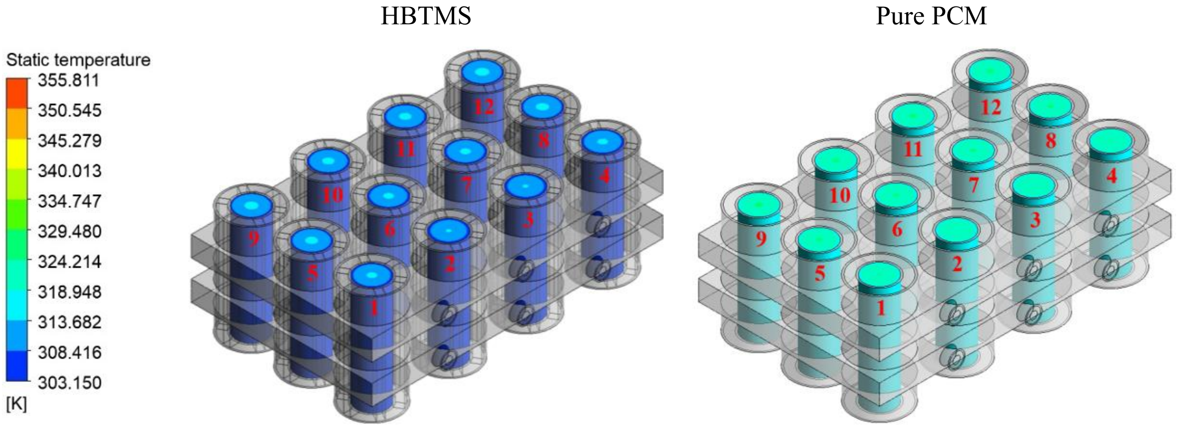

(a) (b)

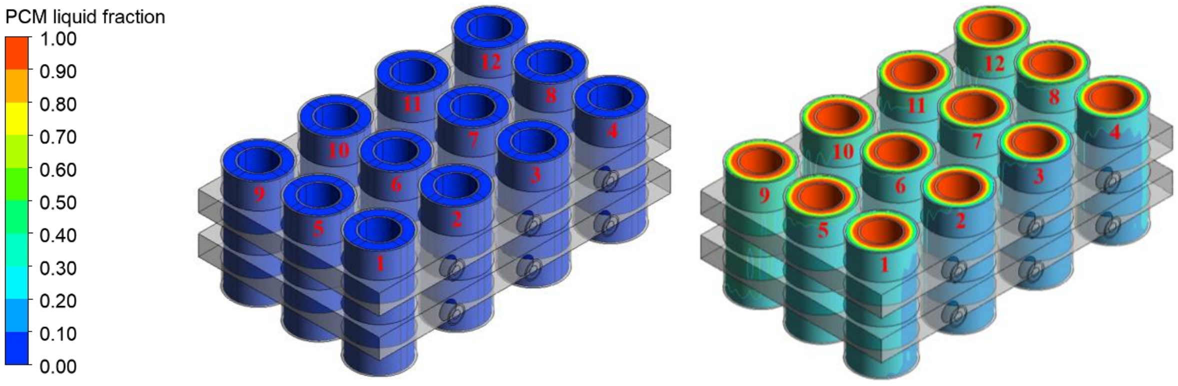

(c) (d)

First Cycle

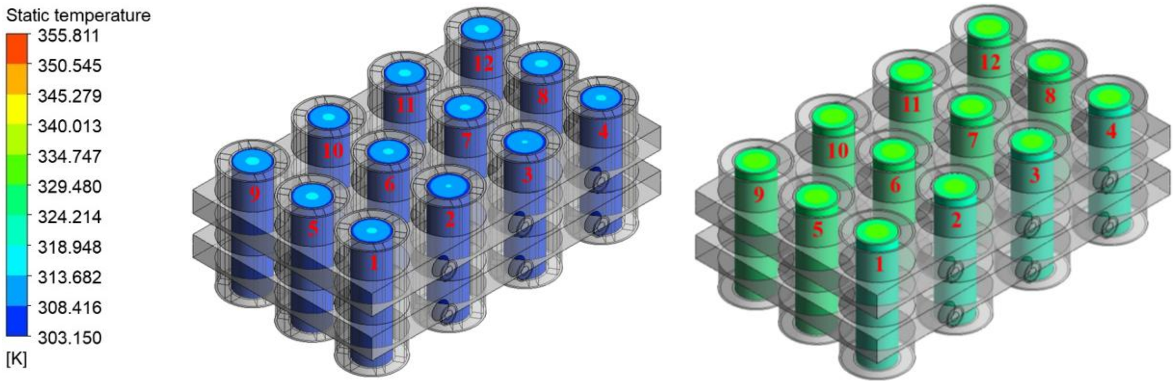

(e) (f)

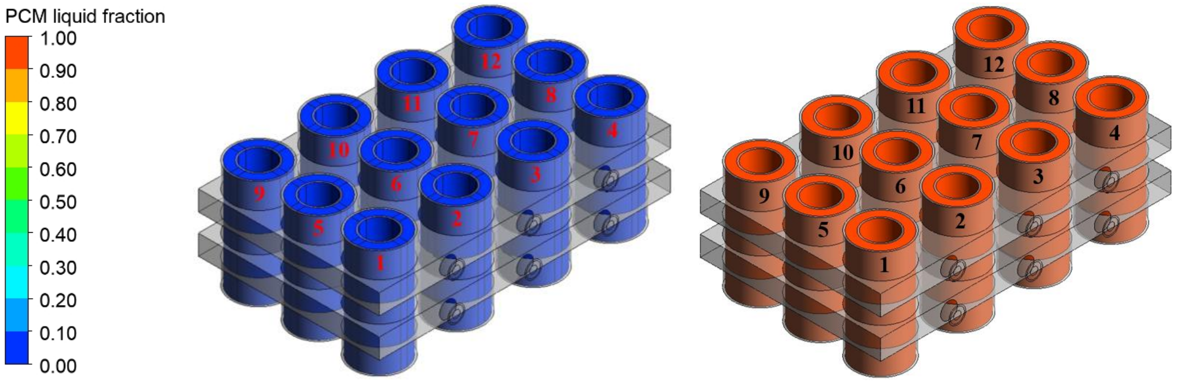

(g) (h)

Fifth Cycle

Figure 6-4. Static temperature and PCM liquid fraction contour plots of the HBTMS and pure PCM under Type II cycles at the end of the first and fifth cycle.

6.1.3 Type III Cycles

The performance of pure PCM and the HBTMS under Type III cycles is presented in Figure 6-5. As shown in Figure 6-5 (a), for the pure PCM, $T_{Max,Sur}$ reached 321.821 K at the end of the 5C discharge during the first cycle and then decreased to approximately 317 K during the subsequent rest period. However, unlike the other cycle types, the higher heat generation during the 3C charging stage causes $T_{Max,Sur}$ to rise again, approaching but remaining just below the safety threshold of 323.15 K by the end of the first cycle. Due to the significantly high heat generation during both discharge and charge phases, the PCM experiences substantial melting. As shown in Figure 6-5 (b), the L_f reached a value of 0.74 by the end of the first cycle. This is further supported by the contour plot in Figure 6-6 (d), which shows a considerable portion of the PCM in the melted state. In contrast, the HBTMS demonstrates a more controlled thermal response. After reaching a maximum $T_{Max,Sur}$ of 312.215 K at the end of the discharge phase, the temperature continued to decline throughout the rest and charging periods, reaching approximately 310 K by the end of the first cycle. However, this final temperature is higher than the values observed at the end of the first cycles in Type I and II, reflecting the increased thermal load in Type III cycles. As shown in Figure 6-6 (a), a larger temperature gradient between the core and surface of the battery was observed by the end of the first cycle under Type III cycles. This gradient is more pronounced in the pure PCM, as illustrated in Figure 6-6 (b), due to its limited thermal conductivity and inability to effectively manage the intensified heat generation. Nevertheless, the HBTMS continues to support stable thermal behaviour. As with the previous cycle types, the PCM undergoes melting during discharge and is fully solidified by the end of the cycle, thereby restoring its latent heat capacity and ensuring consistent thermal performance.

During subsequent cycles, the pure PCM, as illustrated in Figure 6-5 (a), exhibited increasingly unfavourable thermal performance. The system exceeded the safety threshold of 323.15 K from the second to fifth cycles, with maximum $T_{Max,Sur}$ recorded at 321.821 K, 333.956 K, 344.566 K, 347.143 K, and 347.742 K during the first to fifth cycles, respectively. These values represent increases of 6.939 K, 15.074 K, 16.487 K, and 16.523 K compared to the corresponding maximum temperatures under Type I cycles, indicating significant heat accumulation over time. As shown in Figure 6-5 (b), the pure PCM undergoes rapid PCM melting, with full melting occurring as early as the second cycle. This is further supported by Figure 6-6 (h), which reveals that the PCM does not solidify in the subsequent cycles. This behaviour is primarily attributed to the limited heat transfer in the pure PCM and the elevated heat generation associated with 5C discharge and 3C charge. Consequently, the system fails to dissipate heat effectively, leading to sustained PCM saturation and severe temperature rise. Additionally, the difference in $T_{Max,Sur}$ between cycles becomes less pronounced after PCM saturation, particularly in the fourth and fifth cycles. In contrast, the HBTMS consistently maintains stable thermal performance, as in previous cycle types. The maximum $T_{Max,Sur}$ is limited to approximately 312.526 K, representing only a marginal increase of 0.34 K compared to Type I cycles, and remains 10.62 K below the safety limit. The static temperature contour plots in Figure 6-6 (a) and (e) reveal that the temperature gradient between the battery surface and core remains nearly unchanged between the first and fifth cycles, confirming the consistent thermal regulation offered by the HBTMS. By comparison, under pure PCM, the core temperature increases significantly and reaches 355.811 K by the end of the fifth cycle, as evident in Figure 6-6 (f). This further demonstrates the thermal instability and poor heat dissipation of the pure PCM under high thermal loads. As shown in Figure 6-5 (b) and the liquid fraction contour plots (Figure 6-6 (c) and (g)), the HBTMS continues to support PCM melting during discharge and complete solidification by the end of each cycle. This enables full restoration of the latent heat capacity and ensures effective thermal cycling and long-term durability.

In terms of the ΔT_{Max}, both systems maintained values below the safety limit of 5 K under Type III cycles, as illustrated in Figure 6-5 (c). For the pure PCM ΔT_{Max} increased to approximately 1.8 K during the second cycle, coinciding with the complete melting of the PCM. In the subsequent three cycles, ΔT_{Max} slightly decreased and stabilised at around 1.5 K, likely due to the fully melted state of the PCM and the reduced thermal gradients resulting from saturation. The HBTMS exhibited a similar performance trend to that observed in Type II cycles, with maximum ΔT_{Max} of approximately 2.5 K across the different cycles, an increase of about 0.5 K compared to Type I cycles. These values fluctuated in the range of 1.2 to 2.5 K, influenced by the cyclic melting and solidification of the PCM as well as the variable heat generation during different phases of each cycle. In contrast to the earlier cycle types, the HBTMS shows a slightly higher ΔT_{Max} of around 0.25 K at the end of each cycle compared to the pure PCM. This is likely due to the increased thermal load in Type III cycles and the resulting temperature gradients within the hybrid system, despite its superior overall cooling performance and thermal stability.

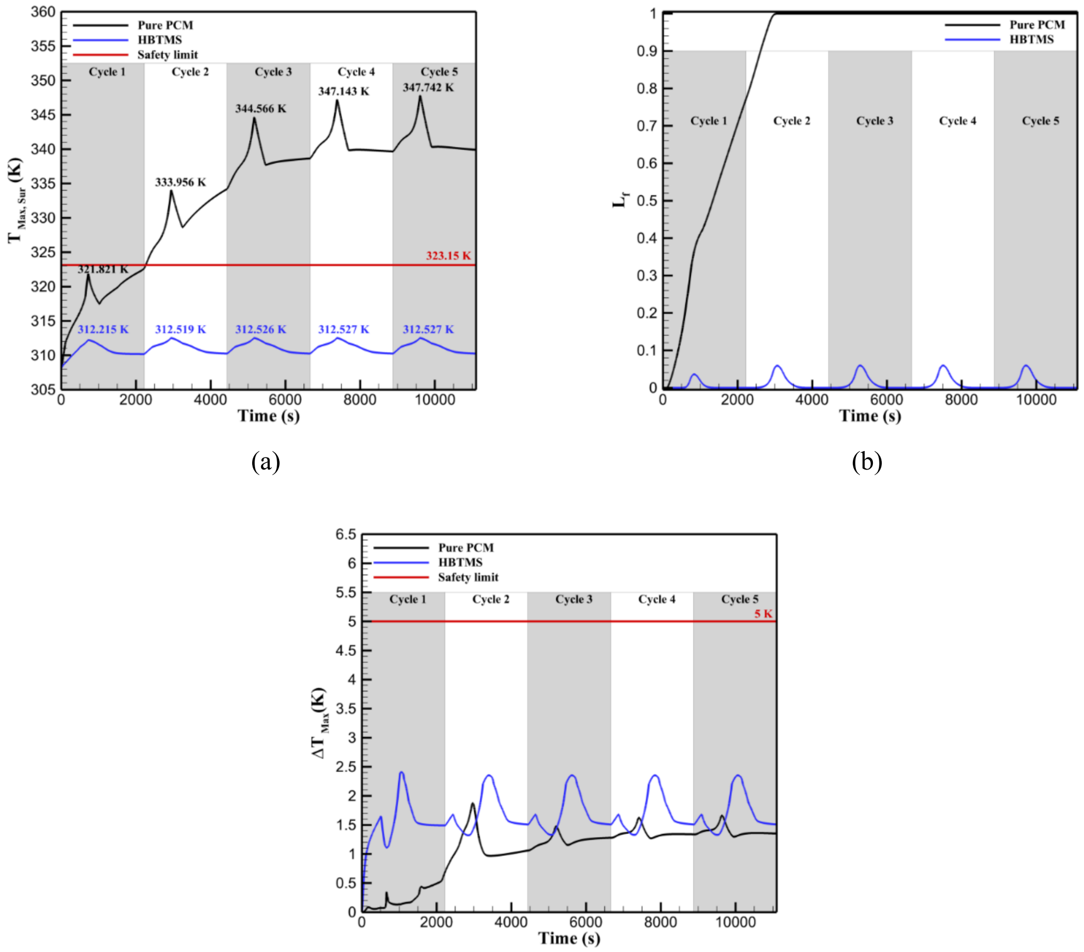

(a) (b)

(c)

Figure 6-5. Performance of the HBTMS under Type III cycles in terms of (a) maximum battery surface temperature, (b) PCM liquid fraction, and (c) maximum temperature difference within the battery module.

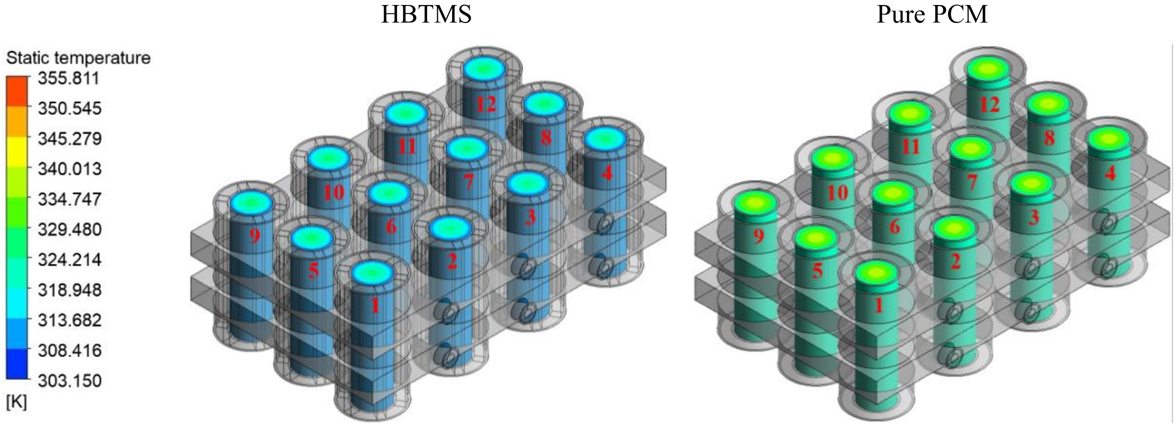

(a) (b)

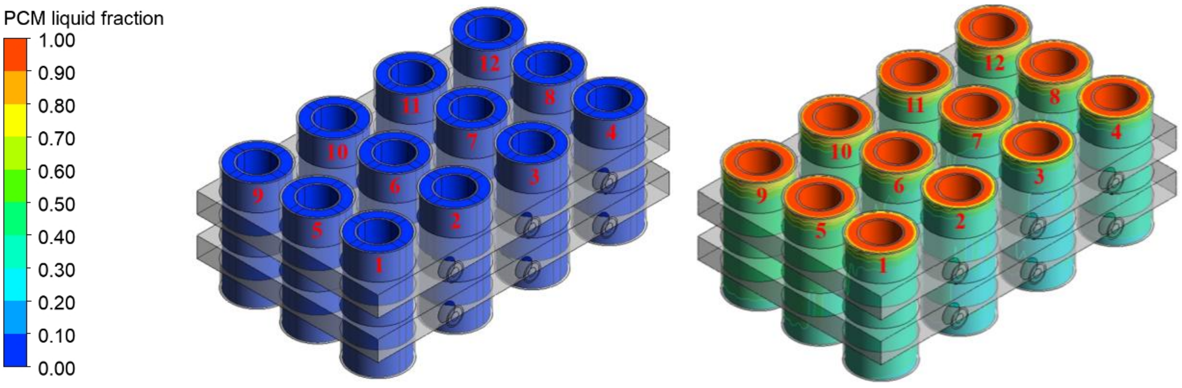

(c) (d)

First Cycle

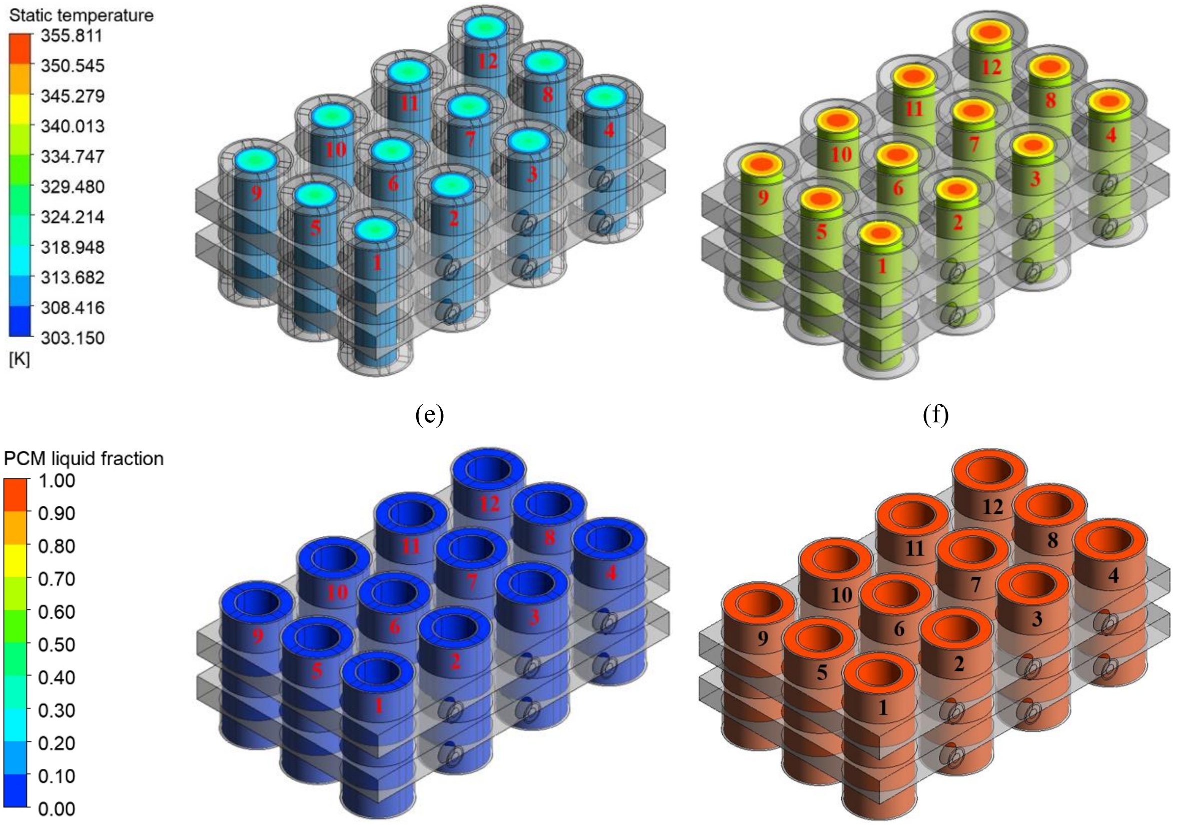

(g) (h)

Fifth Cycle

Figure 6-6. Static temperature and PCM liquid fraction contour plots of the HBTMS and pure PCM under Type III cycles at the end of the first and fifth cycle.

These cyclic results are relevant to EV duty as vehicle operation comprises repeated high-load events and subsequent recovery periods (parking, reduced power demand, or controlled cooldown), during which the thermal management system must restore favourable conditions for the next event. The ability of the HBTMS to maintain both a reduced peak temperature and low temperature non-uniformity over successive cycles indicates that the combined latent-heat buffering and enhanced heat transfer pathways can remain effective under repeated thermal loading, rather than only during a single discharge. From a scalability standpoint, this behaviour supports the feasibility of module-level deployment, since pack-level reliability is strongly influenced by the persistence of thermal margins and uniformity over cycles. Therefore, the observed cyclic stability strengthens the applicability of the proposed HBTMS to EV modules operating under realistic transient usage patterns.

Chapter 7: Conclusions and Future Work

7.1 Conclusions

Effective thermal management is essential for maintaining the safety, efficiency, and operational longevity of lithium-ion batteries (LIBs), particularly under high-power demand conditions. In response to the thermal challenges associated with high C-rate operation, this research proposed and numerically investigated a novel Hybrid Battery Thermal Management System (HBTMS) that synergistically combines phase change material (PCM), copper metal foam in the form of porous fins and porous layers, and liquid cooling.

This hybrid approach was designed to exploit the latent heat absorption of PCMs, the high heat removal capacity of liquid cooling, and the enhanced conduction and convection performance offered by copper foam with interconnected pore structure. The integration of these complementary mechanisms facilitated more effective thermal regulation and improved system responsiveness under dynamic cyclic conditions, while also contributing to increased energy density and overall thermal efficiency.

A comprehensive and validated numerical framework was developed using ANSYS Fluent, incorporating different models to simulate transient battery heat generation (based on the Bernardi model), phase change dynamics (via the enthalpy-porosity method), and porous media flow (via the Darcy–Brinkman–Forchheimer model). To reflect the complex heat exchange within porous domains, both Local Thermal Equilibrium (LTE) and Local Thermal Non-Equilibrium (LTNE) models were implemented. The numerical models were validated against experimental results from the literature concerning battery temperature profiles, PCM behaviour, and porous-enhanced cooling systems.

Additionally, a multi-objective optimisation strategy was employed using Taguchi Design of Experiments (DOE) and Analysis of Variance (ANOVA), enabling identification of the most influential parameters governing HBTMS behaviour and facilitating the selection of an optimised configuration that balances maximum temperature suppression, uniformity, energy consumption, and energy density.

Through this comprehensive methodology, the study delivers a significant advancement in hybrid cooling strategies for high-performance LIB systems. The principal results obtained from this study are as follows.

- ✓ The proposed HBTMS incorporating PCM with copper foam fins and liquid cooling with copper foam layers significantly reduced the $T_{Max,Sur}$ by 9.18 K (2.9%) compared to the pure PCM. The $T_{Max,Sur}$ reduction for PCM with solid fins, PCM with copper foam fins, and PCM with copper foam fins and liquid cooling were 6.6 K (2.1%), 7.52 K (2.3%), and 8.89 K (2.8%), respectively, compared to pure PCM.
- ✓ ΔT_{Max} was maintained well below 5 K for various HBTMS configurations, ensuring a uniform temperature distribution across the battery module and each battery cell.
- ✓ The addition of copper foam layers in HBTMS provided a PEC value exceeding one, indicating enhanced heat transfer outweighs the increase in pressure drop.
- ✓ The system's energy density was notably improved, with copper foam fins providing a 25% enhancement over solid fins due to their reduced weight, while the optimised HBTMS design achieved comparable thermal performance with fewer cooling plates, resulting in an additional 11% improvement.
- ✓ Across all performance indicators, ambient temperature consistently emerged as the most influential factor, followed by coolant temperature, inlet mass flow rate, and the number of cooling plates. Parameters related to the copper foam structures, including thickness, porosity, and pore density of both the fins and layers, were found to have moderate to low impact, serving primarily to fine-tune system performance.
- ✓ Multi-objective optimisation using the "mean of means" method identified the optimal design configuration as comprising two cooling plates, an ambient temperature of 308.15 K, a coolant temperature of 298.15 K, and a coolant flow rate of 0.001 kg/s. For the copper foam configuration, the optimum performance was achieved with a fin thickness of 4 mm, six fins at a porosity of 0.8 and 20 PPI pore density, and layers of 2 mm thickness, 0.8 porosity, and 20 PPI. This combination achieved a favourable balance between thermal regulation by minimising both $T_{Max,Sur}$ and ΔT_{Max} and structural efficiency by maximising both PEC and E_d.
- ✓ The cyclic performance evaluation demonstrated that the proposed HBTMS markedly outperforms pure PCM under repeated high-rate discharge–rest–charge cycles. Unlike the pure PCM system, which exhibited thermal degradation, incomplete solidification, and rising surface temperatures beyond the safety threshold, the HBTMS consistently maintained the $T_{Max,Sur}$ at least 10 K below the limit, ensured complete PCM re-solidification, and preserved latent heat recovery. Moreover, it sustained temperature uniformity with ΔT_{Max} within 2–2.5 K across all scenarios, even under the most demanding

conditions. These results highlight the HBTMS's superior thermal stability, durability, and suitability for long-term high-load battery operation.

7.2 Future Work

While the present study has demonstrated the enhanced thermal performance and reliability of the proposed HBTMS under a range of operational scenarios, several avenues remain for future research to build upon these findings. Further investigations are needed to refine the current model, explore alternative materials and configurations, and validate the system's effectiveness under real-world conditions. The following suggestions outline potential directions to enhance the design, scalability, and practical deployment of the HBTMS in advanced battery applications.

1. Entropy Generation and Exergy Analysis

Incorporate entropy generation rate and exergy-based analysis into the design and optimisation of the HBTMS to better understand thermodynamic irreversibility, identify sources of exergy loss, and enhance overall system efficiency.

2. Battery Degradation Modelling

Integrate battery degradation mechanisms into the thermal model to assess the long-term effects of temperature variations and cycling on battery health and capacity fade, thereby supporting more predictive and robust system design.

3. Multi-Stage Phase Change Materials (PCMs)

Explore the use of multi-stage PCMs with different melting points to create a broader and more continuous thermal buffering range, enabling better control over temperature fluctuations during cycling.

4. Influence of Different Metal Foam Materials

Assess the impact of different metal foam materials (aluminium, nickel, copper) and structural properties on thermal conductivity, heat transfer performance, and energy density within the HBTMS.

5. PCM Selection Based on Ambient Conditions

Evaluate the performance of different PCMs with various melting temperatures under a range of ambient temperatures, including scenarios where ambient temperature is significantly above or below the PCM melting point.

6. On-Demand Liquid Cooling Control

Implement a temperature-dependent control strategy for the liquid cooling system to activate the pump only when necessary. This would reduce energy consumption during low-load periods and enhance the overall energy efficiency of the system.

7. Real-World Driving Cycle Simulations

Extend the thermal performance analysis to include real driving cycles and a broader spectrum of environmental and operational conditions to evaluate system behaviour under practical usage scenarios.

8. PCM Expansion During Melting

Investigate the volumetric expansion of PCMs during phase transition, and its effect on the mechanical integrity, packaging constraints, and pressure distribution within the battery module.

9. Sustainability and Recycling Considerations

Explore the recyclability of BTMS components with a focus on sustainable material selection, end-of-life recovery processes, and environmental impact. Lifecycle assessments should be conducted to quantify the ecological footprint of different HBTMS designs.

10. Advanced Modelling Approaches

Apply data-driven techniques such as machine learning and artificial neural networks to enhance thermal performance predictions, parameter optimisation, and fault diagnosis in complex operational environments.

11. Experimental Validation of Metal Foam Integration

Conduct experimental investigations to validate the thermal enhancement effects of metal foam integration in HBTMS configurations and to benchmark simulation outcomes with physical test results (Appendix A).

References

1. Olabi, A. and M.A. Abdelkareem, *Renewable energy and climate change.* Renewable and Sustainable Energy Reviews, 2022. **158**: p. 112111.
2. Brand, C., J. Anable, I. Ketsopoulou, and J. Watson, *Road to zero or road to nowhere? Disrupting transport and energy in a zero carbon world.* Energy Policy, 2020. **139**: p. 111334.
3. Davies, J., M. Grant, J. Venezia, and J. Aamidor, *Greenhouse gas emissions of the US transportation sector: Trends, uncertainties, and methodological improvements.* Transportation research record, 2007. **2017**(1): p. 41-46.
4. Foley, A. and A.G. Olabi, *Renewable energy technology developments, trends and policy implications that can underpin the drive for global climate change.* Renewable and Sustainable Energy Reviews, 2017. **68**: p. 1112-1114.
5. Abo-Khalil, A.G., M.A. Abdelkareem, E.T. Sayed, H.M. Maghrabie, A. Radwan, H. Rezk, and A. Olabi, *Electric vehicle impact on energy industry, policy, technical barriers, and power systems.* International Journal of Thermofluids, 2022. **13**: p. 100134.
6. Liu, K., K. Li, Q. Peng, and C. Zhang, *A brief review on key technologies in the battery management system of electric vehicles.* Frontiers of mechanical engineering, 2019. **14**(1): p. 47-64.
7. Jaguemont, J. and J. Van Mierlo, *A comprehensive review of future thermal management systems for battery-electrified vehicles.* Journal of Energy Storage, 2020. **31**: p. 101551.
8. Sevugan, P.A., M. Pradeep, A. Krishnaswamy, and K. Karunamurthy, *Battery thermal management system for electric vehicles using phase change materials.* Materials Today: Proceedings, 2022. **51**: p. 1604-1611.
9. Brady, M., *Assessment of battery technology for rail propulsion application*. 2017, United States. Federal Railroad Administration.
10. Jhariya, M., A.K. Dewangan, S.Q. Moinuddin, S. Kumar, A. Ahmad, and A.K. Yadav, *Research progress on efficient battery thermal management system (BTMs) for electric vehicles using composite phase change materials with liquid cooling and nanoadditives.* Journal of Thermal Analysis and Calorimetry, 2024. **149**(23): p. 13653-13680.
11. Nagasubramanian, G., *Electrical characteristics of 18650 Li-ion cells at low temperatures.* Journal of applied electrochemistry, 2001. **31**: p. 99-104.
12. Burow, D., K. Sergeeva, S. Calles, K. Schorb, A. Boerger, C. Roth, and P. Heitjans, *Inhomogeneous degradation of graphite anodes in automotive lithium ion batteries under low-temperature pulse cycling conditions.* Journal of Power Sources, 2016. **307**: p. 806-814.
13. Ouyang, M., Z. Chu, L. Lu, J. Li, X. Han, X. Feng, and G. Liu, *Low temperature aging mechanism identification and lithium deposition in a large format lithium iron phosphate battery for different charge profiles.* Journal of Power Sources, 2015. **286**: p. 309-320.
14. Jaguemont, J., L. Boulon, Y. Dube, and F. Martel, *Thermal management of a hybrid electric vehicle in cold weather.* IEEE Transactions on Energy Conversion, 2016. **31**(3): p. 1110-1120.

15. Lei, Z., Z. Maotao, X. Xiaoming, and G. Junkui, *Thermal runaway characteristics on NCM lithium-ion batteries triggered by local heating under different heat dissipation conditions.* Applied Thermal Engineering, 2019. **159**: p. 113847.
16. Ramadass, P., B. Haran, R. White, and B.N. Popov, *Capacity fade of Sony 18650 cells cycled at elevated temperatures: Part I. Cycling performance.* Journal of power sources, 2002. **112**(2): p. 606-613.
17. Doughty, D.H., *Li Ion Battery Abuse Tolerance Testing-An Overview*. 2006.
18. Wang, C., T. Lin, J. Huang, and Z. Rao, *Temperature response of a high power lithium-ion battery subjected to high current discharge.* Materials Research Innovations, 2015. **19**(sup2): p. S2-156-S2-160.
19. Wang, Q., B. Jiang, B. Li, and Y. Yan, *A critical review of thermal management models and solutions of lithium-ion batteries for the development of pure electric vehicles.* Renewable and Sustainable Energy Reviews, 2016. **64**: p. 106-128.
20. Feng, X., C. Xu, X. He, L. Wang, G. Zhang, and M. Ouyang, *Mechanisms for the evolution of cell variations within a LiNixCoyMnzO2/graphite lithium-ion battery pack caused by temperature non-uniformity.* Journal of cleaner production, 2018. **205**: p. 447-462.
21. Pesaran, A., M. Keyser, G. Kim, S. Santhanagopalan, and K. Smith, *Tools for designing thermal management of batteries in electric drive vehicles (presentation)*. 2013, National Renewable Energy Lab.(NREL), Golden, CO (United States).
22. Jiang, Z. and Z. Qu, *Lithium–ion battery thermal management using heat pipe and phase change material during discharge–charge cycle: A comprehensive numerical study.* Applied Energy, 2019. **242**: p. 378-392.
23. Rao, Z., Z. Qian, Y. Kuang, and Y. Li, *Thermal performance of liquid cooling based thermal management system for cylindrical lithium-ion battery module with variable contact surface.* Applied Thermal Engineering, 2017. **123**: p. 1514-1522.
24. Greco, A., X. Jiang, and D. Cao, *An investigation of lithium-ion battery thermal management using paraffin/porous-graphite-matrix composite.* Journal of Power Sources, 2015. **278**: p. 50-68.
25. Qin, P., M. Liao, D. Zhang, Y. Liu, J. Sun, and Q. Wang, *Experimental and numerical study on a novel hybrid battery thermal management system integrated forced-air convection and phase change material.* Energy Conversion and Management, 2019. **195**: p. 1371-1381.
26. Ling, Z., F. Wang, X. Fang, X. Gao, and Z. Zhang, *A hybrid thermal management system for lithium ion batteries combining phase change materials with forced-air cooling.* Applied energy, 2015. **148**: p. 403-409.
27. Liu, L., X. Zhang, and X. Lin, *Recent Developments of Thermal Management Strategies for Lithium-Ion Batteries: A State-of-The-Art Review.* Energy Technology, 2022. **10**(6): p. 2101135.
28. Bamdezh, M. and G. Molaeimanesh, *The path from conventional battery thermal management systems to hybrid battery thermal management systems for electric vehicles, opportunities and challenges.* Journal of Energy Storage, 2024. **100**: p. 113160.
29. Patel, J.R. and M.K. Rathod, *Recent developments in the passive and hybrid thermal management techniques of lithium-ion batteries.* Journal of Power Sources, 2020. **480**: p. 228820.
30. Zare, P., N. Perera, J. Lahr, and R. Hasan, *A novel thermal management system for cylindrical lithium-ion batteries using internal-external fin-enhanced phase change material.* Applied Thermal Engineering, 2024. **238**: p. 121985.

31. Keyhani-Asl, A., N. Perera, J. Lahr, and R. Hasan, *Porous media and foam application in battery thermal management systems: A comprehensive review focused on its impact, numerical modeling, and experimental preparation.* Journal of Energy Storage, 2024. **93**: p. 112306.
32. Sun, Z., Y. Guo, C. Zhang, J. Whitehouse, Q. Zhou, H. Xu, and C. Wang, *Experimental study of battery passive thermal management system using copper foam-based phase change materials.* International Journal of Thermofluids, 2023. **17**: p. 100255.
33. Li, B., L. Zhang, B. Shang, and Y. Huo, *Numerical investigation on heat transfer characteristics in battery thermal management with phase change material composited by toroidal porous medium.* International Communications in Heat and Mass Transfer, 2024. **154**: p. 107414.
34. Rajan, J.T., V.S. Jayapal, M. Krishna, K.M. Firose, S. Vaisakh, A.K. John, and A. Suryan, *Analysis of battery thermal management system for electric vehicles using 1-Tetradecanol phase change material.* Sustainable Energy Technologies and Assessments, 2022. **51**: p. 101943.
35. Buonomo, B., O. Manca, F. Menale, and S. Nardini. *Numerical investigation on the thermal control of lithium batteries for electric cars using metal foams and phase change materials*. in *Journal of Physics: Conference Series*. 2021. IOP Publishing.
36. El Idi, M.M., M. Karkri, and M.A. Tankari, *A passive thermal management system of Li-ion batteries using PCM composites: Experimental and numerical investigations.* International Journal of Heat and Mass Transfer, 2021. **169**: p. 120894.
37. Nield, D.A. and A. Bejan, *Convection in porous media*. Vol. 3. 2006: Springer.
38. Ki, S., J. Lee, S. Kim, J. Seong, J. Shim, S. Oh, S. Cho, S. Bang, D. Seo, and J. Kim, *An energy-efficient battery thermal management system incorporating a porous metal-based multiscale flow manifold.* Energy Conversion and Management, 2022. **269**: p. 116147.
39. Xu, J., Z. Guo, Z. Xu, X. Zhou, and X. Mei, *A systematic review and comparison of liquid-based cooling system for lithium-ion batteries.* eTransportation, 2023. **17**: p. 100242.
40. Keyhani-Asl, A., N. Perera, J. Lahr, and R. Hasan, *Innovative hybrid battery thermal management system incorporating copper foam porous fins and layers with phase change material and liquid cooling.* Applied Thermal Engineering, 2025. **268**: p. 125848.
41. Rabiei, M., A. Gharehghani, and A.M. Andwari, *Enhancement of battery thermal management system using a novel structure of hybrid liquid cold plate.* Applied Thermal Engineering, 2023. **232**: p. 121051.
42. Jiang, W., G. Feng, H. Wang, Z. Chang, X. Tan, J. Ji, Y. Zhang, and J. Zhou, *Analysis of hybrid active-passive prismatic Li-ion battery thermal management system using phase change materials with porous-filled mini-channels.* Journal of Energy Storage, 2024. **80**: p. 110144.
43. Liu, H., S. Ahmad, Y. Shi, and J. Zhao, *A parametric study of a hybrid battery thermal management system that couples PCM/copper foam composite with helical liquid channel cooling.* Energy, 2021. **231**: p. 120869.
44. Yang, H., Z. Wang, R. Bao, B. Zhang, X. Zhu, and H. Wang, *A novel hybrid battery thermal management system using TPMS structure and delayed cooling scheme.* Applied Thermal Engineering, 2025. **259**: p. 124901.
45. Zhang, X., Z. Li, L. Luo, Y. Fan, and Z. Du, *A review on thermal management of lithium-ion batteries for electric vehicles.* Energy, 2022. **238**: p. 121652.

46. Al-Zareer, M., I. Dincer, and M.A. Rosen, *A review of novel thermal management systems for batteries.* International Journal of Energy Research, 2018. **42**(10): p. 3182-3205.
47. Angani, A., H.-W. Kim, M.-H. Hwang, E. Kim, K.-M. Kim, and H.-R. Cha, *A comparison between Zig-Zag plated hybrid parallel pipe and liquid cooling battery thermal management systems for Lithium-ion battery module.* Applied Thermal Engineering, 2023. **219**: p. 119599.
48. Zadeh, P.G., Y. Wang, and J.D. Chung, *Thermal management modeling for cylindrical lithium-ion battery packs considering safety and lifespan.* Journal of Mechanical Science and Technology, 2022. **36**(7): p. 3727-3733.
49. Wu, W., S. Wang, W. Wu, K. Chen, S. Hong, and Y. Lai, *A critical review of battery thermal performance and liquid based battery thermal management.* Energy conversion and management, 2019. **182**: p. 262-281.
50. Zare, P., N. Perera, J. Lahr, and R. Hasan, *Solid-liquid phase change materials for the battery thermal management systems in electric vehicles and hybrid electric vehicles–A systematic review.* Journal of Energy Storage, 2022. **52**: p. 105026.
51. Waseem, M., M. Ahmad, A. Parveen, and M. Suhaib, *Battery technologies and functionality of battery management system for EVs: Current status, key challenges, and future prospectives.* Journal of Power Sources, 2023. **580**: p. 233349.
52. Xiaoqing, Z., W. Zhenpo, W. Hsin, and W. Cong, *Review of thermal runaway and safety management for lithium-ion traction batteries in electric vehicles.* Journal of mechanical engineering, 2020. **56**(14): p. 91-118.
53. de Santoli, L., R. Paiolo, and G.L. Basso, *An overview on safety issues related to hydrogen and methane blend applications in domestic and industrial use.* Energy Procedia, 2017. **126**: p. 297-304.
54. Al-Zareer, M., I. Dincer, and M.A. Rosen, *A novel approach for performance improvement of liquid to vapor based battery cooling systems.* Energy Conversion and Management, 2019. **187**: p. 191-204.
55. Al-Zareer, M., I. Dincer, and M.A. Rosen, *A novel phase change based cooling system for prismatic lithium ion batteries.* International Journal of Refrigeration, 2018. **86**: p. 203-217.
56. Crafts, C.C., D.H. Doughty, J. McBreen, and E.P. Roth, *Advanced technology development program for lithium-ion batteries: thermal abuse performance of 18650 Li-ion cells*. 2004, Sandia National Laboratories.
57. Wu, W., W. Wu, and S. Wang, *Thermal management optimization of a prismatic battery with shape-stabilized phase change material.* International Journal of Heat and Mass Transfer, 2018. **121**: p. 967-977.
58. Saw, L.H., Y. Ye, and A.A. Tay, *Integration issues of lithium-ion battery into electric vehicles battery pack.* Journal of Cleaner Production, 2016. **113**: p. 1032-1045.
59. Akinlabi, A.H. and D. Solyali, *Configuration, design, and optimization of air-cooled battery thermal management system for electric vehicles: A review.* Renewable and Sustainable Energy Reviews, 2020. **125**: p. 109815.
60. Rahn, C.D. and C.-Y. Wang, *Battery systems engineering*. 2013: John Wiley & Sons.
61. Nikdel, M., *Various battery models for various simulation studies and applications.* Renewable and Sustainable Energy Reviews, 2014. **32**: p. 477-485.
62. Lin, J., X. Liu, S. Li, C. Zhang, and S. Yang, *A review on recent progress, challenges and perspective of battery thermal management system.* International Journal of Heat and Mass Transfer, 2021. **167**: p. 120834.
63. Guo, M., G. Sikha, and R.E. White, *Single-particle model for a lithium-ion cell: Thermal behavior.* Journal of The Electrochemical Society, 2010. **158**(2): p. A122.

64. Chen, Z., D.L. Danilov, R.A. Eichel, and P.H. Notten, *Porous electrode modeling and its applications to Li-ion batteries.* Advanced Energy Materials, 2022. **12**(32): p. 2201506.
65. Jokar, A., B. Rajabloo, M. Désilets, and M. Lacroix, *Review of simplified Pseudo-two-Dimensional models of lithium-ion batteries.* Journal of Power Sources, 2016. **327**: p. 44-55.
66. Xu, M., Z. Zhang, X. Wang, L. Jia, and L. Yang, *A pseudo three-dimensional electrochemical–thermal model of a prismatic LiFePO4 battery during discharge process.* Energy, 2015. **80**: p. 303-317.
67. Gomez, J., R. Nelson, E.E. Kalu, M.H. Weatherspoon, and J.P. Zheng, *Equivalent circuit model parameters of a high-power Li-ion battery: Thermal and state of charge effects.* Journal of Power Sources, 2011. **196**(10): p. 4826-4831.
68. Xie, Y., W. Li, X. Hu, C. Zou, F. Feng, and X. Tang, *Novel mesoscale electrothermal modeling for lithium-ion batteries.* IEEE Transactions on Power Electronics, 2019. **35**(3): p. 2595-2614.
69. Al Hallaj, S., H. Maleki, J.-S. Hong, and J.R. Selman, *Thermal modeling and design considerations of lithium-ion batteries.* Journal of power sources, 1999. **83**(1-2): p. 1-8.
70. Wang, Z., J. Ma, and L. Zhang, *Finite element thermal model and simulation for a cylindrical Li-ion battery.* IEEE Access, 2017. **5**: p. 15372-15379.
71. Di Domenico, D., G. Fiengo, and A. Stefanopoulou, *Lithium-ion battery state of charge estimation with a kalman filter based on a electrochemical model*, in *2008 IEEE International Conference on Control Applications*. 2008, IEEE. p. 702-707.
72. Gerver, R.E. and J.P. Meyers, *Three-dimensional modeling of electrochemical performance and heat generation of lithium-ion batteries in tabbed planar configurations.* Journal of The Electrochemical Society, 2011. **158**(7): p. A835.
73. Chen, S., C. Wan, and Y. Wang, *Thermal analysis of lithium-ion batteries.* Journal of power sources, 2005. **140**(1): p. 111-124.
74. Bernardi, D., E. Pawlikowski, and J. Newman, *A general energy balance for battery systems.* Journal of the electrochemical society, 1985. **132**(1): p. 5.
75. Abada, S., G. Marlair, A. Lecocq, M. Petit, V. Sauvant-Moynot, and F. Huet, *Safety focused modeling of lithium-ion batteries: A review.* Journal of Power Sources, 2016. **306**: p. 178-192.
76. Jindal, P., R. Katiyar, and J. Bhattacharya, *Evaluation of accuracy for Bernardi equation in estimating heat generation rate for continuous and pulse-discharge protocols in LFP and NMC based Li-ion batteries.* Applied Thermal Engineering, 2022. **201**: p. 117794.
77. Saechan, P. and I. Dhuchakallaya, *Numerical study on the air-cooled thermal management of Lithium-ion battery pack for electrical vehicles.* Energy Reports, 2022. **8**: p. 1264-1270.
78. Rizk, R., H. Louahlia, H. Gualous, P. Schaetzel, and G. Alcicek, *Experimental analysis on Li-ion battery local heat distribution.* Journal of Thermal Analysis and Calorimetry, 2019. **138**: p. 1557-1571.
79. Weng, J., X. Yang, G. Zhang, D. Ouyang, M. Chen, and J. Wang, *Optimization of the detailed factors in a phase-change-material module for battery thermal management.* International Journal of Heat and Mass Transfer, 2019. **138**: p. 126-134.
80. Yates, M., M. Akrami, and A.A. Javadi, *Analysing the performance of liquid cooling designs in cylindrical lithium-ion batteries.* Journal of Energy Storage, 2021. **33**: p. 100913.

81. Wang, F., J. Cao, Z. Ling, Z. Zhang, and X. Fang, *Experimental and simulative investigations on a phase change material nano-emulsion-based liquid cooling thermal management system for a lithium-ion battery pack.* Energy, 2020. **207**: p. 118215.
82. Robinson, J.B., J.A. Darr, D.S. Eastwood, G. Hinds, P.D. Lee, P.R. Shearing, O.O. Taiwo, and D.J. Brett, *Non-uniform temperature distribution in Li-ion batteries during discharge–A combined thermal imaging, X-ray micro-tomography and electrochemical impedance approach.* Journal of Power Sources, 2014. **252**: p. 51-57.
83. Gungor, S., E. Cetkin, and S. Lorente, *Thermal and electrical characterization of an electric vehicle battery cell, an experimental investigation.* Applied Thermal Engineering, 2022. **212**: p. 118530.
84. Liu, Z., B. Wang, Y. Tan, and P. Li, *Thermal management of lithium-ion battery pack under demanding conditions and long operating cycles using fin-enhanced PCMs/water hybrid cooling system.* Applied Thermal Engineering, 2023. **233**: p. 121214.
85. Bashiri, A.H., A. Sangtarash, and M. Zamani, *The effect of the porous media on thermal management of lithium-ion battery pack; a comparative and numerical study.* Thermal Science and Engineering Progress, 2022. **34**: p. 101427.
86. Karimi, G. and X. Li, *Thermal management of lithium-ion batteries for electric vehicles.* International Journal of Energy Research, 2013. **37**(1): p. 13-24.
87. Fathabadi, H., *A novel design including cooling media for Lithium-ion batteries pack used in hybrid and electric vehicles.* Journal of Power Sources, 2014. **245**: p. 495-500.
88. Fathabadi, H., *High thermal performance lithium-ion battery pack including hybrid active–passive thermal management system for using in hybrid/electric vehicles.* Energy, 2014. **70**: p. 529-538.
89. Cao, W., C. Zhao, Y. Wang, T. Dong, and F. Jiang, *Thermal modeling of full-size-scale cylindrical battery pack cooled by channeled liquid flow.* International journal of heat and mass transfer, 2019. **138**: p. 1178-1187.
90. Wang, H., T. Tao, J. Xu, X. Mei, X. Liu, and P. Gou, *Cooling capacity of a novel modular liquid-cooled battery thermal management system for cylindrical lithium ion batteries.* Applied Thermal Engineering, 2020. **178**: p. 115591.
91. EL IDI, M.M., M. KARKRI, M.A. TANKARI, and S. VINCENT, *Hybrid cooling based battery thermal management using composite phase change materials and forced convection.* Journal of Energy Storage, 2021. **41**: p. 102946.
92. Yayathi, S., W. Walker, D. Doughty, and H. Ardebili, *Energy distributions exhibited during thermal runaway of commercial lithium ion batteries used for human spaceflight applications.* Journal of Power Sources, 2016. **329**: p. 197-206.
93. Schuster, E., C. Ziebert, A. Melcher, M. Rohde, and H.J. Seifert, *Thermal behavior and electrochemical heat generation in a commercial 40 Ah lithium ion pouch cell.* Journal of Power Sources, 2015. **286**: p. 580-589.
94. Saito, Y., M. Shikano, and H. Kobayashi, *Heat generation behavior during charging and discharging of lithium-ion batteries after long-time storage.* Journal of Power Sources, 2013. **244**: p. 294-299.
95. Ye, Y., L.H. Saw, Y. Shi, and A.A. Tay, *Numerical analyses on optimizing a heat pipe thermal management system for lithium-ion batteries during fast charging.* Applied Thermal Engineering, 2015. **86**: p. 281-291.
96. Onda, K., T. Ohshima, M. Nakayama, K. Fukuda, and T. Araki, *Thermal behavior of small lithium-ion battery during rapid charge and discharge cycles.* Journal of Power sources, 2006. **158**(1): p. 535-542.

97. Zhang, J., J. Huang, Z. Li, B. Wu, Z. Nie, Y. Sun, F. An, and N. Wu, *Comparison and validation of methods for estimating heat generation rate of large-format lithium-ion batteries.* Journal of Thermal Analysis and Calorimetry, 2014. **117**: p. 447-461.
98. Kim, J.-S., J. Prakash, and J. Selman, *Thermal Characteristics of Li x Mn2 O 4 Spinel.* Electrochemical and solid-state letters, 2001. **4**(9): p. A141.
99. Kobayashi, Y., H. Miyashiro, K. Kumai, K. Takei, T. Iwahori, and I. Uchida, *Precise electrochemical calorimetry of LiCoO2/graphite lithium-ion cell: Understanding thermal behavior and estimation of degradation mechanism.* Journal of the Electrochemical Society, 2002. **149**(8): p. A978.
100. Habibishandiz, M. and M. Saghir, *A critical review of heat transfer enhancement methods in the presence of porous media, nanofluids, and microorganisms.* Thermal Science and Engineering Progress, 2022. **30**: p. 101267.
101. Rashidi, S., M.H. Kashefi, K.C. Kim, and O. Samimi-Abianeh, *Potentials of porous materials for energy management in heat exchangers–A comprehensive review.* Applied energy, 2019. **243**: p. 206-232.
102. Cooper, S., D. Eastwood, J. Gelb, G. Damblanc, D. Brett, R. Bradley, P. Withers, P. Lee, A. Marquis, and N. Brandon, *Image based modelling of microstructural heterogeneity in LiFePO4 electrodes for Li-ion batteries.* Journal of Power Sources, 2014. **247**: p. 1033-1039.
103. Kamath, P.M., C. Balaji, and S. Venkateshan, *Convection heat transfer from aluminium and copper foams in a vertical channel–An experimental study.* International Journal of Thermal Sciences, 2013. **64**: p. 1-10.
104. Fu, J., H.R. Thomas, and C. Li, *Tortuosity of porous media: Image analysis and physical simulation.* Earth-Science Reviews, 2021. **212**: p. 103439.
105. Hsu, C.-T. and P. Cheng, *Thermal dispersion in a porous medium.* International Journal of Heat and Mass Transfer, 1990. **33**(8): p. 1587-1597.
106. Özgümüş, T., M. Mobedi, Ü. Özkol, and A. Nakayama, *Thermal dispersion in porous media—a review on the experimental studies for packed beds.* Applied Mechanics Reviews, 2013. **65**(3): p. 031001.
107. Li, Z. and Z.-G. Wu, *Numerical study on the thermal behavior of phase change materials (PCMs) embedded in porous metal matrix.* Solar Energy, 2014. **99**: p. 172-184.
108. Zhang, C.-W., S.-R. Chen, H.-B. Gao, K.-J. Xu, Z. Xia, and S.-T. Li, *Study of thermal management system using composite phase change materials and thermoelectric cooling sheet for power battery pack.* Energies, 2019. **12**(10): p. 1937.
109. Sedeh, M.M. and J. Khodadadi, *Thermal conductivity improvement of phase change materials/graphite foam composites.* Carbon, 2013. **60**: p. 117-128.
110. Jiang, K., G. Liao, E. Jiaqiang, F. Zhang, J. Chen, and E. Leng, *Thermal management technology of power lithium-ion batteries based on the phase transition of materials: A review.* Journal of Energy Storage, 2020. **32**: p. 101816.
111. Niu, Z., J. Yu, X. Cui, X. Yang, Y. Sun, and J. Yan, *Experimental investigations on the thermal energy storage performance of shell and tube unit with composite phase change materials.* Energy Procedia, 2019. **158**: p. 4889-4896.
112. Yang, X., Z. Guo, Y. Liu, L. Jin, and Y.-L. He, *Effect of inclination on the thermal response of composite phase change materials for thermal energy storage.* Applied energy, 2019. **238**: p. 22-33.
113. Zhang, P., X. Xiao, Z. Meng, and M. Li, *Heat transfer characteristics of a molten-salt thermal energy storage unit with and without heat transfer enhancement.* Applied Energy, 2015. **137**: p. 758-772.

114. Yang, X., S. Feng, Q. Zhang, Y. Chai, L. Jin, and T.J. Lu, *The role of porous metal foam on the unidirectional solidification of saturating fluid for cold storage.* Applied energy, 2017. **194**: p. 508-521.
115. Aswin Karthik, C., P. Kalita, X. Cui, and X. Peng, *Thermal management for prevention of failures of lithium ion battery packs in electric vehicles: A review and critical future aspects.* Energy Storage, 2020. **2**(3): p. e137.
116. Giuliano, M.R., A.K. Prasad, and S.G. Advani, *Experimental study of an air-cooled thermal management system for high capacity lithium–titanate batteries.* Journal of power sources, 2012. **216**: p. 345-352.
117. Saw, L.H., Y. Ye, M.C. Yew, W.T. Chong, M.K. Yew, and T.C. Ng, *Computational fluid dynamics simulation on open cell aluminium foams for Li-ion battery cooling system.* Applied Energy, 2017. **204**: p. 1489-1499.
118. Shuja, S., B.S. Yilbas, and S. Khan, *Flow over a porous structure in a square cavity: Effects of the porous structure size and porosity on the heat transfer performance and fluid pressure loss.* Heat Transfer Research, 2015. **46**(12).
119. Zhang, W., G. Wang, J. Ma, Z. Wang, and E. Wang, *TThe effect of porosity on heat transfer and mass transfer of Mg-3Ni-2MnO2 hydrogen storage materials reaction bed.* International Journal of Modern Physics B, 2009. **23**: p. 940-946.
120. Li, W., Z. Qu, Y. He, and Y. Tao, *Experimental study of a passive thermal management system for high-powered lithium ion batteries using porous metal foam saturated with phase change materials.* Journal of power sources, 2014. **255**: p. 9-15.
121. Mohammadian, S.K., S.M. Rassoulinejad-Mousavi, and Y. Zhang, *Thermal management improvement of an air-cooled high-power lithium-ion battery by embedding metal foam.* Journal of Power Sources, 2015. **296**: p. 305-313.
122. Hussain, A., C.Y. Tso, and C.Y. Chao, *Experimental investigation of a passive thermal management system for high-powered lithium ion batteries using nickel foam-paraffin composite.* Energy, 2016. **115**: p. 209-218.
123. Heyhat, M.M., S. Mousavi, and M. Siavashi, *Battery thermal management with thermal energy storage composites of PCM, metal foam, fin and nanoparticle.* Journal of Energy Storage, 2020. **28**: p. 101235.
124. Akolkar, A. and J. Petrasch, *Tomography based pore-level optimization of radiative transfer in porous media.* International Journal of Heat and Mass Transfer, 2011. **54**(23-24): p. 4775-4783.
125. Arasteh, H., R. Mashayekhi, D. Toghraie, A. Karimipour, M. Bahiraei, and A. Rahbari, *Optimal arrangements of a heat sink partially filled with multilayered porous media employing hybrid nanofluid.* Journal of Thermal Analysis and Calorimetry, 2019. **137**: p. 1045-1058.
126. Ranjbaran, Y.S., S.J. Haghparast, M. Shojaeefard, and G. Molaeimanesh, *Numerical evaluation of a thermal management system consisting PCM and porous metal foam for Li-ion batteries.* Journal of Thermal Analysis and Calorimetry, 2020. **141**: p. 1717-1739.
127. Balaji, D., R. Velraj, and M.R. Murthy, *A review of the role of passive techniques on heat transfer enhancement of horizontal tube falling film and flooded evaporators.* Journal of Enhanced Heat Transfer, 2018. **25**(3).
128. Tian, Y. and C.-Y. Zhao, *A numerical investigation of heat transfer in phase change materials (PCMs) embedded in porous metals.* Energy, 2011. **36**(9): p. 5539-5546.
129. Zhao, C., D. Zhou, and Z. Wu. *Heat transfer enhancement of phase change materials (PCMs) in low and high temperature thermal storage by using porous materials*. in *International Heat Transfer Conference*. 2010.

130. Wang, C., T. Lin, N. Li, and H. Zheng, *Heat transfer enhancement of phase change composite material: Copper foam/paraffin.* Renewable energy, 2016. **96**: p. 960-965.

131. Yang, J., L. Yang, C. Xu, and X. Du, *Experimental study on enhancement of thermal energy storage with phase-change material.* Applied Energy, 2016. **169**: p. 164-176.

132. Mancin, S., A. Diani, L. Doretti, K. Hooman, and L. Rossetto, *Experimental analysis of phase change phenomenon of paraffin waxes embedded in copper foams.* International Journal of Thermal Sciences, 2015. **90**: p. 79-89.

133. Zhang, Z., J. Cheng, and X. He, *Numerical simulation of flow and heat transfer in composite PCM on the basis of two different models of open-cell metal foam skeletons.* International Journal of Heat and Mass Transfer, 2017. **112**: p. 959-971.

134. Hong, S.-T. and D.R. Herling, *Open-cell aluminum foams filled with phase change materials as compact heat sinks.* Scripta Materialia, 2006. **55**(10): p. 887-890.

135. Wang, Z., Z. Zhang, L. Jia, and L. Yang, *Paraffin and paraffin/aluminum foam composite phase change material heat storage experimental study based on thermal management of Li-ion battery.* Applied Thermal Engineering, 2015. **78**: p. 428-436.

136. Ali, H.M., M.M. Janjua, U. Sajjad, and W.-M. Yan, *A critical review on heat transfer augmentation of phase change materials embedded with porous materials/foams.* International Journal of Heat and Mass Transfer, 2019. **135**: p. 649-673.

137. Zhao, W., D.M. France, W. Yu, T. Kim, and D. Singh, *Phase change material with graphite foam for applications in high-temperature latent heat storage systems of concentrated solar power plants.* Renewable Energy, 2014. **69**: p. 134-146.

138. Guo, C.-x., G.-l. Hu, and Z.-j. Luo, *Preparation and thermal properties of graphite foam/eutectic salt composite as a phase change energy storage material.* Carbon, 2015. **93**: p. 1087.

139. Song, J.-l., Q.-g. Guo, Y.-j. Zhong, X.-q. Gao, Z.-h. Feng, F. Zhen, J.-l. Shi, and L. Lang, *Thermophysical properties of high-density graphite foams and their paraffin composites.* New Carbon Materials, 2012. **27**(1): p. 27-34.

140. Lopez, J., Z. Acem, and E.P. Del Barrio, *KNO3/NaNO3–Graphite materials for thermal energy storage at high temperature: Part II.–Phase transition properties.* Applied Thermal Engineering, 2010. **30**(13): p. 1586-1593.

141. Hussain, A., I.H. Abidi, C.Y. Tso, K.C. Chan, Z. Luo, and C.Y. Chao, *Thermal management of lithium ion batteries using graphene coated nickel foam saturated with phase change materials.* International journal of thermal sciences, 2018. **124**: p. 23-35.

142. Buonomo, B., O. Manca, D. Ercole, and S. Nardini. *Numerical simulation of thermal energy storage with phase change material and aluminum foam*. in *Sixth International Conference on Porous Media and Its Applications in Science, Engineering and Industry*. 2016.

143. Zheng, H. and C. Wang, *Numerical and experimental studies on the heat transfer performance of copper foam filled with paraffin.* Energies, 2017. **10**(7): p. 902.

144. Dietrich, B., G. Schell, E. Bucharsky, R. Oberacker, M. Hoffmann, W. Schabel, M. Kind, and H. Martin, *Determination of the thermal properties of ceramic sponges.* International Journal of Heat and Mass Transfer, 2010. **53**(1-3): p. 198-205.

145. Ambreen, T., H. Niyas, P. Kanti, H.M. Ali, and C.-W. Park, *Experimental investigation on the performance of RT-44HC-nickel foam-based heat sinks for thermal management of electronic gadgets.* International Journal of Heat and Mass Transfer, 2022. **188**: p. 122591.

146. Wang, D., X. Wu, G. Owens, and H. Xu, *Porous carbon-based thermally conductive materials: fabrication, functions and applications.* Chinese Journal of Structural Chemistry, 2022. **42**: p. 100006.

147. Al-Waeli, A.H., K. Sopian, J.H. Yousif, H.A. Kazem, J. Boland, and M.T. Chaichan, *Artificial neural network modeling and analysis of photovoltaic/thermal system based on the experimental study.* Energy Conversion and Management, 2019. **186**: p. 368-379.
148. Alshaer, W., S. Nada, M. Rady, E.P. Del Barrio, and A. Sommier, *Thermal management of electronic devices using carbon foam and PCM/nano-composite.* International Journal of Thermal Sciences, 2015. **89**: p. 79-86.
149. Nield, D.A. and A. Bejan, *Mechanics of fluid flow through a porous medium*, in *Convection in porous media*. 2017. p. 1-35.
150. Vafai, K., *Handbook of porous media*. 2015: Crc Press.
151. Forchheimer, P., *Wasserbewegung durch boden.* Zeitschrift des Vereines Deutscher Ingenieure, 1901. **45**(50): p. 1781-1788.
152. Durlofsky, L. and J. Brady, *Analysis of the Brinkman equation as a model for flow in porous media.* The Physics of fluids, 1987. **30**(11): p. 3329-3341.
153. Haddad, S., *Thermal instability in Brinkman porous media with Cattaneo–Christov heat flux.* International journal of heat and mass transfer, 2014. **68**: p. 659-668.
154. Brinkman, H.C., *A calculation of the viscous force exerted by a flowing fluid on a dense swarm of particles.* Flow, Turbulence and Combustion, 1949. **1**: p. 27-34.
155. Bera, P. and A. Khalili, *Stability of mixed convection in an anisotropic vertical porous channel.* Physics of Fluids, 2002. **14**(5): p. 1617-1630.
156. Mahmoudi, Y., K. Hooman, and K. Vafai, *Convective heat transfer in porous media*. 2019: CRC Press.
157. Esfe, M.H., M. Bahiraei, H. Hajbarati, and M. Valadkhani, *A comprehensive review on convective heat transfer of nanofluids in porous media: Energy-related and thermohydraulic characteristics.* Applied Thermal Engineering, 2020. **178**: p. 115487.
158. Kiani, M., M. Ansari, A.A. Arshadi, E. Houshfar, and M. Ashjaee, *Hybrid thermal management of lithium-ion batteries using nanofluid, metal foam, and phase change material: an integrated numerical–experimental approach.* Journal of Thermal Analysis and Calorimetry, 2020. **141**(5): p. 1703-1715.
159. Zhao, Y., B. Zou, J. Ding, and Y. Ding, *Experimental and numerical investigation of a hybrid battery thermal management system based on copper foam-paraffin composite phase change material and liquid cooling.* Applied Thermal Engineering, 2023. **218**: p. 119312.
160. Hamidi, S., T. Heinze, B. Galvan, and S. Miller, *Critical review of the local thermal equilibrium assumption in heterogeneous porous media: Dependence on permeability and porosity contrasts.* Applied Thermal Engineering, 2019. **147**: p. 962-971.
161. Pati, S., A. Borah, M.P. Boruah, and P.R. Randive, *Critical review on local thermal equilibrium and local thermal non-equilibrium approaches for the analysis of forced convective flow through porous media.* International communications in heat and mass Transfer, 2022. **132**: p. 105889.
162. Pan, Y., G. Xu, W. Li, and C. Zhong, *A novel numerical cubic filament model and method for the two-energy equation in porous media.* International Journal of Heat and Mass Transfer, 2015. **80**: p. 688-697.
163. Torabi, M., N. Karimi, G. Peterson, and S. Yee, *Challenges and progress on the modelling of entropy generation in porous media: a review.* International Journal of Heat and Mass Transfer, 2017. **114**: p. 31-46.
164. Faizurrahmany, Z., *Brief overview on Local Thermal Non-Equilibrium modeling of heat and mass transfer in open porous materials.* Academic Journal of Civil Engineering, 2019. **37**(1): p. 374-377.

165. Kasaeian, A., R. Daneshazarian, O. Mahian, L. Kolsi, A.J. Chamkha, S. Wongwises, and I. Pop, *Nanofluid flow and heat transfer in porous media: a review of the latest developments.* International Journal of Heat and Mass Transfer, 2017. **107**: p. 778-791.
166. Sardari, P.T., H.I. Mohammed, D. Giddings, M. Gillott, and D. Grant, *Numerical study of a multiple-segment metal foam-PCM latent heat storage unit: Effect of porosity, pore density and location of heat source.* Energy, 2019. **189**: p. 116108.
167. Al-Sumaily, G.F., A. Al Ezzi, H.A. Dhahad, M.C. Thompson, and T. Yusaf, *Legitimacy of the local thermal equilibrium hypothesis in porous media: A comprehensive review.* Energies, 2021. **14**(23): p. 8114.
168. Vadasz, P., *On the paradox of heat conduction in porous media subject to lack of local thermal equilibrium.* International journal of heat and mass transfer, 2007. **50**(21-22): p. 4131-4140.
169. Lin, W., G. Xie, J. Yuan, and B. Sundén, *Comparison and analysis of heat transfer in aluminum foam using local thermal equilibrium or nonequilibrium model.* Heat Transfer Engineering, 2016. **37**(3-4): p. 314-322.
170. Torabi, M., N. Karimi, K. Zhang, and G. Peterson, *Generation of entropy and forced convection of heat in a conduit partially filled with porous media–local thermal non-equilibrium and exothermicity effects.* Applied Thermal Engineering, 2016. **106**: p. 518-536.
171. Al-Sumaily, G.F., H.M. Hussen, and M.C. Thompson, *Validation of thermal equilibrium assumption in free convection flow over a cylinder embedded in a packed bed.* International Communications in Heat and Mass Transfer, 2014. **58**: p. 184-192.
172. Li, Y., L. Gong, H. Lu, D. Zhang, and B. Ding, *Thermal modeling and analysis of metal foam heat sink with thermal equilibrium and non-equilibrium models.* Computer Modeling in Engineering & Sciences, 2020. **123**(2): p. 895-912.
173. Roohani Isfahani, S.N., M.R. Salimpour, and E. Shirani, *Numerical study and sensitivity analysis on convective heat transfer enhancement in a heat pipe partially filled with porous material using LTE and LTNE methods.* Heat Transfer—Asian Research, 2019. **48**(8): p. 4342-4353.
174. Amiri, A. and K. Vafai, *Analysis of dispersion effects and non-thermal equilibrium, non-Darcian, variable porosity incompressible flow through porous media.* International journal of heat and mass transfer, 1994. **37**(6): p. 939-954.
175. Dehghan, M., M.T. Jamal-Abad, and S. Rashidi, *Analytical interpretation of the local thermal non-equilibrium condition of porous media imbedded in tube heat exchangers.* Energy Conversion and Management, 2014. **85**: p. 264-271.
176. Chen, C.-C., P.-C. Huang, and H.-Y. Hwang, *Enhanced forced convective cooling of heat sources by metal-foam porous layers.* International Journal of Heat and Mass Transfer, 2013. **58**(1-2): p. 356-373.
177. Elliott, A., M. Torabi, N. Karimi, and S. Cunningham, *On the effects of internal heat sources upon forced convection in porous channels with asymmetric thick walls.* International Communications in Heat and Mass Transfer, 2016. **73**: p. 100-110.
178. Duval, F., F. Fichot, and M. Quintard, *A local thermal non-equilibrium model for two-phase flows with phase-change in porous media.* International Journal of Heat and Mass Transfer, 2004. **47**(3): p. 613-639.
179. Kim, S.J. and S.P. Jang, *Effects of the Darcy number, the Prandtl number, and the Reynolds number on local thermal non-equilibrium.* International Journal of Heat and Mass Transfer, 2002. **45**(19): p. 3885-3896.
180. Torabi, M., C. Dickson, and N. Karimi, *Theoretical investigation of entropy generation and heat transfer by forced convection of copper–water nanofluid in a porous*

channel—Local thermal non-equilibrium and partial filling effects. Powder Technology, 2016. **301**: p. 234-254.

181. Jiang, P.-X., G.-S. Si, M. Li, and Z.-P. Ren, *Experimental and numerical investigation of forced convection heat transfer of air in non-sintered porous media.* Experimental Thermal and Fluid Science, 2004. **28**(6): p. 545-555.
182. Betchen, L.J. and A.G. Straatman, *The development of a volume-averaged entropy-generation function for nonequilibrium heat transfer in high-conductivity porous foams.* Numerical Heat Transfer, Part B: Fundamentals, 2008. **53**(5): p. 412-436.
183. Buonomo, B., O. Manca, and G. Lauriat, *Forced convection in micro-channels filled with porous media in local thermal non-equilibrium conditions.* International Journal of Thermal Sciences, 2014. **77**: p. 206-222.
184. Rashidi, S., A. Ijadi, and Z. Dadashi, *Potentials of porous materials for temperature control of lithium-ion batteries.* Journal of Energy Storage, 2022. **51**: p. 104457.
185. Deng, Z., X. Liu, C. Zhang, Y. Huang, and Y. Chen, *Melting behaviors of PCM in porous metal foam characterized by fractal geometry.* International Journal of Heat and Mass Transfer, 2017. **113**: p. 1031-1042.
186. Sharma, D.K. and A. Prabhakar, *A review on air cooled and air centric hybrid thermal management techniques for Li-ion battery packs in electric vehicles.* Journal of Energy Storage, 2021. **41**: p. 102885.
187. Westbrook, M.H., *The Electric Car: Development and future of battery, hybrid and fuel-cell cars*. 2002: IET.
188. Wang, T., K. Tseng, and J. Zhao, *Development of efficient air-cooling strategies for lithium-ion battery module based on empirical heat source model.* Applied Thermal Engineering, 2015. **90**: p. 521-529.
189. Olabi, A., H.M. Maghrabie, O.H.K. Adhari, E.T. Sayed, B.A. Yousef, T. Salamah, M. Kamil, and M.A. Abdelkareem, *Battery thermal management systems: recent progress and challenges.* International Journal of Thermofluids, 2022. **15**: p. 100171.
190. Wang, Y., Y. Yu, Z. Jing, C. Wang, G. Zhou, and W. Zhao, *Thermal performance of lithium-ion batteries applying forced air cooling with an improved aluminium foam heat sink design.* International Journal of Heat and Mass Transfer, 2021. **167**: p. 120827.
191. Yang, M., G. Mathew, H. Nemati, and M. Moghimi, *A novel approach for active cooling of a battery at cell level: Air-cooled mini-channel heat sink, enhanced with intermittent metal foam.* Journal of Energy Storage, 2024. **81**: p. 110374.
192. Wang, P., D. Qin, T. Wang, and J. Chen, *Thermal Performance Analysis of Gradient Porosity Aluminium Foam Heat Sink for Air-Cooling Battery Thermal Management System.* Applied Sciences, 2022. **12**(9): p. 4628.
193. Mohammadian, S.K. and Y. Zhang, *Cumulative effects of using pin fin heat sink and porous metal foam on thermal management of lithium-ion batteries.* Applied Thermal Engineering, 2017. **118**: p. 375-384.
194. Mohammadian, S.K. and Y. Zhang, *Temperature uniformity improvement of an air-cooled high-power lithium-ion battery using metal and nonmetal foams.* Journal of Heat Transfer, 2016. **138**(11): p. 114502.
195. Lu, M., X. Zhang, J. Ji, X. Xu, and Y. Zhang, *Research progress on power battery cooling technology for electric vehicles.* Journal of Energy Storage, 2020. **27**: p. 101155.
196. Shahjalal, M., T. Shams, M.E. Islam, W. Alam, M. Modak, S.B. Hossain, V. Ramadesigan, M.R. Ahmed, H. Ahmed, and A. Iqbal, *A review of thermal management for Li-ion batteries: Prospects, challenges, and issues.* Journal of Energy Storage, 2021. **39**: p. 102518.

197. Al-Hallaj, S. and J.R. Selman, *Thermal modeling of secondary lithium batteries for electric vehicle/hybrid electric vehicle applications.* Journal of power sources, 2002. **110**(2): p. 341-348.
198. Wu, W., W. Wu, and S. Wang, *Thermal optimization of composite PCM based large-format lithium-ion battery modules under extreme operating conditions.* Energy Conversion and Management, 2017. **153**: p. 22-33.
199. Mohamed, S.A., F.A. Al-Sulaiman, N.I. Ibrahim, M.H. Zahir, A. Al-Ahmed, R. Saidur, B. Yılbaş, and A. Sahin, *A review on current status and challenges of inorganic phase change materials for thermal energy storage systems.* Renewable and Sustainable Energy Reviews, 2017. **70**: p. 1072-1089.
200. Subramanian, M., A.T. Hoang, B. Kalidasan, S. Nižetić, J.M. Solomon, D. Balasubramanian, C. Subramaniyan, G. Thenmozhi, H. Metghalchi, and X.P. Nguyen, *A technical review on composite phase change material based secondary assisted battery thermal management system for electric vehicles.* Journal of Cleaner Production, 2021. **322**: p. 129079.
201. Shen, Z.-G., S. Chen, X. Liu, and B. Chen, *A review on thermal management performance enhancement of phase change materials for vehicle lithium-ion batteries.* Renewable and Sustainable Energy Reviews, 2021. **148**: p. 111301.
202. Murali, G., G. Sravya, J. Jaya, and V.N. Vamsi, *A review on hybrid thermal management of battery packs and it's cooling performance by enhanced PCM.* Renewable and Sustainable Energy Reviews, 2021. **150**: p. 111513.
203. Chen, J., S. Kang, E. Jiaqiang, Z. Huang, K. Wei, B. Zhang, H. Zhu, Y. Deng, F. Zhang, and G. Liao, *Effects of different phase change material thermal management strategies on the cooling performance of the power lithium ion batteries: A review.* Journal of Power Sources, 2019. **442**: p. 227228.
204. Cicconi, P., P. Kumar, and P. Varshney, *A support approach for the modular design of Li-ion batteries: A test case with PCM.* Journal of Energy Storage, 2020. **31**: p. 101684.
205. Maghrabie, H.M., K. Elsaid, E.T. Sayed, A. Radwan, A.G. Abo-Khalil, H. Rezk, M.A. Abdelkareem, and A. Olabi, *Phase change materials based on nanoparticles for enhancing the performance of solar photovoltaic panels: A review.* Journal of Energy Storage, 2022. **48**: p. 103937.
206. Hamut, H.S., N. Javani, and I. Dinçer, *Thermal management of electric vehicle battery systems*. 2016: John Wiley & Sons.
207. Jaguemont, J., N. Omar, P. Van den Bossche, and J. Mierlo, *Phase-change materials (PCM) for automotive applications: A review.* Applied thermal engineering, 2018. **132**: p. 308-320.
208. Rao, Z. and S. Wang, *A review of power battery thermal energy management.* Renewable and Sustainable Energy Reviews, 2011. **15**(9): p. 4554-4571.
209. Amine, K., J. Liu, and I. Belharouak, *High-temperature storage and cycling of C-LiFePO4/graphite Li-ion cells.* Electrochemistry communications, 2005. **7**(7): p. 669-673.
210. Shim, J. and K.A. Striebel, *Characterization of high-power lithium-ion cells during constant current cycling: Part I. Cycle performance and electrochemical diagnostics.* Journal of power sources, 2003. **122**(2): p. 188-194.
211. Spitthoff, L., P.R. Shearing, and O.S. Burheim, *Temperature, ageing and thermal management of lithium-ion batteries.* Energies, 2021. **14**(5): p. 1248.
212. Liang, Z., R. Wang, A.H. Malt, M. Souri, M. Esfahani, and M. Jabbari, *Systematic evaluation of a flat-heat-pipe-based thermal management: Cell-to-cell variations and battery ageing.* Applied Thermal Engineering, 2021. **192**: p. 116934.

213. Iasiello, M., N. Bianco, W.K. Chiu, and V. Naso, *The effects of variable porosity and cell size on the thermal performance of functionally-graded foams.* International Journal of Thermal Sciences, 2021. **160**: p. 106696.
214. Zhang, J., X. Li, G. Zhang, H. Wu, Z. Rao, J. Guo, and D. Zhou, *Experimental investigation of the flame retardant and form-stable composite phase change materials for a power battery thermal management system.* Journal of Power Sources, 2020. **480**: p. 229116.
215. Fang, M., J. Zhou, H. Fei, K. Yang, and R. He, *Porous-material-based composite phase change materials for a lithium-ion battery thermal management system.* Energy & Fuels, 2022. **36**(8): p. 4153-4173.
216. Saxena, V., A. Sharma, R. Kothari, S.K. Sahu, and S.I. Kundalwal, *Analysis of Li-ion battery under high discharge rate embedded with metal foam phase change composite: A numerical study.* Journal of Energy Storage, 2024. **84**: p. 110752.
217. Kurşun, B., E. Toklu, F. Polat, and M. Balta, *The effect of outer container geometry on the thermal management of lithium-ion batteries with a combination of phase change material and metal foam.* Journal of Energy Storage, 2024. **80**: p. 110227.
218. Zhou, J., M. Fang, K. Yang, K. Lu, H. Fei, P. Mu, and R. He, *A novel MOF/RGO-based composite phase change material for battery thermal management.* Applied Thermal Engineering, 2023. **227**: p. 120383.
219. Li, J., J. Huang, Z. Liu, M. Cao, R. Chen, and Y. Zhang, *Developing ternary composite phase change materials with two different phase change temperatures for battery thermal management.* Applied Thermal Engineering, 2023. **227**: p. 120357.
220. Zhou, D., Y. Luo, C. Bi, X. Li, J. Deng, W. Yang, and C. Li, *Experimental and simulative investigation on battery thermal management system with structural optimization of composite phase change material.* Journal of Energy Storage, 2023. **60**: p. 106613.
221. Zhang, G., Y. Sun, C. Wu, X. Yan, W. Zhao, and C. Peng, *Low-cost and highly thermally conductive lauric acid–paraffin–expanded graphite multifunctional composite phase change materials for quenching thermal runaway of lithium-ion battery.* Energy Reports, 2023. **9**: p. 2538-2547.
222. Mei, J., G. Shi, H. Liu, Z. Wang, and M. Chen, *Investigation on the optimization strategy of phase change material thermal management system for lithium-ion battery.* Journal of Energy Storage, 2022. **55**: p. 105365.
223. Zhang, J., X. Li, G. Zhang, Y. Wang, J. Guo, Y. Wang, Q. Huang, C. Xiao, and Z. Zhong, *Characterization and experimental investigation of aluminum nitride-based composite phase change materials for battery thermal management.* Energy Conversion and Management, 2020. **204**: p. 112319.
224. Cao, M., J. Huang, and Z. Liu, *The enhanced performance of phase-change materials via 3D printing with prickly aluminum honeycomb for thermal management of ternary lithium batteries.* Advances in Materials Science and Engineering, 2020. **2020**: p. 1-11.
225. Barnes, D. and X. Li, *Battery thermal management using phase change material-metal foam composite materials at various environmental temperatures.* Journal of Electrochemical Energy Conversion and Storage, 2020. **17**(2): p. 021106.
226. Veismoradi, A., A. Modir, M. Ghalambaz, and A. Chamkha, *A phase change/metal foam heatsink for thermal management of battery packs.* International Journal of Thermal Sciences, 2020. **157**: p. 106514.
227. Mehrabi-Kermani, M., E. Houshfar, and M. Ashjaee, *A novel hybrid thermal management for Li-ion batteries using phase change materials embedded in copper foams combined with forced-air convection.* International Journal of Thermal Sciences, 2019. **141**: p. 47-61.

228. He, J., X. Yang, and G. Zhang, *A phase change material with enhanced thermal conductivity and secondary heat dissipation capability by introducing a binary thermal conductive skeleton for battery thermal management.* Applied Thermal Engineering, 2019. **148**: p. 984-991.
229. Zou, D., X. Liu, R. He, S. Zhu, J. Bao, J. Guo, Z. Hu, and B. Wang, *Preparation of a novel composite phase change material (PCM) and its locally enhanced heat transfer for power battery module.* Energy Conversion and Management, 2019. **180**: p. 1196-1202.
230. Buonomo, B., D. Ercole, O. Manca, and F. Menale, *Thermal cooling behaviors of lithium-ion batteries by metal foam with phase change materials.* Energy Procedia, 2018. **148**: p. 1175-1182.
231. Pan, M. and Y. Zhong, *Experimental and numerical investigation of a thermal management system for a Li-ion battery pack using cutting copper fiber sintered skeleton/paraffin composite phase change materials.* International Journal of Heat and Mass Transfer, 2018. **126**: p. 531-543.
232. Wang, X., Y. Xie, R. Day, H. Wu, Z. Hu, J. Zhu, and D. Wen, *Performance analysis of a novel thermal management system with composite phase change material for a lithium-ion battery pack.* Energy, 2018. **156**: p. 154-168.
233. Luo, J., D. Zou, Y. Wang, S. Wang, and L. Huang, *Battery thermal management systems (BTMs) based on phase change material (PCM): A comprehensive review.* Chemical Engineering Journal, 2022. **430**: p. 132741.
234. Alipanah, M. and X. Li, *Numerical studies of lithium-ion battery thermal management systems using phase change materials and metal foams.* International Journal of Heat and Mass Transfer, 2016. **102**: p. 1159-1168.
235. Chapotard, C. and D. Tondeur, *Dynamics of latent heat storage in fixed beds a non-linear equilibrium model—the analogy with chromatography.* Chemical Engineering Communications, 1983. **24**(4-6): p. 183-204.
236. Khedher, N.B., J.M. Mahdi, H.S. Majdi, W.K. Al-Azzawi, S. Dhahbi, and P. Talebizadehsardari, *A hybrid solidification enhancement in a latent-heat storage system with nanoparticles, porous foam, and fin-aided foam strips.* Journal of Energy Storage, 2022. **56**: p. 106070.
237. Lei, J., C. Yang, X. Huang, Z. Li, and Y. Zhang, *Solidification enhancement of phase change materials using nanoparticles and metal foams with nonuniform porosity.* Journal of Energy Storage, 2021. **44**: p. 103420.
238. Li, W., T. Zhang, B. Li, F. Cui, and L. Liu, *Experimental investigation on combined thermal energy storage and thermoelectric system by using foam/PCM composite.* Energy Conversion and Management, 2021. **243**: p. 114429.
239. Lv, Y., X. Yang, X. Li, G. Zhang, Z. Wang, and C. Yang, *Experimental study on a novel battery thermal management technology based on low density polyethylene-enhanced composite phase change materials coupled with low fins.* Applied Energy, 2016. **178**: p. 376-382.
240. Zhao, Y., B. Zou, T. Zhang, Z. Jiang, J. Ding, and Y. Ding, *A comprehensive review of composite phase change material based thermal management system for lithium-ion batteries.* Renewable and Sustainable Energy Reviews, 2022. **167**: p. 112667.
241. Wu, W., X. Yang, G. Zhang, X. Ke, Z. Wang, W. Situ, X. Li, and J. Zhang, *An experimental study of thermal management system using copper mesh-enhanced composite phase change materials for power battery pack.* Energy, 2016. **113**: p. 909-916.

242. Kumar, R., A. Mitra, and T. Srinivas, *Role of nano-additives in the thermal management of lithium-ion batteries: A review.* Journal of Energy Storage, 2022. **48**: p. 104059.

243. Xie, J., Z. Ge, M. Zang, and S. Wang, *Structural optimization of lithium-ion battery pack with forced air cooling system.* Applied Thermal Engineering, 2017. **126**: p. 583-593.

244. Kim, G.-H. and A. Pesaran, *Battery thermal management design modeling.* World Electric Vehicle Journal, 2007. **1**(1): p. 126-133.

245. Deng, Y., C. Feng, E. Jiaqiang, H. Zhu, J. Chen, M. Wen, and H. Yin, *Effects of different coolants and cooling strategies on the cooling performance of the power lithium ion battery system: A review.* Applied Thermal Engineering, 2018. **142**: p. 10-29.

246. Kumar, P., D. Chaudhary, P. Varshney, U. Varshney, S.M. Yahya, and Y. Rafat, *Critical review on battery thermal management and role of nanomaterial in heat transfer enhancement for electrical vehicle application.* Journal of Energy Storage, 2020. **32**: p. 102003.

247. Abdelkareem, M.A., H.M. Maghrabie, A.G. Abo-Khalil, O.H.K. Adhari, E.T. Sayed, A. Radwan, K. Elsaid, T. Wilberforce, and A. Olabi, *Battery thermal management systems based on nanofluids for electric vehicles.* Journal of Energy Storage, 2022. **50**: p. 104385.

248. Liu, L., X. Zhang, and X. Lin, *Recent Developments of Thermal Management Strategies for Lithium-Ion Batteries: A State-of-The-Art Review.* Energy Technology, 2022. **31**: p. 2101135.

249. Karimi, D., H. Behi, J. Van Mierlo, and M. Berecibar, *Advanced Thermal Management Systems for High-Power Lithium-Ion Capacitors: A Comprehensive Review.* Designs, 2022. **6**(3): p. 53.

250. Choi, H., H. Kim, P. Park, and H. Lee, *Development of a mini-channel and metal foam-assisted static immersion cooling and preheating system for electric vehicle battery thermal management.* Case Studies in Thermal Engineering, 2025. **70**: p. 106145.

251. Jongpluempiti, J., P. Vengsungnle, S. Poojeera, S. Eiamsa-ard, N. Naphon, A. Srichat, K. Manatura, and P. Naphon, *Thermal profile analysis of 18650 Li-ion battery module with embedded copper foam in the nanofluid cooling jacket.* Case Studies in Chemical and Environmental Engineering, 2025. **11**: p. 101208.

252. Du, X., Z. Wang, Q. Gao, H. Yang, R. Bao, and S. Xiong, *Study on novel battery thermal management using triply periodic minimal surface porous structures liquid cooling channel.* Applied Thermal Engineering, 2024. **257**: p. 124384.

253. Xu, Y., X. Li, X. Liu, Y. Wang, X. Wu, and D. Zhou, *Experiment investigation on a novel composite silica gel plate coupled with liquid-cooling system for square battery thermal management.* Applied Thermal Engineering, 2021. **184**: p. 116217.

254. Buidin, T.I.C. and F. Mariasiu, *Battery thermal management systems: Current status and design approach of cooling technologies.* Energies, 2021. **14**(16): p. 4879.

255. Khaboshan, H.N., K. Kadirgama, D. Ramasamy, V. Talele, P. Zhao, H. Tyagi, and N. Miljkovic, *Thermal uniformity analysis of a hybrid battery pack using integrated phase change material, metal foam, and counterflow minichannels.* Applied Thermal Engineering, 2025. **259**: p. 124910.

256. Lee, S., H. Lee, Y.J. Jun, and H. Lee, *Hybrid battery thermal management system coupled with paraffin/copper foam composite phase change material.* Applied Energy, 2024. **353**: p. 122043.

257. Yu, X., Y. Tao, and Q. Deng, *Experimental study on thermal management of batteries based on the coupling of metal foam-paraffin composite phase change materials and air cooling.* Journal of Energy Storage, 2024. **84**: p. 110891.

258. Moaveni, A., M. Siavashi, and S. Mousavi, *Passive and hybrid battery thermal management system by cooling flow control, employing nano-PCM, fins, and metal foam.* Energy, 2024. **288**: p. 129809.
259. Yang, H., M. Li, Z. Wang, and B. Ma, *A compact and lightweight hybrid liquid cooling system coupling with Z-type cold plates and PCM composite for battery thermal management.* Energy, 2023. **263**: p. 126026.
260. Khaboshan, H.N., F. Jaliliantabar, A.A. Abdullah, and S. Panchal, *Improving the cooling performance of cylindrical lithium-ion battery using three passive methods in a battery thermal management system.* Applied Thermal Engineering, 2023. **227**: p. 120320.
261. Kiani, M., S. Omiddezyani, A.M. Nejad, M. Ashjaee, and E. Houshfar, *Novel hybrid thermal management for Li-ion batteries with nanofluid cooling in the presence of alternating magnetic field: an experimental study.* Case Studies in Thermal Engineering, 2021. **28**: p. 101539.
262. Zhao, Y., Q. Li, B. Zou, T. Zhang, L. Jin, G. Qiao, B. Nie, Y. Huang, and Y. Ding, *Performance of a liquid cooling-based battery thermal management system with a composite phase change material.* International Journal of Energy Research, 2020. **44**(6): p. 4727-4742.
263. Mashayekhi, M., E. Houshfar, and M. Ashjaee, *Development of hybrid cooling method with PCM and Al2O3 nanofluid in aluminium minichannels using heat source model of Li-ion batteries.* Applied Thermal Engineering, 2020. **178**: p. 115543.
264. Bamdezh, M., G. Molaeimanesh, and S. Zanganeh, *Role of foam anisotropy used in the phase-change composite material for the hybrid thermal management system of lithium-ion battery.* Journal of Energy Storage, 2020. **32**: p. 101778.
265. Zhang, W., J. Qiu, X. Yin, and D. Wang, *A novel heat pipe assisted separation type battery thermal management system based on phase change material.* Applied Thermal Engineering, 2020. **165**: p. 114571.
266. Li, J. and H. Zhang, *Thermal characteristics of power battery module with composite phase change material and external liquid cooling.* International Journal of Heat and Mass Transfer, 2020. **156**: p. 119820.
267. Zhao, Y., B. Zou, C. Li, and Y. Ding, *Active cooling based battery thermal management using composite phase change materials.* Energy Procedia, 2019. **158**: p. 4933-4940.
268. An, Z., X. Chen, L. Zhao, and Z. Gao, *Numerical investigation on integrated thermal management for a lithium-ion battery module with a composite phase change material and liquid cooling.* Applied Thermal Engineering, 2019. **163**: p. 114345.
269. Jiang, L., H. Zhang, J. Li, and P. Xia, *Thermal performance of a cylindrical battery module impregnated with PCM composite based on thermoelectric cooling.* Energy, 2019. **188**: p. 116048.
270. Xie, Y., J. Tang, S. Shi, Y. Xing, H. Wu, Z. Hu, and D. Wen, *Experimental and numerical investigation on integrated thermal management for lithium-ion battery pack with composite phase change materials.* Energy Conversion and Management, 2017. **154**: p. 562-575.
271. Shi, S., Y. Xie, M. Li, Y. Yuan, J. Yu, H. Wu, B. Liu, and N. Liu, *Non-steady experimental investigation on an integrated thermal management system for power battery with phase change materials.* Energy conversion and management, 2017. **138**: p. 84-96.
272. Miao, Y., P. Hynan, A. Von Jouanne, and A. Yokochi, *Current Li-ion battery technologies in electric vehicles and opportunities for advancements.* Energies, 2019. **12**(6): p. 1074.

273. Jiaqiang, E., M. Yue, J. Chen, H. Zhu, Y. Deng, Y. Zhu, F. Zhang, M. Wen, B. Zhang, and S. Kang, *Effects of the different air cooling strategies on cooling performance of a lithium-ion battery module with baffle.* Applied Thermal Engineering, 2018. **144**: p. 231-241.
274. Zhang, F., F. Lu, B. Liang, Y. Zhu, H. Gou, K. Xiao, and Y. He, *Thermal performance analysis of a new type of branch-fin enhanced battery thermal management PCM module.* Renewable Energy, 2023. **206**: p. 1049-1063.
275. Taheri, P., M. Yazdanpour, and M. Bahrami, *Transient three-dimensional thermal model for batteries with thin electrodes.* Journal of Power Sources, 2013. **243**: p. 280-289.
276. Ambekar, S., P. Rath, and A. Bhattacharya, *A novel PCM and TCE based thermal management of battery module.* Thermal Science and Engineering Progress, 2022. **29**: p. 101196.
277. Zhang, H., H.W. Mu, Y. Zhang, and J. Han, *Calculation and characteristics analysis of lithium ion batteries' internal resistance using HPPC test.* advanced materials research, 2014. **926**: p. 915-918.
278. Xin, S., C. Wang, and H. Xi, *Thermal management scheme and optimization of cylindrical lithium-ion battery pack based on air cooling and liquid cooling.* Applied Thermal Engineering, 2023. **224**: p. 120100.
279. Lai, Y., W. Wu, K. Chen, S. Wang, and C. Xin, *A compact and lightweight liquid-cooled thermal management solution for cylindrical lithium-ion power battery pack.* International Journal of Heat and Mass Transfer, 2019. **144**: p. 118581.
280. Zhao, C., W. Cao, T. Dong, and F. Jiang, *Thermal behavior study of discharging/charging cylindrical lithium-ion battery module cooled by channeled liquid flow.* International journal of heat and mass transfer, 2018. **120**: p. 751-762.
281. Huang, H., H. Wang, J. Gu, and Y. Wu, *High-dimensional model representation-based global sensitivity analysis and the design of a novel thermal management system for lithium-ion batteries.* Energy Conversion and Management, 2019. **190**: p. 54-72.
282. Voller, V.R. and C. Prakash, *A fixed grid numerical modelling methodology for convection-diffusion mushy region phase-change problems.* International journal of heat and mass transfer, 1987. **30**(8): p. 1709-1719.
283. Fadl, M. and P.C. Eames, *Numerical investigation of the influence of mushy zone parameter Amush on heat transfer characteristics in vertically and horizontally oriented thermal energy storage systems.* Applied Thermal Engineering, 2019. **151**: p. 90-99.
284. Mahdi, J.M. and E.C. Nsofor, *Melting enhancement in triplex-tube latent heat energy storage system using nanoparticles-metal foam combination.* Applied energy, 2017. **191**: p. 22-34.
285. Al-Abidi, A.A., S. Mat, K. Sopian, M. Sulaiman, and A.T. Mohammad, *Internal and external fin heat transfer enhancement technique for latent heat thermal energy storage in triplex tube heat exchangers.* Applied thermal engineering, 2013. **53**(1): p. 147-156.
286. Fourie, J.G. and J.P. Du Plessis, *Pressure drop modelling in cellular metallic foams.* Chemical Engineering Science, 2002. **57**(14): p. 2781-2789.
287. Yang, X., T.J. Lu, and T. Kim, *An analytical model for permeability of isotropic porous media.* Physics Letters A, 2014. **378**(30-31): p. 2308-2311.
288. Liu, Z., Y. Yao, and H. Wu, *Numerical modeling for solid–liquid phase change phenomena in porous media: Shell-and-tube type latent heat thermal energy storage.* Applied energy, 2013. **112**: p. 1222-1232.

289. Wang, P., X. Wang, Y. Huang, C. Li, Z. Peng, and Y. Ding, *Thermal energy charging behaviour of a heat exchange device with a zigzag plate configuration containing multi-phase-change-materials (m-PCMs).* Applied energy, 2015. **142**: p. 328-336.
290. Maerefat, M., S.Y. Mahmoudi, and K. Mazaheri, *Numerical simulation of forced convection enhancement in a pipe by porous inserts.* Heat Transfer Engineering, 2011. **32**(1): p. 45-56.
291. Hacen, D., A. Boughamoura, and S.B. Nasrallah, *Forced pulsating flow and heat transfer in a tube partially filled with a porous medium.* Journal of Porous Media, 2006. **9**(1): p. 1-14.
292. Alazmi, B. and K. Vafai, *Constant wall heat flux boundary conditions in porous media under local thermal non-equilibrium conditions.* International Journal of Heat and Mass Transfer, 2002. **45**(15): p. 3071-3087.
293. Calmidi, V.V. and R.L. Mahajan, *Forced convection in high porosity metal foams.* Journal of Heat Transfer, 2000. **122**(3): p. 557-565.
294. Calmidi, V. and R. Mahajan, *The effective thermal conductivity of high porosity fibrous metal foams.* Journal of Heat Transfer, 1999. **121**(2): p. 466-471.
295. Amiri, A., K. Vafai, and T. Kuzay, *Effects of boundary conditions on non-Darcian heat transfer through porous media and experimental comparisons.* Numerical Heat Transfer, Part A: Applications, 1995. **27**(6): p. 651-664.
296. Incropera, F.P., D.P. DeWitt, T.L. Bergman, and A.S. Lavine, *Fundamentals of heat and mass transfer*. Vol. 6. 1996: Wiley New York.
297. Xu, H., Z. Qu, and W. Tao, *Analytical solution of forced convective heat transfer in tubes partially filled with metallic foam using the two-equation model.* International Journal of Heat and Mass Transfer, 2011. **54**(17-18): p. 3846-3855.
298. Vatanparast, M.A., S. Hossainpour, A. Keyhani-Asl, and S. Forouzi, *Numerical investigation of total entropy generation in a rectangular channel with staggered semi-porous fins.* International Communications in Heat and Mass Transfer, 2020. **111**: p. 104446.
299. Mahmoudi, Y. and N. Karimi, *Numerical investigation of heat transfer enhancement in a pipe partially filled with a porous material under local thermal non-equilibrium condition.* International Journal of Heat and Mass Transfer, 2014. **68**: p. 161-173.
300. Patankar, S.V., *Numerical heat transfer and fluid flow*. 2018: CRC press.
301. Roy, R.K., *Design of experiments using the Taguchi approach: 16 steps to product and process improvement*. 2001: John Wiley & Sons.
302. Phadke, M.S., *Quality engineering using robust design*. 1995: Prentice Hall PTR.
303. Bademlioglu, A., A. Canbolat, N. Yamankaradeniz, and O. Kaynakli, *Investigation of parameters affecting Organic Rankine Cycle efficiency by using Taguchi and ANOVA methods.* Applied Thermal Engineering, 2018. **145**: p. 221-228.
304. Sudhakaran, S., M. Terese, Y. Mohan, A.D. Thampi, and S. Rani, *Influence of various parameters on the cooling performance of battery thermal management systems based on phase change materials.* Applied Thermal Engineering, 2023. **222**: p. 119936.
305. LLC, M. *Methods and formulas for analyse Taguchi design*. 2024 18 December 2024]; Available from: https://support.minitab.com/en-us/minitab/help-and-how-to/statistical-modeling/doe/how-to/taguchi/analyze-taguchi-design/methods-and-formulas/methods-and-formulas/.
306. Rangappa, R. and S. Rajoo, *Effect of thermo-physical properties of cooling mass on hybrid cooling for lithium-ion battery pack using design of experiments.* International Journal of Energy and Environmental Engineering, 2019. **10**(1): p. 67-83.
307. Roache, P.J., *Perspective: a method for uniform reporting of grid refinement studies.* Journal of Fluid Engineering, 1994. **116**(3): p. 405-413.

308. Division, A.S.o.M.E.F.E., *Quantification of Uncertainty in Computational Fluid Dynamics*. 1993: American Society of Mechanical Engineers.
309. Oliveira, R., G. Justi, and G. Lopes, *Grid convergence study of a cyclone separator using different mesh structures.* Chemical Industry and Chemical Engineering Quarterly, 2017. **23**(3): p. 311-320.
310. Hu, X., F. Zhu, and X. Gong, *Experimental and numerical study on the thermal behavior of phase change material infiltrated in low porosity metal foam.* Journal of Energy Storage, 2019. **26**: p. 101005.
311. Amani, M., M. Ameri, and A. Kasaeian, *The experimental study of convection heat transfer characteristics and pressure drop of magnetite nanofluid in a porous metal foam tube.* Transport in Porous Media, 2017. **116**: p. 959-974.
312. Tian, L.-L., X. Liu, S. Chen, and Z.-G. Shen, *Effect of fin material on PCM melting in a rectangular enclosure.* Applied Thermal Engineering, 2020. **167**: p. 114764.
313. Torabi, M., K. Zhang, G. Yang, J. Wang, and P. Wu, *Heat transfer and entropy generation analyses in a channel partially filled with porous media using local thermal non-equilibrium model.* Energy, 2015. **82**: p. 922-938.
314. Saha, S.K., H. Ranjan, M.S. Emani, and A.K. Bharti, *Performance evaluation criteria in heat transfer enhancement*. 2020: Springer.
315. Shokouhmand, H., F. Jam, and M. Salimpour, *The effect of porous insert position on the enhanced heat transfer in partially filled channels.* International Communications in Heat and Mass Transfer, 2011. **38**(8): p. 1162-1167.
316. Parveez, B., N.A. Jamal, H. Anuar, Y. Ahmad, A. Aabid, and M. Baig, *Microstructure and mechanical properties of metal foams fabricated via melt foaming and powder metallurgy technique: A review.* Materials, 2022. **15**(15): p. 5302.
317. Teamah, M.A., W.M. El-Maghlany, and M.M.K. Dawood, *Numerical simulation of laminar forced convection in horizontal pipe partially or completely filled with porous material.* International Journal of Thermal Sciences, 2011. **50**(8): p. 1512-1522.
318. Lu, W., T. Zhang, and M. Yang, *Analytical solution of forced convective heat transfer in parallel-plate channel partially filled with metallic foams.* International Journal of Heat and Mass Transfer, 2016. **100**: p. 718-727.
319. Nimvari, M.E., M. Maerefat, and M. El-Hossaini, *Numerical simulation of turbulent flow and heat transfer in a channel partially filled with a porous media.* International Journal of Thermal Sciences, 2012. **60**: p. 131-141.
320. Patel, J.R. and M.K. Rathod, *Phase change material selection using simulation-oriented optimization to improve the thermal performance of lithium-ion battery.* Journal of Energy Storage, 2022. **49**: p. 103974.
321. Naik, A.B. and A.C. Reddy, *Optimization of tensile strength in TIG welding using the Taguchi method and analysis of variance (ANOVA).* Thermal Science and Engineering Progress, 2018. **8**: p. 327-339.
322. Qazi, M.I., M. Abas, R. Khan, W. Saleem, C.I. Pruncu, and M. Omair, *Experimental investigation and multi-response optimization of machinability of AA5005H34 using composite desirability coupled with PCA.* Metals, 2021. **11**(2): p. 235.
323. Wang, J., W. Mei, B. Mao, and Q. Wang, *Investigation on the temperature control performance and optimization strategy of a battery thermal management system combining phase change and liquid cooling.* Applied Thermal Engineering, 2023. **232**: p. 121080.
324. Liu, Z., S. Ji, B. Wang, and P. Li, *Lightweight lithium-ion battery hybrid cooling system and intermittent cycle operation strategy design under demanding conditions.* International Communications in Heat and Mass Transfer, 2025. **160**: p. 108304.

Appendices

Appendix A

Developed User Defined Function (UDF) for battery heat generation modelling for single discharge and cyclic discharge–rest–charge

Single discharge

```
#include "udf.h"

/* Define constant values */
#define C_0 2.6 /* Battery capacity in Ampere-hours */
#define C_rate 5.0 /* Discharge C-rate */
#define BatteryVolume 1.65321e-5 /* Volume of the battery in cubic meters */

/* Define UDF for heat generation */
DEFINE_SOURCE(heat_generation_source, c, t, dS, eqn)
{
    real I, q_gen, SOC, T, dE_dT;
    real current_time;
    real R_e;
    real q_gen_V;

    /* Get T from Fluent in Kelvin */
    T = C_T(c, t); /* Mean temperature of the battery */

    /* Calculate current (I) */
    I = C_rate * C_0;

    /* Calculate state of charge (SOC) */
    current_time = CURRENT_TIME; /* Assign value to current_time */
    SOC = 1.0 - (I * current_time / (C_0 * 3600));

    /* Calculate (dE/dT) */
    dE_dT = (-0.355 + 2.154 * SOC - 2.869 * pow(SOC, 2) + 1.028 * pow(SOC, 3))*1e-
3;

    /* Calculate R_e */
    if (T >= 293.15 && T < 303.15) /* Temperature range: 20°C to 30°C */
    {
        R_e = (4301 * pow(SOC, 6) - 15496 * pow(SOC, 5) + 22391 * pow(SOC, 4) -
16531 * pow(SOC, 3) + 6559 * pow(SOC, 2) - 1334 * SOC + 166)*1e-3;
    }
    else if (T >= 303.15 && T < 313.15) /* Temperature range: 30°C to 40°C */
    {
        R_e = (2989 * pow(SOC, 6) - 10480 * pow(SOC, 5) + 14700 * pow(SOC, 4) -
10514 * pow(SOC, 3) + 4036 * pow(SOC, 2) - 793 * SOC + 107)*1e-3;
    }
    else if (T >= 313.15 && T < 323.15) /* Temperature range: 40°C to 50°C */
    {
        R_e = (1559 * pow(SOC, 6) - 5365 * pow(SOC, 5) + 7378 * pow(SOC, 4) - 5181
* pow(SOC, 3) + 1962 * pow(SOC, 2) - 382 * SOC + 66)*1e-3;
```

```
    }
    else if (T >= 323.15 && T < 333.15) /* Temperature range: 50°C to 60°C */
    {
        R_e = (1559 * pow(SOC, 6) - 5374 * pow(SOC, 5) + 7367 * pow(SOC, 4) - 5121
* pow(SOC, 3) + 1898 * pow(SOC, 2) - 355 * SOC + 58)*1e-3;
    }
    else if (T >= 333.15) /* Temperature range: 60°C and above */
    {
        R_e = (992 * pow(SOC, 6) - 3406 * pow(SOC, 5) + 4667 * pow(SOC, 4) - 3263
* pow(SOC, 3) + 1225 * pow(SOC, 2) - 233 * SOC + 48)*1e-3;
    }

    /* Calculate heat generation */
    q_gen = I * I * R_e - I * T * dE_dT;

    /* Calculate heat generation per unit volume */
    q_gen_V = q_gen / BatteryVolume;

    return q_gen_V;
}
```

Discharge–rest–charge cycles

```
#include "udf.h"

/* Define constant values */
#define C_0 2.6 /* Battery capacity in Ampere-hours */
#define BatteryVolume 1.65321e-5 /* Volume of the battery in cubic meters */


/* Define UDF for heat generation */
DEFINE_SOURCE(heat_generation_source, c, t, dS, eqn)
{
    real q_gen_V;          /* Heat generation per unit volume */
    real current_time;     /* Current time in the simulation */
    real cycle_time;       /* Time within the current cycle */
    real total_cycle_time = 2220.0; /* Total cycle time */
    int cycle_number;      /* Track the cycle number */
    int max_cycles = 5;   /* Define the maximum number of cycles */

    real I, SOC, T, dE_dT, R_e, q_gen;
    real heat_gen_factor = 1.0; /* Scaling factor for heat generation */

    /* Get the current time from Fluent */
    current_time = CURRENT_TIME;

    /* Calculate the current cycle number */
    cycle_number = (int)floor(current_time / total_cycle_time);

    /* Calculate time within the current cycle */
    cycle_time = current_time - total_cycle_time * cycle_number;

    /* Get temperature from Fluent */
    T = C_T(c, t);

    /* Calculate current (I) */
    I = C_rate * C_0;
```

```
    /* Calculate SOC using cycle_time */
    SOC = MAX(0.0, MIN(1.0, 1.0 - (I * cycle_time / (C_0 * 3600))));

    /* Determine the phase */
    if (cycle_time <= 720.0) {
        /* Discharge phase */
       /* Calculate (dE/dT) */
    dE_dT = (-0.355 + 2.154 * SOC - 2.869 * pow(SOC, 2) + 1.028 * pow(SOC, 3))*1e-
3;

    /* Calculate R_e */
    if (T >= 293.15 && T < 303.15) /* Temperature range: 20°C to 30°C */
    {
        R_e = (4301 * pow(SOC, 6) - 15496 * pow(SOC, 5) + 22391 * pow(SOC, 4) -
16531 * pow(SOC, 3) + 6559 * pow(SOC, 2) - 1334 * SOC + 166)*1e-3;
    }
    else if (T >= 303.15 && T < 313.15) /* Temperature range: 30°C to 40°C */
    {
        R_e = (2989 * pow(SOC, 6) - 10480 * pow(SOC, 5) + 14700 * pow(SOC, 4) -
10514 * pow(SOC, 3) + 4036 * pow(SOC, 2) - 793 * SOC + 107)*1e-3;
    }
    else if (T >= 313.15 && T < 323.15) /* Temperature range: 40°C to 50°C */
    {
        R_e = (1559 * pow(SOC, 6) - 5365 * pow(SOC, 5) + 7378 * pow(SOC, 4) - 5181
* pow(SOC, 3) + 1962 * pow(SOC, 2) - 382 * SOC + 66)*1e-3;
    }
    else if (T >= 323.15 && T < 333.15) /* Temperature range: 50°C to 60°C */
    {
        R_e = (1559 * pow(SOC, 6) - 5374 * pow(SOC, 5) + 7367 * pow(SOC, 4) - 5121
* pow(SOC, 3) + 1898 * pow(SOC, 2) - 355 * SOC + 58)*1e-3;
    }
    else if (T >= 333.15) /* Temperature range: 60°C and above */
    {
        R_e = (992 * pow(SOC, 6) - 3406 * pow(SOC, 5) + 4667 * pow(SOC, 4) - 3263
* pow(SOC, 3) + 1225 * pow(SOC, 2) - 233 * SOC + 48)*1e-3;
    }

    /* Calculate heat generation */
    q_gen = I * I * R_e - I * T * dE_dT;

    /* Calculate heat generation per unit volume */
    q_gen_V = q_gen / BatteryVolume;

    } else if (cycle_time <= 1020.0) {
        /* Rest phase */
        q_gen_V = 0.0;
    } else {
        /* Charge phase */
        q_gen_V = heat_gen_factor * (2.6910 / BatteryVolume);
    }

    return q_gen_V;
}
```

Appendix B

Experimental setup and design overview of the hybrid battery thermal management system

Experimental approach

This research encompasses the development of an experimental framework aimed at designing a hybrid battery thermal management system. To conduct experimental tests, various HBTMS designs for single cells and battery packs will be 3D printed using an EP-M250 3D metal printer based on metal powder bed fusion technology or selective laser melting. The 3D printing process includes manufacturing battery and PCM housings as well as cooling plates. The thermophysical properties of AlSi10Mg powder that will be used for 3D printing are presented in Table 7-1. Copper tubes will be integrated into the cooling plates to facilitate water flow. Longitudinal copper foam fins and layers, cut from copper metal foams, will be press-fitted to the PCM housing and copper tube. Detailed design of the HBTMS for a single cell and battery pack are presented in Figure 7-1 and Figure 7-2, respectively. For both HBTMS, a 16 mm diameter hole has been considered at the bottom for the required connections along with sufficient space for the wires in the stand section. To provide enough space for thermocouples to be installed on the battery surface, a 2 mm gap has been taken into account between the battery and the inner wall of the battery housing. Also, it is important to avoid any thermal resistance in the mentioned gap. Therefore, after proper installation of the thermocouples, the gap will be filled with thermally conductive material (Fischer Elektronik silicon-free thermal compound).

Table 7-1. AlSi10Mg thermophysical properties

Density (g/cm^3)	Thermal conductivity (W/m.K)	Specific heat capacity (J/kg.K)	Coefficient of thermal expansion (1/K)
2.68	120-190	905	23×10^{-6}

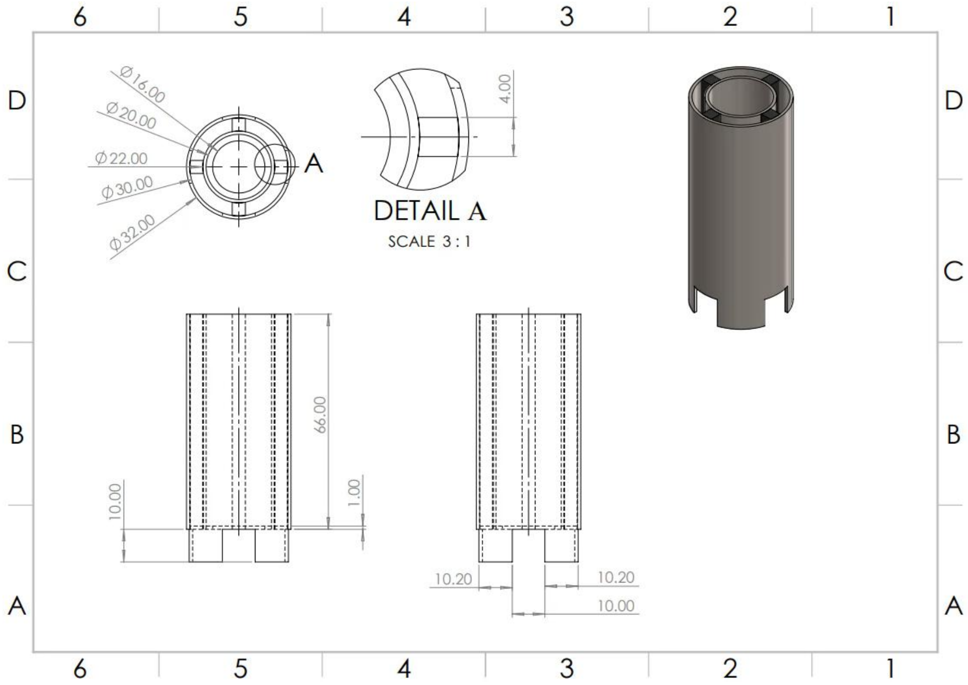

Figure 7-1. Dimensional details of designed HBTMS for single cell.

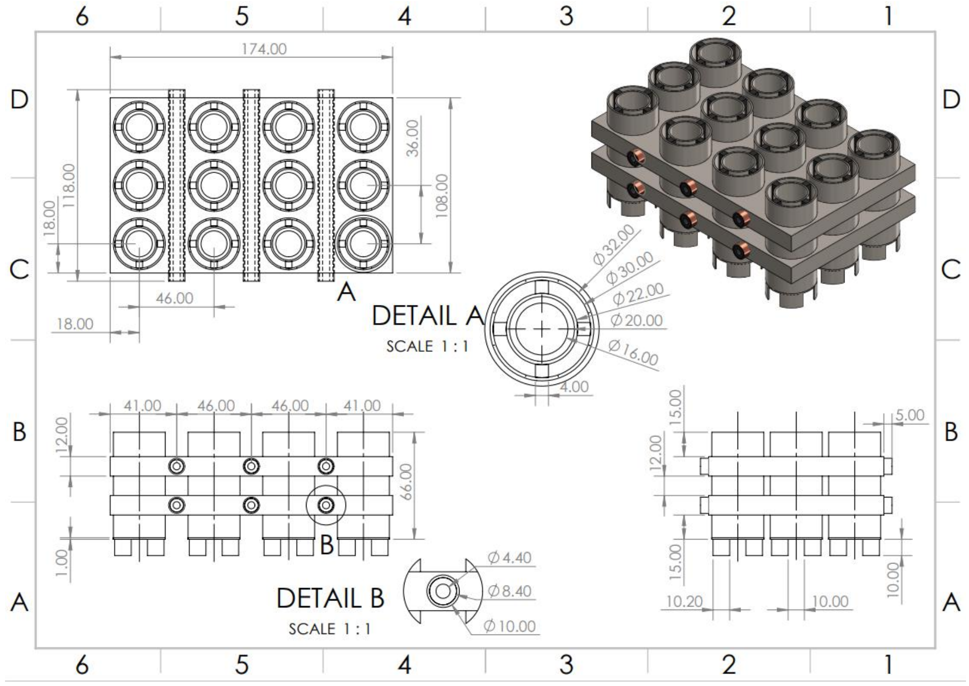

Figure 7-2. Dimensional details of designed HBTMS for battery pack.

The Samsung 25R 18650 2500 mAh high drain flat top lithium-ion battery, shown in Figure 7-3, will be used for the tests. The battery's specifications are provided in Table 7-2. For charging and discharging the battery, a Chroma programmable battery charge/discharge tester device (Model 17216-6-6), depicted in Figure 7-4, will be employed. This device includes suitable connectors and software from the manufacturer to design charge and discharge cycles and to capture the battery's current and voltage. To measure surface temperature, K-type thermocouples (Picotech SE027) will be attached to the battery's surface using high-temperature adhesive tape. A Picotech TC-08 data logger will record the temperature readings. As shown in Figure 7-5, in order to connect the battery cycler connectors, nickel belts will be welded to battery ends using a spot welder device (BIFRC).

Sketch of the experimental setup of the HBTMS for single cell and battery pack is presented in Figure 7-6. After calibration and ensuring the proper function, the thermal management efficacy of the HBTMS utilising PCM, copper foam fins, and liquid cooling will be evaluated through a series of experimental tests. Variations will be made to the charging/discharging rates and operating conditions to test various scenarios. To confirm the validity and accuracy of the experimental results, all tests will be conducted repeatedly.

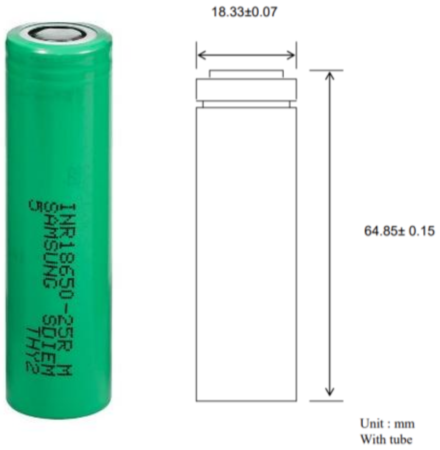

Figure 7-3. Samsung 25R 18650 battery dimensions.

Table 7-2. Specification of a Samsung 25R 18650 battery.

Parameter	Value
Nominal Capacity	2500 mAh
Nominal Voltage	3.7 V
Discharge End Voltage	2.5 V
Standard Charging Current	1.25 A
Charging Maximum Voltage	4.20 V
Continuous Discharging Current	20A
Dimensions	65 mm (L) x 18 mm (D)
Weight	45g
Positive Cap	Flat top
Operational Temperature Range	0 to 50 degrees C (best below 30 degrees C)

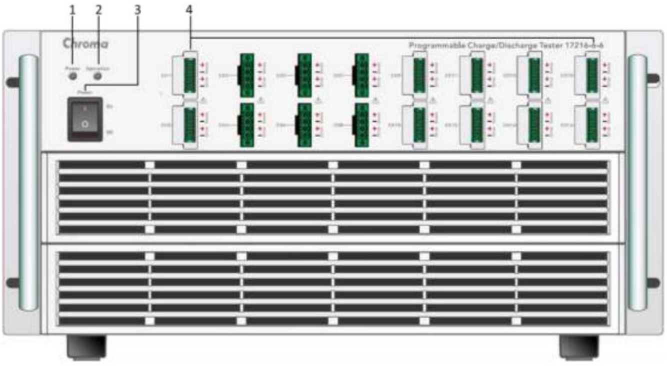

Figure 7-4. Chroma battery tester device.

(a)

Figure 7-5. Handheld spot welding device.

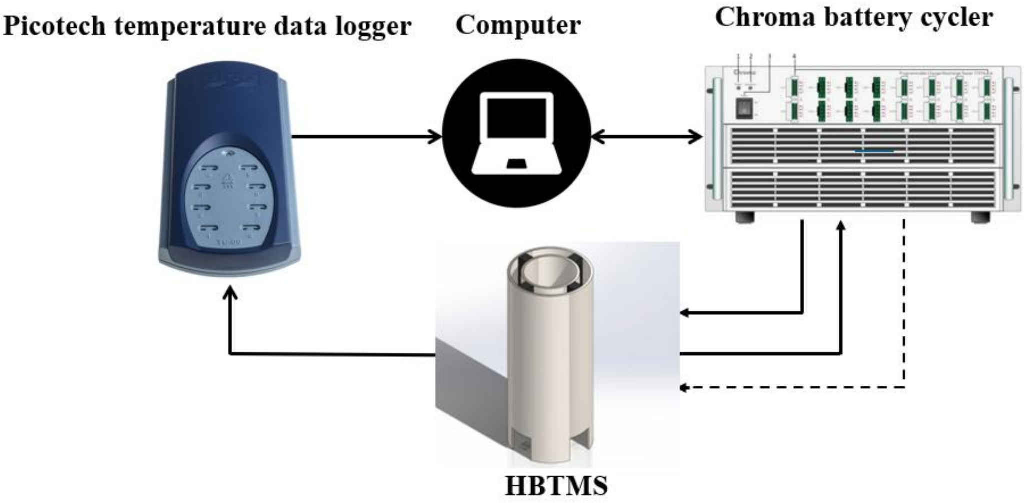

(a)

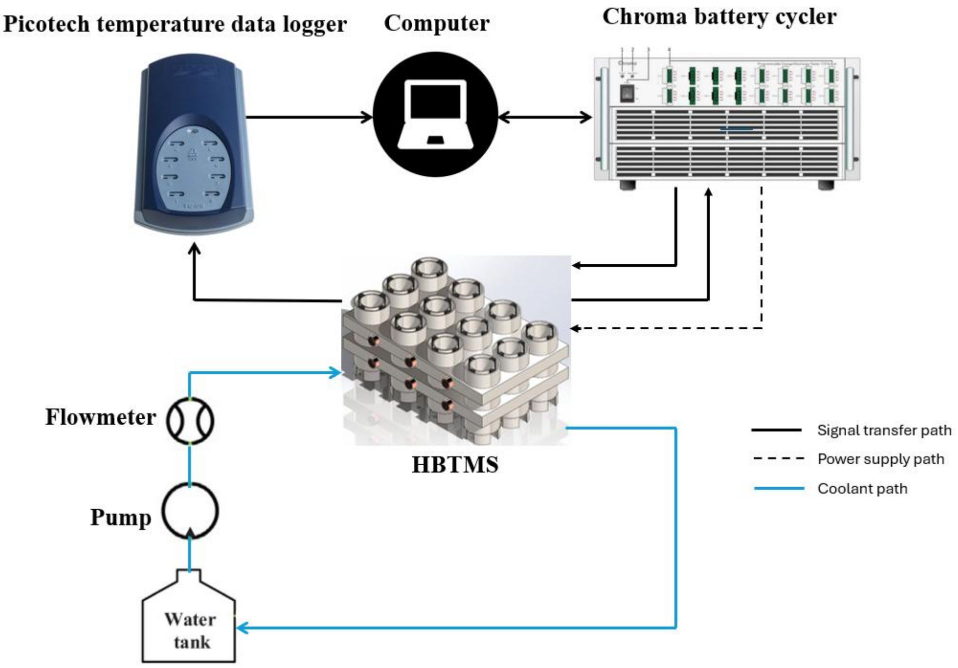

(b)

Figure 7-6. Sketch of the experimental set up of HBTMS for (a) single cell and (b) battery pack

Risk assessment

For the experimental study of HBTMS, a comprehensive risk assessment was conducted, incorporating evaluations for various hazards as outlined in the Material Safety Data Sheets (MSDS) and the Control of Substances Hazardous to Health (COSHH) assessments. The investigation entailed handling various chemicals, notably paraffin wax as the Phase Change Material (PCM), and lithium-ion batteries.

The MSDS for paraffin wax (Sigma-Aldrich, CAS No. 8002-74-2) indicated that, although not classified as hazardous under Regulation (EC) No. 1272/2008, PPE such as gloves, safety goggles, and masks were required to mitigate exposure risks. The COSHH assessment detailed safe handling and storage practices, noting daily use of approximately 100 grams of PCM, which is melted and poured into battery modules. Proper ventilation and cool, dry storage were emphasised.

For the lithium-ion batteries (Samsung SDI, INR18650-25R), the COSHH assessment highlighted the necessity of constant temperature and voltage monitoring during experiments to prevent overcharging and potential fire or explosion hazards. The batteries, used daily in quantities of 9 to 12, posed risks through inhalation, skin contact, and ingestion if damaged. PPE such as face masks, gloves, and safety goggles were mandated, along with storage arrangements to keep the batteries dry, protected from sunlight, and securely locked.

The risk assessment form considered a range of potential hazards, such as falls and trips caused by trailing cables, electric shocks, chemical exposure, fire and explosion risks, respiratory problems resulting from battery leakage, slips and trips, back injuries from manual handling, contact with sharp edges, and burns. Identified control measures included routine visual inspections, utilisation of warning signals, and verification of equipment functionality. Further suggested measures include rearranging the space to avoid the presence of loose cables, conducting Portable Appliance Testing (PAT) after any modifications, and providing SOP and EOP. The final risk ratings were modified to accurately represent the decreased hazards following the implementation of these controls.

Nickel belt spot welding

To connect the Chroma battery cycler device wires, which require two wires for each end of the battery, nickel belts are spot-welded to both ends of the battery. This process is illustrated in Figure 7-7. The welding is performed using gear 3, which has been selected to ensure safe and effective welding, as demonstrated in Figure 7-7 (a). Once the nickel belts are securely welded to the battery, wires are connected to these belts. The connection is made using crocodile clip ends, which clamp onto the welded nickel belts, as depicted in Figure 7-7 (b). This method ensures a stable and reliable electrical connection between the battery and the Chroma battery cycler device.

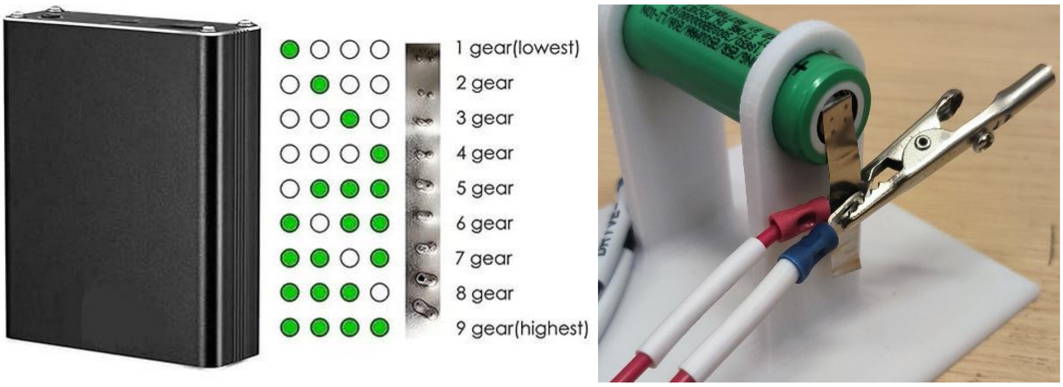

(a) (b)

Figure 7-7. (a) Spot welding device gears and (b) connection of the battery cycler wires.

Battery cycler software

The Chroma battery cycler software user manual was reviewed to gain familiarity with its features and functionalities. Details regarding the 18650 batteries, used as the device under test (DUT), were provided in the software's parameters section. As illustrated in Figure 7-8, a test plan was developed using this software, encompassing the charging and discharging processes of the battery cell.

The test plan includes sub-recipes such as charging with a constant current-constant voltage (CC-CV) method, followed by a constant current (CC) discharge. Initially, the battery is charged with a constant current of 1.25 A (standard charge) or 4 A (fast charge) until the voltage reaches 4.2 V. Subsequently, the charging process continues at a constant voltage of 4.2 V. The discharge of the fully charged battery is carried out at a constant current of 2.5 A. Additionally; appropriate cut-off conditions have been established to terminate each step. The specified current and voltage values were selected based on the battery's datasheet.

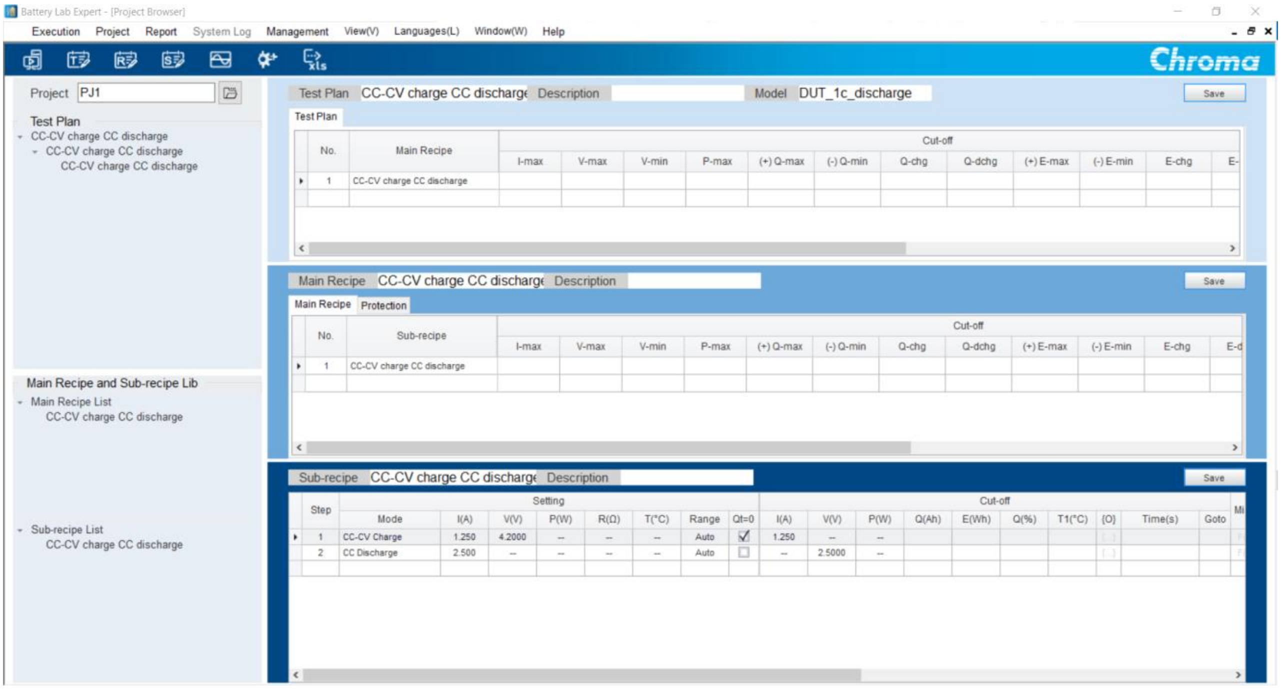

Project PJ1

Test Plan
- CC-CV charge CC discharge
  - CC-CV charge CC discharge
    - CC-CV charge CC discharge

Main Recipe and Sub-recipe Lib
- Main Recipe List
  - CC-CV charge CC discharge
- Sub-recipe List
  - CC-CV charge CC discharge

Test Plan CC-CV charge CC discharge Description Model DUT_1c_discharge

Test Plan

No.	Main Recipe	Cut-off										
		I-max	V-max	V-min	P-max	(+) Q-max	(-) Q-min	Q-chg	Q-dchg	(+) E-max	(-) E-min	E-chg
1	CC-CV charge CC discharge											

Main Recipe CC-CV charge CC discharge Description

Main Recipe | Protection

No.	Sub-recipe	Cut-off										
		I-max	V-max	V-min	P-max	(+) Q-max	(-) Q-min	Q-chg	Q-dchg	(+) E-max	(-) E-min	E-chg
1	CC-CV charge CC discharge											

Sub-recipe CC-CV charge CC discharge Description

Step	Setting								Cut-off									
	Mode	I(A)	V(V)	P(W)	R(Ω)	T(°C)	Range	Qt=0	I(A)	V(V)	P(W)	Q(Ah)	E(Wh)	Q(%)	T1(°C)	{O}	Time(s)	Goto
1	CC-CV Charge	1.250	4.2000	--	--	--	Auto	☑	1.250	--	--							
2	CC Discharge	2.500	--	--	--	--	Auto	☐	--	2.5000	--							

Figure 7-8. Developed test plan for single battery charge and discharge.

Battery holder design

As depicted in Figure 7-9, a single battery holder was designed, and 3D printed using an FDM 3D printing machine. ABS filament, known for its high melting temperature of 110°C, was used in the printing process. Consequently, the printed battery holder is suitable for the specified charge and discharge rates. This holder will be employed for initial charge and discharge tests, as well as for studying the heat generation behaviour of the battery using heat flux sensor.

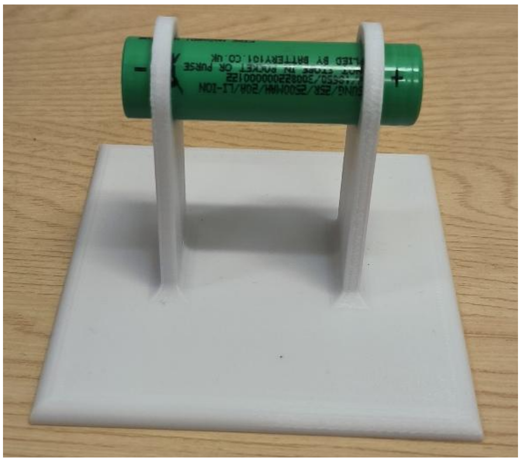

Figure 7-9. Printed battery holder.

Hindering factors and challenges

One of the major challenges in the current investigation has been the construction of the experimental rig for the HBTMS. This task has required additional funding for consumables, particularly the copper metal foams used as porous fins and layers. Due to the lack of precision cutting equipment within the university's workshop, the metal foams must be cut to exact specifications through external suppliers. Another key hindrance has been the delayed full functionality of the 3D metal printer, which is essential for fabricating the custom aluminium components of the HBTMS designed for both single-cell and battery pack configurations. In addition, the implementation of risk assessment measures has faced delays, including the repair and upgrade of ventilation systems and the purchase of certified battery storage units, both of which were affected by prolonged maintenance schedules and delivery lead times. Limitations in temperature-controlled testing environments, such as environmental or thermal chambers, have further constrained the ability to conduct battery experiments under regulated thermal conditions. Furthermore, technical issues have been encountered with the Chroma software, particularly with executing the developed test plan and establishing a stable connection with PCs on the BCU domain. The issues related to battery cycler have since been addressed by coordinating with the IT department to remove the PC from the university domain and through continued consultation with the software supplier.